Editor's Biographies

Lan Li

Lan Li, Ph.D., is an assistant professor of Materials Science and Engineering at Boise State University in Idaho. Dr. Li finished her doctorate in Nanomaterials at the University of Cambridge in the U.K. in 2006, followed by working at the Bio-Nano Electronic Research Center of Toyo University in Japan. She conducted her research as a post-doc associate at the Physics Department of University of Florida and Center for Materials Informatics of Kent State University in Ohio. At Kent State, she worked in collaboration with national labs and universities on the development of computational materials research codes and the transformation of these research codes into modules suitable for effective use in undergraduate education. In 2011, she became a NIST-ARRA senior fellow, working at the National Institute of Standards and Technology in Gainthersburg, Maryland, on energy and sustainability. In late 2012, she joined the Department of Materials Science and Engineering at Boise State University in Idaho. Her research interests include polymers, composite materials for nanoparticles, carbon materials, and porous materials, focused on energy and environmental applications. Currently, she leads the Materials Theory and Modeling Group at Boise State.

Dr. Li was awarded a senior fellowship by the American Recovery and Reinvestment Act Program, as well as the 2014 TMS (The Mineral, Metals and Materials Society) MPMD (Materials Processing & Manufacturing Division) Young Leader Professional Development Award. She presently serves as a vice-chair of the TMS Education Committee and a member of the TMS Integrated Computational Materials Engineering Committee.

Jeffrey Sharp

Jeffrey Sharp, Ph.D., joined Marlow in 1995 as a Member of the Technical Staff, and is now a Sr. Member of the Technical Staff and Sr. Manager of the Materials Research and Development Department. Dr. Sharp's degrees are a B.S. in physics (1986) from the University of Central Arkansas and a Ph.D. in physics (1992) from the University of Tennessee. Immediately prior to joining Marlow, he was a National Research Council Postdoctoral Fellow working at NIST in Gaithersburg, Maryland. At Marlow, Dr. Sharp has guided the conception, development and scale-to-production of Marlow's proprietary MAM/MAM+ bismuth telluride alloys, which have been in production since 2001. Recently, Dr. Sharp led an effort that created a lower cost version of the MAM process to support new business opportunities. He and his team are also working to improve bismuth telluride alloys produced by the Bridgman process. In addition, Dr.

In Polymer Composites for Energy Harvesting, Conversion, and Storage; Li, L., et al.;
ACS Symposium Series; American Chemical Society: Washington, DC, 2014.

Sharp's team pursues new thermoelectric materials with higher performance for both cooling and power generation, including a current effort to commercialize skutterudite alloys for power generation. Dr. Sharp's other responsibilities include peer review activities, intellectual property assessment, and technology strategy/roadmap development.

Winnie Wong-Ng

Winnie Wong-Ng received a B. Sc. degree in Chemistry (minor in Physics) from the Chinese University of Hong Kong, a Ph.D. degree in Inorganic Chemistry from Louisiana State University, followed by post-doctoral and research associate/lecturer appointments in the Chemistry Department of University of Toronto, Canada. After working for the International Centre for Diffraction Data (ICDD) as a critical review scientist and crystallographer, she joined the Ceramics Division of National Institute of Standards and Technology (NIST) as a staff chemist in 1988, where she has been employed since then. Her main research areas at NIST have included measurements and standards of technologically important materials in bulk and thin and thick film forms. Her research has focused on the phase equilibria, X-ray crystallography, and crystal chemistry of oxide materials. Currently she is the leader of the project "Measurements, Standards, and Data for Energy Conversion Materials" in the Materials for Energy and Sustainable Development Group of the Materials Measurement Science Division. She also works on the CO_2 Mitigation project.

She is a fellow of three scientific organizations: the American Crystallographic Association, the American Ceramic Society, and ICDD. She received two Bronze Medals from the United States Department of Commerce (2002 and 2008) for her superconductivity research, the 2004 McMurdie Award from ICDD for her contributions to the Powder Diffraction File, and the 2007 Spriggs Phase Equilibria Award from the American Ceramic Society. She has more than 300 publications and has given more than 250 presentations including 60 invited talks. She is also a co-organizer of about 40 symposia/workshops at various scientific meetings,

She is an associate editor of Journal American Ceramic Society and is the international report editor of Powder Diffraction. She was on the Board of Directors of ICDD (2010-2014), and was a member of the Board of Directors of the Applied Superconductivity Conference (2006-2012). She was the past chair of the Electronics Division of the American Ceramic Society (2005-2006), the past chair of Ceramics Subcommittee of ICDD (1994-2000), and the local chair of the 1998 American Crystallographic Association annual meeting in Arlington, VA. She has served as Secretary/treasurer of U.S. National Committee for Crystallography (USNCCr, 2000-2003), past president of NIST Association of Asian Pacific Americans (2000-2003), guest editor of a special issue of J. Research of NIST (2001), and guest co-editor of a special issue of J. American Ceramic Society (2007-2008).

Polymer Composites for Energy Harvesting, Conversion, and Storage

In Polymer Composites for Energy Harvesting, Conversion, and Storage; Li, L., et al.;
ACS Symposium Series; American Chemical Society: Washington, DC, 2014.

In Polymer Composites for Energy Harvesting, Conversion, and Storage; Li, L., et al.;
ACS Symposium Series; American Chemical Society: Washington, DC, 2014.

ACS SYMPOSIUM SERIES **1161**

Polymer Composites for Energy Harvesting, Conversion, and Storage

Lan Li, Editor
Boise State University
Boise, Idaho

Winnie Wong-Ng, Editor
National Institute of Standards and Technology
Gaithersburg, Maryland

Jeff Sharp, Editor
Marlow Industries
Dallas, Texas

Sponsored by the
ACS Division of Polymer Chemistry, Inc.

American Chemical Society, Washington, DC

Distributed in print by Oxford University Press

In Polymer Composites for Energy Harvesting, Conversion, and Storage; Li, L., et al.;
ACS Symposium Series; American Chemical Society: Washington, DC, 2014.

Library of Congress Cataloging-in-Publication Data

Polymer composites for energy harvesting, conversion, and storage / Lan Li, editor, Boise State University, Boise, Idaho, Winnie Wong-Ng, editor, National Institute of Standards and Technology, Gaithersburg, Maryland, Jeff Sharp, editor, Marlow Industries, Dallas, Texas ; sponsored by the ACS Division of Polymer Chemistry, Inc., American Chemical Society, Washington, DC.

pages cm. -- (ACS symposium series ; 1161)

Includes bibliographical references and index.

ISBN 978-0-8412-2936-5 (permanent paper) 1. Energy harvesting--Materials. 2. Polymers--Electric properties. 3. Polymeric composites--Electric properties. I. Li, Lan (Materials scientist) II. Wong-Ng, W. (Winnie) III. Sharp, J. (Jeffrey), 1964-

TK2897.P65 2014

621.042--dc23

2014019004

The paper used in this publication meets the minimum requirements of American National Standard for Information Sciences—Permanence of Paper for Printed Library Materials, ANSI Z39.48n1984.

Distributed in print by Oxford University Press

PRINTED IN THE UNITED STATES OF AMERICA

Foreword

The ACS Symposium Series was first published in 1974 to provide a mechanism for publishing symposia quickly in book form. The purpose of the series is to publish timely, comprehensive books developed from the ACS sponsored symposia based on current scientific research. Occasionally, books are developed from symposia sponsored by other organizations when the topic is of keen interest to the chemistry audience.

Before agreeing to publish a book, the proposed table of contents is reviewed for appropriate and comprehensive coverage and for interest to the audience. Some papers may be excluded to better focus the book; others may be added to provide comprehensiveness. When appropriate, overview or introductory chapters are added. Drafts of chapters are peer-reviewed prior to final acceptance or rejection, and manuscripts are prepared in camera-ready format.

As a rule, only original research papers and original review papers are included in the volumes. Verbatim reproductions of previous published papers are not accepted.

ACS Books Department

In Polymer Composites for Energy Harvesting, Conversion, and Storage; Li, L., et al.;
ACS Symposium Series; American Chemical Society: Washington, DC, 2014.

Preface

The 245th American Chemical Society (ACS) Meeting and Exposition was held in the Morial Convention Center, New Orleans, Louisiana, on April 7–11, 2013. The ACS's meeting core theme was The Chemistry of Energy and Food. This proceedings volume contains articles that were presented at the symposium on Polymer Composites for Energy Harvesting, Conversion and Storage. The symposium has brought together experts from the different areas of polymer composite research to address the scientific, engineering, economic, environmental, and health issues involved in the production and use of polymer composites. The symposium has also provided a forum for researchers to introduce the high-performance, low-cost, and environmentally friendly polymer composites and techniques for energy applications into the marketplace.

Based on the symposium content, we invited the speakers to turn their symposium presentations and research work into 9 chapters for this proceedings volume. The volume explores polymer composites in terms of their chemical synthesis, characterization, and applications in the energy field, from photovoltaics to fuel cells, from thermoelectrics to energy harvesting and storage. The articles include state-of-art synthesis, characterization, and measurement techniques applied to polymer composites. Such methods addressed the key challenges involved in the processing of polymer composites, such as structural and morphological control, interface characterization, property optimization, and the identification of potential candidates for desired performance, etc. The order of the articles in the proceedings volume is different from that of their presentations at the meeting. This volume contains updates to existing polymer composite publications with the newest research work in energy applications, as well as reviews that present new evaluation and analyses of published research. In summary, all the articles in the proceedings volume reveal the latest research on polymer composites, and are available source material for researchers and managers working in this field.

The success of the symposium and the publication of the proceedings could not have been possible without the effort and support of the ACS and other organizers of the program. We acknowledge Mr. Tim Marney, Ms. Aimee Greene, and Ms. Arlene Furman for their involvement in editing and producing this book. Special thanks are due to the speakers, authors, manuscript reviewers, and ACS program coordinators and officials for their contributions.

In Polymer Composites for Energy Harvesting, Conversion, and Storage; Li, L., et al.;
ACS Symposium Series; American Chemical Society: Washington, DC, 2014.

Lan Li, Ph.D.
Department of Materials Science and Engineering
Boise State University
1910 University Drive
Boise, ID 83725-2090
lanli@boisestate.edu (e-mail)

Winnie Wong-Ng, Ph.D.
Materials for Energy and Sustainable Development Group
Materials Measurement Science Division
National Institute of Standards and Technology (NIST)
100 Bureau Drive, Stop 8520
Gaithersburg, MD 20899

Jeff W. Sharp, Ph.D.
Materials Research and Development Department
Marlow Industries, Inc.
10451 Vista Park Road
Dallas, Texas 75238

Chapter 1

Advances in Piezoelectric Polymer Composites for Vibrational Energy Harvesting

Cary Baur,*[,1] Daniel J. Apo,[2] Deepam Maurya,[2] Shashank Priya,[2] and Walter Voit[3]

[1]Department of Chemistry, and The Alan G. MacDiarmid Nanotech Institute, The University of Texas at Dallas, 800 W. Campbell Road, Richardson, Texas 75080, U.S.A.
[2]Bio-inspired Materials and Devices Laboratory (BMDL), Center for Energy Harvesting Materials and Systems (CEHMS), Virginia Polytechnic Institute and State University, 310 Durham Hall, Blacksburg, Virginia 24061, U.S.A.
[3]Department of Materials Science and Engineering, Department of Mechanical Engineering, Department of Bioengineering, and The Alan G. MacDiarmid Nanotech Institute, The University of Texas at Dallas, 800 W. Campbell Road, Richardson, Texas 75080, U.S.A.
***E-mail: cary.baur@utdallas.edu.**

This chapter provides an overview of piezoelectric vibrational energy harvesting and outlines significant advances in polymer composites for harvesting applications. The piezoelectric phenomenon is described and relevant equations are provided and explained. Several prominent types of piezoelectric materials are discussed, followed by a description of the advances made through the combination of polymers and particles to create piezoelectric composites. An in-depth description detailing how to significantly increase the piezoelectricity of poly(vinylidene difluoride) through the incorporation of carbon nanomaterials such as single-walled nanotubes (SWNTs) and Buckminster fullerenes (C_{60}) is given, followed by the description of a new, lead-free ceramic material that is a promising candidate for use in non-toxic polymer composites. Finally, a comprehensive description of the design and modeling of piezoelectric polymer composite bimorphs for vibrational energy harvesting is provided.

In Polymer Composites for Energy Harvesting, Conversion, and Storage; Li, L., et al.;
ACS Symposium Series; American Chemical Society: Washington, DC, 2014.

An Introduction to Piezoelectric Energy Harvesting

The ever decreasing size and energy consumption of small electronics has driven recent efforts to enable "self-powered" devices that require no external power for operation, either continuous or punctuated. The ability to power small devices though ambient, harness-able energy is leading to a paradigm shift in modern wireless communication in which many objects around us, such as sensors and transmitters, can remain in constant communication (*1*),. Termed the "Internet of Things", these wireless networks work collectively to both monitor and perform designated tasks with no battery replacement or recharging and are enabled by persistent sensor nodes and underlying harvesting technologies (*2*). These advances have led to a growing body of research in the field of vibrational energy harvesting to enable the powering of systems through environmental vibrations. Vibration-harvesting solutions continue to be improved with new materials and composites and optimized through clever engineering solutions. Concurrently, low power electronics researchers continue to reduce power consumption and energy demands for increasingly complex sensors and sensing systems, leading to a convergence which will yield new paradigms for information exchange that will permeate many facets of life in society. Today's bottlenecks in interacting with smart devices, such as frequent replacement of batteries or charging limited to discrete locations will be eliminated.

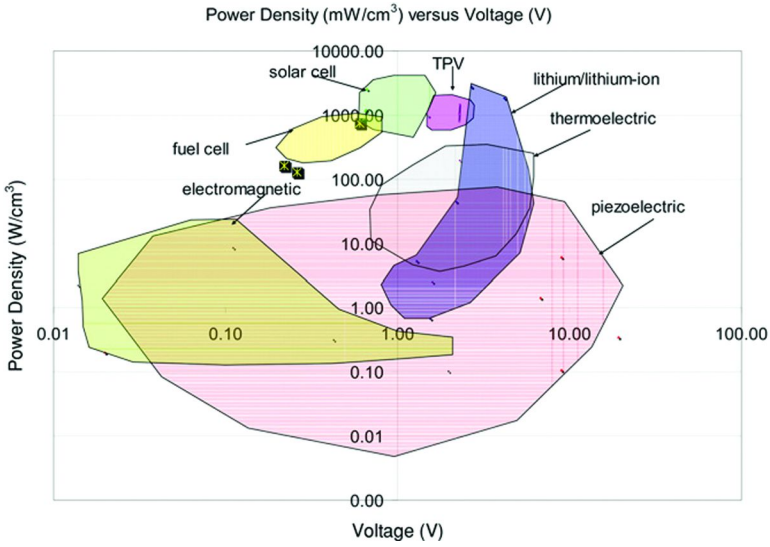

Figure 1. Power Density vs. Voltage Plot of Various Regenerative Power Supplies. Reproduced with permission from (6), 2008, © IOP Publishing.

There are three well known vibrational-to-electrical energy transduction mechanisms: electromagnetic, electrostatic, and piezoelectric (*3*). While all three mechanisms have been extensively explored over the last decade,

In Polymer Composites for Energy Harvesting, Conversion, and Storage; Li, L., et al.;
ACS Symposium Series; American Chemical Society: Washington, DC, 2014.

several prominent review articles have placed emphasis on piezoelectric energy harvesting due to its large power densities and ease of application (*4*, *5*). The power density vs. voltage plot (Figure 1) shows that piezoelectric materials cover the largest range of power densities, comparable to those of lithium ion batteries and thermoelectric generators (*6*). In addition, while most energy harvesting mechanisms yield very low voltages that require processing and up-converting to produce a usable voltage, piezoelectric harvesters can create voltages large enough to be used directly.

While it should be noted that the power density of a material is not sufficient to absolutely compare its effectiveness in a harvesting device without knowing the input energy, it does give a rough idea of the possibilities and limitations. It is apparent from this graph that piezoelectrics have one of the best combinations of power density and voltage potential and emerging synthetic techniques for engineering polymeric piezoelectric composites hold tremendous promise for solution processable harvesting solutions with sufficient properties.

Piezoelectric materials have non-centrosymmetric point groups resulting in net distortion from their equilibrium positions with the application of an electric field or mechanical stress. This property allows for the conversion of mechanical stress into electrical charge, known as the "direct" effect, and the conversion of electrical fields to mechanical strain, the "converse" effect (*7–9*). Pressure sensors, structural measurement and vibrational energy-scavenging devices utilize the direct piezoelectric effect, while the converse piezoelectric effect enables shape control, active vibrational dampening, and actuation (*10–13*). The two most common piezoelectric parameters are the piezoelectric strain coefficient, *d*, and the piezoelectric voltage coefficient, *g*. The *d* and *g* coefficients are tensors of rank 3 defined as follows:

$$d_{ij} = \frac{dP_i}{d\sigma_j} \qquad \text{and} \qquad g_{ij} = \frac{dE_i}{d\sigma_j} \tag{1}$$

$$\text{i} = 1, 2, 3 \text{ and } \text{j} = 1, 2, 3, 4, 5, 6$$

where P_i is the polarization vector, E_i is the electric field vector, and σ_j is the stress tensor. The two scripts *i* and *j* represent the relative directions of the values. In practical terms, the d_{33} coefficient is used to denote the induced polarization (parallel to the direction in which the material is polarized) per unit stress, or the induced strain per electric field and is typically measured in pico coulombs per Newton. The g_{33} coefficient denotes the induced electric field (parallel to the direction in which the material is polarized) per unit stress, or the induced strain per electric displacement and is typically expressed in millivolt meters per Newton

Further, d_{ij} and g_{ij} can be related by:

$$g_{ij} = \frac{d_{ij}}{\varepsilon_0 \varepsilon_r} \tag{2}$$

where ε_0 is the permittivity of free space typically measured in Farads per meter and ε_r is the relative dielectric constant, a dimensionless number. From this relationship it can be observed that piezoelectric materials with high dielectric

In Polymer Composites for Energy Harvesting, Conversion, and Storage; Li, L., et al.;
ACS Symposium Series; American Chemical Society: Washington, DC, 2014.

constants generally have high *d* values and materials with low dielectric constants have high *g* values. For energy harvesting applications large *d* and *g* values are required along with material compliance and flexibility.

While the *d* and *g* coefficients provide insight into the generated charge per unit applied force, the total efficiency of energy conversion, known as the electro-mechanical coupling factor, *k*, can be expressed between 0 and 1 as (*14*):

$$k_{ij} = \frac{d_{ij}}{\sqrt{\varepsilon_o \varepsilon_r s_{ij}}} \quad (3)$$

where s_{ij} is the compliance (or inverse of stiffness) typically measured in meters per Newton (*15*). This relationship is somewhat intuitive in that one would expect a stiffer material to experience larger internal strains, resulting in a larger internal energy. Likewise, while increasing the dielectric constant allows for a greater amount of internal charge generation, it also increases the capacitance and the force needed to displace charge, resulting in a lower efficiency.

Table 1. Piezoelectric and Dielectric Constants of Common Piezoelectric Material*

Material	*Relative Dielectric Constant, ε_r*	*Piezoelectric Charge Constant, d_{33} (pC/N)*	*Piezoelectric Voltage Constant, g_{33} (10^{-3} V m/N)*
$BaTiO_3$	1700	191	12.6
Quartz	4.5	2.3 (d 11)	50.0
PVDF	13	-33	-339.0
PZT-4	1300	289	25.1

* Reproduced with permission from ((*16*)), 2008, © Springer.

While the piezoelectric effect can be found in materials such as quartz, ceramics, and polymers, most piezoelectric based energy harvesting applications utilize ceramics due to their high *d* values. As shown in Table 1, ceramic materials such as barium titanate ($BaTiO_3$) and lead zirconate titanate (PZT) have piezoelectric charge constant (d_{33}) values in the hundreds of pico coulombs per Newton, while the best performing polymer, poly(vinylidene difluoride) (PVDF), possesses a much lower constant of 33 (*16*). Practically speaking, this renders ceramics much more suitable than polymers for strain dependent applications such as actuators. However, PVDF possesses a large g_{33} voltage constant due to its relatively low dielectric constant, making it a much more sensitive material than ceramics, requiring little force to trigger a piezoelectric response. Because of this property, PVDF is used largely in pressure and acoustic sensors.

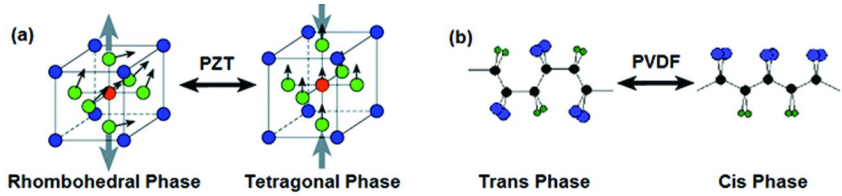

Figure 2. The non-piezoelectric (left) and piezoelectric (right) structures of (a) lead zirconate titanate (PZT) – blue atoms are Pb, green atoms are O, orange atoms are either Zr or Ti and (b) PVDF – black atoms are C, blue atoms are F, and green atoms are H. Reproduced with permission from (17), 2010, © Royal Society of Chemistry.

PZT (Figure 2(a)) possesses a rhombohedral structure at high temperatures, but upon cooling to below the Curie temperature, the unit cell conforms to a tetragonal phase, with the center zirconium or titanium atom displaced out of the geometric center, giving rise to a permanent charge displacement and piezoelectricity (*17*). While relatively high d_{33} constants allow ceramics to produce large voltages sufficient to charge a battery, they are naturally limited by their high stiffness, brittleness, and low processability. For many growing, high-value applications, compliant materials with lower mechanical impedance, cost and driving voltages are required (*18*).

The discovery of piezoelectric polymers has led to a relatively new class of elastically compliant electroactive materials (*19–21*). Piezoelectric polymers have been incorporated into a broad range of applications including sensors, actuators, ultrasonic imaging, integrated microelectromechanical systems and ferroelectric memory devices (*22*). PVDF, shown in Figure 2(b), naturally occurs largely in the non-piezoelectric *trans* phase. Through processing techniques such as thermal treatment and drawing under specific conditions, the polymer can be transformed into the piezoelectric *cis* phase in which permanent fluorine-carbon dipoles are developed. However, the low voltage and force generation of piezoelectric polymers have greatly limited their application (*23*). In order to enhance the performance of piezoelectric polymers, composites incorporating ceramic particles, inorganics and carbon nanomaterial have been fabricated to increase strength, stiffness, dielectric constant and piezoelectricity.

The majority of piezoelectric harvesting devices are comprised of bimorph (two layers) cantilever beams that are mounted directly to the source of vibration. Local vibration causes the cantilever to oscillate, resulting in charge movement and the production of an alternating current (*24*). Figure 3(left) shows a schematic representation of a typical energy harvesting bimorph. The harvester shown is composed of two piezoelectric strips that sandwich an electrode of varying thickness and stiffness, depending on the desired vibrational frequency. The outer surfaces of the bimorph are electroded with a compliant conductive metal (copper, gold etc.). The piezoelectric elements are usually electrically poled in opposite directions, thus resulting in complimentary strains with an applied voltage.

Bimorphs can be configured in either antiparallel or parallel configurations. While antiparallel actuators have only outer electrodes of applied opposite voltage, parallel systems have an inner electrode that is of opposite voltage as both of the outer electrodes (*25*).

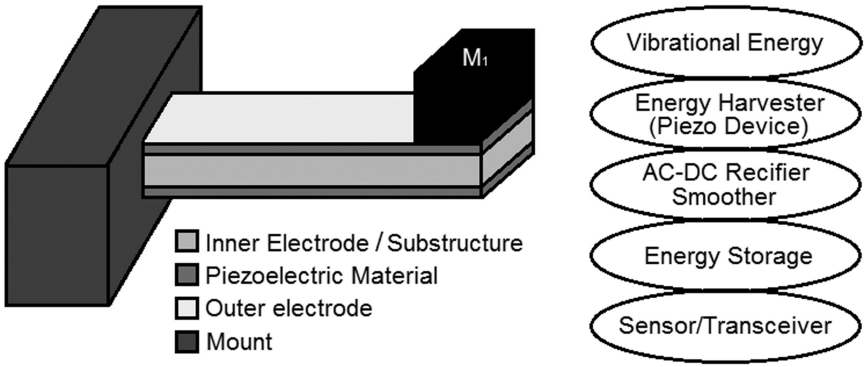

Figure 3. Piezoelectric Bimorph (Left) Piezoelectric Energy Harvesting System (Right).

A general energy harvesting circuit is described in Figure 3(right). The energy generation from the bimorph strip is in the form of an alternating current, thus resulting in a signal that must be converted into a DC voltage via a voltage rectifier in order to charge a capacitor or battery. The rectified DC voltage is often run through a smoothing capacitor or impedance controller to optimize power transfer to the energy storage unit. Finally, the harvested energy is used to power a small electronic device such as a sensor or transceiver.

Significant Advances in Piezoelectric Polymer/Ceramic Composites

In order to overcome the low compliance of ceramics and the low piezoelectricity of polymers, Newnham and other researches at Pennsylvania State University introduced piezoelectric composites which combined passive polymer matrixes with piezoelectric ceramic particles, utilizing the distinct advantages of each material (*26–29*). In their work, they identified a distinction in properties between particle connectivity patterns in composites, and introduced nomenclature to differentiate these composites. The composites are annotated in the format of *x-y*, where *x* is the number of dimensions in which the particles are continuously connected to each other, and *y* is the number of dimension in which the matrix is connected to itself. For example, a randomly oriented composite in which the particles are not connected in a defined pattern would be denoted *0-3*, whereas a pillar type composite would be denoted *1-3*. Polymer-ceramic composites with *0-1* connectivity have been widely researched in the past to improve flexibility, dielectric performance and piezoelectricity.

In Polymer Composites for Energy Harvesting, Conversion, and Storage; Li, L., et al.;
ACS Symposium Series; American Chemical Society: Washington, DC, 2014.

Table 2. Significant 0-1 Ceramic/Polymer Composites

Ceramic	*% Volume*	*Host*	d_{33}	*Source*
PTCa	50	Epoxy	22	(*30*)
PTCa	65	P(VDF-TrFE)	28	(*31*)
PTCa	20-50	Rubber	17-44	(*32*)
Pt	70	Acrylic	32	(*33*)
Pzt	67	PVDF	48	(*34*)
Pzt	50	P(Vdf-TrFE)	10	(*31*)
$(Pb,Bi)TiO_3$	35	Epoxy	41	(*35*)

A number of groups have explored the addition of piezoelectric ceramics into both passive and active polymers. Table 2 presents a few significant advances in composites in the published literature. Non-piezoelectric host polymers such as rubbers, thermosetting epoxies and acrylics have been successfully composited with piezoelectric ceramics such as lead titanate (PT), calcium modified lead titanate (PTCa), lead titanium oxide ($PbTiO_3$) and lead zirconate titanate (PZT). These composites have resulted in piezoelectric d values roughly equal to that of PVDF. However, the best results have been attained when using a piezoelectric ceramic and piezoelectric polymer, resulting in a 50% increase in d_{33} with the incorporation of PZT ceramic into PVDF (*34*).

Dias and Das Gupta fabricated composites of varying piezoelectric ceramics and polymers (both passive and active) (*31*). Composites of PTCa and poly(vinylidene difluoride – tri-fluoroethylene) P(VDF-TrFE) were studied and it was found that a d_{33} value of 55 pC/N could be achieved. The piezoelectricity of the composite was limited by the electrical breakdown of the material, which was close to the coercive field of the ceramic particles. Their conclusion was that although the d_{33} increased significantly, the g_{33} was naturally lowered. However, composites offer advantages such as being easier to polarize and the ability to be self-supporting, needing no additional substrate.

Furukawa, Fujino, Ishida and Fukada explored composite systems of various polymers with PZT particles, leading to their proposal of the model shown in Figure 4, where *0-3* composites possess the average properties of the polymer and ceramic, where *Y* is the Young's Modulus measured in mega Pascals (MPa) and ε is the elastic constant (*36*, *37*). When this model was used to predict *d* and permittivity values for a composite by other groups, it was found that both values were often higher than expected. In order to account for the deviations in this modeling of 0-3 connectivity, Pardo, Mendiola and Alemany introduced a new model that assumes that the composite contains a certain amount of mixed connectivity, 0-3, 1-3, 2-3 (*38*). Zewdie and Brouers produced a similar calculation technique based on local field coefficients and both models have been verified as reasonably accurate (*39*).

In Polymer Composites for Energy Harvesting, Conversion, and Storage; Li, L., et al.;
ACS Symposium Series; American Chemical Society: Washington, DC, 2014.

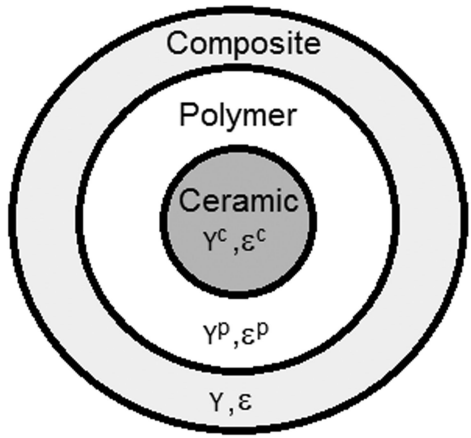

Figure 4. 0-3 composites theoretically show approximately the average properties of the components. Reproduced with permission from (36), 1976, © IOP Publishing.

Recent Advances in Piezoelectric Polymer/Nanocarbon Composites

In the past, carbon nanotubes (CNTs) have been used to improve piezoelectric performance of PVDF through an increase in Young's modulus (*40–42*). These reports, however, yielded no comprehensive mechanism of piezoelectric enhancement. More recently, Baur incorporated both Buckminster fullerenes (C_{60}) and single-walled carbon nanotubes (SWNT) into PVDF and reported a 2× increase in piezoelectricity for both composites. C_{60} molecules are comprised of an sp^2 hybridized structure similar to that of CNTs, but are spherical opposed to the tubular structure of CNTs (*43*). The difference in size and geometry of these particles, while possessing similar structure and electrical properties, allows for a useful comparison to be made, and mechanisms of enhancement to be illuminated.

Figure 5 shows the relationship between the weight percentage of the particles and the Young's modulus (Y) of the composites (*44*). While PVDF exhibits a modulus of 1.2 GPa, the addition of 0.05 wt% SWNT increases the modulus to over 1.3 GPa with a maximum of 1.35 GPa at 0.1 wt%. The increase in Young's modulus is limited by both entanglements among the nanotubes and also inhomogeneities in the system. The C_{60} composites as compared to the SWNTs have relatively less effect on increasing the modulus per added weight, but more favorable mixing leads to composites that allow for higher loading levels and ultimately can yield higher maximum moduli in excess of 1.55 GPa.

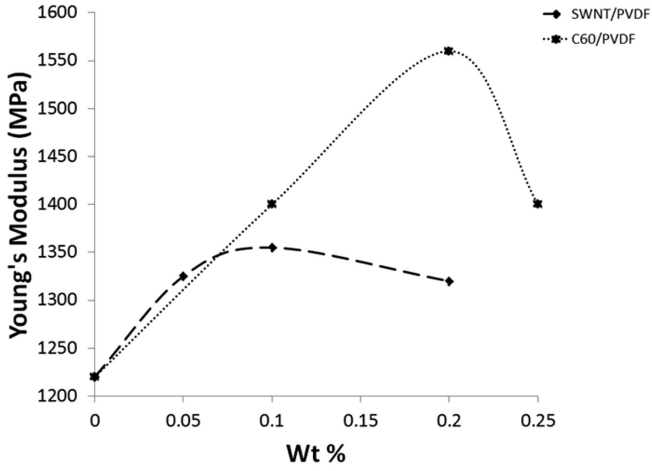

Figure 5. Young's Modulus (Y) of PVDF-C_{60} and PVDF-SWNT as a function of nanoparticle wt%. Reproduced with permission from (44), 2012, © AIP Publishing.

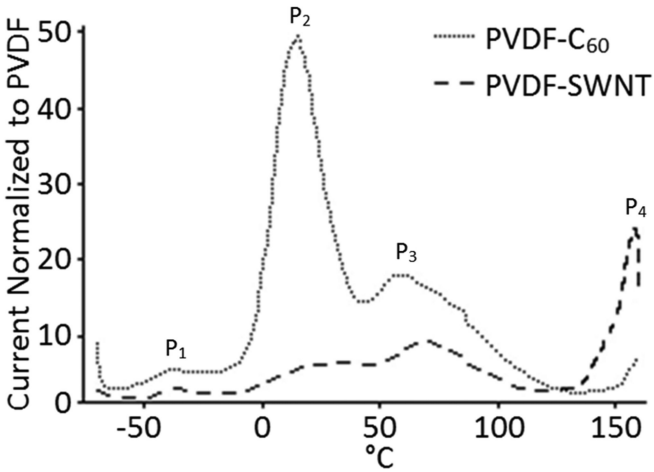

Figure 6. TSC spectra of differential current produced from 0.1 wt% PVDF-SWNT and PVDF-C_{60} normalized to PVDF. Reproduced with permission from (44), 2012, © AIP Publishing.

Although SWNT and C_{60} molecules are not piezoelectric by themselves, they provide excellent sources of polarizable electrons. In order to determine the amount of polarizable trapped charge added to the system, thermally stimulated current (TSC) was conducted on the composited, poled samples (*45*). A TSC cycle consists of heating a charge containing material and mapping both the amount of escaped current and temperature of escape. It is known that charges

In Polymer Composites for Energy Harvesting, Conversion, and Storage; Li, L., et al.;
ACS Symposium Series; American Chemical Society: Washington, DC, 2014.

can be injected into macroscopic voids in porous polymers to create oriented, "quasi-dipoles" known as electrets (*45*). Through TSC, it has been revealed that the internal charge of a porous polymer can be increased more than 50-fold through the addition of space charge and charge injection (*46*). Likewise, charge also can be trapped in dielectric boundaries such as adjoining crystalline/amorphous regions, known as interfacial polarization (*47*). Segmental mobility of interfacial charges increase upon thermal activation to allow "hopping" between charged surface reservoirs to create current bands (*48*). Generally, the deeper and more isolated charges generally require higher temperatures to escape.

There are four dominant peaks in a TSC curve of poled PVDF; two that correspond to the relaxation of polarized dipoles and two from the release of trapped charge in the material (*49*). The spectral peaks measured here clearly show the corresponding four dominant peaks, however the current discharged is much greater than those previously reported for pure PVDF (Figure 6).

The first peak, P_1, is due to the depolarization of dipoles in the amorphous region as relaxation back to the energetically-favored random orientations occurs. P_2 corresponds to the release of subsurface interfacial charge from the material. The C_{60} composite shows an intense, sharp P_2 peak from 0 to 40 °C that is nearly 50 times that of pure PVDF, while the SWNT composite shows a less intense peak 6 times greater. C_{60}, due to its symmetric geometry, allows for a homogenous nanocomposite with a vast number of small uniformly dispersed, low activation energy interfacial charges that are readily mobilized through charge hopping. The SWNT composite shows a less intense P_2 peak due to greater overlap between nanoparticles that create low resistance pathways allowing charge dissipation.

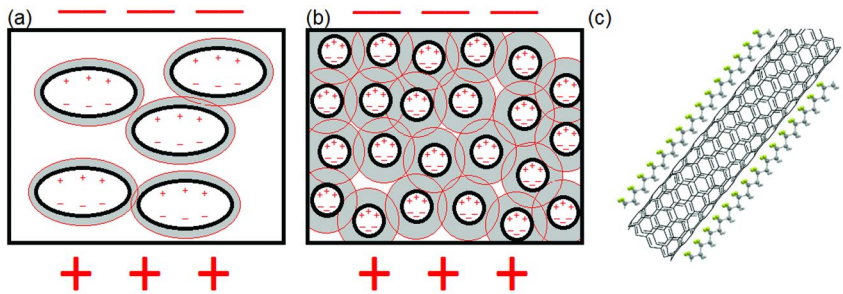

Figure 7. (a) A typical electret material with large, heterogeneous space charge affecting a small area (b) a homogenous electretic system with extended poling fields, created by C_{60} in the material (c) a carbon nanotube with aligned surrounding PVDF due to field enhancement. Reproduced with permission from (44), 2012, © AIP Publishing.

The P_3 peaks correspond roughly to the Curie temperature of the composites, the temperature at which all polarization in the crystalline regions of the polymer is lost and the charges are released. The C_{60} and SWNT composites show P_3 peaks

In Polymer Composites for Energy Harvesting, Conversion, and Storage; Li, L., et al.;
ACS Symposium Series; American Chemical Society: Washington, DC, 2014.

that are roughly 18 and 9 times greater than pure PVDF, respectively. A large release of current at the Curie temperature indicates an efficient polarization of dipoles in the material. This is rational considering delocalization of electrons in both C_{60} and SWNTs can produce 2× local field enhancements when under an electrical field, resulting in an extension of the effective poling radius (Figure 7) (*50*). The delocalized electrons in both C_{60} and SWNT are stabilized by the surrounding dipoles in the polymer, creating macro-dipole sites and increasing charge density. The final peak, P_4, beginning around 150 °C, corresponds to the flow temperature of the PVDF. Upon melting, the remaining high activation energy trapped charges are liberated from the material. Due to natural inhomogeneity, the SWNT composite contains large amounts of charge trapped at deep levels which are released upon melting (25 times), while the C_{60} composite has less charge remaining (7 times PVDF).

As shown in Table 3, the SWNT composites reach a maximum of 65 pC/N at a loading level of just 0.05 wt%, before declining. The C_{60} composite shows a similar increase with a maximum d_{31} value of 63 pC/N. Pure PVDF samples made in the same manner as the composites show a d_{31} of 32 pC/N; thus, the optimized composites exhibit d_{31} values double that of pure PVDF.

Table 3. Piezoelectric d_{31} (pC/N) Values for Composites

Wt %	*0*	*0.05*	*0.1*	*0.2*	*0.25*
C_{60}	32	36	44	63	59
Swnt	32	65	62	54	Na

Figure 8 shows a polarization vs. electrical (PE) field loop for the composites at a voltage of ±10 V. PE-hysteresis loops can give an indication of the ability to polarize a material and the dielectric constant at a particular frequency. All samples show an open curve, which can only be caused by internal heterogeneous charge. The area and slope for both of the nanocomposites greatly increase compared to pure PVDF, and further increases with loading percentage, but is naturally limited by conductivity at high loading levels. The increase in the remnant polarization in the materials is indicative of the fact that molecular dipoles are able to align with the applied electric field. We also observe a leftward shift in the hysteresis loops which is indicative of the formation of an internal bias due to the presence of defect dipoles. In this case, the bias field can be attributed to the net ordering of the interfacial charges as discussed in Figure 7.

The instantaneous slope of the hysteresis curve yields the permittivity of the material ($\varepsilon_0\varepsilon_r$), where ε_r is the relative permittivity and ε_0 is the vacuum permittivity (8.85 pF/m).

In Polymer Composites for Energy Harvesting, Conversion, and Storage; Li, L., et al.;
ACS Symposium Series; American Chemical Society: Washington, DC, 2014.

Shown in Figure 8, there is an increase in ε_r to 11.5 at 0.2 wt% for the SWNT samples, and a larger increase in ε_r to 13.2 for the C_{60} composites, both samples are conductive above this level. There is a slow decrease in ε_r observed in the C_{60} composites after the maximum as opposed to the sharp deterioration in the SWNT due to the spherical shape of C_{60}, which allows for a higher loading level without conduction through the samples due to less overlap. Conductivity measurements revealed that at a loading level of 0.1%, the SWNT composite was 300% more conductive than the C_{60} composite, however, the difference jumped to 1000× at 0.25 wt% at higher levels.

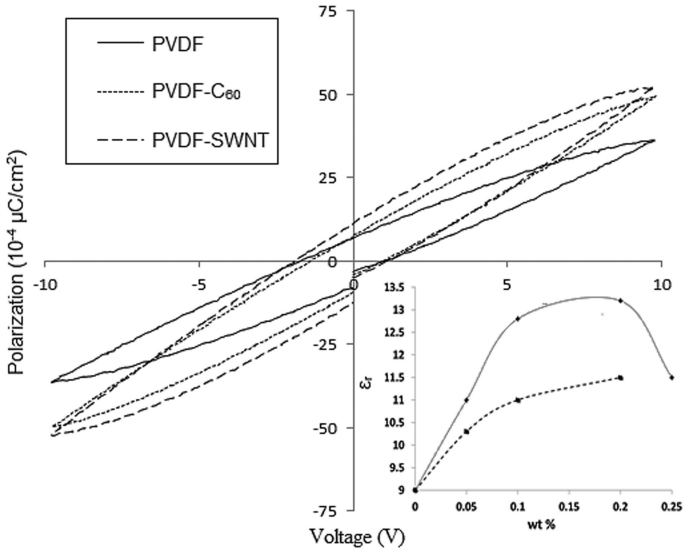

Figure 8. PE Hysteresis loop of pure PVDF, PVDF-C_{60} (0.1 wt%), PVDF-SWNT (0.1 wt%). Inset dielectric constant (ε_r) profiles vs. Wt%. Reproduced with permission from (44), 2012, © AIP Publishing.

In equation 3, if one assumes a constant d_{31}, the k_{31} is proportional to the square of the Y and inversely proportional to ε_r. Thus, one then would expect that by increasing the Y and decreasing ε_r, a very electromechancally-efficient material can be realized. However, it is impossible to change only one variable. For example, as Y is increased through the addition of the nanoparticles, ε_r generally increases due to the creation of dielectric boundaries. This results in a performance tradeoff. According to literature, pure PVDF has a k_{31} value of 0.12, and when calculated using the values measured here a k_{31} of 0.125 is obtained (*51*). The maximum k_{31} for the C_{60} composites occurs at a loading level of 0.2 wt with a value of 0.23, 1.84 times that of pure PVDF. The maximum for the SWNT occurs at a loading level of 0.05 wt% with a value of 0.25, a value 2 times that of pure PVDF.

Piezoelectricity in Nanostructured $Na_{0.5}Bi_{0.5}TiO_3$-$BaTiO_3$ (NBT-BT) Whiskers

An important step in the synthesis of novel, advanced piezoelectric polymer composites is the design of particles which retain their piezoelectricity when manufactured on a micro or nano-scale. The synthesis of nanostructured materials with high piezoelectric response has been very challenging due to the decrease in piezoelectricity with reduction in grain size. The piezoelectric response has been found to be highly dependent on the ferroelectric domain size, which is correlated to the grain size (*52*). Consequently, the grain size near threshold dimensions has a significant effect on the piezoelectric response of the corresponding system (*53–55*). In a polycrystalline ceramic, the domain size (D) is related to grain size (G) by:

$$D \propto G^p$$

Where *p* is a parabolic scaling factor (*52*):

$p < 1/2$ for $G > 10\ \mu m$
$p = 1/2$ for $10\ \mu m > G > 1\ \mu m$
$p > 1/2$ for $G < 1\ \mu m$

However, below a critical grain size, the motion of domain boundaries is confined by geometrical restrictions (Figure 9) resulting in a reduced functional response (*52*).

Effect of grain size on piezoelectric, dielectric and ferroelectric properties has been widely studied in literature and experiments have been conducted at different length scales to validate models (*56*, *57*). Many of these studies have taken place owing to the needs of shrinking capacitor dimensions while improving performance. It is well established that piezoelectric and dielectric properties drop rapidly below the critical grain size (~80 – 100 nm) (*58*, *59*). High resolution microscopy combined with surface tension measurements indicate that surface bond contraction due to the small grain size induces a compressive stress on the inner part of a grain, an effect that becomes significant in the nanometer size range. This induced stress causes a decrease of the Curie temperature and spontaneous polarization with a decreasing grain size. The domain wall contribution has an opposite effect compared with surface bond contraction effects. When the grain size decreases to a value comparable to the width of the domain walls, pinning points develop inside the grains and domain wall motion is inhibited. The reduced wall mobility causes a decrease in the relative permittivity. The measured dielectric constant experiences competition between the increase of relative permittivity by surface bond contraction and a decrease by the domain wall pinning effect (*60–64*).

In Polymer Composites for Energy Harvesting, Conversion, and Storage; Li, L., et al.;
ACS Symposium Series; American Chemical Society: Washington, DC, 2014.

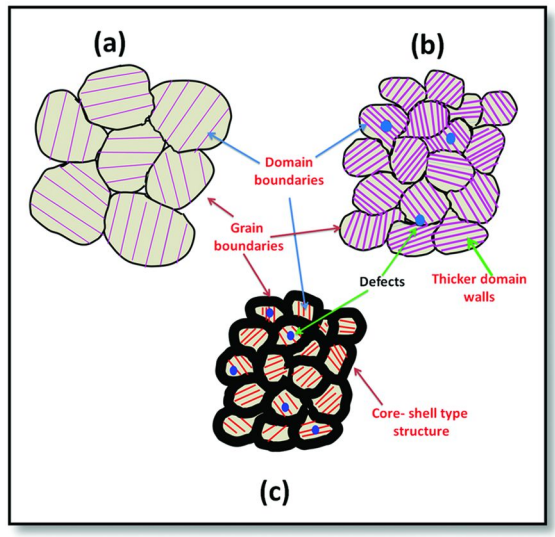

Figure 9. (a) Macroscopic domain structure within bigger grains, (b) smaller domains with thick domain walls in the system with smaller grain size and high piezoelectric response, (c) very small grain size depicting core-shell type structure. In this scenario, grain boundaries impede the domain wall motion.

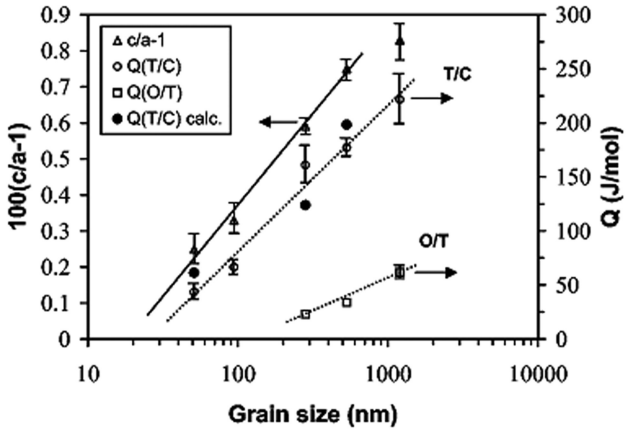

Figure 10. Variation in tetragonality with grain size in $BaTiO_3$. The heat of transition versus grain size for tetragonal →cubic (O) and of orthorhombic → tetragonal (□).

In Polymer Composites for Energy Harvesting, Conversion, and Storage; Li, L., et al.;
ACS Symposium Series; American Chemical Society: Washington, DC, 2014.

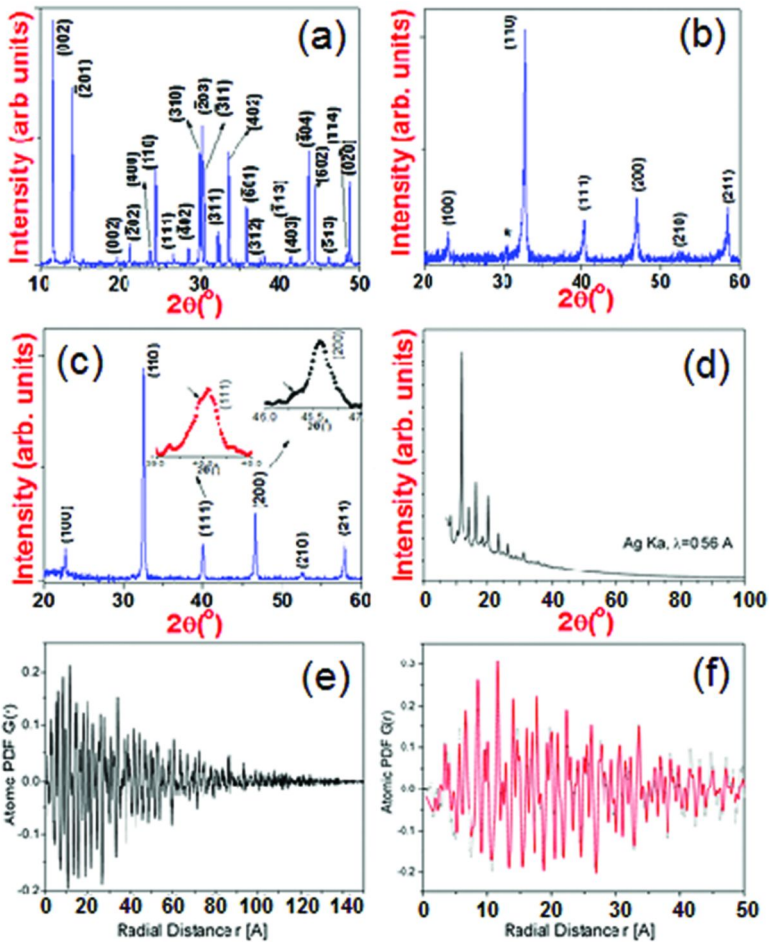

Figure 11. Cu Kα x-ray diffraction data at RT for (a) NTO powder whiskers with monoclinic symmetry, (b) NBT-BT processed at 800 °C indexed with reference to cubic phase, (c) NBT-BT processed at 900 °C with inset depicting a magnified view of (111) and (200) reflections, where c stands for cubic phase. The high energy X-ray diffraction data of NBT-BT/900 °C (d) and the respective atomic probably density function (PDF) (e). The low-r part of the experimental PDF data is shown in (f). The data can be fitted very well with a structure model (line in red) based on the rhombohedral (S.G R3c) structure of NBT perovskite.

Figure 10 shows the grain size effect on the ferroelectric phase transition behavior in $BaTiO_3$ (*65*). The change in transition has been quantified in terms of variations in critical exponent (γ) estimated from the modified Curie-Weiss law. Significant structural changes have been found to occur with a change in the

In Polymer Composites for Energy Harvesting, Conversion, and Storage; Li, L., et al.;
ACS Symposium Series; American Chemical Society: Washington, DC, 2014.

morphology such as a decrease in tetragonality (c/a) as shown in Figure 10. In fact, a correlation can be made between the effects arising from the decrease in grain size to those arising from an increase in the operating temperature (*63*). Based upon this discussion, the reduction in magnitude of the piezoelectric coefficient is expected if the material is synthesized in the form of nanowires, nanotubes, nano-whiskers, etc. This challenge needs to be overcome in order to facilitate the development of nanoscale structures. We have recently demonstrated a process for the synthesis of nanostructured whiskers that was found to exhibit a piezoelectric response while possessing grain sizes on the order of ~100 nm. These nano-structured NBT-BT whiskers are expected to be promising loading components in the design of the polymer/ceramic composites

Figure 11(a) shows the XRD patterns of the $Na_2Ti_6O_{13}$ (NTO) whiskers taken with Cu Kα radiation allowing high resolution in reciprocal space. The data confirmed that these whiskers were crystallized in the monoclinic phase (*66*). In order to confirm the formation of the perovskite phase, the Cu Kα XRD patterns (Figure 11(b) and (c)) were recorded on topochemically synthesized NBT-BT whiskers at 800 and 900°C. The NBT-BT whiskers synthesized at 900°C were found to crystallize in perovskite phase (Figure 11(c)). However, the specimen processed at 800°C was found to show small impurity peaks suggesting incomplete topochemical reaction.

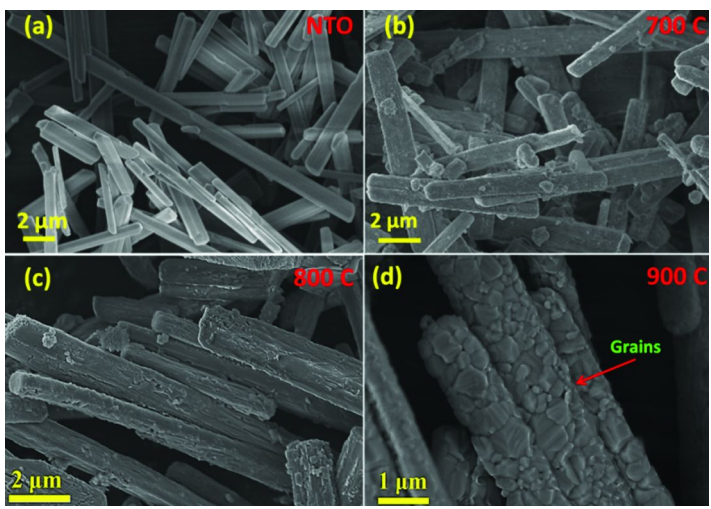

Figure 12. SEM micrographs of (a) NTO whisker matrix. Whiskers after reaction at (b) 700°C, (c) 800°C and (d) 900°C. The length of whiskers varies from 7.0-20 µm and the width varies from 0.30 – 1.0 µm.

A small shoulder appearing in the magnified view of the (111) and (200) peaks in the inset is attributed to the MPB composition of the NBT-BT system, Figure 11(c). High energy XRD using AgKα radiation was performed on NBT-BT whiskers synthesized at 900°C (Figure 11(d)), and was reduced to an atomic probably density function (PDF) shown in Figure 11(e). The well-defined peaks observed in experimental PDF were attributed to the high real space distances and the PDF peaks were found to decay to zero after 10-15 nm. This distance was considered as the distance of structural coherence/crystallite domain size in this material. Therefore, the grains observed in SEM were composed of relatively small nano-sized crystallites (10-15 nm). The PDF results were found to be well matched with the rhombohedral R3c structure of NBT suggesting polar nature (*67*).

The morphology of various whiskers synthesized at various temperatures is depicted in Figure 12. Despite the structural transformation during the synthesis process, the overall whisker morphology was intact at all the temperatures. Interestingly, the whiskers synthesized at 900°C were found to show distinct polycrystalline nature with densely packed grains. However, the specimens processed at lower temperature were not showing grain growth, but small change in morphology due to the diffusion of Ba^{2+} and Bi^{3+} during the reaction.

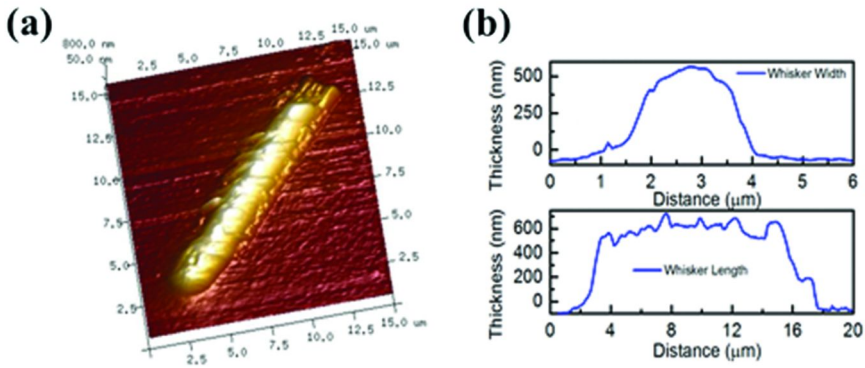

Figure 13. (a) The morphology of NBT-BT whiskers, (b) dimension of NBTBT whisker.

Figure 13 shows the topography, length and breadth of the whisker. Figure 13(a) is an atomic force microscope image of a 15 μm × 15 μm section of an NBT-BT whisker with z-axis resolution of less than 1 μm. Figure 13(b) is a contour plot which helps visualize a single pass across the ceramic nanowhisker across its width (top) and length (bottom). This gives further indication of the several micron width and relative symmetry of the whisker and some indication of the surface roughness across the length of the whisker.

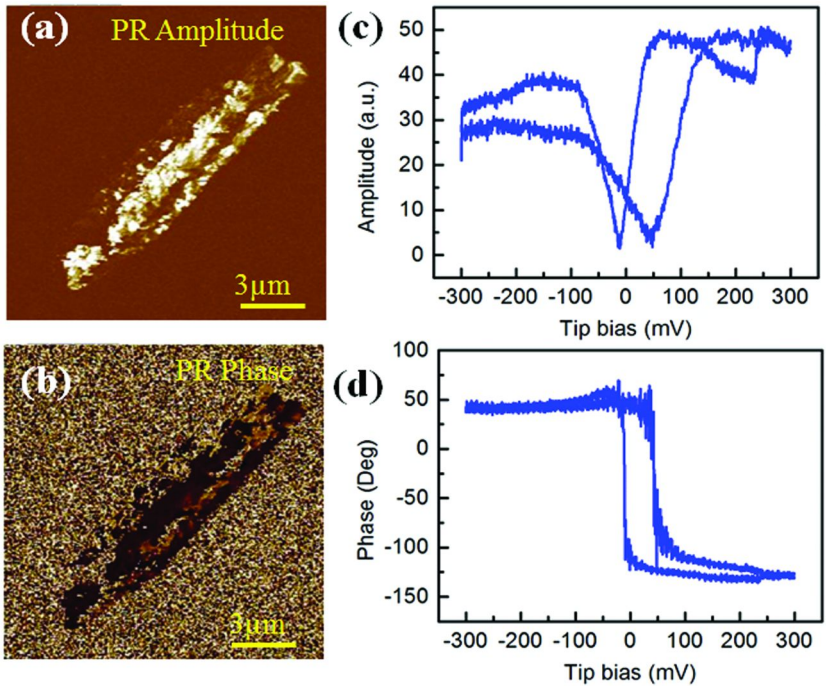

Figure 14. Piezoresponse of NBTBT whiskers: (a) Amplitude image, (b) phase image, (c) ramp-mode amplitudes, (d) ramp-mode phase angle.

The overall shape of the whiskers was maintained even after reaction at different temperatures despite of noticeable change in surface morphology. In order to confirm the piezoelectric response of these whiskers, piezoresponse force microscopy (PFM) was performed (Figure 14). Figure 14(a) and (b) show the amplitude and phase signal image, respectively. The amplitude signal shows the polarization magnitude; however, the phase signal depicts the polarization direction. The contrast change has been found to suggest presence of nano-scale domains in NBT-BT whiskers. The butterfly loops (Figure 14(c)) and phase saturation (Figure 14(d) in conjunction with the high energy x-ray diffraction data indicate the presence of piezoelectricity in nanostructured NBT-BT whiskers. These whiskers provide opportunity to develop composites with PVDF based polymers that can be utilized in various applications including energy harvesting (*68*).

Vibrational Energy Harvester Design for Polymer Composites

Piezoelectric polymer composites are flexible and therefore useful for energy harvesting applications involving stretching, compression, vibration, and magnetic fields (with an added magnetostrictive layer). One obvious application environment is the human body (*69*). External items around the human body such

In Polymer Composites for Energy Harvesting, Conversion, and Storage; Li, L., et al.;
ACS Symposium Series; American Chemical Society: Washington, DC, 2014.

as wristbands, straps on clothes and wristwatch bands become stretched as the human body undergoes motion. Other applications include microsurgical devices and pacemakers which can be powered by having flexible piezoelectric energy harvesters incorporated.

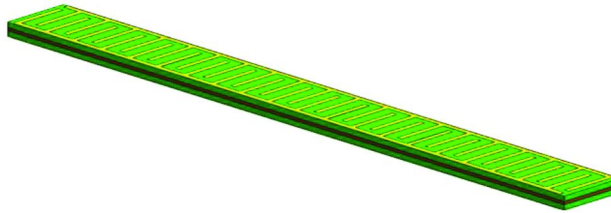

Figure 15. Piezoelectric energy harvester (d_{33} bimorph).

Figures 15 and 16(top) show a piezoelectric energy harvester which has been designed as a d_{33} bimorph. There are two layers of flexible piezoelectric which sandwich a support layer. Two interdigitated electrode patterns are also designed on the piezoelectric layers. This design of the harvester layers ensures the neutral axis is in the support layer and the energy harvesting potential of the piezoelectrics are maximized. A major unique advantage of using flexible piezoelectrics in energy harvesting is their ability to harvest significant power from the longitudinal (d_{33}) and transverse (d_{31}) modes as opposed to traditional energy harvesters which rely on transverse vibrations alone. As shown in Figure 16 (bottom), tensile and compressive forces can be applied in all directions to the harvester thus creating strain and generating charge in the piezoelectric layers.

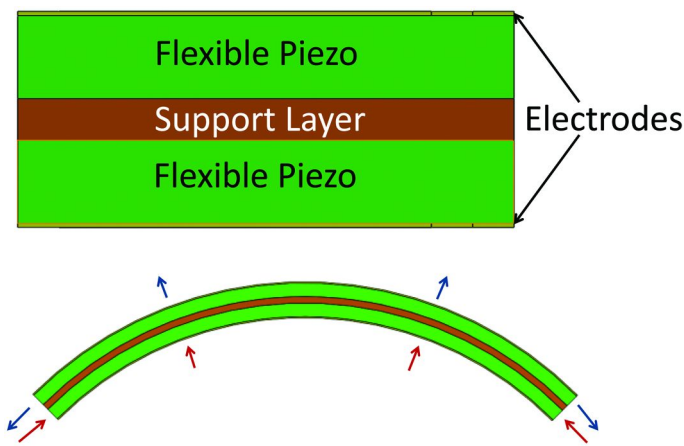

Figure 16. (Top) Cross section of the harvester (Bottom) Forces applied to flexible piezoelectric. Red arrow = compressive force, blue arrow = tensile force.

In Polymer Composites for Energy Harvesting, Conversion, and Storage; Li, L., et al.;
ACS Symposium Series; American Chemical Society: Washington, DC, 2014.

Low frequency piezoelectric energy harvesters have been investigated in literature. Flexible piezoelectric energy harvesters can incorporate known low frequency (<100 Hz) configurations such as zigzags (*70*) and spirals (*71–73*) depending on the application of the harvester. The energy harvesting potential of the proposed harvester is thus improved when longitudinal and transverse forces are applied to the harvester at its known low resonance frequency.

To fabricate the harvester, two layers of the flexible piezoelectric are laminated on a support layer (e.g. brass) using epoxy resin to form a trilayer laminate. Next, the trilayer laminate is machined/milled/cut into the desired configuration or shape of the harvester. Finally, interdigitated electrode (gold or copper) patterns are deposited or laminated on both sides of the fabricated structure.

Bimorph Modeling

Effective Mechanical Properties

The effective properties required for calculating the natural frequencies and energy response of beams include the effective Young's modulus, Y, the effective shear modulus, G, the effective mass per unit length, ρA, and the effective Poisson's ratio, v.

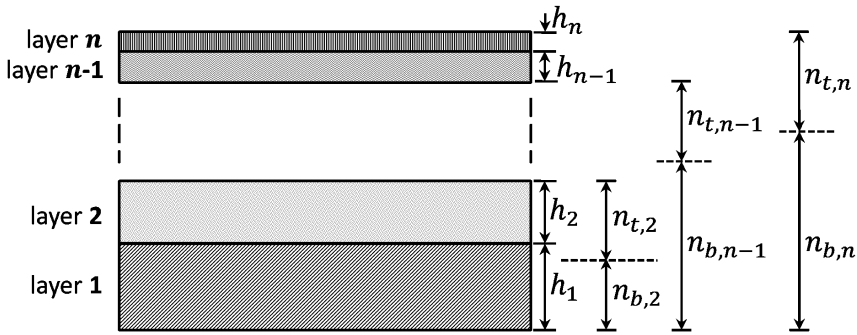

Figure 17. Cross section of a beam composed of n layers.

Consider a beam with two or more layers. If we rearrange the layers (from bottom to top) in descending order of their thicknesses, we can obtain a well-defined cross-section as shown in Figure 17. For n layers, the equations for the distance to the neutral axis can be written as (*74*):

$$n_{b,n} = \frac{h_n^2 + 2h_n h_{e,n-1} + \frac{Y_{e,n-1}}{Y_n} h_{e,n-1}^2}{2\left(h_n + \frac{Y_{e,n-1}}{Y_n} h_{e,n-1}\right)} \tag{4}$$

$$n_{t,n} = \frac{h_n^2 + 2\frac{Y_{e,n-1}}{Y_n} h_n h_{e,n-1} + \frac{Y_{n-1}}{Y_n} h_{e,n-1}^2}{2\left(h_n + \frac{Y_{e,n-1}}{Y_n} h_{e,n-1}\right)}$$

The effective flexural rigidity for a beam with *n* layers can be written as (*74*):

$$YI = (YI)_n = \frac{W}{3}\begin{bmatrix} Y_{e,n-1}\left(n_{b,n}^3 + \left(n_{t,n} - h_n\right)^3\right) + \\ Y_n\left(n_{t,n}^3 - \left(n_{t,n} - h_n\right)^3\right) \end{bmatrix} \tag{5}$$

where

$$Y_{e,n-1} = \frac{W}{3I_{e,n-1}}\begin{bmatrix} Y_{e,n-2}\left(n_{b,n-1}^3 + \left(n_{t,n-1} - h_{n-1}\right)^3\right) + \\ Y_{n-1}\left(n_{t,n-1}^3 - \left(n_{t,n-1} - h_{n-1}\right)^3\right) \end{bmatrix} \tag{6}$$

and this is expanded further until Y_1 is expressed. Therefore for *n* layers, there are $n - 1$ flexural rigidity equations to be solved in order to obtain the overall effective flexural rigidity. Note that any term with subscript *e* indicates an effective property and not the property of a single layer. For example, $Y_{e,n-1}$ denotes the effective Young's modulus for layers 1 to $n - 1$ while Y_{n-1} denotes the Young's modulus for layer $n - 1$ only. The effective thickness for *n* layers is simply a sum of the thicknesses of all the *n* layers, while the effective area moment of inertia for *n* layers is calculated assuming the *n* layers comprise a single beam.

The effective mass per unit length and Poisson's ratio for a beam with *n* layers can be calculated from rule of mixtures and expressed as (respectively):

$$\rho A = W\sum_{i=1}^{n} \rho_i h_i \tag{7}$$

and

$$\nu = \frac{1}{\sum_i^n h_i}\sum_{i=1}^{n} \nu_i h_i \tag{8}$$

The effective shear modulus, *G*, can be obtained from:

$$G = \frac{Y}{2(1+\nu)} \tag{9}$$

In Polymer Composites for Energy Harvesting, Conversion, and Storage; Li, L., et al.;
ACS Symposium Series; American Chemical Society: Washington, DC, 2014.

Natural Frequencies and Output Response

The modeling of the harvester can be carried out using finite element software or mathematical code. Finite Element method is suitable for simple analysis of the harvester (especially for complex shapes) while a mathematically derived code provides insight into the effects of different parameters on the behavior of the harvester. Overall, modeling is highly dependent on the shape of the harvester

Assuming the piezoelectric material is poled along the length of the beam, towards the anode, and all the material underneath the electrode is assumed to be poled, the total electrical energy of a d_{33} beam (and thus the voltage and power response) can derived from the combination of the piezoelectric and structural layers. The energy produced from a cantilever beam under a static end load is (*75*):

$$U = \sum_{i=1}^{n} \int_{s_i} \int_{0}^{W} \left(\int_{0}^{h_p} dU_p dz + \int_{-h_s}^{0} dU_s dz \right) dy dx \tag{10}$$

where dU_p and dU_s are the energy terms for small volumes of the piezoelectric and support materials, h_p and h_s are the total thicknesses of the piezoelectric and support layers, s_i refers to each individual section between the electrodes, n is the number of sections, and W is the width of the beam. For each segment spacing, s_i, a percentage of the piezoelectric material is considered to be poled in the 3-direction, as defined by the percent poling factor, $\%d_{33}$, which can vary from 0 to 1. The spacing and width of the electrodes can be optimized based on the harvester configuration to obtain optimal power response.

Energy Harvesting Applications of Piezoelectric Polymer Composites

Piezoelectric polymers have been found useful for many different applications including sensing, energy harvesting and actuation. Table 4 lists a few significant studies related to the use of piezoelectric polymers for energy harvesting applications. The platforms with the highest surface area and stretching tend to exhibit the highest power output (e.g. ocean waves).

Other energy harvesting applications for flexible polymers could involve integration into environments with considerable surface area for stretching. Thus, the reliance on resonance frequencies and high excitations can be eliminated. These applications, some of which are already in development, could include smart clothing, wristwatch straps, key straps, necklaces, belts, and footwear. For successful integration however, piezoelectric polymers must overcome some challenges:

- Torsion/twisting and rough handling
- Decrease in piezoelectric properties with increase in temperature, and
- Washing (clothing)

PVDF in off-resonance conditions is a promising transduction material for the vibration energy harvesters. The electric energy available under AC stress excitation from a parallel plate capacitor is given as:

$$U = \frac{1}{2}CV^2 \quad \text{or} \quad \text{energy per unit volume, } u = \frac{1}{2}d.g.X^2 \tag{11}$$

where U is the energy, C is the capacitance, V is the voltage, and X is the applied stress. A piezoelectric material with high energy density is characterized by a high product of piezoelectric voltage constant (g) and piezoelectric strain constant (d), given as ($d.\ g$), along with high magnitude of g coefficient. There are two extreme cases of high energy density material, PVDF piezoelectric polymer (d_{33} = 33 pC/N, $\varepsilon_{33}/\varepsilon_o$ = 13, g_{33} = 286.7 x10^{-3} m^2/C) and relaxor piezoelectric single crystals such as PZN – 7%PT (d_{33} = 2500 pC/N, $\varepsilon_{33}/\varepsilon_o$ = 6700, g_{33} = 42.1 x10^{-3} m^2/C). It can be seen from this data that piezoelectric polymer has the highest piezoelectric voltage constant, g_{33}, of 286.7 x10^{-3} m^2/C and relaxor-based single crystals have the highest product ($d_{33}.g_{33}$) of the order of 105250 x 10^{-15} m^2/N.

Table 4. Notable Piezoelectric Harvesters Employing Polymers

Author (Year)	*Application/ Source*	*Average Power (mW)*	*Piezoelectric material*
Granstrom et al (2007) (*76*)	Backpack strap	3.8	PVDF
Sun et al (2011) (*77*)	Human respiration	0.1	PVDF
Nishigaki (2013) (*78*)	Flag in the wind	7×10^{-3}	PVDF/Kapton
Vatansever et al (2012) (*79*)	Wind and Rain	8.5×10^{-2} (peak power)	PVDF/OPV hybrid
Van den Ende et al (2012) (*80*)	Automobile tire	0.1	PVDF-PZT
Chiba et al (2008) (*81*)	Ocean waves	250	EPAM
Aureli et al (2006) (*82*)	Static body of water	1×10^{-6}	IPMC

EPAM - Electroactive Polymer Artificial Muscle. PVDF – Polyvinylidene Flouride. PZT – Lead Zirconate Titanate. OPV – Organic Photovoltaic. IPMC – Ionic Polymer Metal Composite.

A future energy harvesting application for flexible polymers could involve a shift from mobile or outside sources of energy to inside buildings and homes. Piezoelectric polymers could produce significant power response when integrated into objects such as door closers, door push bars, window blinds, curtains, chairs and sofas. These devices can be easily connected (wirelessly or otherwise) to act as power switches for lighting and sensing. A schematic of the piezoelectric polymer integration into a door push bar is depicted in Figure 18.

In Polymer Composites for Energy Harvesting, Conversion, and Storage; Li, L., et al.;
ACS Symposium Series; American Chemical Society: Washington, DC, 2014.

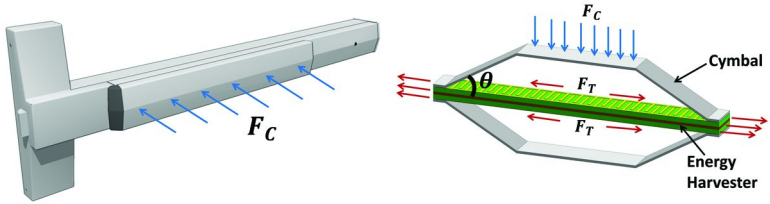

Figure 18. (Left) Door push bar with compressive force applied by hand. (Right) Forces applied to flexible piezoelectric cymbal energy harvester.

The mechanism depicted in Figure 18 is based on the piezoelectric cymbal design which involves amplifying the induced compression to create significant tension (stretching) in the piezoelectric polymer. The tensile force (F_T) in the piezoelectric polymer can be obtained as:

$$F_T = F_c \cot\theta \tag{12}$$

where F_C is the compressive force applied to the top of the cymbal device, and θ is the angle of the cymbal. The cymbal angle must be smaller than 45 degrees for force amplification to occur. Also, the smaller the angle (below 45 degrees), the higher will be the force amplification.

Summary

As wireless technology and device connectivity continues to grow, there is an ever increasing demand for self-powered sensors and transmitters which can largely be operated persistently. Piezoelectric vibrational energy harvesters show great promise in meeting this demand. While piezoelectric harvesters offer high regenerative potential power outputs, they are currently limited by either their stiffness, brittleness and low sensitivity (ceramics) or their low piezoelectric response and temperature tolerance (polymers). Many significant composites have been reported building upon the strengths of both ceramics and polymers to create novel materials that perform beyond that of their individual components. While there is still much progress to be made in the field of piezoelectric polymer composites, these materials will play a large role in powering small electronics in the years to come.

References

1. Atzori, L.; Iera, A.; Morabito, G. *Comput. Networks* **2010**, *54*, 2787.
2. Erturk, A.; Inman, D. J. *Piezoelectric Energy Harvesting*; Wiley.com, 2011.
3. Williams, C.; Yates, R. B. *Sens.Actuators, A* **1996**, *52*, 8.
4. Priya, S. *J. Electroceram.* **2007**, *19*, 167.
5. Sodano, H. A.; Inman, D. J.; Park, G. *Shock Vib. Dig.* **2004**, *36*, 197.
6. Cook-Chennault, K.; Thambi, N.; Sastry, A. *Smart Mater. Struct.* **2008**, *17*, 043001.

7. Ballato, A. *IEEE Trans. Ultrason., Ferroelect. Freq. Control* **1995**, *42*, 916.
8. Jaffe, B.; Cook, W. R., Jr.; Jaffe, H. *Piezoelectric Ceramics (Nonmetallic Solids, No. 3)*; Academic: New York, 1971.
9. Cady, W. G. *Piezoelectricity; An Introduction to the Theory and Applications of Electromechanical Phenomena in Crystals*, revised ed.; Dover: Mineola, NY, 1964.
10. Kim, J.; Loh, K. J.; Lynch, J. P. *Proc. SPIE* **2008**, *6932*, 693232/1.
11. Anton, S. R.; Sodano, H. A. *Smart Mater. Struct.* **2007**, *16*, R1.
12. Yu, Y.; Zhang, X. N.; Xie, S. L. *Smart Mater. Struct.* **2009**, *18*, 095006/1.
13. A., A. B. *Aoustic Fields and Waves in Solids*; Krieger Publishing Company: Melbourne, 1990.
14. *IEEE Standard on Piezoelectricity*; New York, 1978.
15. *Smart Materials*; Schwartz, M., Ed.; CRC Press: Boca Raton, FL, 2009.
16. Priya, S.; Inman, D. J. *Energy Harvesting Technologies*; Springer: New York, 2008 [electronic resource]
17. Qi, Y.; McAlpine, M. C. *Energy Environ. Sci.* **2010**, *3*, 1275.
18. Ramaratnam, A.; Jalili, N. *J. Intell. Mater. Syst. Struct.* **2006**, *17*, 199.
19. Kunstler, W.; Wegener, M.; Seiss, M.; Gerhard-Multhaupt, R. *Appl. Phys. A* **2001**, *73*, 641.
20. Newman, B. A.; Chen, P.; Pae, K. D.; Scheinbeim, J. I. *J. Appl. Phys.* **1980**, *51*, 5161.
21. Fukada, E. *Key Eng. Mater.* **1994**, *92-93*, 143.
22. Zhang, S.; Zhang, N.; Huang, C.; Ren, K.; Zhang, Q. *Adv. Mater. (Weinheim, Ger.)* **2005**, *17*, 1897.
23. Levi, N.; Czerw, R.; Xing, S.; Iyer, P.; Carroll, D. L. *Nano Lett.* **2004**, *4*, 1267.
24. Ottman, G. K.; Hofmann, H. F.; Bhatt, A. C.; Lesieutre, G. A. *IEEE Trans. Power Electron.* **2002**, *17*, 669.
25. Jiang, S.; Li, X.; Guo, S.; Hu, Y.; Yang, J.; Jiang, Q. *Smart Mater. Struct.* **2005**, *14*, 769.
26. Newnham, R. E.; Skinner, D. P.; Cross, L. E. *Mater. Res. Bull.* **1978**, *13*, 525.
27. Ploss, B.; Ploss, B.; Shin, F. G.; Chan, H. L. W.; Choy, C. L. *IEEE Trans. Dielectr. Electr. Insul.* **2000**, *7*, 517.
28. Cui, C.; Baughman, R. H.; Iqbal, Z.; Kazmar, T. R.; Dahlstrom, D. K. *Synth. Met.* **1997**, *85*, 1391.
29. Venkatragavaraj, E.; Satish, B.; Vinod, P. R.; Vijaya, M. S. *J. Phys. D: Appl. Phys.* **2001**, *34*, 487.
30. Garner, G.; Shorrocks, N.; Whatmore, R.; Goosey, M.; Seth, P.; Ainger, F. *Ferroelectrics* **1989**, *93*, 169.
31. Dias, C. J.; Das-Gupta, D. K. *IEEE Trans. Dielectr. Electr. Insul.* **1996**, *3*, 706.
32. Banno, H.; Ogura, K.; Sobue, H.; Ohya, K. *Jpn. J. Appl. Phys. Suppl.* **1987**, *26*, 153.
33. Hanner, K.; Safari, A.; Newnham, R.; Runt, J. *Ferroelectrics* **1989**, *100*, 255.
34. Yamada, T.; Ueda, T.; Kitayama, T. *J. Appl. Phys.* **1982**, *53*, 4328.
35. Han, K.; Safari, A.; Riman, R. E. *J. Am. Ceram. Soc.* **1991**, *74*, 1699.

36. Furukawa, T.; Fujino, K.; Fukada, E. *Jpn. J. Appl. Phys.* **1976**, *15*, 2119.
37. Furukawa, T.; Ishida, K.; Fukada, E. *J. Appl. Phys.* **1979**, *50*, 4904.
38. Pardo, L.; Mendiola, J.; Alemany, C. *J. Appl. Phys.* **1988**, *64*, 5092.
39. Zewdie, H.; Brouers, F. *J. Appl. Phys.* **1990**, *68*, 713.
40. Sreekumar, T. V.; Liu, T.; Min, B. G.; Guo, H.; Kumar, S.; Hauge, R. H.; Smalley, R. E. *Adv. Mater. (Weinheim, Ger.)* **2004**, *16*, 58.
41. Wang, L.; Dang, Z.-M. *Appl. Phys. Lett.* **2005**, *87*, 042903/1.
42. Salehi-Khojin, A.; Hosseini, M. R.; Jalili, N. *Compos. Sci. Technol.* **2009**, *69*, 545.
43. Kroto, H. W.; Heath, J. R.; O''Brien, S. C.; Curl, R. F.; Smalley, R. E. *Nature (London)* **1985**, *318*, 162.
44. Reprinted with permission from *J. Appl. Phys.* **2012**, 112; http://dx.doi.org/10.1063/1.4768923. Copyright [2012], A. P. L.
45. Bauer, S.; Bauer-Gogonea, S.; Dansachmuller, M.; Graz, I.; Leonhartsberger, H.; Salhofer, H.; Schwoediauer, R. *Proc. - IEEE Ultrason. Symp.* **2003**, 370.
46. Fischer, P.; Roehl, P. *Prog. Colloid Polym. Sci.* **1977**, *62*, 149.
47. Das-Gupta, D. K.; Doughty, K.; Brockley, R. S. *J. Phys. D* **1980**, *13*, 2101.
48. Galikhanov, M. F.; Eremeev, D. A.; Deberdeev, R. Y. *Russ. J. Appl. Chem.* **2003**, *76*, 1651.
49. Mizutani, T.; Yamada, T.; Ieda, M. *J. Phys. D* **1981**, *14*, 1139.
50. Amusia, M. Y.; Baltenkov, A. S. *Los Alamos Natl. Lab., Prepr. Arch., Phys.* **2006**, 1.
51. Harrison, J. S.; Ounaies, Z. *Encyclopedia of Smart Materials*; Biderman, A., Ed.; John Wiley & Sons Ltd: New York, 2002; p 162.
52. Cao, W.; Randall, C. A. *J. Phys. Chem. Solids* **1996**, *57*, 1499.
53. Randall, C. A.; Kim, N.; Kucera, J. P.; Cao, W.; Shrout, T. R. *J. Am. Ceram. Soc.* **1998**, *81*, 677.
54. Rödel, J.; Jo, W.; Seifert, K. T.; Anton, E. M.; Granzow, T.; Damjanovic, D. *J. Am. Ceram. Soc.* **2009**, *92*, 1153.
55. Petkov, V.; Buscaglia, V.; Buscaglia, M.; Zhao, Z.; Ren, Y. *Phys. Rev. B* **2008**, *78*, 054107.
56. Martirena, H.; Burfoot, J. *J. Phys. C: Solid State Phys.* **1974**, *7*, 3182.
57. Choudhury, S.; Li, Y.; Krill, C., III; Chen, L. *Acta Mater.* **2007**, *55*, 1415.
58. Sundar, V. K., N.; Randall, C. A.; Yimnirun, R.; Newnham, R. E. In *Proc. 10th IEEE Int. Symp. Appl. Ferroelectr.* 1996; p 935.
59. Lu, C. J.; Ren, S. B.; Shen, H. M.; Liu, J. S.; Wang, Y. N. *J. Phys. Condens. Matter.* **1996**, *8*, 8011.
60. Sakaki, C.; Newalkar, B. L.; Komerneni, S.; Uchino, K. *Jpn. J. Appl. Phy.* **2001**, *40*, 6907.
61. Jin, B. M.; Kim, J.; Kim, S. C. *Appl. Phys. A* **1997**, *65*, 53.
62. Shaw, T. M.; Trolier-McKinstry, S.; McIntyre, P. C. *Ann. Rev. Mater. Sci.* **2000**, *30*, 263.
63. Zhao, Z.; Buscaglia, V.; Viviani, M.; Buscaglia, M. T.; Mitoseriu, L.; Testino, A. *Phys. Rev. B* **2004**, *70*, 024107.
64. Uchino, K. *Piezoelectric Actuators and Ultrasonic Motors*; Kluwer Academic Publishers: Norwell, MA, 1997.

65. Kang, B. S.; Choi, D. G.; Choi, S. K. *J. Mater. Sci.: Mater. Electron.* **1998**, *32*, S232.
66. Andersson, S.; Wadsley, A. *Acta Crystallogr.* **1962**, *15*, 194.
67. Vakhrushev, S.; Ivanitskii, B.; Kvyatkovskii, B.; Maistrenko, A.; Malysheva, R.; Okuneva, N.; Parfenova, N. *Fiz. Tverd. Tela (Leningrad)* **1983**, *25*, 2613.
68. Maurya, D.; Murayama, M.; Priya, S. *J. Am. Ceram. Soc.* **2011**, *94*, 2857.
69. Kiziroglou, M. E.; He, C.; Yeatman, E. M. *Electron. Lett.* **2010**, *46*, 166.
70. Karami, M. A.; Inman, D. J. *J. Vib. Acoust.* **2011**, *133*, 011002.
71. Amin Karami, M.; Yardimoglu, B.; Inman, D. J. *J. Sound Vib.* **2010**, *329*, 5584.
72. Choi, W.; Jeon, Y.; Jeong, J. H.; Sood, R.; Kim, S. *J. Electroceram.* **2006**, *17*, 543.
73. Deterre, M.; Lefeuvre, E.; Zhu, Y.; Woytasik, M.; Bosseboeuf, A.; Boutaud, B.; Dal Molin, R. In *Micro Electro Mechanical Systems (MEMS), 2013 IEEE 26th International Conference on*; 2013, p 249; DOI: 10.1109/MEMSYS.2013.6474224.
74. Apo, D. J.; Sanghadasa, M.; Priya, S. *Energy Harvesting*; in review.
75. Knight, R.; Mo, C.; Clark, W. *J. Electroceram.* **2011**, *26*, 14.
76. Jonathan, G.; Joel, F.; Henry, A. S.; Kevin, F. *Smart Mater. Struct.* **2007**, *16*, 1810.
77. Sun, C.; Shi, J.; Bayerl, D. J.; Wang, X. *Energy Environ. Sci.* **2011**, *4*, 4508.
78. Nishigaki, T. Development of a piezoelectric polymer energy harvesting flag. In *Active and Passive Smart Structures and Integrated Systems*; SPIE - International Society for Optical Engineering: Bellingham, WA, 2013; Vol. 8688, p 86881K.
79. Vatansever, D.; Hadimani, R. L.; Shah, T.; Siores, E. In *Adaptive, Active and Multifunctional Smart Materials Systems*; Vincenzini, P., Hahn, Y. B., Iannotta, S., Lendlein, A., Palermo, V., Paul, S., Sibilia, C., Silva, S. R. P., Srinivasan, G., Eds.; Trans. Tech. Publications: Zurich, Switzerland, 2013; Vol. 77, p 297.
80. Ende, D. A. v. d.; Wiel, H. J. v. d.; Groen, W. A.; Zwaag, S. v. d. *Smart Mater. Struct.* **2012**, *21*, 015011.
81. Chiba, S.; Waki, M.; Kornbluh, R.; Pelrine, R. 2008; Vol. 6927, p 692715.
82. Matteo, A.; Chekema, P.; Maurizio, P.; Sean, D. P. *Smart Mater. Struct.* **2010**, *19*, 015003.

Chapter 2

Dye-Sensitized Polymer Composites for Sunlight Harvesting

Sam-Shajing Sun*,[1,2] and Amanda Harding[1]

[1]Center for Materials Research, Norfolk State University, Norfolk, Virginia 23504, U.S.A.
[2]Chemistry Department, Norfolk State University, Norfolk, Virginia 23504, U.S.A.
***E-mail: ssun@nsu.edu.**

A series of molecular dyes and donor-type conjugated polymers and the composites of the dye/polymer pairs have been investigated for potential high efficiency sunlight harvesting and photoelectric energy conversion applications. Specifically, molecular dyes can minimize the photo-generated charge carrier recombination and improve the photon capture when their frontier orbitals lie between the donor-type polymers and acceptors, and the dyes exhibit high absorption coefficients. This study also reveals that photoluminence quenching (PL) of dye/polymer composites could be due to either photo-induced charge transfer or molecular aggregation in solid state or solution. In the case of aggregation, an increase in the PL emission could be caused by the de-aggregation of molecular aggregates, which can be induced by either solvents or polymers.

In Polymer Composites for Energy Harvesting, Conversion, and Storage; Li, L., et al.;
ACS Symposium Series; American Chemical Society: Washington, DC, 2014.

Introduction

Renewable, clean, and cost effective energy materials and technology development has become one of the top global tasks for the sustainable development of human society. Solar energy has become a top choice due to its clean and renewable nature. Current commercially available inorganic solar cells convert sunlight directly into electricity at photoelectric power conversion efficiencies generally between 15-45%, but inorganic solar cells suffer from high cost, rigidity, brittleness, heavy weight, and in some cases, a limited supply of feedstock materials, and toxicity of certain materials or elements being used (*1*, *2*). Newly developed organic and polymer-based solar cells are attractive due to their low cost, flexibility, lightweight, abundant feedstock materials supply, and low or non toxicity (*3*–*6*). However, currently reported organic and polylmeric solar cells suffer from low efficiencies (less than 11%) (*6*). Such low efficiency can be attributed to three major losses; namely, photon loss, exciton loss, and carrier loss (*3*–*5*).

Photon loss can be attributed mainly to a mismatch between the material's energy gap and the radiant solar spectrum. For instance, the most abundant sunlight photons at the Earth's surface have energies between 1-2 eVs (sunlight at air mass AM 1.5). The energies of these photons corresponds well with the energy gaps of most inorganic-based semiconductors, such as silicon, GaAs, Ge, *etc*. (*1*, *2*). Most organic/polymer-based semiconductors have energy gaps above 2 eV (*3*–*7*), which is higher than the energy of most of sunlight photons. As a result, many sunlight photons are unable to produce excitons in the organic and polymeric photovoltaic materials.

Exciton loss is severe in organic/polymer systems because the binding energy of the organic exciton (Frenckel exciton) is far above the ambient temperature. Thus, its dissociation is solely dependent on the space charge field, which is an electric field located at the interface between a donor and an acceptor (*3*–*6*). Additionally, the Frenckel exciton typically has a lifetime of pico- or nanoseconds, which corresponds to an average excition diffusion length of less than 50 nanometers (*3*–*6*). In the current state of the art organic/polymer donor/acceptor binary blended solar cell systems, the donor/acceptor phase domains are often larger than the average excition diffusion length. The consequence of large domains in these systems is that the exciton will decay to its ground bound state if it does not reach the donor/acceptor interface within its lifetime.

The carrier loss in currently reported organic/polymer optoelectronic systems is also severe due to poor or hard-to-control polymer solid state morphologies. In these systems, the charges that have been separated must diffuse through their respective materials (holes in donor domains and electrons in acceptor domains). In the donor/acceptor blend systems, the processing methods used would result in a disordered pathway to the electrodes. Many charges that overcome the first two loss hurdles (photon loss and exciton loss) are unable to reach the electrodes of the solar cell, resulting in poor performance.

In order to address these losses, we have designed and investigated a dye-sensitized donor-dye-acceptor triple-component polymeric materials system as shown in Figure 1, in which the donors are hole-transporting conjugated

In Polymer Composites for Energy Harvesting, Conversion, and Storage; Li, L., et al.;
ACS Symposium Series; American Chemical Society: Washington, DC, 2014.

polymers, and the acceptors are electron-transporting polymers or other n-type semiconductors. Advantages of this triple system (as compared to the donor/acceptor binary system) include:

1) A variety of dyes are available which can be tailored to improve photon capture with better photon matched energy gaps and higher absorption coefficients;
2) The probability of photo-generated geminate electron-hole pair recombination is minimized due to better electrical and physical separation of the electron from the hole in the triple system. For instance, the photo-induced geminate electron/hole pair recombination can be as high as 75% (*8*).
3) The exciton loss can be significantly minimized due to close proximity (much less than the average excition diffusion length) of the excitons to either the dye-donor interface or to the dye-acceptor interface.

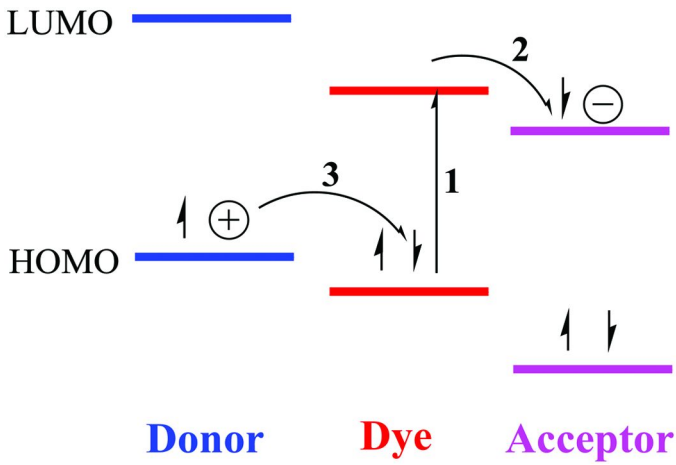

Figure 1. Scheme of a polymer based donor-dye-acceptor triple-component materials system for potential high efficiency solar energy conversion applications.

Results and Discussion

To evaluate such dye-sensitized polymer systems, the first step is to identify dye/polymer pairs with matching frontier orbital levels, energy gaps, and high sunlight absorption coefficients. Figure 2 exhibits several dyes and polymers that we have preliminarily studied:

1) Zinc 2,9,16,23-tetra-*tert*-butyl-29*H*,31*H*-phthalocyanine (ttb-ZnPc, or simply **ZnPc**)
2) Methylene Blue (**MB**) and New Methylene Blue N (**NMB**)
3) *cis*-Bis(isothiocyanato)(2,2′-bipyridyl-4,4′-dicarboxylato)(4,4′-di-nonyl-2′-bipyridyl)ruthenium(II) (**Z-907**)
4) regio-regular Poly(3-hexylthiophene-2,5-diyl) (rr-P3HT or simply **P3HT**)
5) regio-regular Poly(3-dodecylthienylenevinylene)s (rr-C12-PTV or simply **C12-PTV**)

NMB is a more processable and functionalizable version of the common MB (Figure 2), and NMB exhibits almost the same electronic/optical properties as MB. Materials pairing requires suitable frontier orbital levels (as exhibited in Figure 3), and complementary light absorption across the solar visible light spectrum (Figures 4 and 5).

Each material was selected for particular properties, some of which are listed in Table 1. P3HT is a commercially available donor type regio-regular conjugated polymer notable for excellent charge carrier mobility and low band gap. The absorption coefficient of C12-PTV is almost three times higher than that of P3HT, but C12-PTV does not exhibit fluorescence emission. The dye Z-907 boasts a low band gap (1.6 eV) and two carboxylic acid functional groups, which allow for covalent linkage to a suitable polymer main chain. While the absorption coefficient of Z-907 is higher than that of P3HT, the dyes NMB and ZnPc exhibit absorption coefficients in the next order of magnitude as compared with P3HT.

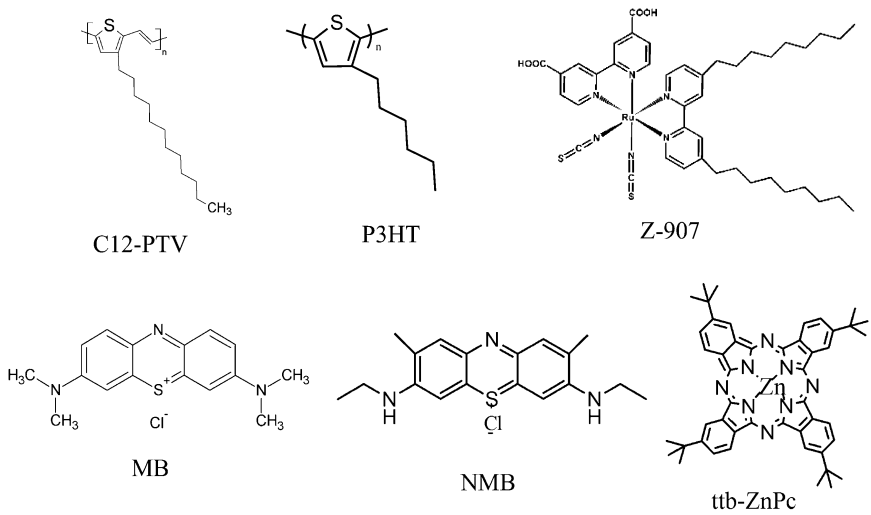

Figure 2. Chemical structures of several polymers and dyes investigated.

In Polymer Composites for Energy Harvesting, Conversion, and Storage; Li, L., et al.;
ACS Symposium Series; American Chemical Society: Washington, DC, 2014.

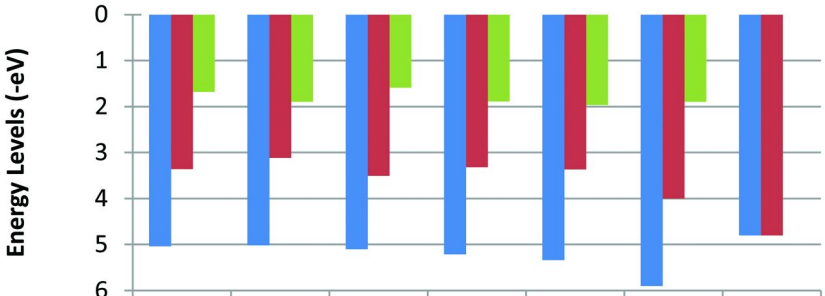

	C12-PTV	P3HT	Z907	MB	ZnPc	PCBM	m-SWCNT
HOMOs	5.04	5.02	5.1	5.21	5.34	5.9	4.8
LUMOs	3.36	3.12	3.51	3.32	3.37	4	4.8
Eg	1.68	1.9	1.59	1.89	1.97	1.9	0

Figure 3. Frontier orbital levels (HOMOs and LUMOs) and energy gaps (E_gs) of several materials studied.

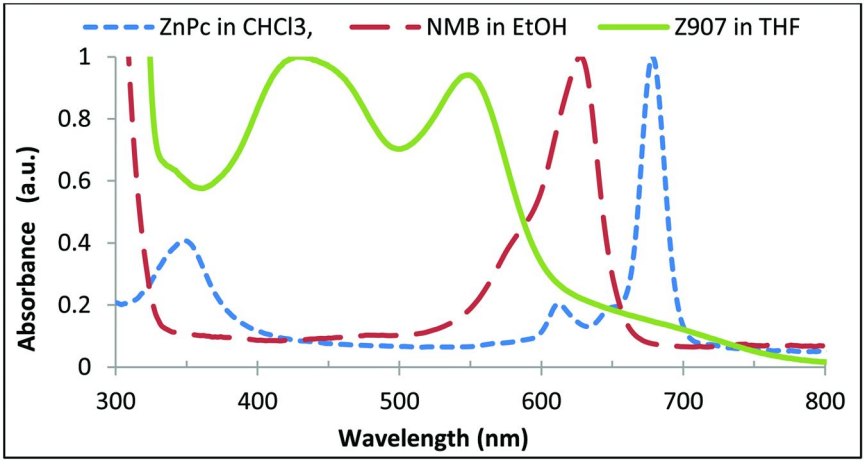

Figure 4. Normalized UV-Vis absorption spectra of ZnPc, NMB, and Z907, all in solution.

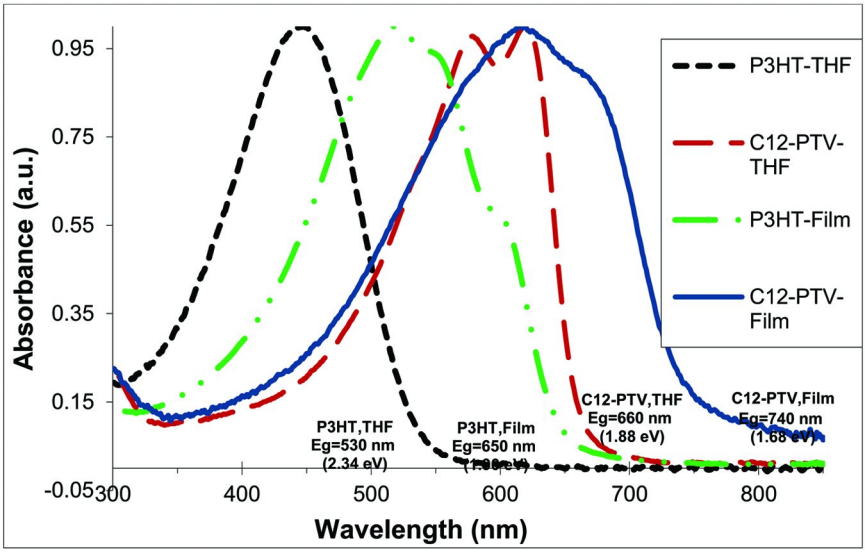

Figure 5. Normalized UV-Vis absorption spectra of P3HT and C12-PTV in both THF and thin films.

Table 1. Solution Absorption Data of the Dyes and Polymers Studied

	ZnPc	*NMB*	*Z907*	*C12-PTV*	*P3HT*
VIS Abs λ_{max} (nm)	678	628	555	625	450
Absorbance Max	0.75	0.58	0.32	0.24	1.01
Weight (mg)	2.6	2.8	2.3	2	1.69
Formula Weight	802.34	347.91	870.1	278.5	168.3
Solvent	1000 mL $CHCl_3$	1000 mL EtOH	100 mL THF	1000 mL $CHCl_3$	100 mL $CHCl_3$
Concentration (M)*	3.11E-06	5.63E-06	2.51E-05	7.18E-06	1.00E-04
Abs Coeff. (cm^{-1}/M)	241742	102165	12908	33770	10075

* Corrected for impurities (*e.g.*, 70% dye content in NMB sample).

In Polymer Composites for Energy Harvesting, Conversion, and Storage; Li, L., et al.;
ACS Symposium Series; American Chemical Society: Washington, DC, 2014.

As discussed earlier, the match of the polymer/dye frontier orbitals is essential for efficient photo induced electron transfer between the polymer and the dye, and that process typically results in PL quenching (if one of the pair exhibits photoluminescence). Figure 6 gives the THF solution PL emission spectrum at an excitation wavelength of 470nm of pristine Z-907 (top red curve), and the Z-907/ C12-PTV blend mixture with two different concentrations of C12-PTV (lower two curves). The Z-907 concentration remains the same in all three cases. As Figure 6 reveals, C12-PTV quenches the PL of Z-907; a positive sign of photo-induced charge separation between C12-PTV and Z-907. Similarly, the PL quenching of the MB/C12-PTV pair at 470 nm excitation is shown in Figure 7, where C12-PTV itself does not generate measurable PL (*9*), and a blend of 1:1 acetone/chloroform solutions was used in order to ensure good solubility of both materials. Similarly, the PL quenching of NMB/P3HT at 470nm excitation is shown in Figure 8, where a blend of 1:1 acetone/chloroform solutions was also used.

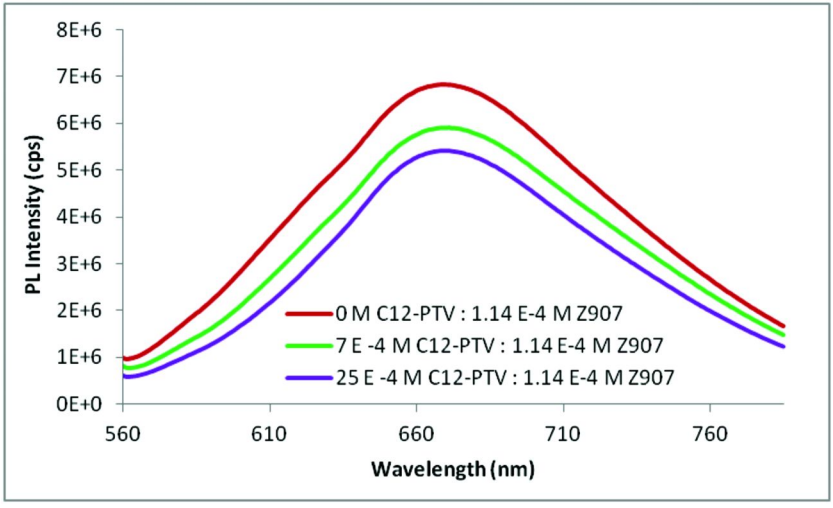

Figure 6. Fluorescence spectra of fixed concentration Z907 with increasing concentration of C12-PTV in THF.

In Polymer Composites for Energy Harvesting, Conversion, and Storage; Li, L., et al.;
ACS Symposium Series; American Chemical Society: Washington, DC, 2014.

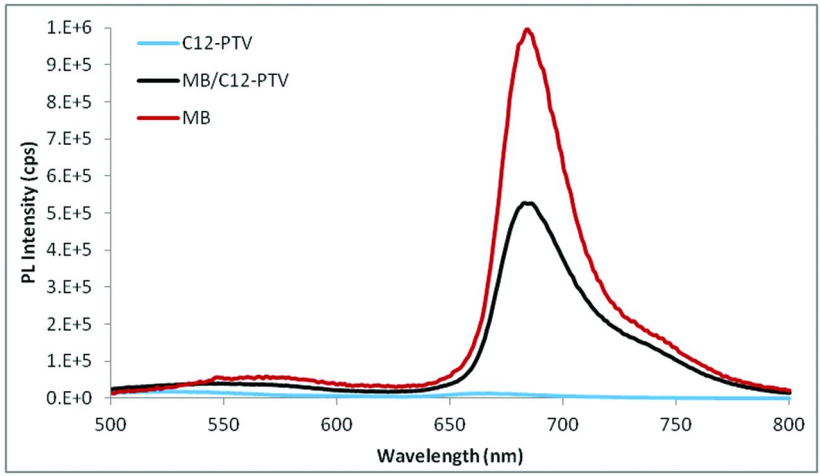

Figure 7. Fluorescence spectra of C12-PTV, MB, and C12-PTV/MB equi-molar blend in 1:1 acetone/chloroform solutions.

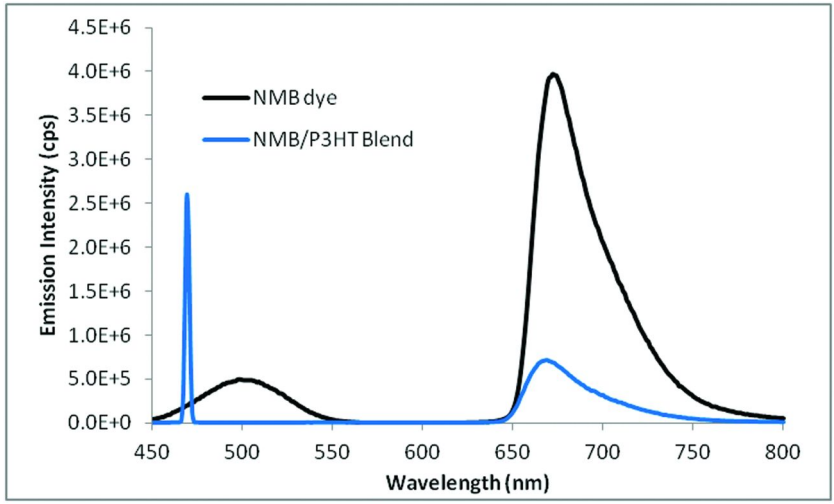

Figure 8. Fluorescence spectra of NMB, and NMB/P3HT equi-molar blend in 1:1 acetone/chloroform solutions.

Both MB and NMB exhibit similar electronic properties with a maximum absorption peak around 630 nm and an optical energy gap around 1.9eV (Figure 4). MB and NMB appear attractive for optoelectronic applications due to their relatively large molar absorption coefficients (Table 1) and absorption range.

For the ZnPc/P3HT pair, Figure 9 shows solid thin film UV-Vis absorption spectra of the pristine ZnPc (green long-dashed curve), the pristine P3HT (red solid curve), and the ZnPc/P3HT composite blend (black short-dashed curve). Since the absorption of the ZnPc covers radiation ranges of 300-500nm and 600-800nm, and

In Polymer Composites for Energy Harvesting, Conversion, and Storage; Li, L., et al.;
ACS Symposium Series; American Chemical Society: Washington, DC, 2014.

the absorption of the P3HT covers a radition range of 400-600nm, the ZnPc/P3HT pair appears ideal for a solid state device light harvesting application in 300-800nm range such as solar cell applications. Additionally, ZnPc exhibits the largest molar absorption coefficient among all materials studied here (see Table 1). Figure 10 exhibits the UV-VIS absorption spectra of the ZnPc, P3HT and ZnPc/P3HT in chloroform solution where sharper peaks can be seen. We attribute this to fewer or no inter-chain interactions in solution compared to thin film.

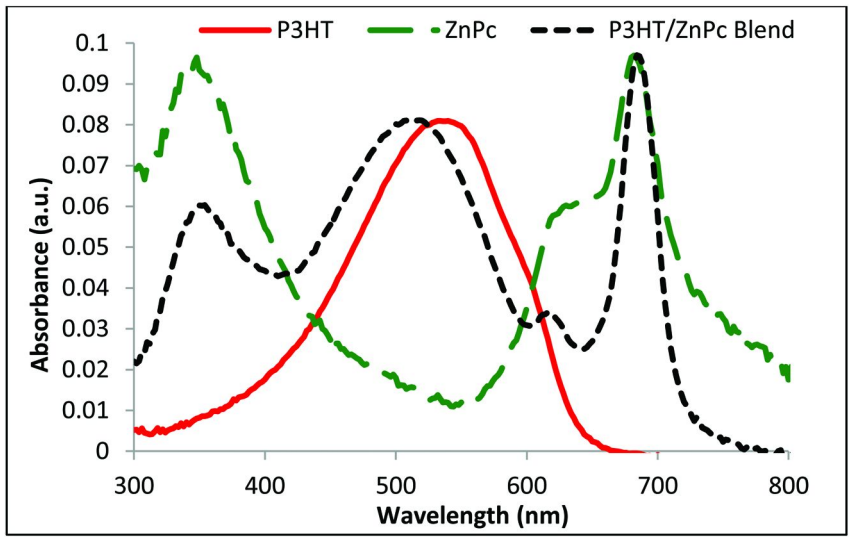

Figure 9. Normalized UV-Vis spectra of P3HT (red solid), ZnPc (green long-dashed), and P3HT/ZnPc blend (black short-dashed), in thin films.

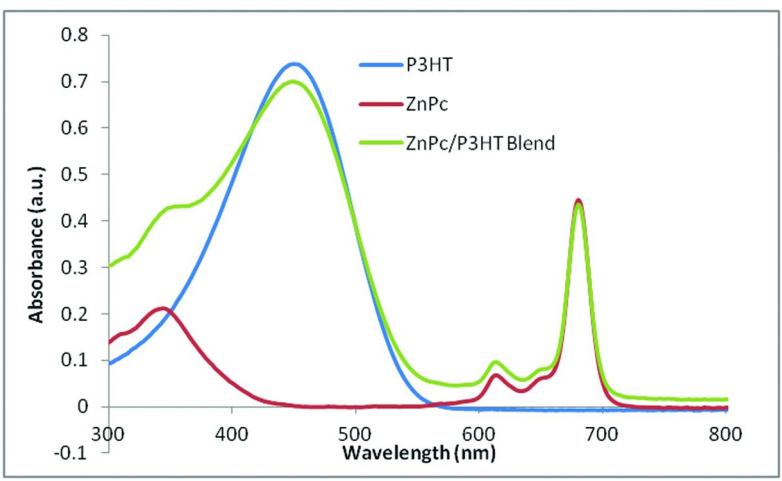

Figure 10. UV-Vis spectra of P3HT, ZnPc, and P3HT/ZnPc in chloroform.

In Polymer Composites for Energy Harvesting, Conversion, and Storage; Li, L., et al.;
ACS Symposium Series; American Chemical Society: Washington, DC, 2014.

Because the ZnPc/P3HT absorption curve traces the combination of the individual absorption curves of P3HT and of ZnPc, we can conclude that there is no evidence of ground state charge transfer, indicating that ZnPc/P3HT are a promising pair for photoelectric applications, in which photo-induced charge transfer is essential. PL quenching studies of donor and acceptor pairs are crucial for optoelectronic such as solar cell device development.

As you can see from Figure 10, the absorbance maxima for P3HT and ZnPc are 450 nm and 680 nm, respectively. The PL emission spectra of P3HT excited at each of these wavelengths is given in Figures 11 and 12. At 360nm excitation, P3HT is expected to undergo a single photon absorption/emission process. When the P3HT is excited at 680nm (1.8 eV), well below the P3HT single photon absorption energy gap (2.3eV, Figure 4), P3HT emits weakly at its typical PL photon peak at about 570 nm (2.18 eV, Figure 12). We tentatively attribute this to P3HT two photon absorption (TPA) at 680nm excitation (corresponding to a two photon total energy of 3.6eV) followed by a single photon emission at 570nm (2.18 eV). The TPA phenomenon in P3HT has been reported before (*10*).

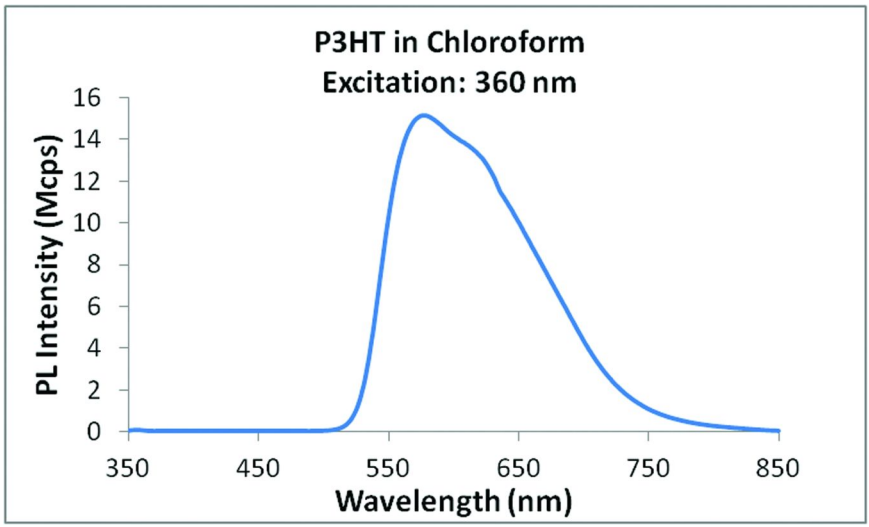

Figure 11. PL emission spectrum of P3HT at 360nm excitation in chloroform.

To investigate PL quenching and potential charge transfer of the ZnPc/P3HT pair in solution, emission spectra were recorded at 360 nm and 680 nm while the concentration of one species was held constant, and the concentration of the other species was increased. Figure 13 shows the PL peak intensity of the P3HT emission as a function of ZnPc concentration. In this experiment, [P3HT] was fixed at 1 x 10^{-4} M with increasing ZnPc concentration at excitation of a) 360 nm (single photon absorption for both ZnPc and P3HT) and b) 680 nm (single photon absorption for ZnPc but two photon absorption for P3HT). In both studies, the concentration of ZnPc remained below 1x10^{-4} M.

In Polymer Composites for Energy Harvesting, Conversion, and Storage; Li, L., et al.;
ACS Symposium Series; American Chemical Society: Washington, DC, 2014.

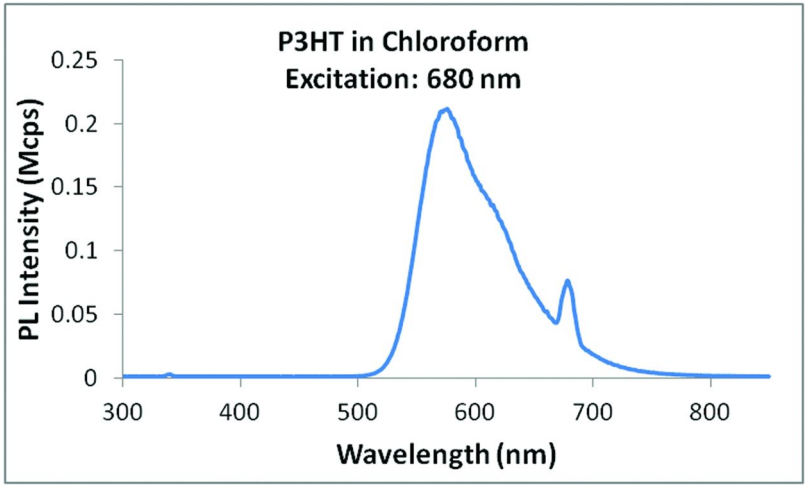

Figure 12. PL emission spectrum of P3HT at 680nm excitation in chloroform.

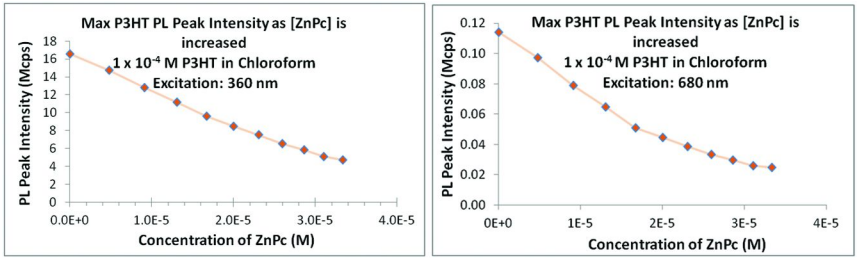

(a) (b)

Figure 13. Fluorescence emission maxima of P3HT (1 x 10-4 M in $CHCl_3$) with increasing concentration of ZnPc at excitations 360 nm (a) and 680 nm (b).

Figure 14 shows the PL peak intensity of the ZnPc emission as a function of P3HT concentration. In this experiment, [ZnPc] was fixed at 1 x 10^{-5} M with increasing P3HT concentration at excitation of a) 360 nm (single photon absorption for both ZnPc and P3HT) and b) 680 nm (single photon absorption for ZnPc but two photon absorption for P3HT). In both studies, the concentration of P3HT remained below 1x10^{-6} M. Again, photo-induced charge transfer between P3HT and ZnPc appears obvious when ZnPc and P3HT concentrations are both less than 1 x 10^{-4} M.

In Polymer Composites for Energy Harvesting, Conversion, and Storage; Li, L., et al.;
ACS Symposium Series; American Chemical Society: Washington, DC, 2014.

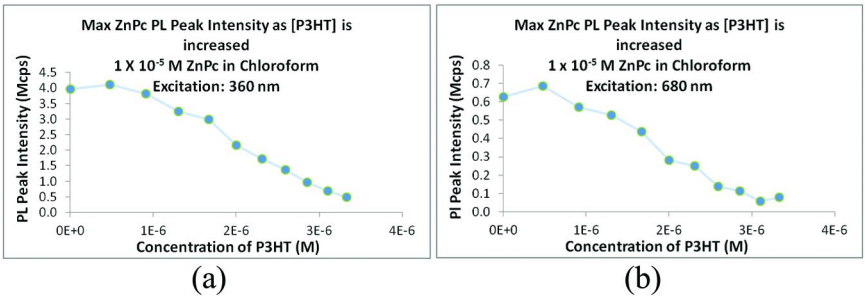

Figure 14. Fluorescence emission maxima of ZnPc (1 x 10^{-5} M in $CHCl_3$) with increasing concentration of P3HT at excitations 360 nm (a) and 680 nm (b).

Figure 15 exhibits the Stern-Volmer (SV) plot of the ZnPc/P3HT pair in a 1:1 chloroform/acetone solution where 1x10^{-4} M P3HT PL is quenched by ZnPc up to 2.5 x 10^{-5} M at 360 nm, and a PL quenching coefficient K_{sv} of 794 M^{-1} is obtained.

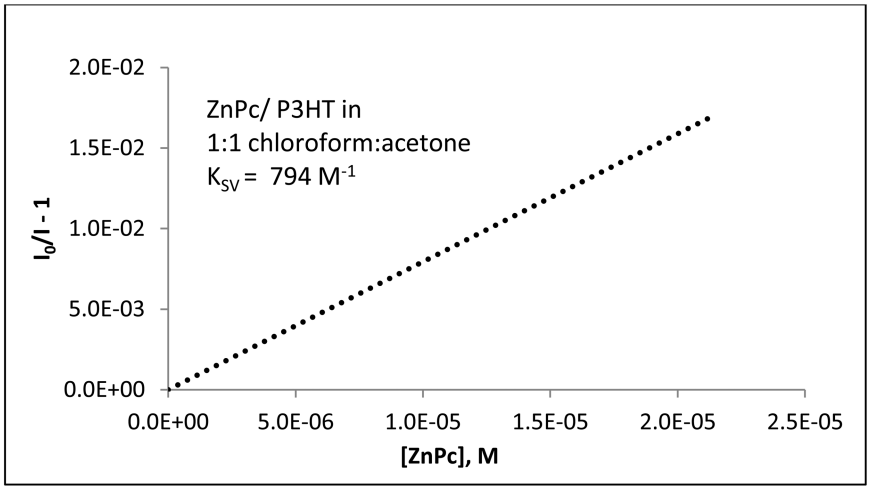

Figure 15. Stern-Volmer plot of P3HT PL (1 x 10^{-4} M in 1:1 chloroform:acetone) quenched by ZnPc (below 2.5 x 10^{-5} M) at 360 nm excitation.

Figure 16 shows the PL spectra of the ZnPc/P3HT pair excited at 360 nm, where the concentration of the ZnPc is fixed at 1 x 10^{-4} M while the concentration of P3HT is increased. Interestingly and suprisingly, the ZnPc emission peak at around 700 nm increases as the P3HT concentration inceases!

To futher investigate and explain the ZnPc PL increase phenomena, these experiments were carried out at various concentrations of both species. Figure 17 provides the ZnPc PL peak maxima when ZnPc concentration is fixed at $1x10^{-4}$ M, and [P3HT] is increased at a) 360 nm excitation (single photon absorption for both ZnPc and P3HT), and b) 680 nm excitation (single photon absorption for ZnPc but two photon absorption for P3HT). It appears that regardless of the P3HT absorption process (single or two-photon), the PL emission peak of $1x10^{-4}$ M ZnPc increases as [P3HT] increases, up to 4 x 10^{-5} M.

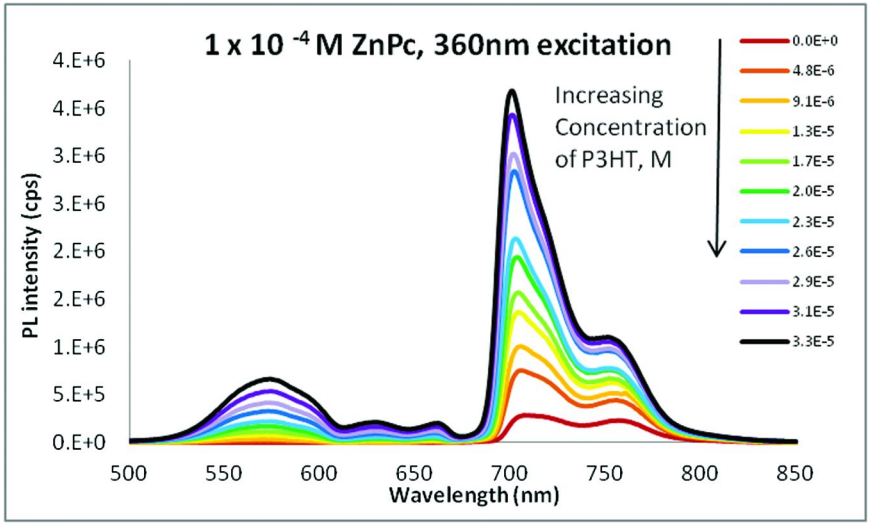

Figure 16. Fluorescence spectra of ZnPc/P3HT pair with ZnPc concentration fixed at 1 x 10^{-4} M and P3HT concentration increasing at 360nm excitation.

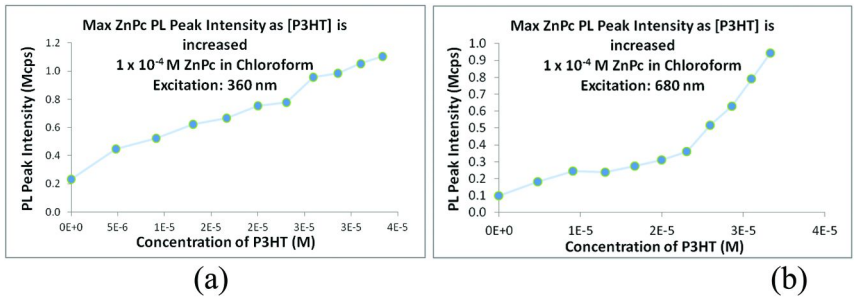

Figure 17. Fluorescence emission maxima of ZnPc (1 x 10^{-4} M in $CHCl_3$) with increasing concentration of P3HT at excitations 360 nm (a) and 680 nm (b).

In Polymer Composites for Energy Harvesting, Conversion, and Storage; Li, L., et al.;
ACS Symposium Series; American Chemical Society: Washington, DC, 2014.

Furthermore, when both species' concentrations were increased (while keeping the dye:polymer ratio constant between sets of experiments), the same increase in ZnPc PL was observed as the [P3HT] was increased, as shown in Figure 18. The PL emission increase of ZnPc is obvioius when [ZnPc] is fixed at 1 x 10^{-3} M and [P3HT] increasing up to 4 x 10^{-4} M.

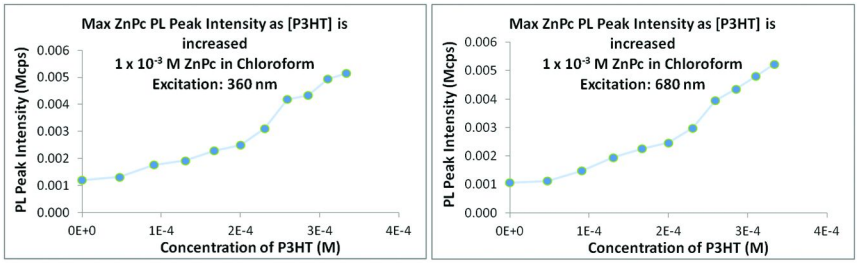

(a) (b)

Figure 18. Fluorescence emission maxima of ZnPc (1 x 10^{-3} M in $CHCl_3$) with increasing concentration of P3HT at excitations 360nm (a) and 680nm (b).

This study shows that when the ZnPc concentration is less than 1x10^{-4} M, P3HT quenches the PL of ZnPc possibly due to photo-induced charge transfer between the dye and the polymer. When the concentration of ZnPc is at or over 1x10^{-4}M, an increase of P3HT concentration causes an increase of the ZnPc PL even if the ZnPc concentration remains the same. Clearly the optoelectronic properties of the ZnPc are very different below or above 1x10^{-4} M.

Based on literature reports, phthalocyanine (Pc) dyes are known to form molecular aggregrates such as dimers or larger clusters in solution. This aggregation depends on the phthalocyanine's substituents, concentration, and the solvent used. It is also well known that these aggregates are not emissive, resulting in PL quenching as the ratio of monomeric species: aggregated species increases (*11*, *12*). Although ZnPc was synthesized with four bulky aliphatic groups specifically to inhibit its aggregation, it has been reported that it still forms aggregates in solution, even at low concentration.

It has also been reported that molecular dyes can be deaggregated by certain molecules. These de-aggregating molecules induced a similar PL increase in the dye as the concentration of the de-aggregating species was increased (*13*). De-aggregation can be accomplished via solvents or certain molecular species that interact strongly with the dye molecules. In our studies as shown in Figure 19, when the ZnPc concentration is fixed at 1x10^{-4} M, at very low P3HT concentrations (less than 1x10^{-4} M), PL quenching of ZnPc has been observed. However, as the P3HT concentration increases to over 1x10^{-3} M, the PL of ZnPc starts to increase.

Based on our experimental results and the literature reports referenced above, we propose that ZnPc forms dimers or higher order aggregates in solutions of chloroform at a concentration of 1x10^{-4} M or above. Upon introducing a long, bulky molecule, such as a polymer, in high concentration, the dye aggregates begin to break apart, restoring the dye's natural emission intensity.

In Polymer Composites for Energy Harvesting, Conversion, and Storage; Li, L., et al.;
ACS Symposium Series; American Chemical Society: Washington, DC, 2014.

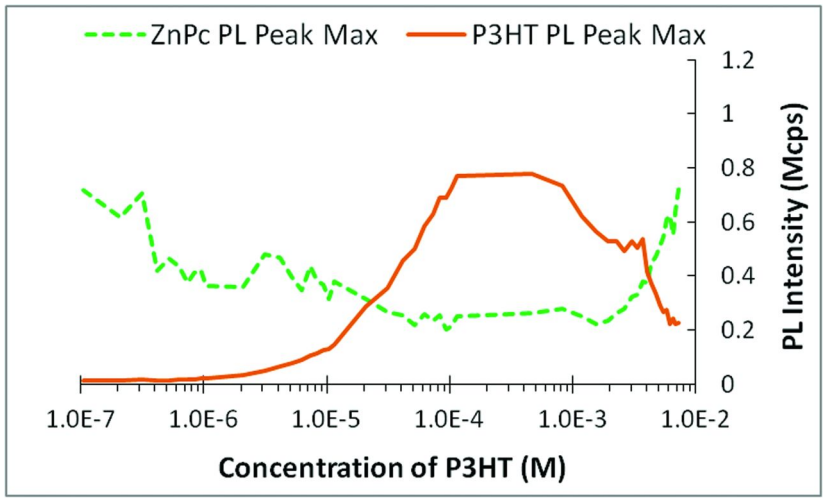

Figure 19. PL emission spectra of ZnPc (green dashed line) and P3HT (orange solid line) with increasing P3HT concentration, excited at 360 nm.

P3HT is also known to form aggregates in solution and in the solid state, depending on solvent, concentration, and processing conditions (*14*, *15*). The interactions between the thiophene rings of P3HT can be either *intra*chain or *inter*chain interactions, based on whether the rings involved are on the same polymer chain (*14*). Interchain interactions involve polymer chains that stack next to each other, overlapping the p-orbitals that carry the delocalized electrons. Intrachain interactions involve a coiling of the polymer chain due to the interaction of rings within that chain, preventing the overlap of p-orbitals on the inside of the coil (*16*). As the polymer backbone becomes more coiled, the overlap of p-orbitals allowing for conjugation decreases, eventually being eliminated at sharp bends in the polymer chain (*17*). It is well known that decreased conjugation in organic photovoltaic polymers increases the band gap energy (*17*). This increase of the P3HT energy gap can be due to a raised LUMO level, a lower HOMO level, or both. These two types of P3HT aggregation may be present in the same sample (*14*), complicating the morphological and current-voltage characterization of P3HT based solar cell devices. As Figure 19 exhibits, the initial PL increase of P3HT at low concentrations can be attributed to the P3HT density increase. However, after about $1x10^{-4}$ M, the PL of P3HT starts to level off. After $1x10^{-3}$ M, the PL of P3HT decreases, which can be attributed to P3HT aggregation.

To provide further evidence that the increase in PL of ZnPc is due to de-aggregation, an experiment was performed in the same manner as the previous experiments, using pyridine as a known de-aggregating species, and holding [ZnPc] constant. Pyridine has been reported to solvate certain highly conjugated molecules via pi-pi interactions. As Figure 20 shows, when [pyridine] is added while keeping [ZnPc] constant, the PL of ZnPc remains constant and at a higher intensity, regardless of the concentration of polymer. This indicates that pyridine inhibits the aggregation of ZnPc immediately, resulting in full PL emission.

In Polymer Composites for Energy Harvesting, Conversion, and Storage; Li, L., et al.;
ACS Symposium Series; American Chemical Society: Washington, DC, 2014.

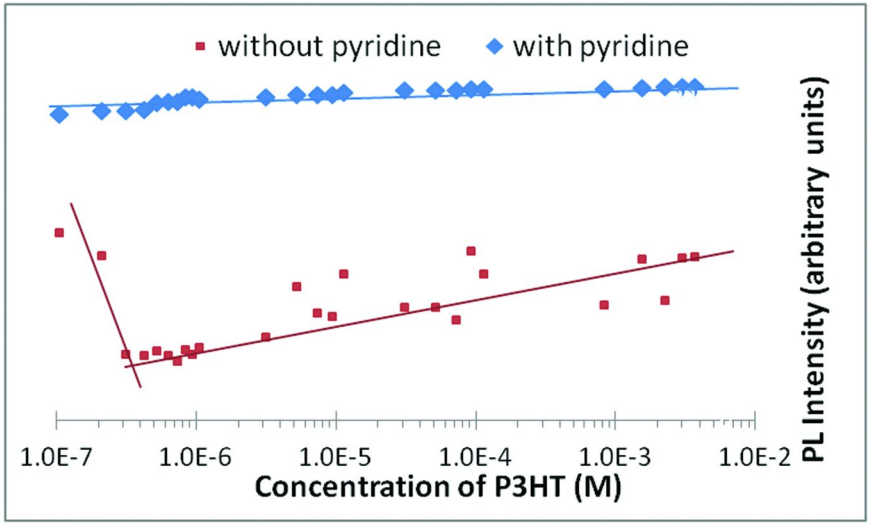

Figure 20. PL emission intensity of ZnPc in ZnPc/P3HT composite in chloroform with pyridine (top curve) and without pyridine (bottom curve).

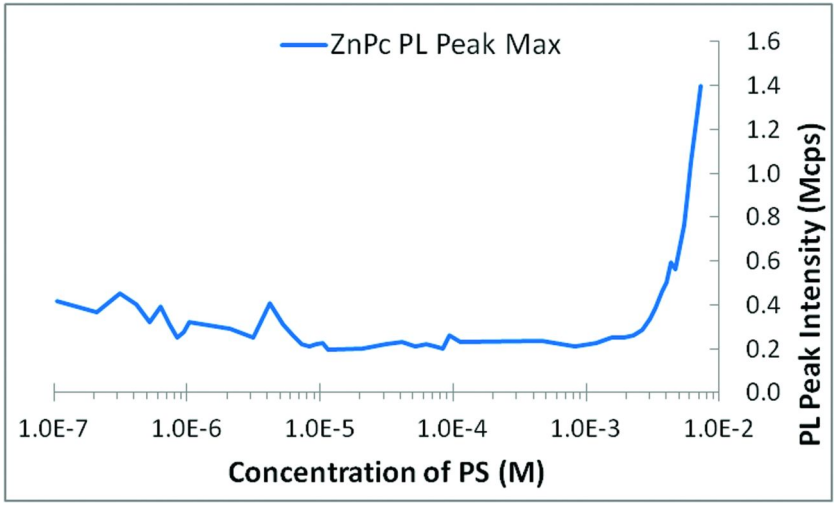

Figure 21. 1 x 10^{-4} M ZnPc PL emission intensity versus polystyrene (PS) concentration in chloroform solution.

In order to determine whether the electronic or physical nature of P3HT induces ZnPc de-aggregation, polystyrene (PS) was used as a potential de-aggregator of ZnPc. Because PS is not expected to participate in energy transfer with ZnPc, any de-aggregation of the dye induced by this polymer

In Polymer Composites for Energy Harvesting, Conversion, and Storage; Li, L., et al.;
ACS Symposium Series; American Chemical Society: Washington, DC, 2014.

is likely due to the bulkiness of the polymer. As Figure 21 shows, a ZnPc PL increase is also induced by increasing PS concentration at higher ZnPc concentration. Most importantly, the PL of pristine ZnPc in chloroform decreases as its concentration increases (Figure 22), which is clear evidence of a typical molecular aggregation-induced PL quenching, *i.e.*, ZnPc aggregates heavily at higher concentrations, quenching its PL in chloroform solution. From these results, we can conclude that the ZnPc PL increase at higher P3HT concentration can be attributed to de-aggregation of the dye as a result of the polymer concentration increase.

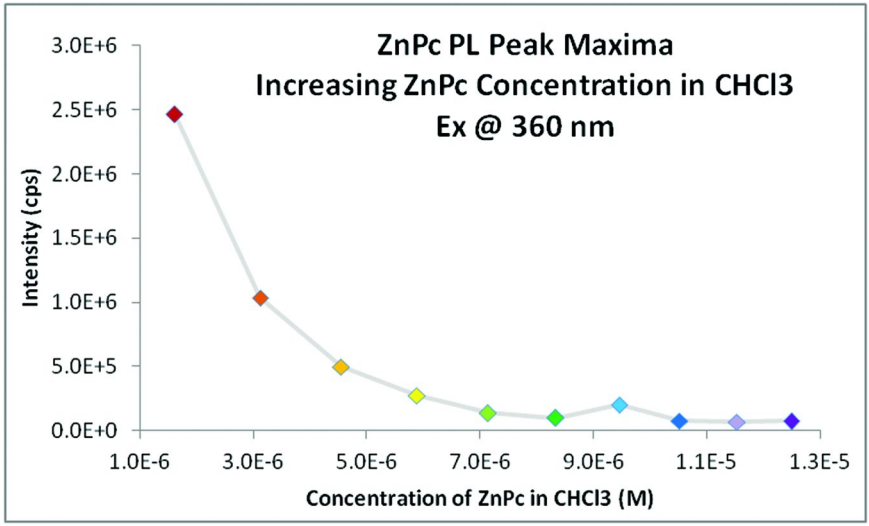

Figure 22. PL emission intensity of ZnPc as its concentration is increased in chloroform solution.

Summary

In summary, the newly developed C12-PTV conjugated polymer exhibited about three times more intense molar light absorption coefficient as well as lower optical energy gap compared to the popular P3HT, thus C12-PTV is expected to capture sunlight photons more effectively than that of P3HT. However, in order for C12-PTV based optoelectronic devices to surpass the P3HT devices, the charge mobility, the chemical stability, and the frontier orbital matches of C12-PTV with other acceptor-type materials and electrodes need to be investigated and optimized. Z-907 dye has the advantage of two carboxylic acid functional groups that are readily available for covalent chemical attachment to other materials such as polymers or inorganic semiconducting oxides, and Z-907 also has a relatively low energy gap, but its molar absorption coefficient is only slightly better than that of P3HT. On the other hand, MB (or NMB) dyes have about ten times more

In Polymer Composites for Energy Harvesting, Conversion, and Storage; Li, L., et al.;
ACS Symposium Series; American Chemical Society: Washington, DC, 2014.

intense light molar absorption coefficient than P3HT, but MB dyes are not readily processable like other dyes; more synthetic chemistry work is needed. ZnPc dye has almost twenty-four times more intense molar light absorption coefficient than P3HT, and its absorption peaks complement that of P3HT and C12-PTV. One important and interesting discovery is that at relatively low ZnPc/P3HT concentrations (for instance, less than $1x10^{-4}$M), P3HT/ZnPc pair appears to undergo a photo-induced charge transfer between P3HT and ZnPc causing PL quenching. However, at relatively high ZnPc concentrations (*e.g.*, equal or over $1x10^{-4}$M), polymer induced de-aggregation of ZnPc results in PL increase. However, if molecular dyes are covalently incorporated onto the polymer, the dye aggregation can be well controlled, and such studies are underway.

Acknowledgments

This material is based upon work supported, in part, by project awards from the Army Research Office (award #W911NF-11-1-0158), the National Science Foundation (award #1036494), and the Department of Energy (award #DE-EE-0004002).

References

1. Kazmerski, L. *J. Electron Spectrosc. Relat. Phenom.* **2006**, *150*, 105–135.
2. *Handbook of Photovoltaic Science and Engineering*, 2nd ed.; Luque, A, Hegedus, S., Eds.; Wiley: West Sussex, England, 2009.
3. *Organic Photovoltaics: Mechanisms, Materials and Devices*; Sun, S., Sariciftci, N., Eds.; CRC Press: Boca Raton, FL, 2005.
4. Sun, S. Organic and Polymeric Solar Cells. In *Handbook of Organic Electronics and Photonics*; Nalwa, S. H., Ed.; American Scientific Publishers: Los Angeles, CA, 2008; Vol. 3, Chapter 7, pp 313−350.
5. Sun, S.; O'Neill, H. Sunlight Energy Conversion via Organics. In *Handbook of Photovoltaic Science and Engineering*, 2nd ed.; Luque, A., Hegedus, S., Eds.; Wiley: West Sussex, England, 2009; pp 675−715.
6. Li, G.; Zhu, R.; Yang, Y. *Nat. Photonics* **2012**, *6*, 153–161.
7. *Handbook of Conducting Polymers*, 3rd ed.; Skotheim, T. A., Elsenbaumer, R. L., Reynolds, J. R., Eds., CRC Press: Boca Raton, FL, 2007.
8. Westenhoff, S.; Howard, I.; Hodgkiss, J.; Kirov, K.; Bronstein, H.; Williams, C.; Greenham, N.; Friend, R. *J. Am. Chem. Soc.* **2008**, *130* (41), 13653–13658.
9. Zhang, C.; Matos, T.; Li, R.; Sun, S.; Lewis, J.; Zhang, J.; Jiang, X. *Polym. Chem.* **2010**, *1*, 663–669.
10. Meyera, R. K.; Bennera, R. E.; Vardenya, Z. V.; Liessa, M.; Ozakib, M.; Yoshinob, K.; Dingc, Y.; Barton, T. *Tetrahedron* **2006**, *62*, 2123–2131.
11. Li, H.; Nguyen, N.; Fronczek, F.; Vicente, M. *Tetrahedron* **2009**, *65*, 3357–3363.
12. Dhami, S.; de Mello, A.; Rumbles, G.; Bishop, S.; Phillips, D; Beeby, A. *Photochem. Photobiol.* **1995**, *61*, 341–346.

13. Sessler, J. L.; Jayawickramarajah, J.; Gouloumis, A.; Dan Pantos, G.; Torres, T.; Guldi, D. *Tetrahedron* **2006**, *62*, 2123–2131.
14. Clark, J.; Silva, C.; Friend, R.; Spano, F. *Phys. Rev. Lett.* **2007**, *98*, 206406.
15. Park, Y.; Lee, H.; Choi, Y.; Kwak, D.; Cho, J.; Lee, S.; Cho, K. *Adv. Funct. Mater.* **2009**, *19*, 1200–1206.
16. Schwartz, B. *Annu. Rev. Phys. Chem.* **2003**, *54*, 141–172.
17. Bredas, J.; Silbey, R.; Boudreaux, D.; Chana, R. *J. Am. Chem. Soc.* **1983**, *105*, 6555–6559.

Chapter 3

Synthesis and Process-Dependent Film Structure of All-Conjugated Copolymers for Organic Photovoltaics

Yen-Hao Lin and Rafael Verduzco*

Department of Chemical and Biomolecular Engineering, MS-362, Rice University, 6100 Main Street, Houston, Texas 77005
***E-mail: rafaelv@rice.edu.**

Donor-acceptor all-conjugated block copolymers can be used to build organic photovoltaics (OPVs) with improved interfacial structure, broader light absorption, and enhanced performance. The past decade has seen significant progress in the synthesis and structure analysis of all-conjugated block copolymers. One system in particular – Poly(3–alkylthiophene)–*b*–poly(9′,9′–dioctylfluorene) (P3AT–*b*–PF) – has served as a model system for developing new synthetic techniques and analyzing the microstructure in thin films, in the melt, and in the solutions. This article reviews work with P3AT–*b*–PF block copolymers, emphasizing both material synthesis and analysis of crystallinity, micro-phase segregation in films, and aggregation in solutions. This overview demonstrates significant advances in the preparation and characterization of all-conjugated block copolymers and emphasizes remaining challenges in the application of all-conjugated block copolymers for OPVs.

In Polymer Composites for Energy Harvesting, Conversion, and Storage; Li, L., et al.;
ACS Symposium Series; American Chemical Society: Washington, DC, 2014.

1. Introduction

Conjugated polymers have received enormous attention since their discovery in the late 70s, recognized by the Nobel Prize in Chemistry awarded in 2000 (*1*). Conjugated polymers are currently being investigated for organic electronic applications, including light emitting diodes (OLEDs) (*2–7*), field-effect transistors (OFETs) (*8–11*), photovoltaics (OPVs) (*12–15*), sensors (*16*, *17*), and electrochromic devices (*18*) and they offer potentially low-cost solution processing strategies other benefits such as flexibility and transparency (*19–21*).

Achieving efficient solution-processed polymer OPVs is a significant challenge and a current area of research emphasis (*22–31*). Conjugated polymer OPVs are made by depositing one or more conjugated organic molecules or polymers in a thin film of few hundred nanometers. The large absorption coefficients of conjugated polymer enables ~ 100 nm thin photovoltaic active layers (*32*). This active layer is sandwiched between anode and cathode electrodes (as shown in Figure 1). The absorption of a photon results in an electron/hole pair known as an exciton which must be separated into distinct charges to generate a useful current. This is in contrast to inorganic photovoltaics where free charges are created upon light absorption (*33*). Generating a useful current requires separating the exciton into distinct charges, which must occur within the short lifetime of the photoexcited state (*34–37*). The exciton is most efficiently separated at the interface between donor and acceptor semiconductors, therefore optimizing the active layer structure is important for achieving efficient OPV performance.

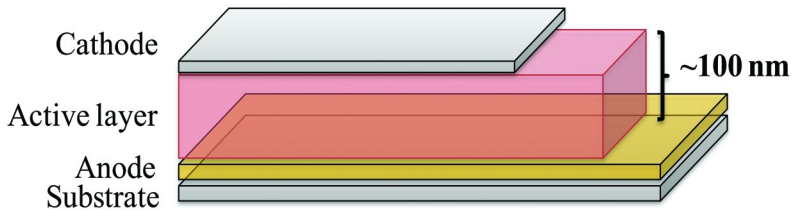

Figure 1. Representative configuration of an OPV device. The active layer is comprised of a blend of electron-donor and electron-acceptor organic semiconductors.

A schematic for bulk-heterojunction OPVs consisting of both conjugated polymer and fullerene is shown in Figure 2a. In general, the final active layer structure is a result of various non-equilibrium processes, including polymer crystallization and phase separation, that occur during film casting and annealing (*24*, *38*). A variety of methods have been implemented to control the length scale interface structure and crystallinity of the active layers including the use of processing additives (*39–41*) and top-down approaches to patterning (*42–44*).

In Polymer Composites for Energy Harvesting, Conversion, and Storage; Li, L., et al.;
ACS Symposium Series; American Chemical Society: Washington, DC, 2014.

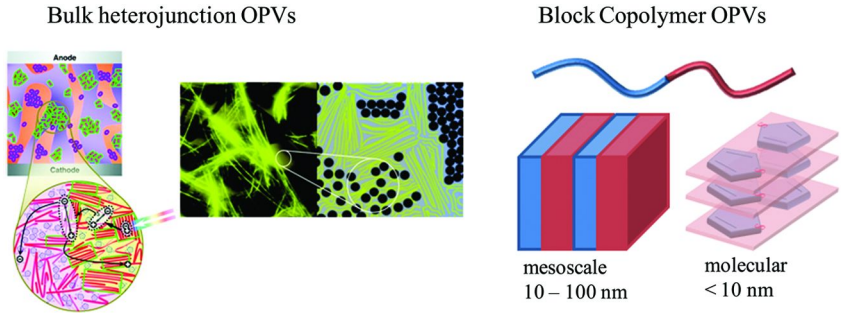

Figure 2. Schematics for the active layer morphologies of bulk heterojunction OPVs (left) and all-conjugated block copolymer OPVs (right). (Reproduced with permission from references (22) and (31). Copyright 2011 American Chemical Society.)

Block copolymers comprised of two-conjugated polymer blocks, known as all-conjugated block copolymers (*45*), can potentially address many of the current challenges in morphology and interfacial structure control for OPVs. All-conjugated block copolymers are an emerging class of materials comprised of two or more conjugated polymer chains. Such block copolymers combine the optoelectronic properties of semiconductive polymers with structure control through micro-phase segregation (*46–48*) and crystallization (*49*, *50*). Donor-acceptor all-conjugated block copolymers comprised of both hole-conductive (*p*-type) and electron-conductive (*n*-type) polymer blocks are of particular interest for OPVs (*51*, *52*). Selected examples of all-conjugated block copolymers are shown in Scheme 1 (*45*, *49*, *53–63*). The micro-phase segregation of diblock copolymer typically leads to domain sizes of 5-100 nm with various morphologies, depending on the volume fraction of block (*64*, *65*). As shown in Figure 2, all-conjugated block copolymers can potentially self-assemble into well-defined donor and acceptor domains with controlled size and orientation.

Recent work has demonstrated significant progress in the design, synthesis, and characterization of all-conjugated block copolymers (*49*, *66–69*). All-conjugated block copolymers have recently demonstrated efficienties near 3 % in a block copolymer device (*70*). However, further progress requires advances in both the synthesis and processing-structure-property relationships. Here, we review the synthesis and characterization of all-conjugated block copolymers with a specific emphasis on conjugated block copolymers that incorporate both poly(alkylthiophene) (P3AT) and poly(dialkylfluorene) (PF) polymer blocks. P3AT-*b*-PF block copolymers were among the first all-conjugated block copolymers reported (*45*), and significant progress has been made in the synthesis and characterization of these materials. Progress with P3AT-*b*-PF can provide valuable lessons for other systems and fundamental insight into the properties of all-conjugated block copolymers. The structure of P3AT-*b*-PF along with other all-conjugated block copolymers reported is shown in Scheme 1.

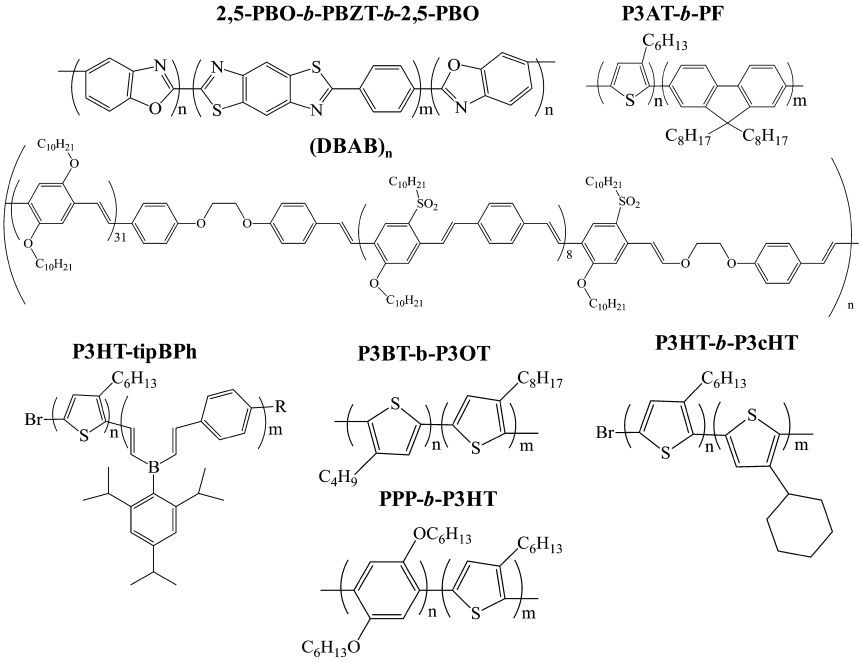

Scheme 1. Different all-conjugated block copolymer structures reported in the literature. 2,5-PBO-b-PBZT-b-2,5-PBO (61), P3HT-b-PF (45), $(DBAB)_n$ (71), P3HT-tipBPh (72), P3BT-b-P3OT (73), P3HT-b-P3cHT (74) and PPP-b-P3HT (75).

Below, we review synthetic approaches and processing-structure-property relationships in all-conjugated block copolymers, emphasizing results with P3AT-*b*-PF block copolymers. The synthesis of well-defined, all-conjugated block copolymers has been a significant challenge in the field, and over the past several years new synthetic approaches have emerged based on copper-catalyzed click chemistry and stepwise polymerizations. Understanding the microstructure of all-conjugated block copolymer films is crucial to their application, and distinguishing between crystallization and micro-phase segregation requires characterization using a variety of techniques. We show that varying processing conditions results in dramatic changes to the film morphology on a model series of poly(3-alkylthiophene)–*b*-poly(9′,9′-dioctyl fluorene) (P3AT-*b*-PF). We present work from our group and also others that have synthesized and characterized P3AT-*b*-PF. While we focus primarily on work with P3AT-*b*-PF, there have been significant advances in the synthesis and processing of other conjugated block polymer films as can be found in other publications (*49*, *76*) and recent reviews (*37*, *51*, *77–80*).

In Polymer Composites for Energy Harvesting, Conversion, and Storage; Li, L., et al.;
ACS Symposium Series; American Chemical Society: Washington, DC, 2014.

2. Synthesis of P3AT-*b*-PF All-Conjugated Block Copolymers

Most approaches for making donor-acceptor all-conjugated block copolymers, which incorporate both *n*- and *p*-type polymer blocks, rely on distinct polymerization reactions for each polymer block, including GRIM, Suzuki-Miyaura, and Stille polymerization reactions (*45*, *49*, *54*, *63*, *83*, *84*). All-conjugated block copolymers are generally synthesized from two general strategies depicted schematically in Figure 3: (a) through a macro-reagent approach involving sequential polymerization reactions; and (b) through the coupling of two conjugated polymers with controlled end-functionalities. Both strategies have advantages and limitations. While the macro-reagent approach is generally more straightforward and versatile, the coupling approach gives better control over the molecular weight of each polymer block separately. However, the coupling approach requires good end-group control for two separate conjugated polymer blocks. Below, we review recent applications and advances in these synthetic approaches applied to the synthesis of P3AT-*b*-PF (*45*, *81–83*).

Alternative approaches to the two mentioned above are limited but include the "all-GRIM" approach which has been applied for the synthesis of block copolythiophenes (*56*, *57*, *68*, *73–75*, *81*, *85–91*) and P3HT-*b*-PF (*85*). The advantage of "all-GRIM" is potentially improved control over the polymerization reaction of both blocks. However, "all-GRIM" is limited in terms of applicability to different monomeric repeat units. The reader is referred to recent reviews for more information on this synthetic approach (*92–94*).

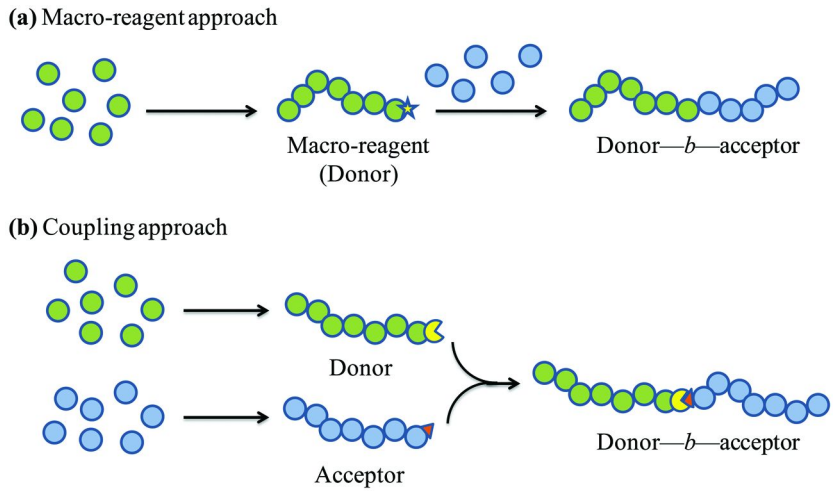

Figure 3. Approaches for synthesis of all-conjugated block copolymers via (a) macro- reagent and (b) covalent/supramolecular coupling.

In Polymer Composites for Energy Harvesting, Conversion, and Storage; Li, L., et al.;
ACS Symposium Series; American Chemical Society: Washington, DC, 2014.

2.1. All-Conjugated Block Copolymer Synthesis Using a Macroreagent Approach

The first example of a macro-reagent approach applied to the synthesis of P3AT-*b*-PF all-conjugated block copolymers was reported by the Scherf group (*83*). Their synthetic method involved the synthesis of a poly(3-hexylthiophene) (P3HT) macro-reagent followed by a Suzuki-Miyaura polycondensation reaction to synthesize the PF block. Several subsequent studies have taken advantage of this general approach to synthesize all-conjugated block copolymers, using Suzuki-Miayaura or other polycondensation reactions for the synthesis of the second polymer block (*45*, *49*, *53*, *63*, *66*, *68*, *84*, *95*). The versatility of this general approach is reflected in the variety of block copolymers reported using this scheme. However, a drawback of these methods is that they typically result in relatively low molecular weight block copolymers with significant amounts of homopolymer impurities that can only be removed using tedious column purification techniques (*26*, *49*, *63*).

An improved approach for synthesizing all-conjugated block copolymers using Suzuki-Miyaura and GRIM with little or no homopolymer approaches was recently demonstrated by our group (*67*). GRIM is first carried out to synthesize an end-functionalized P3HT (P3HT-Br) macroreagent, and P3HT-Br is subsequently utilized in a Suzuki-Miyaura polymerization reaction to make all-conjugated P3HT block copolymers (Scheme 2). A high degree of end functionalization of the P3HT-Br macroreagent is required to avoid residual P3HT homopolymer impurities, and this was accomplished using LiCl as an additive for the preparation of bromo-chloromagnesio -hexylthiophene monomer. LiCl has been shown to be an effective additive for accelerating Grignard formation and producing P3HT with a high degree of end-group functionality (*96–98*). P3HT-Br was prepared using standard methods by the addition of Ni(dppp)Cl_2 catalyst to the monomer solution to initiate GRIM (*99*). Three different P3HT macroreagents were prepared using this approach, as shown in Table I.

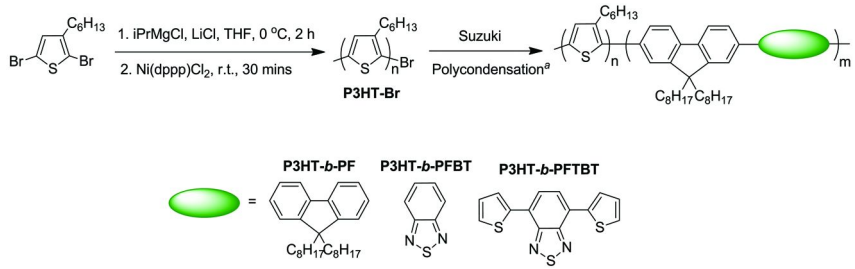

Scheme 2. Preparation of all-conjugated P3HT block copolymers via Grignard metathesis polymerization with LiCl additive followed by Suzuki-Miyaura Polycondensation. [a]conditions for Suzuki-Miyaura: $Pd(PPh_3)_4$, toluene, water, 90 °C. An equimolar ratio of 9',9'-dioctylfluorene-2',7'-diboronic acid ester and corresponding dibromo monomer is used. (Adapted with permission from reference (67). Copyright 2013 Royal Society of Chemistry.)

In Polymer Composites for Energy Harvesting, Conversion, and Storage; Li, L., et al.;
ACS Symposium Series; American Chemical Society: Washington, DC, 2014.

Next, P3HT-Br was reacted in a Suzuki-Miyaura polycondensation reaction to prepare three different types block copolymers, each with a P3HT block and a second conjugated polymer block: poly(9′,9′-dioctyl fluorene) (PF), poly(9′,9′-dioctyl fluorene-*alt*-benzo- thiadiazole) (PFBT), and poly(2,7-(9′,9′-dioctyl-fluorene)-*alt*-5,5-(4′,7′-di-2-thienyl-2′,1′,3′, benzothiadiazole) (PFTBT). PF, PFBT, and PFTBT have been previously studied for use in bulk-heterojunction OPVs and OLEDs (*100–102*), and PFTBT is promising for use in block copolymer OPVs because it exhibits a broad absorbance and a low-lying HOMO level (*103*, *104*). A high and low molecular weight P3HT-Br macroreagent was used for each type of block copolymer, resulting in a total of six different block copolymers, as shown in Table I. The formation of triblock copolymers is unlikely due to a low content of P3HT-Br macroreagent used in the Suzuki-Miyaura polycondensation step (roughly 1 mole % relative to monomers).

Table I. Characteristics of All-Conjugated P3HT Block Copolymers SOURCE: Reproduced with permission from reference (*67*). Copyright 2013 Royal Society of Chemistry.

Polymers	*P3HT[a] M_w (PDI)*	*BCP[a] M_w (PDI)*	*DP ratios[b] (P3HT wt%)*
P3HT13-*b*-PF87	6.1 (1.16)	48.4 (1.86)	36:100 (13%)
P3HT25-*b*-PF75	13.5 (1.32)	60.6 (1.87)	81:105 (25%)
P3HT20-*b*-PFBT80	8.5 (1.19	168 (3.61)	51:66 (20%)
P3HT22-*b*-PFBT78	13.5 (1.32)	81.5 (2.24)	81:90 (22%)
P3HT42-*b*-PFTBT58	8.5 (1.19)	19.7 (1.49)	51:17 (42%)
P3HT62-*b*-PFTBT38	13.5 (1.32)	N/A[c]	81:12 (62%)

[a] M_w (kg/mol) and PDI for P3HT and block copolymers determined by comparison to a set of monodisperse polystyrene standards. Head-to-tail regioregularity of P3HT is greater than 93% for all samples as determined from ^{1}H NMR. [b] DP ratios and P3HT content were determined by ^{1}H NMR *via* comparison of the integrated intensity of P3HT aromatic peak (6.9 ppm) and fluorene alkyl peaks (2.2 ppm). [c] P3HT81-*b*-PFTBT12 contains primarily homopolymer impurities, and therefore an estimate for block copolymer molecular weight is not provided.

The molecular weight distributions for each polymer block and corresponding homopolymer impurities can be obtained by size exclusion chromatography with UV/VIS analysis (SEC-UV/VIS) at two distinct wavelengths. The molecular weight distribution for one block was obtained by using a wavelength specific to one polymer block. 450 nm (specific to P3HT), 500 nm (specific to P3HT), and 550 nm (specific to PFTBT) were used for P3HT-*b*-PF, P3HT-*b*-PFBT, and P3HT-*b*-PFTBT, respectively. PF and PFBT exhibit no measureable absorbance at 450 and 500 nm, respectively, while P3HT exhibits no measureable absorbance at 550 nm. A comparison of the characteristics SEC-refractive index trace

In Polymer Composites for Energy Harvesting, Conversion, and Storage; Li, L., et al.;
ACS Symposium Series; American Chemical Society: Washington, DC, 2014.

(SEC-RI) of final block copolymer products produced (Figure 4 and Table I) with previous reports using similar methods (*49*, *63*) indicates that the use of an LiCl additive enables the preparation of much cleaner and higher molecular weight block copolymers. With the exception of P3HT62-*b*-PFTBT38, a clear shift in the molecular weight distribution of the final products is observed relative to the starting P3HT homopolymers. For comparison, our previous attempts at making similar all-conjugated block copolymers using similar methods (but without the LiCl additive) resulted in only modest shifts in the molecular weight distribution along with homopolymer impurities (*63*). Other reports using similar synthetic methods report the presence of significant homopolymer impurities or relatively low molecular weights for the second polymer block (*6*, *26*). The clear shift in the molecular weight distributions of the block copolymer products shown in Figure 4 indicates that little or no residual P3HT homopolymer remains, and all-conjugated block copolymers with a mass-averaged molecular weight M_w as high as 168 kg/mol (relative to polystyrene) are produced. Number-averaged molecular weights for each block estimated by SEC-RI are in relatively good agreement with ^{1}H NMR estimates of P3HT content of the final block copolymers (Table I). In the case of P3HT62-*b*-PFTBT38, the synthesis failed to produce significant amounts of block copolymer due to poor solubility of the PFTBT block and the resulting block copolymer. However, the use of a lower molecular weight P3HT macroreagent in the polycondensation reaction of PFTBT resulted in product with majority block copolymer in P3HT42-*b*-PFTBT58.

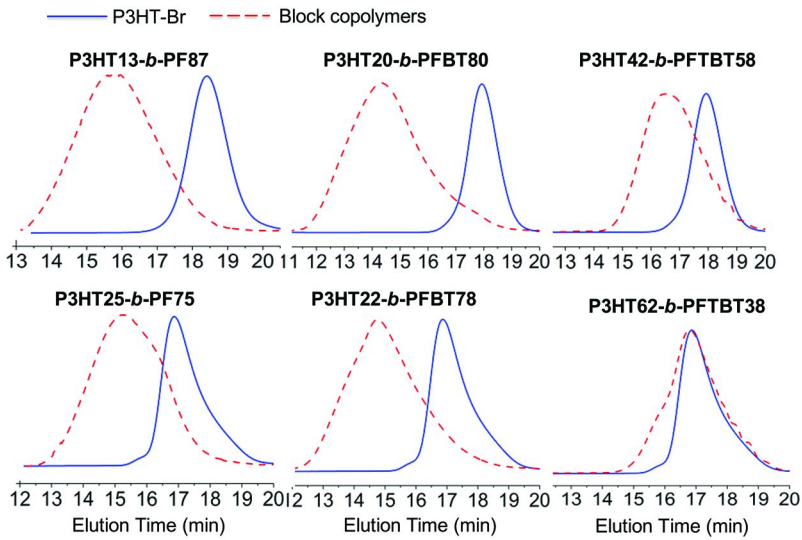

Figure 4. SEC-RI analysis of block copolymers and corresponding P3HT-Br macroreagents. Intensities are normalized for clarity. (Adapted with permission from reference (67). Copyright 2013 Royal Society of Chemistry.)

In summary, the combination of GRIM and Suzuki-Miyaura polymerization reactions can produce all-conjugated block copolymers with some degree of controllable molecular weight and block ratios. GRIM with LiCl additive provides polythiophenes with controlled end-group functionality and molecular weight while the Suzuki-Miyaura reaction has poor control over the molecular weight of the second block. Nonetheless, polycondensation reactions can be qualitatively controlled by varying reaction conditions such as concentration of reagents and reaction time as long as the resulting materials are soluble. The advantage of this strategy is that it can bypass many tedious purification steps such as column chromatography. One drawback to this method is that is limited to polymers that can be prepared by GRIM and by Suzuki-Miyaura. Thus far we have only investigated polythiophene-based all-conjugated block copolymers, but other *p*-type polymer blocks are possible through GRIM (*56*, *59*).

2.2. Synthesis of All-Conjugated Block Copolymers Using Click Coupling Reaction

While the macro-reagent approach has several practical advantages, the relative size of each polymer block cannot be precisely controlled. An alternative route to conjugated block copolymers is to couple two conjugated polymers, which have been independently synthesized, by an efficient chemical reaction. This gives better control over block lengths since each block is synthesized, purified, and characterized prior to coupling. The first donor-acceptor all-conjugated block copolymer reported in the literature was prepared by a coupling approach (*60*, *71*). In addition to material synthesis, work by Sun et al. study demonstrated all-conjugated block copolymer OPVs with near 1 % PCEs. Their synthetic route also produced all-conjugated block copolymers joined by a non-conjugated linker, which the authors hypothesized could reduce the rate of charge recombination. However, few subsequent examples of such an approach have been reported due to the challenge in the synthesis and coupling of conjugated polymers with controlled end-functionality.

Recently, our group investigated the use of copper(I)-catalyzed azide-alkyne "click" coupling to produce P3AT-*b*-PF block copolymers (*50*). Click coupling reactions, in particular copper(I) catalyzed cycloadditions, have been successfully applied as post-polymerization coupling reactions to make rod-coil block copolymers (*105–110*) and block copolythiophenes (*111*) but not previously for the preparation of all-conjugated block copolymers. This synthetic route also produces all-conjugated block copolymers joined by a flexible, non-conjugated linker.

Using a click chemistry approach for the synthesis of P3HT-*b*-PF enables systematic variation of the molecular weight of each polymer block. As shown in scheme 3, P3HT-*b*-PF is synthesized by click coupling of P3HT-alkyne and PF-N_3 in THF in the presence of Cu(I)Br and PMDETA. Details on the preparation of end-functionalized polymeric macroreagents is given in our previous publication (*50*). An excess of the PF macroreagent (20 mol % based on ^{1}H NMR ratio of repeat unit to end group) was added to ensure full reaction of the P3HT-alkyne and

to compensate for any errors in estimates of functionalization. After the reaction was complete, typically less than 8 h or overnight, the product was run through an alumina column, precipitated in hexanes, and washed with boiling hexanes to remove unreacted PF.

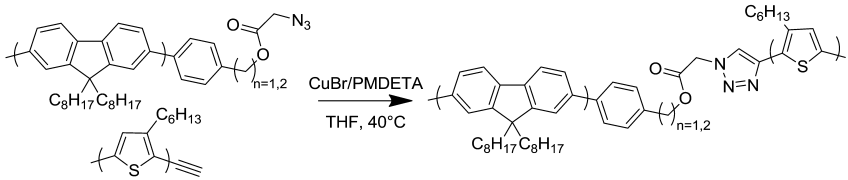

Scheme 3. Preparation of P3HT-b-PF via copper-catalyzed azide-alkyne click chemistry. (Reproduced with permission from reference (50). Copyright 2013 American Chemical Society.)

Table II. P3HT-*b*-PF Conjugated Block Copolymer Samples *via* Click Coupling Reaction. SOURCE: Adapted with permission from reference (*50*). Copyright 2013 American Chemical Society.

Sample	*Mass % P3HT by NMR*	*M_w by SEC-MALLS (kg/mol)*	*PDI*
P3HT79-*b*-PF21	79	19.0	1.22
P3HT64-*b*-PF36	64	17.0	1.27
P3HT52-*b*-PF48	52	17.0	1.53
P3HT32-*b*-PF68	32	18.0	1.38
P3HT23-*b*-PF77	23	19.0	1.50

The click chemistry reaction was carried out with 5 different combinations of P3HT-alkyne and PF-N_3 to yield a series of P3HT-*b*-PF block copolymers (Table II). Similar to the analysis for all-conjugated block copolymers *via* macro-initiator route, the composition, purity, and molecular weight distributions of the final block copolymer products can be determined by ^{1}H NMR and SEC with both MALLS and UV/VIS detection. In all cases, SEC-RI revealed a shift in the molecular weight distribution of the polymeric product relative to the starting macroreagents (see Figure 5a and Supporting Information in the original article (*50*)). A representative example of SEC-UV/VIS analysis is shown for P3HT64-*b*-PF36 in Figure 5b and 5c, and a good match in the molecular weight distributions and at two distinct wavelengths indicates pure block copolymer product with little or no residual homopolymer.

In Polymer Composites for Energy Harvesting, Conversion, and Storage; Li, L., et al.;
ACS Symposium Series; American Chemical Society: Washington, DC, 2014.

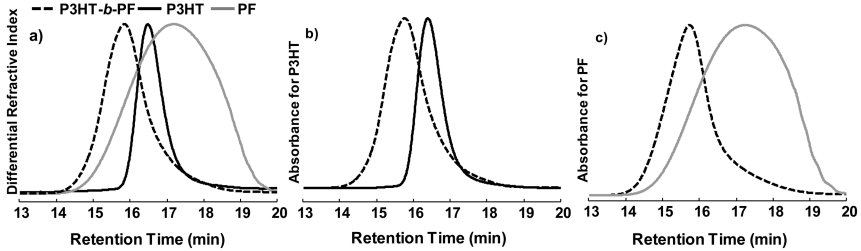

Figure 5. SEC analysis of P3HT64-b-PF36 and corresponding P3HT and PF macroreagents. a) SEC-RI analysis showing a shift in the molecular weight distribution of the final block copolymer relative to the P3HT and PF macroreagents. b) SEC-UV/VIS analysis at 450 nm showing a shift in the molecular weight distribution of the P3HT block relative to the starting P3HT macroreagent. c) SEC-UV/VIS analysis at 300 nm (corrected for the absorbance of the P3HT block) showing a shift in the molecular weight distribution of the PF block relative to starting PF-OH macroreagent. (Reproduced with permission from reference (50). Copyright 2013 American Chemical Society.)

The principle advantage of this synthetic route is the ability to characterize and/or purify the starting materials fully before the coupling reaction, and a single starting polymer may be coupled with multiple different products to give a variety of materials. However, obtaining block copolymer products free of homopolymer impurities is difficult using this route, and requires that both polymeric macroreagents have a high degree of chain-end functionality. For the P3HT-*b*-PF series above, we relied on the differential solubility of each polymer to extract homopolymer impurities, but this is not possible for many block copolymer materials. More recently, this approach was improved through the use of functionalized initiators for the synthesis of both polymer blocks (*112*). The use of functionalized initiators improves the end-group fidelity of both blocks, reducing homopolymer impurities present after coupling (*110*, *113*, *114*).

The work reviewed above demonstrates that versatile synthetic strategies exist to prepare all-conjugated block copolymers. However, challenges remain, including the preparation of block copolymers free of homopolymer impurities and the development of controlled polymerization reactions which will allow for control of the molecular weight and polydispersity of each polymer block. The majority of studies have focused on all-conjugated block copolymers with a poly(3-alkylthiophene) block, but the best performance in bulk heterojunction OPVs has been reported for alternating copolymers produced through polycondensation reactions (*115*). To improve the performance of all-conjugated block copolymer OPV, future work must focus on the development of strategies for incorporating non-thiophene polymer blocks into block copolymers.

3. Process-Dependent Nanostructures for All-Conjugated Block Copolymers

Self-assembly processes in all-conjugated block copolymers remain poorly understood. In particular, unlike for traditional coil-like polymers, crystallization and high glass-transition temperatures can impede the formation of ordered domains through micro-phase segregation. Distinguishing between micro-phase segregation and polymer crystallization in thin films requires a combination of characterization techniques. Below, we review studies exploring processing-structure relationships in P3AT-*b*-PF all-conjugated block copolymers, including their structure in solution, in the bulk, and in thin films.

3.1. Self-Assembly of Amphiphilic P3AT-*b*-PF in Solution

P3AT-*b*-PF block copolymers with one hydrophobic block and one hydrophilic block can self-assemble in solution to form micelles and vesicles. The Scherf and Advincula groups reported the first example of this in P3AT-*b*-PF block copolymers, shown in Figure 6. The P3AT side-chain was modified with a phosphonate group to make the polythiophene block hydrophilic, giving all-conjugated block copolymers that migrate to the air-water interface. The vesicles shown in Figure 6 using both a Langmuir-Blodgett (LB) method and drop casting indicate the formation of micelles and vesicles. The structures result from hydrophobic/hydrophilic interactions and π- π interaction of the hydrophobic segment PF in solutions. This is the first example reporting the self-assembly of an all-conjugated block copolymers in water. All-conjugated block copolymers with one hydrophilic block may be useful for the development of amplifying fluorescent sensors (*116*).

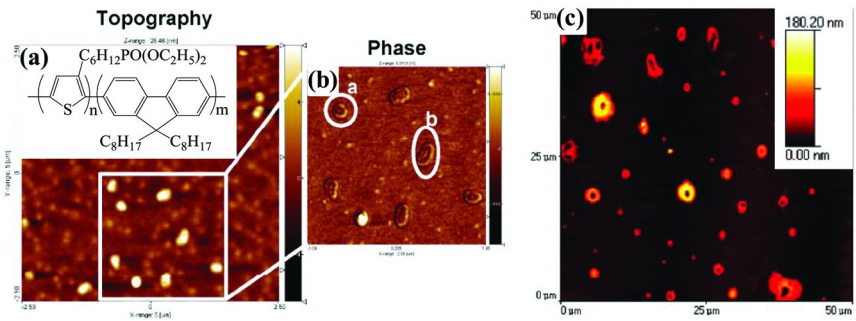

Figure 6. (a) AFM topography, (b) phase image on P3PHT-b-PF films prepared from Langmuir-Blodgett (LB) method at 5mN/m and (c) AFM contact mode image on P3PHT-b-PF films drop-cast from methanol. (Reproduced with permission from reference (45). Copyright 2008 American Chemical Society.)

3.2. Crystallinity in Thermally Treated P3HT-*b*-PF

Polymer crystallinity has a direct impact on properties relevant to performance in OPVs, such as charge-transfer mobility (*117*, *118*). For example, previous literatures report that the performance of OPVs is enhanced with increasing crystallinity of P3HT (*119*, *120*). Thus, for the application of all-conjugated block copolymers in OPVs, crystallization of both blocks may be preferred. P3HT-*b*-PF represents an excellent model system for investigating the crystallinity of both polymer blocks as a function of block ratio, molecular weight, and processing conditions. Both polymer blocks are crystalline, with a crystallization temperature of 220 °C for P3HT and 150 °C for PF. Moreover, regioregular P3HT organizes into lamellar crystalline domains with face-to-face π-π stacking between chains and lamellar stacking through the hexyl side-chains (*121*). In solution processed thin films, the preferred orientation of these crystallites can be dictated to some extent by varying processing conditions (*122*). PF exhibits crystalline, liquid crystalline, or amorphous phases depending on its processing history (*123–125*).

We explored the role of polymer block ratio, molecular weight, and processing through solvent and thermal annealing on a model series of P3HT-*b*-PF. Under thermal annealing, all samples show crystalline features which change depending on the majority block of the block copolymers. As shown in Figure 7, for a series of 5 P3HT-*b*-PF block copolymers made through click chemistry, block copolymers with high PF content show crystallinity characteristic of highly ordered PF α phase crystallites while block copolymers with a high P3HT content show exclusively P3HT crystallites with distinct (*h00*) reflection peaks. P3HT52-*b*-PF48 and P3HT32-*b*-PF68 films show some evidence for co-existence of both P3HT and PF crystallites. GISAXS patterns do not show any reflection peak for any sample in the series. These results indicate no self-assembly of P3HT-*b*-PFs under thermal annealing condition and suggest competitive crystallization is predominant. Other studies on P3HT-*b*-PF block copolymers have found similar results (*112*), including for P3HT-*b*-PF bulk powders (*63*).

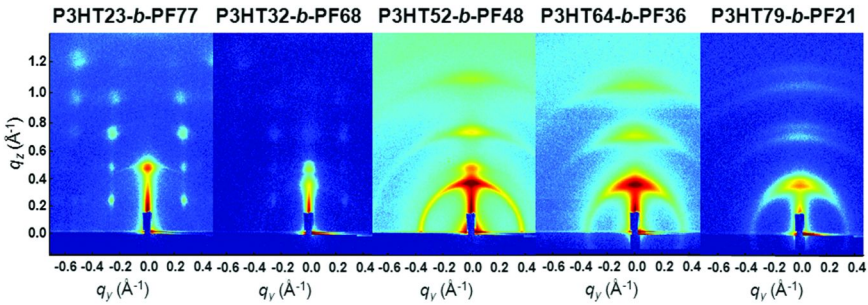

Figure 7. GIWAXS patterns for P3HT-b-PF block copolymer films after thermally annealed at 230 °C and measured at room temperature. (Reproduced with permission from reference (50). Copyright 2013 American Chemical Society.)

In Polymer Composites for Energy Harvesting, Conversion, and Storage; Li, L., et al.;
ACS Symposium Series; American Chemical Society: Washington, DC, 2014.

3.3. Lamellar Structures of Solvent-Treated P3HT-*b*-PFs

The study described in section 3.2 showed that polymer block crystallization was the predominant feature in thermally annealed P3HT-*b*-PF. Thermally annealed films did not show evidence for micro-phase segregation under GISAXS analysis. Prior work with block copolymers has demonstrated that solvent annealing can lead to qualitatively different microstructure and improved long-range ordering (*126*, *127*). Solvent vapor annealing is an effective method for encouraging micro-phase separation of both polymer blocks through increased block mobility.

In recent work, we explored solvent-annealing of a series of P3HT-*b*-PF block copolymers (*128*). We hypothesized that both thermally induced crystallite formation and the poor polymer chain mobility on rigid conjugated polymers within films hindered the self-assembly process. P3HT-*b*-PF films were annealed with chloroform vapor at room temperature. Chloroform is a good solvent for both P3HT and PF and therefore may increase polymer chain mobility during annealing. As shown in Figure 8, highly ordered reflection peaks were observed in out-of-plan direction (q_z) in both GIWAXS and GISAXS of solvent-vapor annealed films. The first order reflection peak of the structure is at $q \sim 0.15$ Å^{-1} (as shown in embedded GISAXS patterns) with a d spacing ~ 4.2 nm for all samples. This indicates the formation of lamellae which is parallel to substrate surface. Surprisingly, the spacing of lamellae is not affected by the relative ratio of polymer block sizes, which contrasts with microphase segregation observed in coil-like block copolymers (*129*). In addition, two in-plane reflection peaks at $q_y \sim 1.45$ Å^{-1} and $q_y \sim 1.63$ Å^{-1} are for planar π-π stacking of PF and P3HT, respectively. The sample with 74 wt% of P3HT shows that P3HT crystallite co-exists with self-assembled lamellae. The result supports our hypothesis that annealing with appearance of a good solvent for both blocks enhances self-assembly of all-conjugated block copolymers.

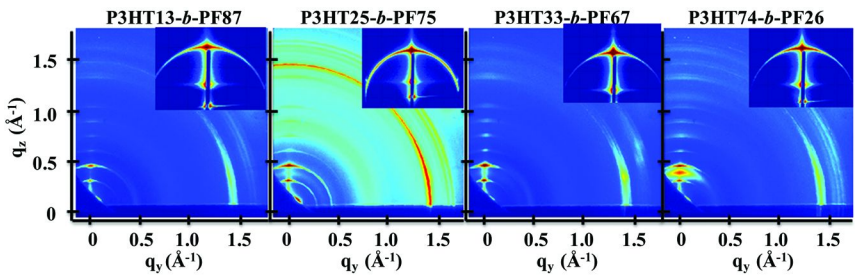

Figure 8. GIWAXS patterns and GISAXS patterns (embedded figures) for P3HT-b-PF block copolymer films after extensive chloroform vapor annealing at room temperature. All of the GISAXS patterns show the first order reflection peak at q ~ 0.15 Å-1.

In Polymer Composites for Energy Harvesting, Conversion, and Storage; Li, L., et al.;
ACS Symposium Series; American Chemical Society: Washington, DC, 2014.

We further explored variations of the processing conditions, specifically: 1) casting samples from 90 °C boiling chloroform solution followed by chloroform annealing and 2) casting samples from room temperature solution followed by thermal annealing in the presence of solvent. As shown in Figure 9, P3HT13-*b*-PF87 film cast from boiling solution shows only PF β phase (*130*) and no P3HT crystzllitazion, but P3HT crystallites form in films with increased P3HT content. In the case of thermally annealed samples, shown in Figure 10, all films show either disorganized crystallites of P3HT and PF or co-existence of two crystallites depending on the block ratios. These tests suggest high-temperature solution casting disrupts crystalline aggregates in solution, resulting in a less-crystalline, disordered film morphology. Conversely, thermal annealing after film casting enhances film crystallinity, with the predominance of P3HT or PF crystals dependent primarily on the relative block ratio.

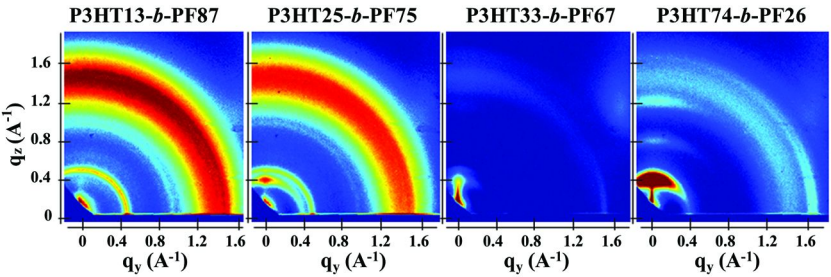

Figure 9. GIWAXS patterns for P3HT-b-PF block copolymer films cast from boiling chloroform solution and measured after extensive chloroform vapor annealing at room temperature.

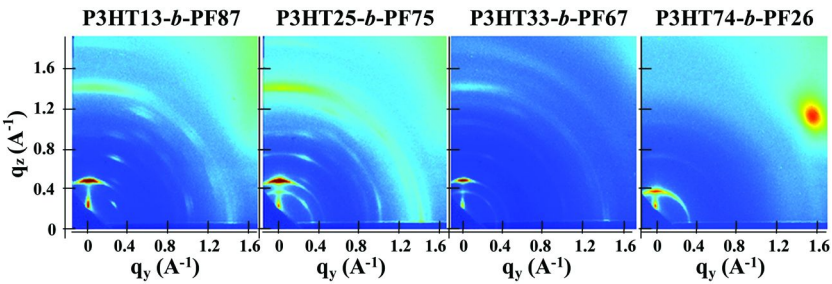

Figure 10. GIWAXS patterns for P3HT-b-PF block copolymer films after thermal annealing at 175 °C in the presence of dichlorobenzene vapor.

In summary, varying solution-casting and annealing conditions has significant impacts on the morphology of all-conjugated block copolymer films. Similar to coil-like polymers, solvent annealing can enhance self-assembly in all-conjugated block copolymers due presumably to enhanced polymer mobility. However,

In Polymer Composites for Energy Harvesting, Conversion, and Storage; Li, L., et al.;
ACS Symposium Series; American Chemical Society: Washington, DC, 2014.

thermally induced crystallites on P3HT and PF can dominate entire morphologies and suppress or compete with self-assembly processes. Also, casting from hot solvents may disrupt solution crystalline aggregates that form in solution (*131*).

While the majority of prior studies on processing dependent structure of all-conjugated BCPs have focused on the P3HT-*b*-PF system, future work will undoubtedly focus on donor-acceptor systems relevant to OPVs. Other processing approaches that have not been applied to all-conjugated block copolymers include include electrospinning, the use of textured or patterned surfaces, and ink-jet printing.

Conclusion

This article summarized recent progress in the synthesis and processing-dependent structure of P3HT-*b*-PF all-conjugated block copolymers. Both macro-reagent approaches and click coupling approaches have been applied to the synthesis of P3HT-*b*-PF. Future works will likely focus on the application of these approaches to donor-acceptor systems and on the development of controlled polymerization approaches applicable to conjugated polymer systems.

Work analyzing the processing-dependent structure of all-conjugated block copolymers has shown that P3HT-*b*-PF can self-assemble into micelles and vesicles in solution, similar to traditional block copolymer systems. In thin films, P3HT-*b*-PF exhibits competitive crystallization, with one block suppressing the crystallization of the second. The block ratio is the primary variable in determining the crystallinity of the final material. Under solvent annealing, a qualitatively different film structure is observed. P3HT-*b*-PF block copolymers self-assemble into lamellae with 4.2 nm spacing, independent of block ratio. This type of self-assembly has not been reported in any other all-conjugated BCP system, and future work will undoubtedly explore similar processing approaches to different all-conjugated block copolymer systems. Finally, varying casting and annealing conditions has a significant impact on crystalline orientation. Crystalline orientation is randomized under high-temperature solvent casting or solvent annealing.

These results provide a wealth of information on P3HT-*b*-PF and indicate potential approaches for directing the structure of all-conjugated block copolymer systems. In particular, long-term solvent annealing may lead to qualitatively different structures in other all-conjugated block copolymer systems compared with just thermal annealing. Block ratio is likely an important variable for balancing crystallinity of both blocks. However, it is unclear how all-conjugated block copolymers with one or more non-crystalline blocks will be affected by thermal and/or solvent annealing. Furthermore, variation of the side-chain structure to enhance enthalpic interaction between polymer blocks (characterized by the Flory-Huggins χ-parameter) may lead to more exotic nanostructures or a stronger driver for self-assembly.

Finally, relationships between film morphology and photovoltaic performance in block copolymer photovoltaics are only beginning to be explored. A recent study reported near 3% PCE in a block copolymer OPV and found crystallization

of the P3HT polymer block along with an edge-on orientation of polymer crystallites (*70*). Future work with BCP OPVs should aim to provide further insight on the relationship between film morphology and electronic properties, including photovoltaic performance.

Acknowledgments

This work was supported by the National Science Foundation under Grant No. CBET-1264703 and the ACS Petroleum Research Fund (Grant # 52345-DNI7). R. Verduzco acknowledges support form Louis and Peaches Owen. Research carried out in part at the Center for Functional Nanomaterials and National Synchrotron Light Source, Brookhaven National Laboratory, which is supported by the U.S. Department of Energy, Office of Basic Energy Sciences, under Contract No. DE-AC02-98CH10886. Use of Advanced Photon Source at Argonne National Laboratory was supported by the U. S. Department of Energy, Office of Science, Office of Basic Energy Sciences, under Contract No. DE-AC02-06CH11357.

References

1. Shirakawa, H.; Louis, E. J.; MacDiarmid, A. G.; Chiang, C. K.; Heeger, A. J. *J. Chem. Soc., Chem. Commun.* **1977**, 578–580.
2. Gustafsson, G.; Cao, Y.; Treacy, G. M.; Klavetter, F.; Colaneri, N.; Heeger, A. J. *Nature* **1992**, *357*, 477–479.
3. Gross, M.; Muller, D. C.; Nothofer, H.-G.; Scherf, U.; Neher, D.; Brauchle, C.; Meerholz, K. *Nature* **2000**, *405*, 661–665.
4. Yang, Y.; Heeger, A. J. *Appl. Phys. Lett.* **1994**, *64*, 1245–1247.
5. Gao, J.; Heeger, A. J.; Lee, J. Y.; Kim, C. Y. *Synth. Met.* **1996**, *82*, 221–223.
6. Carter, S. A.; Angelopoulos, M.; Karg, S.; Brock, P. J.; Scott, J. C. *Appl. Phys. Lett.* **1997**, *70*, 2067–2069.
7. Scott, J. C.; Carter, S. A.; Karg, S.; Angelopoulos, M. *Synth. Met.* **1997**, *85*, 1197–1200.
8. Sirringhaus, H.; Tessler, N.; Friend, R. H. *Science* **1998**, *280*, 1741–1744.
9. Hangarter, C. M.; Bangar, M.; Mulchandani, A.; Myung, N. V. *J. Mater. Chem.* **2010**, *20*, 3131–3140.
10. Janata, J.; Josowicz, M. *Nat. Mater.* **2003**, *2*, 19–24.
11. Facchetti, A. *Chem. Mater.* **2010**, *23*, 733–758.
12. Gunes, S.; Neugebauer, H.; Sariciftci, N. S. *Chem. Rev.* **2007**, *107*, 1324–1338.
13. Thompson, B. C.; Fréchet, J. M. J. *Angew. Chem., Int. Ed.* **2008**, *47*, 58–77.
14. Hoppe, H.; Sariciftci, N. S. *J. Mater. Res.* **2004**, *19*, 1924–1945.
15. Peet, J.; Heeger, A. J.; Bazan, G. C. *Acc. Chem. Res.* **2009**, *42*, 1700–1708.
16. Zhang, X.; Wei, S.; Haldolaarachchige, N.; Colorado, H. A.; Luo, Z.; Young, D. P.; Guo, Z. *J. Phys. Chem. C* **2012**, *116*, 15731–15740.
17. Zhang, X.; Zhu, J.; Haldolaarachchige, N.; Ryu, J.; Young, D. P.; Wei, S.; Guo, Z. *Polymer* **2012**, *53*, 2109–2120.

18. Wei, H.; Yan, X.; Li, Y.; Gu, H.; Wu, S.; Ding, K.; Wei, S.; Guo, Z. *J. Phys. Chem. C* **2012**, *116*, 16286–16293.
19. Krebs, F. C.; Gevorgyan, S. A.; Alstrup, J. *J. Mater. Chem.* **2009**, *19*, 5442–5451.
20. Nielsen, T. D.; Cruickshank, C.; Foged, S.; Thorsen, J.; Krebs, F. C. *Sol. Energy Mater. Sol. Cells* **2010**, *94*, 1553–1571.
21. Krebs, F. C.; Jørgensen, M.; Norrman, K.; Hagemann, O.; Alstrup, J.; Nielsen, T. D.; Fyenbo, J.; Larsen, K.; Kristensen, J. *Sol. Energy Mater. Sol. Cells* **2009**, *93*, 422–441.
22. Chen, W.; Xu, T.; He, F.; Wang, W.; Wang, C.; Strzalka, J.; Liu, Y.; Wen, J.; Miller, D. J.; Chen, J.; Hong, K.; Yu, L.; Darling, S. B. *Nano Lett.* **2011**, *11*, 3707–3713.
23. Scharber, M. C.; Mühlbacher, D.; Koppe, M.; Denk, P.; Waldauf, C.; Heeger, A. J.; Brabec, C. J. *Adv. Mater.* **2006**, *18*, 789–794.
24. Erb, T.; Zhokhavets, U.; Gobsch, G.; Raleva, S.; Stühn, B.; Schilinsky, P.; Waldauf, C.; Brabec, C. J. *Adv. Funct. Mater.* **2005**, *15*, 1193–1196.
25. Zhokhavets, U.; Erb, T.; Gobsch, G.; Al-Ibrahim, M.; Ambacher, O. *Chem. Phys. Lett.* **2006**, *418*, 347–350.
26. Vandewal, K.; Himmelberger, S.; Salleo, A. *Macromolecules* **2013**, *46*, 6379–6387.
27. Guo, X.; Zhou, N.; Lou, S. J.; Smith, J.; Tice, D. B.; Hennek, J. W.; Ortiz, R. P.; Navarrete, J. T. L.; Li, S.; Strzalka, J.; Chen, L. X.; Chang, R. P. H.; Facchetti, A.; Marks, T. J. *Nat. Photonics* **2013**, *7*, 825–833.
28. Chen, H.-Y.; Hou, J.; Zhang, S.; Liang, Y.; Yang, G.; Yang, Y.; Yu, L.; Wu, Y.; Li, G. *Nat. Photonics* **2009**, *3*, 649–653.
29. Son, H. J.; He, F.; Carsten, B.; Yu, L. *J. Mater. Chem.* **2011**, *21*, 18934–18945.
30. Botiz, I.; Darling, S. B. *Macromolecules* **2009**, *42*, 8211–8217.
31. Yin, W.; Dadmun, M. *ACS Nano* **2011**, *5*, 4756–4768.
32. Kietzke, T. *Adv. OptoElectron.* **2007**, 1–15.
33. Gregg, B. A.; Hanna, M. C. *J. Appl. Phys.* **2003**, *93*, 3605–3614.
34. Nayak, P. K.; Narasimhan, K. L.; Cahen, D. *J. Phys. Chem. Lett.* **2013**, *4*, 1707–1717.
35. McNeill, C. R.; Greenham, N. C. *Adv. Mater.* **2009**, *21*, 3840–3850.
36. Hoppe, H.; Sariciftci, N. S.; Meissner, D. *Mol. Cryst. Liq. Cryst.* **2002**, *385*, 113–119.
37. Chen, W.; Nikiforov, M. P.; Darling, S. B. *Energy Environ. Sci.* **2012**, *5*, 8045–8074.
38. Hoppe, H.; Sariciftci, N. S. *J. Mater. Chem.* **2006**, *16*, 45–61.
39. Peet, J.; Soci, C.; Coffin, R. C.; Nguyen, T. Q.; Mikhailovsky, A.; Moses, D.; Bazan, G. C. *Appl. Phys. Lett.* **2006**, *89*, 252105–3.
40. Moon, J. S.; Takacs, C. J.; Cho, S.; Coffin, R. C.; Kim, H.; Bazan, G. C.; Heeger, A. J. *Nano Lett.* **2010**, *10*, 4005–4008.
41. Perez, L. A.; Chou, K. W.; Love, J. A.; van der Poll, T. S.; Smilgies, D.-M.; Nguyen, T.-Q.; Kramer, E. J.; Amassian, A.; Bazan, G. C. *Adv. Mater.* **2013**, *24*, 6305.

42. He, X.; Gao, F.; Tu, G.; Hasko, D.; Huüttner, S.; Steiner, U.; Greenham, N. C.; Friend, R. H.; Huck, W. T. S. *Nano Lett.* **2010**, *10*, 1302–1307.
43. Slota, J. E.; He, X. M.; Huck, W. T. S. *Nano Today* **2010**, *5*, 231–242.
44. Moungthai, S.; Mahadevapuram, N.; Ruchhoeft, P.; Stein, G. E. *ACS Appl. Mater. Interfaces* **2012**, *4*, 4015–4023.
45. Scherf, U.; Gutacker, A.; Koenen, N. *Acc. Chem. Res.* **2008**, *41*, 1086–1097.
46. Tseng, Y.-C.; Darling, S. B. *Polymers* **2010**, *2*, 470–489.
47. Bates, F. S.; Fredrickson, G. H. *Phys. Today* **1999**, *52*, 32–38.
48. Park, C.; Yoon, J.; Thomas, E. L. *Polymer* **2003**, *44*, 6725–6760.
49. Sommer, M.; Komber, H.; Huettner, S.; Mulherin, R.; Kohn, P.; Greenham, N. C.; Huck, W. T. S. *Macromolecules* **2012**, *45*, 4142–4151.
50. Smith, K. A.; Lin, Y.-H.; Dement, D. B.; Strzalka, J.; Darling, S. B.; Pickel, D. L.; Verduzco, R. *Macromolecules* **2013**, *46*, 2636–2645.
51. Sommer, M.; Huettner, S.; Thelakkat, M. *J. Mater. Chem.* **2010**, *20*, 10788–10797.
52. Darling, S. B. *Energy Environ. Sci.* **2009**, *2*, 1266–1273.
53. Botiz, I.; Schaller, R. D.; Verduzco, R.; Darling, S. B. *J. Phys. Chem.C* **2011**, *115*, 9260–9266.
54. Mulherin, R. C.; Jung, S.; Huettner, S.; Johnson, K.; Kohn, P.; Sommer, M.; Allard, S.; Scherf, U.; Greenham, N. C. *Nano Lett.* **2011**, *11*, 4846–4851.
55. Woody, K. B.; Leever, B. J.; Durstock, M. F.; Collard, D. M. *Macromolecules* **2011**, *44*, 4690–4698.
56. Wu, S.; Bu, L.; Huang, L.; Yu, X.; Han, Y.; Geng, Y.; Wang, F. *Polymer* **2009**, *50*, 6245–6251.
57. Lai, Y.-C.; Ohshimizu, K.; Takahashi, A.; Hsu, J.-C.; Higashihara, T.; Ueda, M.; Chen, W.-C. *J. Polym. Sci., Part A: Polym. Chem.* **2011**, *49*, 2577–2587.
58. Ouhib, F.; Khoukh, A.; Ledeuil, J.-B.; Martinez, H.; Desbrières, J.; Dagron-Lartigau, C. *Macromolecules* **2008**, *41*, 9736–9743.
59. Ohshimizu, K.; Takahashi, A.; Higashihara, T.; Ueda, M. *J. Polym. Sci., Part A: Polym. Chem.* **2011**, *49*, 2709–2714.
60. Sun, S.-S.; Zhang, C.; Ledbetter, A.; Choi, S.; Seo, K.; Carl, E.; Bonner, J.; Drees, M.; Sariciftci, N. S. *Appl. Phys. Lett.* **2007**, *90*, 043117.
61. Chen, X. L.; Jenekhe, S. A. *Macromolecules* **1996**, *29*, 6189–6192.
62. Xiao, X.; Fu, Y.; Sun, M.; Li, L.; Bo, Z. *J. Polym. Sci., Part A: Polym. Chem.* **2007**, *45*, 2410–2424.
63. Verduzco, R.; Botiz, I.; Pickel, D. L.; Kilbey, S. M.; Hong, K.; Dimasi, E.; Darling, S. B. *Macromolecules* **2011**, *44*, 530–539.
64. Orilall, M. C.; Wiesner, U. *Chem. Soc. Rev.* **2011**, *40*, 520–535.
65. Matsen, M. W.; Bates, F. S. *Macromolecules* **1996**, *29*, 7641–7644.
66. Nakabayashi, K.; Mori, H. *Macromolecules* **2012**, *45*, 9618–9625.
67. Lin, Y.-H.; Smith, K. A.; Kempf, C. N.; Verduzco, R. *Polym. Chem.* **2013**, *4*, 229–232.
68. Ku, S.-Y.; Brady, M. A.; Treat, N. D.; Cochran, J. E.; Robb, M. J.; Kramer, E. J.; Chabinyc, M. L.; Hawker, C. J. *J. Am. Chem. Soc.* **2012**, *134*, 16040–16046.
69. Wang, J.; Ueda, M.; Higashihara, T. *ACS Macro Lett.* **2013**, *2*, 506–510.

70. Guo, C.; Lin, Y.-H.; Witman, M. D.; Smith, K. A.; Wang, C.; Hexemer, A.; Strzalka, J.; Gomez, E. D.; Verduzco, R. *Nano Lett.* **2013**, *13*, 2957–2963.
71. Zhang, C.; Choi, S.; Haliburton, J.; Cleveland, T.; Li, R.; Sun, S.-S.; Ledbetter, A.; Bonner, C. E. *Macromolecules* **2006**, *39*, 4317–4326.
72. Hinkens, D. M.; Chen, Q.; Siddiki, M. K.; Gosztola, D.; Tapsak, M. A.; Qiao, Q.; Jeffries-El, M.; Darling, S. B. *Polymer* **2013**, *54*, 3510–3520.
73. Wu, P.-T.; Ren, G.; Li, C.; Mezzenga, R.; Jenekhe, S. A. *Macromolecules* **2009**, *42*, 2317–2320.
74. Wu, P.-T.; Ren, G.; Kim, F. S.; Li, C.; Mezzenga, R.; Jenekhe, S. A. *J. Polym. Sci., Part A: Polym. Chem.* **2010**, *48*, 614–626.
75. Yu, X.; Yang, H.; Wu, S.; Geng, Y.; Han, Y. *Macromolecules* **2012**, *45*, 266–274.
76. Wu, Z.-Q.; Liu, D.-F.; Wang, Y.; Liu, N.; Yin, J.; Zhu, Y.-Y.; Qiu, L.-Z.; Ding, Y.-S. *Polym. Chem.* **2013**, *4*, 4588–4595.
77. Yassar, A.; Miozzo, L.; Gironda, R.; Horowitz, G. *Prog. Polym. Sci.* **2013**, *38*, 791–844.
78. Topham, P. D.; Parnell, A. J.; Hiorns, R. C. *J. Polym. Sci., Part B: Polym. Phys.* **2011**, *49*, 1131–1156.
79. Segalman, R. A.; McCulloch, B.; Kirmayer, S.; Urban, J. J. *Macromolecules* **2009**, *42*, 9205–9216.
80. Botiz, I.; Darling, S. B. *Mater. Today* **2010**, *13*, 42–51.
81. Gutacker, A.; Adamczyk, S.; Helfer, A.; Garner, L. E.; Evans, R. C.; Fonseca, S. M.; Knaapila, M.; Bazan, G. C.; Burrows, H. D.; Scherf, U. *J. Mater. Chem.* **2010**, *20*, 1423–1430.
82. Yokozawa, T.; Suzuki, R.; Nojima, M.; Ohta, Y.; Yokoyama, A. *Macromol. Rapid Commun.* **2011**, *32*, 801–806.
83. Tu, G.; Li, H.; Forster, M.; Heiderhoff, R.; Balk, L. J.; Sigel, R.; Scherf, U. *Small* **2007**, *3*, 1001–1006.
84. Scherf, U.; Adamczyk, S.; Gutacker, A.; Koenen, N. *Macromol. Rapid Commun.* **2009**, *30*, 1059–1065.
85. Javier, A. E.; Varshney, S. R.; McCullough, R. D. *Macromolecules* **2010**, *43*, 3233–3237.
86. Hollinger, J.; Jahnke, A. A.; Coombs, N.; Seferos, D. S. *J. Am. Chem. Soc.* **2010**, *132*, 8546–8547.
87. Ge, J.; He, M.; Qiu, F.; Yang, Y. *Macromolecules* **2010**, *43*, 6422–6428.
88. Zhang, Y.; Tajima, K.; Hashimoto, K. *Macromolecules* **2009**, *42*, 7008–7015.
89. Zhang, Y.; Tajima, K.; Hirota, K.; Hashimoto, K. *J. Am. Chem. Soc.* **2008**, *130*, 7812–7813.
90. Chueh, C.-C.; Higashihara, T.; Tsai, J.-H.; Ueda, M.; Chen, W.-C. *Org. Electron.* **2009**, *10*, 1541–1548.
91. He, M.; Zhao, L.; Wang, J.; Han, W.; Yang, Y.; Qiu, F.; Lin, Z. *ACS Nano* **2010**, *4*, 3241–3247.
92. Kiriy, A.; Senkovskyy, V.; Sommer, M. *Macromol. Rapid Commun.* **2011**, *32*, 1503–1517.
93. Okamoto, K.; Luscombe, C. K. *Polym. Chem.* **2011**, *2*, 2424–2434.

94. Verswyvel, M.; Verstappen, P.; De Cremer, L.; Verbiest, T.; Koeckelberghs, G. *J. Polym. Sci., Part A: Polym. Chem.* **2011**, *49*, 5339–5349.
95. Mori, D.; Benten, H.; Ohkita, H.; Ito, S.; Miyake, K. *ACS Appl. Mater. Interfaces* **2012**, *4*, 3325–3329.
96. Lohwasser, R. H.; Thelakkat, M. *Macromolecules* **2011**, *44*, 3388–3397.
97. Kochemba, W. M.; Kilbey, S. M.; Pickel, D. L. *J. Polym. Sci. Part A: Polym. Chem.* **2012**, *50*, 2762–2769.
98. Takahashi, A.; Rho, Y.; Higashihara, T.; Ahn, B.; Ree, M.; Ueda, M. *Macromolecules* **2010**, *43*, 4843–4852.
99. Loewe, R. S.; Ewbank, P. C.; Liu, J. S.; Zhai, L.; McCullough, R. D. *Macromolecules* **2001**, *34*, 4324–4333.
100. Herguth, P.; Jiang, X.; Liu, M. S.; Jen, A. K. Y. *Macromolecules* **2002**, *35*, 6094–6100.
101. Kim, Y.; Cook, S.; Choulis, S. A.; Nelson, J.; Durrant, J. R.; Bradley, D. D. C. *Chem. Mater.* **2004**, *16*, 4812–4818.
102. Calabrese, A.; Schimperna, G.; Po, R.; Yohannes, T.; Debebe, S. E.; Tinti, F.; Camaioni, N. *J. Appl. Phys.* **2011**, *110*, 113106.
103. Lee, W.-Y.; Cheng, K.-F.; Wang, T.-F.; Chueh, C.-C.; Chen, W.-C.; Tuan, C.-S.; Lin, J.-L. *Macromol. Chem. Phys.* **2007**, *208*, 1919–1927.
104. Lee, W.-Y.; Cheng, K.-F.; Wang, T.-F.; Chen, W.-C.; Tsai, F.-Y. *Thin Solid Films* **2010**, *518*, 2119–2123.
105. Tao, Y.; McCulloch, B.; Kim, S.; Segalman, R. A. *Soft Matter* **2009**, *5*, 4219–4230.
106. Kamps, A. C.; Fryd, M.; Park, S.-J. *ACS Nano* **2012**, *6*, 2844–2852.
107. Benanti, T. L.; Kalaydjian, A.; Venkataraman, D. *Macromolecules* **2008**, *41*, 8312–8315.
108. Urien, M.; Erothu, H.; Cloutet, E.; Hiorns, R. C.; Vignau, L.; Cramail, H. *Macromolecules* **2008**, *41*, 7033–7040.
109. Wu, Z.-Q.; Ono, R. J.; Chen, Z.; Li, Z.; Bielawski, C. W. *Polym. Chem.* **2011**, *2*, 300–302.
110. Kempf, C. N.; Smith, K. A.; Pesek, S. L.; Li, X.; Verduzco, R. *Polym. Chem.* **2013**, *4*, 2158–2163.
111. Smeets, A.; Willot, P.; De Winter, J.; Gerbaux, P.; Verbiest, T.; Koeckelberghs, G. *Macromolecules* **2011**, *44*, 6017–6025.
112. Smith, K. A.; Pickel, D. L.; Yager, K.; Kisslinger, K.; Verduzco, R. *J. Polym. Sci., Part A: Polym. Chem.* **2014**, *52*, 154–163.
113. Yokozawa, T.; Yokoyama, A. *Chem. Rev.* **2009**, *109*, 5595–5619.
114. Bronstein, H. A.; Luscombe, C. K. *J. Am. Chem. Soc.* **2009**, *131*, 12894–12895.
115. Carlé, J. E.; Krebs, F. C. *Sol. Energy Mater. Sol. Cells* **2013**, *119*, 309–310.
116. Thomas, S. W.; Joly, G. D.; Swager, T. M. *Chem. Rev.* **2007**, *107*, 1339–1386.
117. Darling, S. B.; Sternberg, M. *J. Phys. Chem. B* **2009**, *113*, 6215–6218.
118. Noriega, R.; Rivnay, J.; Vandewal, K.; Koch, F. P. V.; Stingelin, N.; Smith, P.; Toney, M. F.; Salleo, A. *Nat. Mater.* **2013**, *12*, 1038.

119. Abu-Zahra, N.; Algazzar, M. *J. Sol. Energy Eng.* **2013**, *136*, 021023–021023.
120. Chen, D.; Nakahara, A.; Wei, D.; Nordlund, D.; Russell, T. P. *Nano Lett.* **2010**, *11*, 561–567.
121. Sirringhaus, H.; Brown, P. J.; Friend, R. H.; Nielsen, M. M.; Bechgaard, K.; Langeveld-Voss, B. M. W.; Spiering, A. J. H.; Janssen, R. A. J.; Meijer, E. W.; Herwig, P.; de Leeuw, D. M. *Nature* **1999**, *401*, 685–688.
122. Kline, R. J.; McGehee, M. D.; Kadnikova, E. N.; Liu, J.; Fréchet, J. M. J.; Toney, M. F. *Macromolecules* **2005**, *38*, 3312–3319.
123. Chen, S. H.; Su, A. C.; Chen, S. A. *J. Phys. Chem. B* **2005**, *109*, 10067–10072.
124. Grell, M.; Bradley, D. D. C.; Ungar, G.; Hill, J.; Whitehead, K. S. *Macromolecules* **1999**, *32*, 5810–5817.
125. Peet, J.; Brocker, E.; Xu, Y.; Bazan, G. C. *Adv. Mater.* **2008**, *20*, 1882–1885.
126. Sinturel, C.; Vayer, M.; Morris, M.; Hillmyer, M. A. *Macromolecules* **2013**, *46*, 5399–5415.
127. Darling, S. B. *Prog. Polym. Sci.* **2007**, *32*, 1152–1204.
128. Lin, Y.-H.; Yager, K. G.; Stewart, B.; Verduzco, R. *Soft Matter* **2014**, *10*, 3817.
129. Register, R. A. *Nat. Nanotechnol.* **2013**, *8*, 618–619.
130. Chen, S. H.; Su, A. C.; Su, C. H.; Chen, S. A. *Macromolecules* **2005**, *38*, 379–385.
131. Kiriy, N.; Jähne, E.; Kiriy, A.; Adler, H.-J. *Macromol. Symp.* **2004**, *210*, 359–367.

Chapter 4

Techniques for the Molecular Design of Push-Pull Polymers towards Enhanced Organic Photovoltaic Performance

Racquel C. Jemison[1] and Richard D. McCullough[*,2]

[1]Carnegie Mellon University, 1500 5th Avenue, Pittsburgh, Pennsylvania 15213
[2]Harvard University, 1350 Massachusetts Avenue, Cambridge, Massachusetts 02138
[*]E-mail: Richard_McCullough@harvard.edu.

Organic photovoltaics (OPVs) hold the great promise of providing solutions towards the earth's ever-increasing energy demands. Current environmentally friendly options that have been adapted for large-scale application are primarily inorganic materials with limited sources and high materials and processing costs. Organic alternatives offer the options of inexpensive processing onto flexible, lightweight materials. The insufficient power conversion efficiencies (PCEs) as compared to the inorganic counterparts, however, drastically limit competitiveness of organic materials in the alternative energy market. Current research in the OPV field has primarily focused on maximizing efficiency through a large number of parameters from polymer design and synthesis to device processing and optimization. This review provides an outline of several current polymer design techniques and trends of push-pull and quinoid-type organic polymers to improve OPV performance. This review will highlight techniques towards improving polymer planarity not only through the choice of monomer systems, but also the decorative alkyl chains for solubility and optical property enhancement. Synthetic deviations from traditional, alternating, push-pull copolymer systems, such as ABBA tetramers to hexamers will be explored, as well as novel trends towards enhancement of polymer

In Polymer Composites for Energy Harvesting, Conversion, and Storage; Li, L., et al.;
ACS Symposium Series; American Chemical Society: Washington, DC, 2014.

stability and planarity through the use of thermocleavable moieties. Predictions of the next directions for OPV design will be presented as well.

Introduction

Since the discovery of the highly conductive nature of doped polyacetylene (**P1**) in the late 1970's, researchers have sought to incorporate its simply conjugated structure into new polymers with increased stability and solubility (*1*). The techniques of molecular design has demonstrated a significant impact towards improving air stability, processing capabilities, and electronic performance of conductive organic materials. Some of the earliest successful examples of organic materials for electronic applications utilized the conjugated backbone of polyacetylene but employed aromatic and heterocyclic structures decorated with alkyl chains to address both the issues of sensitivity to oxidation and insolubility (*2*). Several of the first largely successful organic semiconductors include regioregular poly-(3-hexylthiophene) (*rr*-P3HT) (**P2**), (*3*, *4*) poly(2-methoxyl-5-((2′-ethylhexyl)oxy)-1,4-phenylenevinylene) (MEH-PPV) (**P3**), and poly(2-methoxyl-5-((3′,7′-dimethyloctyl)oxy)-1,4-phenylenevineylene (MDMO-PPV) (**P4**) (*5*), whose structures are illustrated in Figure 1. Since then these particular materials, especially *rr*-P3HT, have established themselves as benchmarks for organic photovoltaics (OPVs) and organic field effect transistors (OFETs). The wide-spread and easily adopted use of *rr*-P3HT is attributed to simple Grignard Metathesis polymerization (or GRIM method, also referred to as catalyst transfer polymerization) (*6*, *7*) that yields three-dimensional, self-assembling, conductive nanofibrils on the kilogram scale at room temperature. This self-assembling nature brought it to the forefront of OPV technologies with power conversion efficiencies (PCEs) of 5-6% (while MEH-PPV and MDMO-PPV were limited at 2-3%) (*8*).

With regards to OPVs, organic polymeric materials have a superior advantage over traditional polycrystalline, amorphous, and single crystal silicon solar panels due to the wide range of low-cost processing options, including ink-jet printing, low-temperature processing, and roll-to-roll printing onto lightweight, flexible substrates. Additionally, these man-made, mostly carbon based materials are not source-limited as inorganic materials are. One of the most impending challenges with organic alternatives, however, is the great disparity in PCEs. Silicon-based solar cells have attained PCEs of more than 25%, while the current record for *rr*-P3HT is only 6% with optimization. In order for organic alternatives to be considered a significant competitor, they must attain efficiencies of at least 10% (*9*). This limit on photovoltaic performance is mostly attributed to P3HT's relatively large optical bandgap of 1.85 eV, which restricts absorption of the solar flux to wavelengths of less than 650 nm, capping the maximum photocurrent at 20%. In contrast, $Cu(In,Ga)Se_2$ solar cells have a photocurrent of up to 60% (*10*). Researchers have addressed this challenge with further advances in polymeric design to develop broad absorption/low bandgap polymers. Photovoltaic performance of organic conductive polymers has since increased to a record

In Polymer Composites for Energy Harvesting, Conversion, and Storage; Li, L., et al.;
ACS Symposium Series; American Chemical Society: Washington, DC, 2014.

of 9.31%, achieved by Phillips 66 in collaboration with Solarmer and South China University of Technology (*11*). The most successful OPV devices have utilized bulk heterojunction (BHJ) architectures, which create a bicontinuous intermingling of the donor polymer with a much more electronegative species as the acceptor. The most commonly employed acceptor is [6,6]-phenyl C_{61}-butyric acid methyl ester ($PC_{61}BM$) and occasionally $PC_{71}BM$. Excitons are photogenerated at the interface between the donor and acceptor phases, but are still loosely bound due to Coulombic interactions. An electric field or energetic disorder is then required to free the charges, with the electronegative nature of the acceptor assisting in providing sufficient energy to very quickly and efficiently separate the exciton into a hole and electron pair due to its lower energy state. This photovoltaic architecture thus requires very precisely designed and processed materials to optimize the PCE.

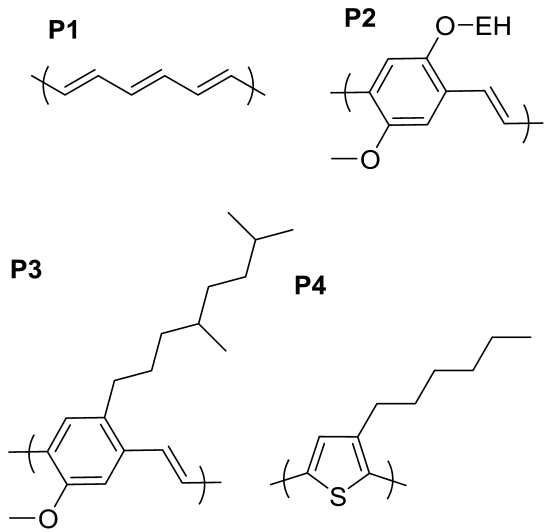

Figure 1. Structures of aforementioned polymers in the introduction.

Donor polymeric materials for OPV applications have many characteristics that must be optimized in order to boost power conversion efficiency, several of the most impactful ones being (1) the polymer planarity, (2) the choice of substituents and functional groups on the selected monomers, (3) the polymer molecular weight, and (4) film morphology. Polymer planarity directly impacts other characteristics, including the HOMO/LUMO energy levels, which subsequently determine the optical bandgap (E_g^{opt}) and charge carrier mobility of a polymer. Towards this end, many successful polymers for OPVs have utilized alternating electron-accepting and electron-withdrawing moieties to create a push-pull

mechanism to draw charges along the polymer backbone. Alternative routes have successfully employed polyaromatic chains that acquire a stable quinoid state to better accommodate charge transfer. The substituent selection and placement can affect not only the polymer planarity, but also the charge-carrying properties of the material due to specific types of aromatic heterocycles and functional groups that can enhance the electron-withdrawing or donating character of the polymer as a whole. The various types of substituents include linear and alkyl chains to enhance solubility, conjugated spacers between electron-withdrawing and electron-accepting units, and even conjugated moieties positioned in the side chain to enhance absorption. Higher molecular weight polymers have mostly demonstrated superior photovoltaic performance compared to shorter chain lengths. Routes towards achieving higher molecular weights are typically achieved through the choice of linear or branched alkyl chains to maximize solubility during the polymerization process. Chain selection must be judicious, however, to avoid steric interference with the polymer backbone that would otherwise cause twisting, and a broader bandgap. Lastly, the BHJ morphology must accommodate efficient exciton formation and dissociation. The challenge comes with accounting for the short exciton diffusion length of approximately 10 nm with phases that are likely to intermingle with much larger distances of 100 nm. Ideally the interpenetrating network of the two phases must have a distance of twice the exciton diffusion length in order to suppress the likelihood of charge recombination, and increase the chances of percolation of those charges to their respective contacts.

This review will first define the performance requirements of conductive materials for successful OPV devices and then outline the above mentioned molecular design requirements by highlighting several examples form recent literature. It will highlight the rationale behind the design techniques and propose potential future directions in this field of research. While the work referenced within this chapter is far from exhaustive of the current work in this vast area, ample reviews that go into further depth in regards to photovoltaic design physics and performance of push-pull conjugated polymers have been recently published, which the reader is strongly encouraged to explore (*8*, *12–19*).

Defining the Problem: What Does the Ideal Donor Material Look Like?

Donor materials for OPV applications have a large number of requirements for optimum performance that far outweigh those for inorganic components simply due to its more complicated nature of charge transfer physics and device architecture. Because inorganic materials have high dielectric constants and generate free electron-hole pairs throughout the device, there is less need for selectivity in regards to specific HOMO and LUMO energy levels, only that there is a minimal bandgap to maximize absorption of the solar photon flux. Organic materials, on the other hand, generate loosely Coulomb bound electron-hole pairs (excitons) at the interface between the donor and acceptor materials. The lower dielectric constant of most conductive p-type materials requires additional energy

In Polymer Composites for Energy Harvesting, Conversion, and Storage; Li, L., et al.;
ACS Symposium Series; American Chemical Society: Washington, DC, 2014.

to separate those charges. Furthermore, because most active donor materials only efficiently carry holes, combination with a more electronegative acceptor phase is required to carry the electrons. Hence, bulk heterojunction (BHJ) architectures, that physically mix the two phases to maximize interfacial area between the two phases, have been heavily utilized in OPVs. This maximized surface area increases photogenerated exciton formation. The HOMO and LUMO energy levels of the two phases must then be carefully chosen to ensure proper charge transfer of the electron from the donor to acceptor, with enough of an offset to prevent back-transfer. The HOMO and LUMO levels must also be carefully matched to the work functions of the contacts for the device.

The energy profile of the donor material directly influences photovoltaic performance through several parameters. The HOMO level of the donor ($HOMO_D$) affects susceptibility to air oxidation, the photovoltage, photocurrent, and open circuit voltage (V_{OC}). Past research has determined that a HOMO energy level of -5.27 eV or deeper is required to attain air stability (*20*). Recent works have found a linear correlation between the V_{OC} and oxidation potential (*9*). The difference between $HOMO_D$ and the LUMO of the acceptor ($LUMO_A$) affect the V_{OC} values, where deeper $HOMO_D$ levels result in increased V_{OC}'s (*21*, *22*). Photovoltage is dependent upon this difference as well as upon the work function of the electrodes. Smaller offsets will improve photovoltage at the expense of exciton dissociation and photocurrent, while a larger difference will improve photocurrent, but negatively impact the V_{OC} (*22*). You and coworkers determined an "ideal" band gap based on the use of $PC_{61}BM$ by taking into consideration its LUMO of -4.2 eV (*23*). Because the difference in LUMO levels of the donor and acceptor phases must be a minimum of 0.3 eV to ensure proper exciton dissociation, this would set an "ideal" $LUMO_D$ at -3.9 eV. The HOMO, to address both air stability and a sufficient V_{OC} must then be set at -5.4 eV yielding an optimum bandgap of 1.5 eV. Other research has found a much higher dependency on the LUMO energy level than the bandgap (*9*). By maintaining the LUMO and varying the bandgap by 0.65 eV, they found only a 1% change in PCE values. Changing the LUMO level by that same amount, however resulted in PCE levels ranging from 3.5 to 8% (*9*).

Most homopolymers have difficulty attaining these requirements on their own, hence push-pull conjugated polymers were introduced by Havinga et al. to provide a balanced approach to energy profile design (*24*, *25*). One theory explaining the positioning of the energy levels of these copolymers works with the premise that during the polymerization, the HOMO and LUMO levels of the withdrawing and donating monomers merge into their respective valence and conduction bands, thus increasing the magnitude with each sequential monomer addition. This affect is heavily dependent upon the degree of overlap between orbitals, which explains why unhindered overlap (from planar polymer backbones) helps to minimize the bandgap (*21*). An alternative theory proposed by the Hutchison group (further explained in the aspects of monomer design section) suggests that this could only be true if there were no interaction between the two species (electron-rich and electron-withdrawing). Instead, the HOMO and LUMO energy levels are a combination of the two (*26*, *27*). Regardless of the means to which the energy levels are positioned, the push-pull interaction created

In Polymer Composites for Energy Harvesting, Conversion, and Storage; Li, L., et al.;
ACS Symposium Series; American Chemical Society: Washington, DC, 2014.

from the withdrawing and donating monomers have proven to be an affective method towards increasing photovoltaic performance. Push-pull polymers can stabilize quinoid-like structures because of the increase in double bond character between repeat units, improve intramolecular charge transfer, and ultimately increase photovoltaic performance (*21*).

In addition to energetic considerations, the donor materials must have sufficient hole mobility, which must closely match the electron mobility of the acceptor in order to avoid recombination of latent charges. Ideal suggested figures have been on the order of 10^{-3} cm^2/V s (*9*). Lastly, solubility of the donor material in organic solvents plays a considerable role on the ultimate performance not only for OPV applications, but OFETs as well. Sufficient solubility during polymerization ensures sufficient chain growth and avoids premature precipitation of the chains. Solubility also plays significant a role in film quality and morphology of solid thin films. The following sections will focus on the various design requirements of p-type materials for OPVs and present several recent examples from the literature. While not all of the design motivations have resulted in successful increases in PCE, much of the work reveals useful structure-property relationships as well as design and synthetic pitfalls to avoid that can be deemed useful for future directions.

Towards Enhanced Polymer Planarity

Stabilization of Quinoid Structure

Quinoid structures have been recently adopted more readily due to increasingly facile synthetic routes. While the primary method to narrowing optical bandgap has been through the use of push-pull copolymers that supposedly determine HOMO and LUMO energy levels from the lowest ionization potential and highest electron affinity of the monomers employed, quinoid structures take advantage of double carbon bonds between monomer units (*28–35*). The quinoid structure can be forced through the fusing of an additional aromatic ring to the main cycle to impose a double bond. The optical absorption of typical push-pull polymers is limited after a certain conjugation length. Quinoid character can circumvent this limitation and further minimize the bandgap by varying the length and ratio of quinoid to aromatic blocks (*21*). Jean-Luc Brédas established the relationship between bandgap and quinoid structure through theoretical work (*36*, *37*) and found that the lowest bandgaps are obtained by polymers with a balance between the quinoid and aromatic structure to ensure that all bond lengths are near equivalent in length. Recent theoretical work by Bérubé and coworkers expanded this theoretical experiment to a series of 200 polymers to find the relationship between band gap and quinoid versus aromatic nature (*38*). He found similar results to Brédas and also tested the accuracy of the donor-acceptor approach method to predict bandgaps, which only considered the average bandgap of the two monomers (from respective homopolymers) plus a minimal Peirel's gap. While this method inaccurately produced experimental bandgap values, the quinoid-aromatic method that they developed held true qualitatively by also

In Polymer Composites for Energy Harvesting, Conversion, and Storage; Li, L., et al.;
ACS Symposium Series; American Chemical Society: Washington, DC, 2014.

considering the number of carbon atoms present and by quantifying the aromatic or quinoid nature of the monomers in question (*38*).

The Hwang research group investigated the effects of increased fused rings and additional carbazole units to test the theory that increased fused rings could indeed enhance quinoid stability and increase the amount of light absorbed (*39*). They studied a group of polymers utilizing quinoxaline and benzodithiophene as a donor (P5-P8) as seen in Figure 2. Quinoxaline is composed of a benzene and pyrazine ring and has been increasingly employed as an acceptor component for push-pull conjugated polymers. P8 had the highest absorption maximum, presumably due to both the reduced steric hindrance and electron-donating character of the carbazole unit. They also found that polymers with asymmetric substitutions had lower LUMO levels than those that were symmetrically substituted (*39*). Hwang ultimately confirmed that an increased number of fused ring systems successfully minimized the optical band gap (and thus increased the amount of absorbed light) and increased PCE from 2.01% to 3.87% between P7 and P8. The resultant properties and performance are summarized in Table 1.

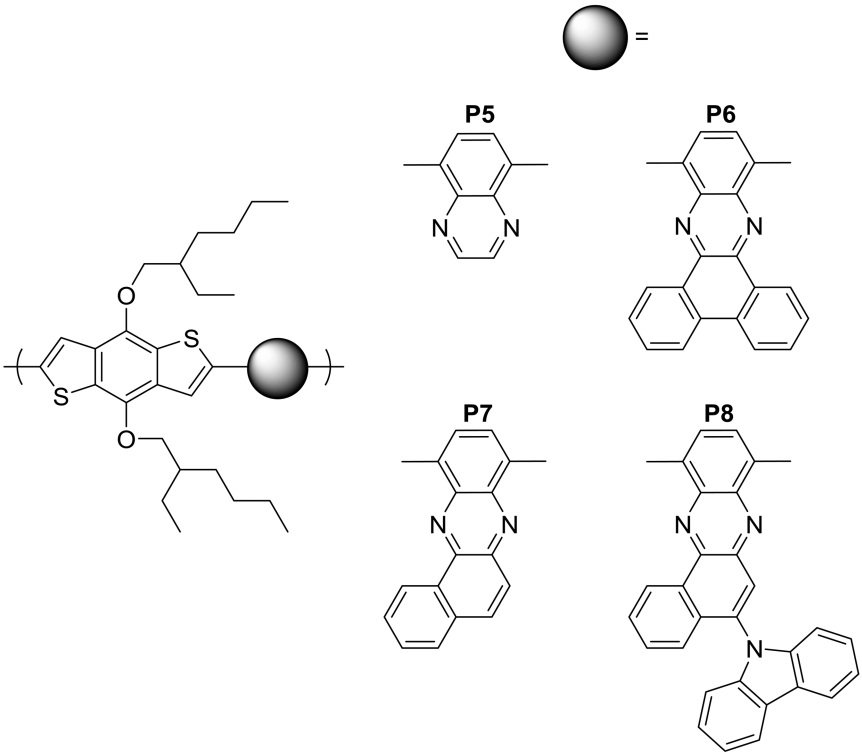

Figure 2. Structures of P5-P8.

In Polymer Composites for Energy Harvesting, Conversion, and Storage; Li, L., et al.;
ACS Symposium Series; American Chemical Society: Washington, DC, 2014.

Imahori and coworkers pursued a unique synthetic method of creating stabilized quinoid, push-pull structures that avoided the use of alkyl chains, by instead opting for thermocleavable moieties that could provide the solubility necessary for polymerization and film casting and create a quinoid structure upon heating (*40*). A copolymer comprised of isothianaphthene (ITN) as a donor and thiazolothiazole as an acceptor was synthesized by starting with bicyclo[2,2,2]octadiene and using a heat activated retro- Diels-Alder reaction shown in Figure 3 to create a blue, insoluble polymer with a bandgap of 1.3 eV (compared to the initial bandgap of 2.1 eV) (P9→P10). While the hole mobility of P10 was acceptable with a value of 2.2 x 10^{-4} cm^2 V^{-1} s^{-1}, the PCE was a mere 0.3% (*40*) (see Table 1 for polymer details). The employment of thermocleavable functional groups proved to be an effective strategy in the past for small molecules such as pentacene (*41–43*) and benzoporphyrin (*44–46*), which achieved PCEs on the order of 5%, however the high HOMO energy level of the **P10** restricted V_{OC} values. Additionally, the J_{SC} values suffered due to the relaxation of the excited states back to the ground state that compromised charge-separation efficiency. Lastly, the polymer suffered from poor morphology that resulted in large interfacial domains. This was, however, an improvement over the precedent donor-donor ITN polymer previously published (*34*).

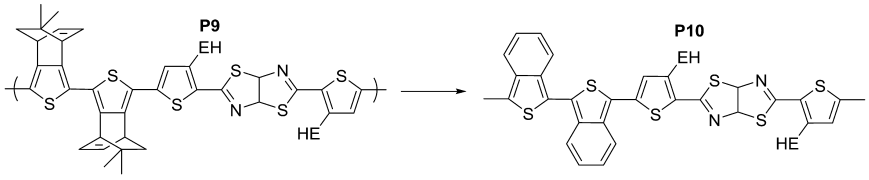

Figure 3. Synthetic scheme to yield P10 from P9.

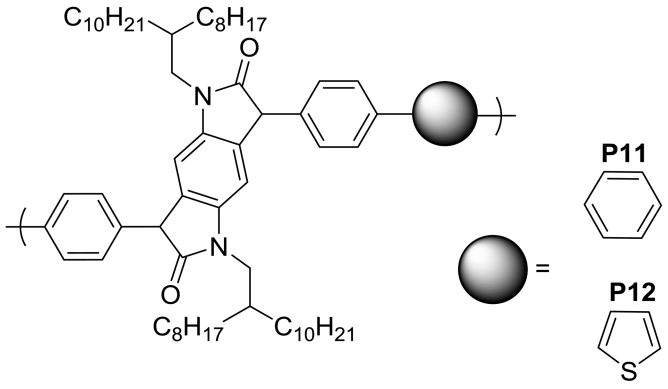

Figure 4. Structure of P11 and 12.

In Polymer Composites for Energy Harvesting, Conversion, and Storage; Li, L., et al.;
ACS Symposium Series; American Chemical Society: Washington, DC, 2014.

Table 1. Summary of Data from Polymer P5-P12

	M_n (kg/mol)	E_g (eV)	HOMO (eV)	μ ($cm^2/V\ s$)[a]	V_{OC} (V)	J_{SC} (mA/cm^2)	FF	PCE (η)	Ref.
P5	10	1.80	-5.19	3.5×10^{-6}	0.65	6.30	0.37	1.54	(*39*)
P6	12	1.55	-5.25	6.0×10^{-5}	0.72	7.74	0.37	2.04	
P7	9	1.67	-5.26	2.7×10^{-5}	0.70	7.63	0.37	2.01	
P8	11	1.54	-5.34	1.5×10^{-4}	0.78	9.68	0.51	3.87	
P9	10	2.1	-5.50	-	0.56	1.95	0.28	0.30	(*40*)
P10	10	1.3	-5.30	1.4×10^{-5} (SCLC) 2.2×10^{-4} (OFET)	0.42	2.41	0.29	0.29	
P11	20	1.9	-5.83	μ_e 2.4×10^{-3}	Not measured				(*47*)
P12	8	1.68	-5.90	μ_e 6.4×10^{-3} μ_h 3.5×10^{-3}					

[a] Hole mobility values unless indicated.

Another example of a relatively new quinoid-designed polymer is benzodipyrrolidone, initially synthesized as a colorant. Its structure is a quinodimethane derivative that is essentially a stretched version of DPP with capabilities for π-π stacking (*47*). Wudl et al. examined these monomers copolymerized with benzene and benzene-thiophene units (**P11**-**P12**) (Figure 4) (*47*). The thiophene analogue had a smaller band gap than the benzene derivative (1.68 eV versus 1.90 eV) and a slightly deeper HOMO energy level. It also demonstrated ambipolar properties with electron and hole charge mobilities of (6.4 x 10^{-3} cm^2/V s and 3.5 x 10^{-3} cm^2/V s respectively) while the benzene derivative was solely an n-type material. To our knowledge, no OPV devices based on this specific polymer were presented at the time of publication; however it demonstrates great potential towards solar cell applications. Work done by other groups utilized the benzodipyrrolidone monomer for both OFET and OPV applications with bithiophene and dithienopyrrole monomers respectively. While thin-film transistor devices demonstrated hole mobility values of 0.03 cm^2/V s (*48*), only modest PCEs of 2.60% (*49*) were obtained.

The Use of Alkyl Chains to Improve Inter- and Intramolecular Interactions

From a synthetic standpoint, the selection of alkyl chains can directly and indirectly influence final polymer characteristics and device performance. Bao et al. recently published a comprehensive review of side-chain engineering techniques that details the most recent research efforts in this area (*18*). Alkyl chains were initially introduced into polymer design to achieve enhanced solubility for increased processing options and extending the length of polymerization (to avoid early precipitation). Solubility also affects film morphology and chain stacking capabilities, and thus OPV performance. Alkyl chains can directly affect the energy bandgap depending on the type of alkyl chain (alkoxy versus alkyl or branched versus linear) and its position. Regioregular architectures have been preferred to minimize steric hindrance (the importance of which has been demonstrated with P3HT) (*7*, *50*, *51*). Bulky branched alkyl chains can induce steric hindrances with neighboring monomers that would otherwise force twisting of the polymer backbone and increase the energy bandgap, thus negatively impatcting the performance for OFETs, and in many cases OPVs as well. This has been the motivation behind the use of phenyl or thiophene conjugated spacers (further detail on these design aspects are provided in the following section) to better accommodate bulky chains between monomer units. Likewise, alkyl chain length can affect both intramolecular packing and charge transport properties. Longer side chains have been found to inhibit device performance through their insulating effects that impede charge movement and contact at the donor-acceptor interface (*52*).

Work from Geng et al. demonstrated the effects of alkyl chain length on both absorption coefficient and OPV performance with the use of N-alkyl dithieno[3,2-b:2′,3′-d]pyrrole-2,1,3-benzothiadiazole alternating copolymers (**P13**-**P15**) (*53*). Increasing the dithienopyrrole (DTP) alkyl chain length from 1-pentylhexyl to 1-hexylhelptyl and 1-octylnonyl (as illustrated in Figure 5), decreased the absorption coefficient, with **P15** absorbing 60% more light than

P13 at a similar film thickness. Additionally, shorter alkyl chains improved film morphology and resulted in increased PCEs (2.80% compared to 1.23% for **P13** and 2.06% for **P14**). The optical bandgaps of all three polymers were relatively similar at around 1.4 eV, which disproves the notion that perhaps it was steric hindrance between the branched alkyl chains interfering with the BT monomers. More details of polymer properties and performance can be found in Table 2. While little explanation for the increase in performance was offered, it could perhaps be that longer branched alkyl chains are forced to twist out of the plane of the polymer backbone, and could limit *inter*molecular π-π stacking capabilities. This could explain why the field effect mobility performance was relatively the same between polymers (mobility values were not presented), but film morphology varied.

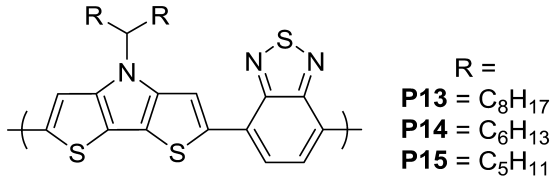

Figure 5. Structures of P13-P15.

Work performed through collaborative work by Li, Ding, and coworkers investigated the effects of branched and alkyl chains on donors and acceptors (**P16-P18**) (*54*), as illustrated in Figure 6. They found that bulkier branched chains on the diketopyrrolopyrrole (DPP) units can increase the resistance needed to accept electrons in reductive process and thus lead to reduced mobility values. Positioning branched chains on both donor and acceptor units had poor mobility values and produced poorly crystalline films, despite having the best solubility of the three polymers. Overall, they found that small, linear alkyl chains can better facilitate chain packing and interaction with fullerene, and thus improve OPV performance. Suh et al. followed up with a similar experiment using bithiophene imide (BTI) electron-accepting monomer with carbazole and thiophene. BTI, in particular, was chosen due to its planar structure and optimum solubility attributed to the increased distance between the alkyl chains of the electron-donating monomer and the imide group located at the heart of the bithiophene imide unit (*55*). The branched alkyl chain of **P19** resulted in higher PCEs than **P20** (both illustrated in Figure 6, with properties and performance summarized in Table 2) decorated with a linear alkyl chain, especially when utilizing a mixed solvent system of ortho-dichlorobenzene with 2% diiodooctane (DIO). Through atomic force microscopy experiments (AFM), they found that the surface roughness of the films decreased substantially with the additive, with **P20** showing more significant improvement. This example demonstrates the significance of OPV performance in regards to alkyl chain-influenced morphology.

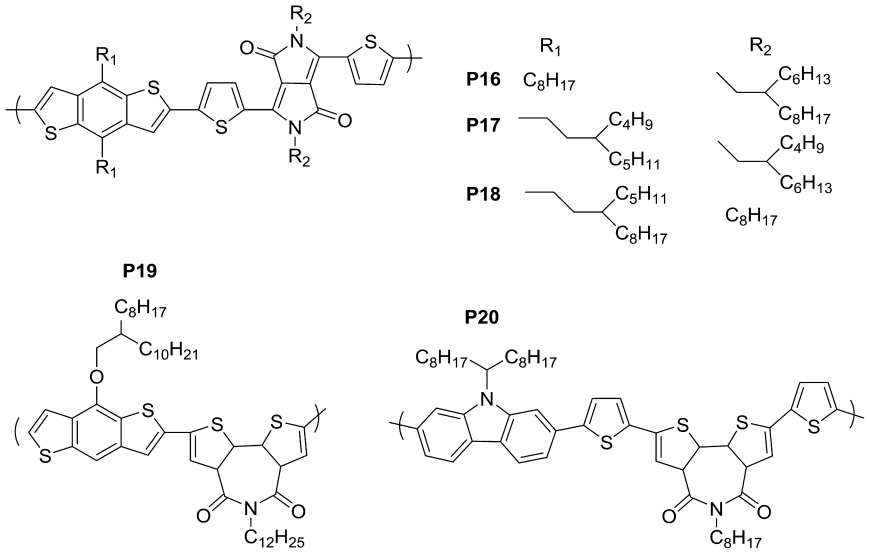

Figure 6. Structures of polymers P16-P20.

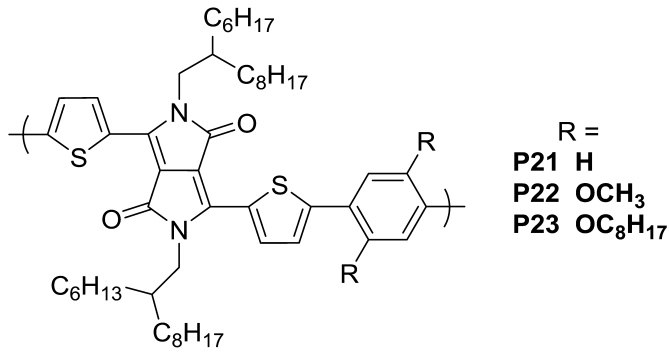

Figure 7. Polymer structures of P21-P23.

Alkoxy chains have long been utilized for their heavy influence on optoelectronic properties in addition to their contributions towards improved solubility. Previous research has demonstrated a red-shifted absorption, higher molecular weights, and higher HOMO levels (which lead to decreased bandgaps) upon addition of alkoxy chains to phenyl spacers (*56–58*). Andersson et al. investigated the influence of alkoxy substituents on diketopyrrolopyrrole (DPP) copolymers by varying the side chains to either methoxy or octyloxy (**P21-P23**) (*59*), as seen in Figure 7. When examining the oligomeric analogues of these polymers, they found higher endo- and exothermic transitions at higher

temperatures. The large dipole moments of methoxy groups provided an enhanced driving force for ordering in the solid state, which resulted in broader, 100 nm red-shifted absorption onsets for alkoxy substituted polymers. The polymers with no substitutions on the phenyl spacer exhibited higher absorption coefficients, potentially due to an increasingly rigid polymer backbone, which can lengthen the effective conjugation length. More details on the polymer can be located in Table 2.

Table 2. Summary of Polymer Properties and Device Performnace for P13-23

	M_n *(kg/mol)*	E_g *(eV)*	*HOMO (eV)*	V_{OC} *(V)*	J_{SC} *(mA/cm²)*	*FF (%)*	*PCE (η)*	*Ref.*
P13	14.9	1.41	-4.89	0.43	6.19	0.46	1.23	(*53*)
P14	15.6	1.42	-4.86	0.43	11.1	0.43	2.06	
P15	17.9	1.43	-4.81	0.54	11.9	0.44	2.80	
P16	42.8	1.45	-5.15	0.71	9.4	0.61	4.1	(*54*)
P17	33.2	1.51	-5.14	0.59	3.4	0.46	0.93	
P18	27.8	1.36	-5.10	0.62	5.2	0.43	1.4	
P19	47	1.90	-5.20	0.93	3.06	0.49	1.49	(*55*)
P20	7.1	1.96	-5.22	0.84	2.48	0.36	0.76	
P21	15	1.52	-5.10	0.78	0.78	0.49	3.9	(*59*)
P22	12	1.34	-4.89	0.59	0.59	0.45	0.9	
P23	29	1.32	-4.88	0.60	0.60	0.46	2.0	

Additional work examining the effects of alkoxy chains on polyselenophenes was done by the Cheng group. Polyselenophenes have demonstrated increased quinodal character with minimal likelihood towards back bone twisting (*60*). Poly(3-hexylselenophene) has a smaller bandgap than P3HT analogues due to the lower LUMO (with relatively the same HOMO), and thus a smaller bandgap (*61*). The smaller ionization potential of selenophene leads to a more photo-oxidation-resistant polymer with localized transitions and intramolecular charge transfer overlaps (*61*). Work performed by Cheng et al. examined an indacenodiselenophene donor material with hexyl and hexyloxy alkyl chains paired with various acceptor monomers, as seen in Figure 8 (**P24-28**) (*62*). Their results, as summarized in Table 3, conflicted with previous findings on the impact of alkoxy chains. They found that there was little impact on optical or electrochemical properties upon exchange of alkyl for alkoxy chains, but because the hexyloxy chain was within the plane of the main polymer chain, it caused

steric hindrance. They also proposed that the lone pair of electrons on oxygen can interact with the π* orbital of the carbon-carbon double bond on the phenyl group and cause steric hindrance, thus the hexylphenyl side chains demonstrated better photovoltaic performance over the octyloxy analogues (*62*).

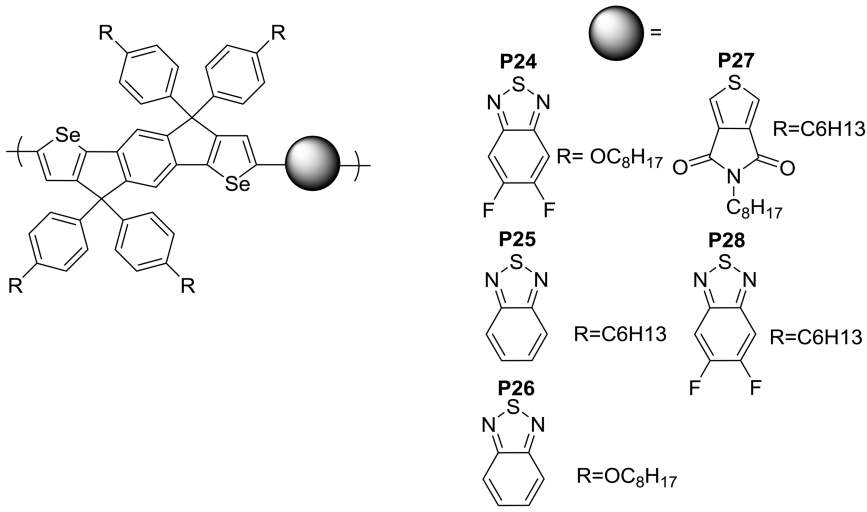

Figure 8. Structures of P24-P28.

Improved solubility does not always have to be in the form of carbon-carbon bonds. An increased number of works have incorporated the use of silane groups as well. Hwang's research group took advantage of triisopropyl silyl (TIPS) functional groups to increase both solubility and oxidative stability, while still maintaining crystallinity through the pi-orbital overlap (*63*). The TIPS groups were affixed to benzodithiophene donor monomers and separated by an alkyne bond (**P29-P30** illustrated in Figure 9). Utilization of this group resulted in a significantly red-shifted absorption due to enhanced π-π interactions and an extended conjugation length. It also demonstrated long –range order in the solid state and had a higher absorption coefficient. When simulating the electron distribution of the HOMO and LUMO levels, the TIPS derivative had less localized electrons within the LUMO due to the electronegative sp-hybridization of the carbon atoms in the TIPS group. Its HOMO level was also slightly deeper, leading to its slightly broader optical bandgap. As a result, its photovoltaic performance (with full details in Table 3) exceeded that of its TIPS-free analogue (4.16% compared to 3.17%) due partially to the superior morphology that accommodated a bicontinuous interpenetrating network with $PC_{71}BM$.

In Polymer Composites for Energy Harvesting, Conversion, and Storage; Li, L., et al.;
ACS Symposium Series; American Chemical Society: Washington, DC, 2014.

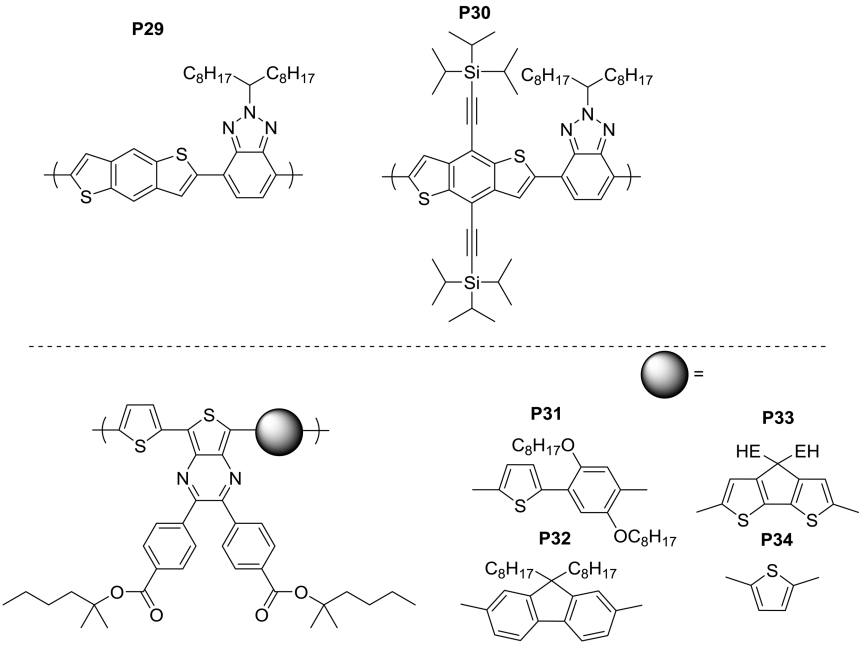

Figure 9. Structure of polymers P29-P34.

While soluble side chains are primarily responsible for solubility, they can also be the source of OPV failure. In MDMO-PPV, for example, homolytic scission of the methoxy bond can drastically reduce PCE over time. Likewise, the photochemical instability of P3HT's alkyl chains have shortened device lifetime as well. Krebs proposed the option of using thermocleavable benzoate esters on dithienylthienopyrazine acceptors (**P31-P34** as seen in Figure 9) to provide temporary solubility for processing purposes, but thermally removing the functional groups post-casting to avoid the potential for future device failure (*64*). The photovoltaic performance of the polymers, as seen in Table 3, decreased post-annealing due to an increase in phase aggregation that reduced charge carrier generation and current densities.

As seen in these examples, the choice of solubilizing groups is critical for OPV device performance. The chains employed can dictate the success of polymerization by ensuring sufficient solubility, influence intra- and intermolecular organization and morphology, and can impact optoelectronic properties as well. The employment of alkoxy chains in push-pull conjugated polymers has been very popular in recent literature. While a great majority of research has determined alkyoxy groups to be beneficial towards performance, there have also been works suggesting otherwise. This lends credence to the hypothesis that the functional group's beneficial contribution is heavily contingent upon the type of monomers used and the design tactics employed.

Table 3. Properties and Performance of Polymers P24-P34

	M_n (kg/mol)	E_g (eV)	HOMO (eV)	V_{OC} (V)	J_{SC} (mA/cm^2)	FF (%)	PCE (η)	Ref.
P24	10.7	1.60	-5.28	0.76	8.45	0.41	2.6	(*62*)
P25	10.8	1.60	-5.28	0.76	11.24	0.45	3.9	
P26	11.5	1.68	-5.32	0.86	6.72	0.32	1.9	
P27	9.3	1.63	-5.38	0.84	9.67	0.47	3.8	
P28	[a]	1.84	-5.43	0.92	9.77	0.50	4.6	
P29	42	1.95	-5.60	0.83	6.61	0.58	3.17	(*63*)
P30	80.5	2.04	-5.76	0.86	10.48	0.46	4.16	
P31	7	1.17	[b]	0.36	3.20	0.51	1.21	(*64*)
P32	42.3	1.37		0.65	1.41	0.44	0.54	
P33	39.4	1.30		0.50	2.22	0.38	0.57	
P34	36.3	1.24		0.55	3.20	0.51	1.21	

[a] Insolubility prevented accurate measurement. [b] Not provided.

The Use of Conjugated Spacers for Planar Structure

The use of spacers started with saturated units to behave as "rods" between donor and acceptor species began back in 1984 and 1985 (*65*, *66*). But the potential impact of conjugated bridges between electron-rich and electron-poor units was first hypothesized even earlier by McConnell in 1961. He reasoned that a closer-maintained energetic resonance could be achieved with the use of these π-bridges (*67*). Research on the role of conjugated spacers such as thiophene or phenyl groups (donor-π-acceptor) in donor-acceptor copolymers has since surged, yet definitive conclusions on their beneficial contributions towards OPV performance has varied. Recent work published by Wei et al. studied the effects of thiophene spacers on two dimensional benzodithiophene-thienopyrroledione (BDT-RT and TPD) copolymers (*68*). This work was inspired by mixed results from previous studies done by Leclerc (*69*), Xie (*70*), Bao (*71*), and Hou (*72*). While Hou found enhanced OPV device performance with employment of the spacers, the other researchers obtained deleterious effects upon their addition. Wei's work examined the effects of conjugated spacers on planarity through modeling of oligomer species and experimental work on two polymers (**P35-P36**, seen in Figure 10) to measure optoelectronic properties and device performance (*68*). The spacers remained coplanar to the acceptor units, but the main chain was distorted by 25˚ between the BDT and acceptor units. At the same time, a significant red-shift, indicative of enhanced effective conjugation length due to increased planarity of the backbone, was observed. The spacer analogue showed red-shifting between the solution and solid state spectra, emphasizing

the positive impact that the spacers played towards improved π-stacking of the polymer chains. Furthermore, it had a 54% higher absorption coefficient which was attributed to the spacer's effects on the electron density of the LUMO (more delocalized over the spacer and TPD) leading to increased extinction coefficients. The OPV device performance, as seen in Table 4, was significantly improved as well.

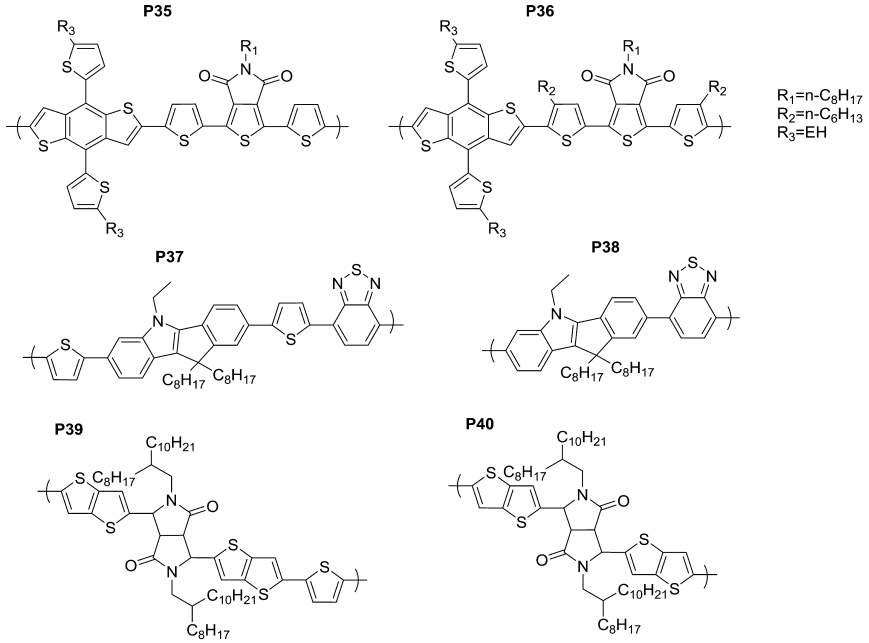

Figure 10. Structures of polymers P35-P40.

Work done by Jin and coworkers evaluated the impact of thiophene spacers on indolocarbazole-benzothiadiazole copolymer systems (**P37-P38**, also illustrated in Figure 10) (*73*). Indolocarbazole's heptacyclic ladder type architecture was employed as a building block due to its ability to red-shift absorption from enhanced planarization. Benzothiadiazole (BT), has been utilized because of the planarity induced by hydrogen-bonding between the nitrogen of the BT unit and the hydrogen in the 3-position of the thiophene. While previous work demonstrated the ability of conjugated spacers such as thiophene for extension of effective conjugation length, little work had been focused on using this spacer for this specific copolymer pairing. They found a number of improvements for the thiophene spacer analogue, including a reduced bandgap of 1.75 eV (compared to 1.99 eV), a higher J_{SC}, FF, PCE, and hole mobility (details provided in Table 4). The spacer showed better intermolecular π-π interaction, optimum π-π* packing, and improved charge mobility (*73*).

In Polymer Composites for Energy Harvesting, Conversion, and Storage; Li, L., et al.;
ACS Symposium Series; American Chemical Society: Washington, DC, 2014.

Work performed by Sirringhaus, McCullouch, and others sought to increase the intermolecular association of DPP-based copolymers by replacing thiophenes with thienothiophene and measuring the impact of a thiophene spacer on OPV device performance (**P39-P40**, Figure 10) (*74*). They noticed that the addition of the spacer led to a blue-shifted absorption maximum, but a red-shifted absorption onset. The ambipolar polymer exhibited an increased hole mobility (1.42 cm^2/V s versus 0.037 cm^2/V s) which led to a PCE of 5.4% compared to 3.0% (see Table 4 for details). A similar experiment was done with a benzothiadiazole and indenoindole copolymer by Jin and coworkers (*73*). They found an increased molecular weight, decreased optical bandgap, and an improvement of the PCE from 1.23% to 3.51% simply by adding thiophene spacers.

Furan and bithiophene spacers have also been utilized in past research. Hsu investigated the effects of thiophene spacers between benzodithiophene and benzodiathiazole (**P41**) (*75*). Wang et al. later followed up with work using the same polymer with furan and bithiophene spacers (**P42-P46**) (*76*, *77*). Figure 11 illustrates each of these polymer structures. The oxygen of the furan ring makes the moiety more electronegative than the thiophene analogue, and can deepen the HOMO energy level (*76*). Through theoretical modeling, they found that the HOMO is delocalized along the length of backbone, while the LUMO remained primarily on the acceptor units. Continued work expanded to examine the effects of chain planarity with the different spacer units. They found that with changing from thiophene to furan, then bithiophene changed the backbone from "z-shaped" to linear (*77*). The performance and additional polymer properties are summarized in Table 4.

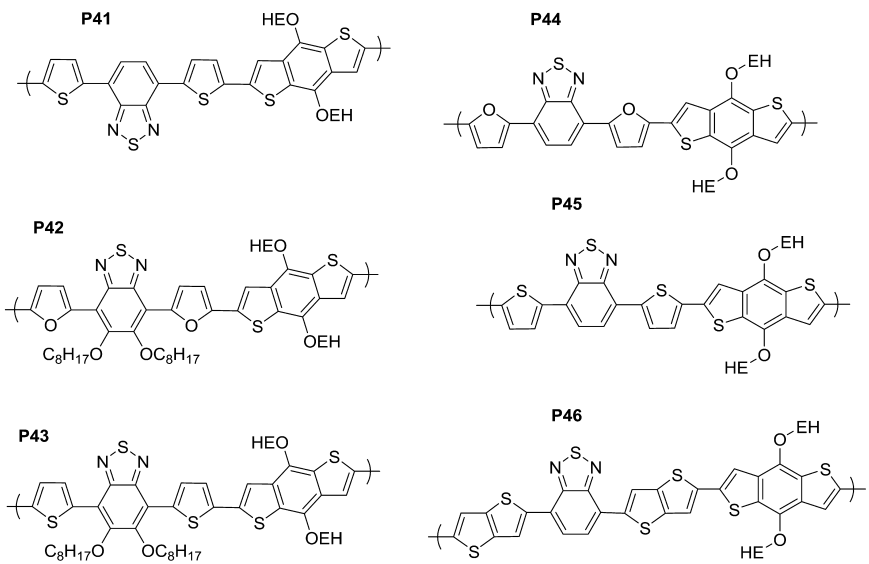

Figure 11. Structures of polymers P41-P46.

In Polymer Composites for Energy Harvesting, Conversion, and Storage; Li, L., et al.;
ACS Symposium Series; American Chemical Society: Washington, DC, 2014.

Table 4. Polymer Properties and OPV Performance

	M_n (kg/mol)	E_g (eV)	HOMO (eV)	μ ($cm^2/V\ s$)	V_{OC} (V)	J_{SC} (mA/cm^2)	FF	PCE (η)	Ref.
P35	18.9	1.85	-5.54	6.1×10^{-3}	0.99	8.70	0.453	3.87	(*68*)
P36	14.6	1.86	-5.30	1.0×10^{-3}	0.92	10.94	0.604	6.08	
P37	23.2	1.99	-5.37	4.03×10^{-6}	0.75	5.1	0.3231	1.23	(*73*)
P38	35.5	1.75	-5.37	1.94×10^{-4}	0.78	9.21	0.5136	3.72	
P39	14.0	1.38	-5.06	μ_e 1.42 μ_h 0.063	0.58	15	0.61	5.4	(*74*)
P40	16.0	1.28	-5.04	μ_h 0.037 μ_e 0.30	0.57	8.9	0.59	3.0	
P41	69.39	1.64	-5.17	7.15×10^{-3}	0.76	8.96	0.59	4.02	(*75*)
P42	6.2	1.96	-5.44	--	0.94	6.5	0.46	2.81	(*76*)
P43	69.39	1.64	-5.17	7.15×10^{-3}	0.76	8.96	0.59	4.02	
P44	10.4	1.96	-5.44	2.1×10^{-3}	0.94	6.50	0.46	2.81	(*77*)
P45	[a]	1.82	-5.35	2.9×10^{-3}	0.82	9.45	0.48	3.71	
P46	32.8	1.78	-5.21	8.6×10^{-3}	0.69	11.34	0.63	4.93	

[a] Insoluble.

A unique method of incorporating spacers/linkers between conjugated systems is through the use of alkyne linkages. Past research has demonstrated higher V_{OC} values by 0.4 V due to its electron withdrawing character that in turn deepens the HOMO energy level and induces red-shifting of the absorbance spectra (*78*, *79*). Experimental work on a benzothiadiazole (BT) and thienoisoindoledione (TID) copolymer linked by alkyne bonds by Braunecker and coworkers found that the quinoid state is stabilized by the fused TID ring and dearomitization of the thiophene. This culminates in an increase of aromatic resonance energy and a reduction of the band gap by 0.4 eV (*80*). Theoretical and experimental follow-up work of 12 ethynylene-linked copolymers was done by the same group to evaluate the overall impact of alkyne linkages (*81*). They surprisingly found an overall blue-shift upon the addition of the linkages. While the HOMO level is deepened, the "push-pull" effect is apparently thwarted. The wide range of monomer combinations done in the study offered additional observable trends as well. For instance, larger bandgaps were created with the combination of strong acceptors and weak donors, whereas the smallest bandgaps were the result of the chosen electron-withdrawing monomers with fused aromatic rings. Past research has indicated that an energy mismatch could explain the phenomenon.

Previous work done by Waisielewski examined the effects of alkyne bridges and their effects on the interactions between donor and acceptor units (*82*). When looking at the absorption properties of four polymers with increasing numbers of pi-conjugated pathways, they found that σ bonds electronically isolated the acceptor from the rest of the polymer. Alkyne bridges, on the other hand drastically changed the communication between the donor and acceptor units. While there were no effects on the charge transfer rate, other work found a decrease in communication ability. The maximum overlap was found to be achieved with antiperiplanar sp^3 hybrid orbitals. Additional experiments by Hrobárik and coworkers examined benzothiazole with a D-π-A-π-D architecture (*83*). When using ethenylene (double bond) spacers, they found larger two-photon cross sections than for ethynylene (triple bond) spacers. They determined that there was a greater amount of charge transfer in alkene bridged polymers because of an increased number of polymers in a relaxed intramolecular charge transfer state. Further studies showed that polymers with the alkene spacer had faster and more efficient charge transfer.

Aspects of Monomer Design

While there are a number of design considerations specifically for electron-rich and electron-withdrawing monomer systems, this review is not intended to provide an in-depth evaluation of the wide variety of monomers employed. Ample reviews have been published specifically on the myriad electron-rich and electron-withdrawing moieties (*8*, *14*, *16*, *17*), with several reviews focusing solely on acceptors (*15*, *84*). This section will focus on just a fraction of the design techniques utilized to manipulate energy levels and thus

OPV performance, including the impact of the heteratom selected for arene systems, the incorporation of conjugated side chains, and a larger view of the polymer to consider the impact of donor-acceptor sequencing patterns.

The Impact of Monomer Heteroatoms and Additional Substituents

The choice of heteroatoms in both electron withdrawing and electron accepting moieties has a significant impact on polymer optoelectronic properties, planarity, and final OPV performance. Several studies have been done to evaluate the impact of the heteroatom in donor monomer systems. Both Reynolds et al. and Leclerc studied fused donor molecules, with Reynolds examining the effects of silicon and germanium (*85*), while Leclerc solely examined silicon (*86*). Silicon has the advantage over carbon-bridged analogues because of its improved hole-transport properties and deeper HOMO energy levels. Dithienogermoles, in turn, have proven beneficial because of their lengthened C-Ge bond lengths of 3.27Å compared to 3.11Å for C-Si bonds. This longer bond better accommodates any attached alkyl chains and increases the potential area for π-π stacking between polymer chains. In Reynolds' study, the silicon analogues had deeper HOMO energy levels (**P47**), with the germole polymer (**P48**, both illustrated in Figure 12) demonstrating the best PCE of 7.3% due to its minimized bandgap (*85*). Leclerc also achieved a PCE of 7.3% with dithienosilole (**P49**) (compared to an efficiency of 6.1% achieved by Reynolds et al.). Further detail on the polymer performance can be found in Table 5.

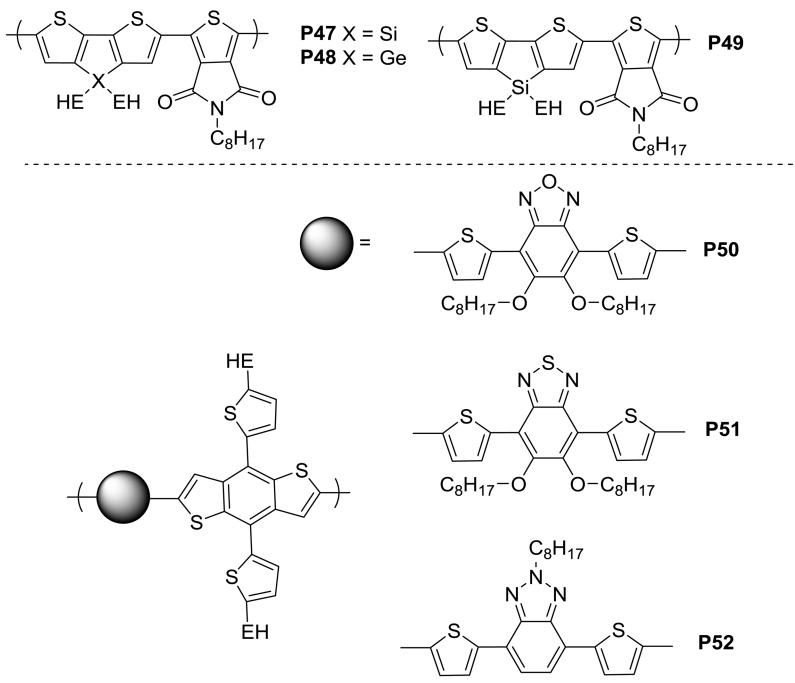

Figure 12. Structures of polymers P47-P52.

In Polymer Composites for Energy Harvesting, Conversion, and Storage; Li, L., et al.;
ACS Symposium Series; American Chemical Society: Washington, DC, 2014.

A similar pattern was found with the examination of substituted benzodithiophenes by Zou and coworkers. They compared benzooxadiazole, benzothiadiazole, and benzotriazole units copolymerized with dithiophene (**P50-P52**) (*87*), all illustrated in Figure 12. The benzooxadiazole analogue attained the best PCE values (5.9%, see Table 5) due to the strong electron accepting character of the oxygen deepening the HOMO level.

Likewise, the introduction of additional heteroatoms and functional groups can substantially improve optoelectronics based on its electron affinity or ionization potential. Muccini et al. incorporated cyano functional groups into dithienosilole to deepen the HOMO energy level (**P53-P56**, Figure 13) (*88*). Dithienosilole was utilized because of silicon's contribution towards lower LUMO levels and reduced bandgaps attributed to efficient mixing of the Si-C σ* and butadiene π* orbital mixing and increased π-π interactions (*89*, *90*). Cyano groups in particular have very strong electron withdrawing capabilities that reduce the HOMO (*91*). The polymers with the –CN substituents had a substantially higher PCE (0.64% for the analogue lacking the substituent compared to 4.90% with dodecylthiophenes along with cyanated thiophenes). More details can be found in Table 5.

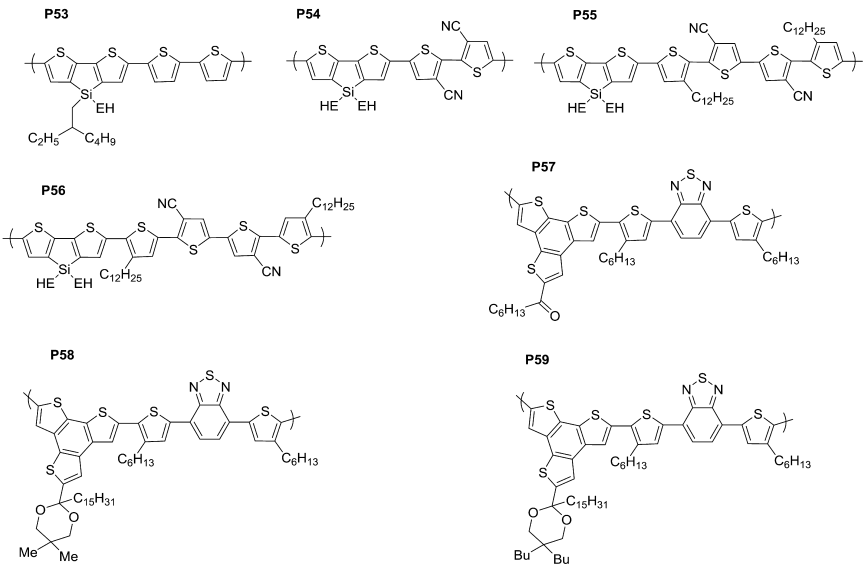

Figure 13. Structures of P53-P59.

Work done by McCulloch measured the effects of post-polymerization ketalization of benzotrithiazine (BTT) copolymers (*92*). Changing the functional groups from the ketone to dimethyltrimethyl ketal and dibutyltrimethylene ketal (**P57-P59**, Figure 14) resulted in a substantial change in polymer properties.

While the ketone analogue had sparing solubility that prevented its application towards OPV devices, the methyl and butyl derivatives had improved PCE values. This occurred at the expense of absorption properties. Upon conversion of the ketone groups to methyl ketal, a disruption of the polymer chain packing led to significant blueshifting that increased the optical bandgap, as seen in Table 5. Theoretical calculations, however, predicted the bandgaps of the methyl and butyl analogues to be narrower due to the electron donating nature of the ketal and a stronger donor-acceptor interaction. This discrepancy could have been attributed to the steric interactions being neglected during calculation.

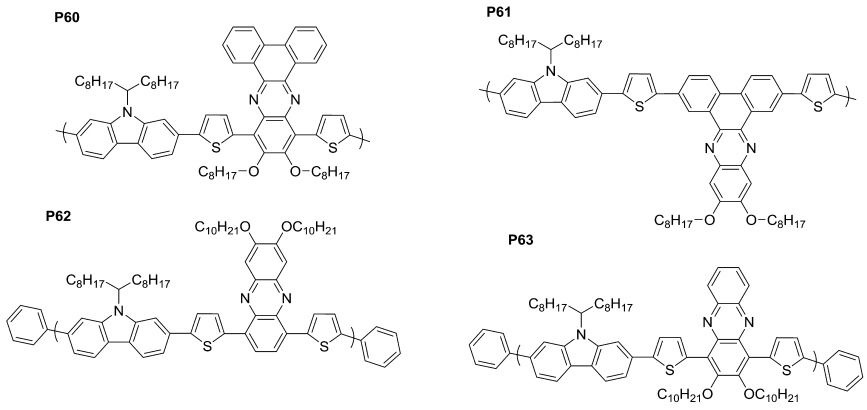

Figure 14. Structures of polymers P60-P63.

Linkage positions have just as much of an impact on OPV performance as the selection of the substituents. Studies performed by Li et al. copolymerized dibenzophenazine and carbazole while varying the connectivity of the dibenzophenazine to the main chain from the -10,13 positions (**P60**) to -2,7 (**P61**) (*93*), as seen in Figure 15. This resulted in a significant increase in number average molecular weight, a decrease of the optical bandgap, and an increase in the PCE from 0.64% to 4.31% (Table 5). Polymer **P60** could better accommodate a quinoid structure, and its slightly more twisted polymer backbone enhanced solubility. The intermolecular donor-acceptor interaction can act as a driving force for self-assembly, and thus increase the organization and charge transfer capabilities (*94*, *95*). Additional studies by Wang et al. focused on the placement of the alkoxy chains at either the -7,8 (**P62**) or -2,3 (**P63**) positions (both illustrated in Figure 15) on phenazine copolymers (*96*). The latter demonstrated higher PCEs despite similar optical bandgaps and V_{OC} values. As seen in Table 5, the molecular weight was much higher (72.1 kDa versus 10.5) and the J_{SC} was also increased. The key difference in performance was attributed to the phase separation behavior with **P62** having sub 300 nm-sized aggregates.

Table 5. Device Performance and Polymer Properties of P47-P63

	M_n (kg/mol)	E_g (eV)	HOMO (eV)	μ ($cm^2/V\ s$)	V_{OC} (V)	J_{SC} (mA/cm^2)	FF	PCE (η)	Ref.
P47	31	1.73	-5.65	--	0.89	11.5	0.65	6.6	(*85*)
P48	48	1.69	-5.60	--	0.40	12.6	0.68	7.3	
P49	28	1.73	-5.57	$1x10^{-4}$	0.88	12.2	0.68	7.3	(*86*)
P50	41.3	1.69	-5.25	0.49	0.84	11.45	0.613	5.9	(*87*)
P51	16.7	1.66	-5.15	0.24	0.75	10.29	0.640	4.94	
P52	3.40	1.78	-4.92	0.54	0.54	9.47	0.606	3.1	
P53	8.6	2.03	-5.22	10^{-5}	0.671	2.22	0.43	0.64	(*88*)
P54	4.6	1.81	-5.63	10^{-5}	0.627	1.94	0.39	0.47	
P55	6.7	1.75	-5.47	$4x10^{-4}$	0.830	8.78	0.62	4.52	
P56	6.4	1.95	-5.52	$6x10^{-4}$	0.850	9.25	0.63	4.90	
P57	16.7	1.58	-5.23	--	Poor solubility				(*92*)
P58	16.7	1.65	-5.06	--	0.71	4.76	0.48	1.63	
P59	16.7	1.66	-5.03	--	0.77	6.91	0.37	1.97	
P60	29.1	1.94	-5.37	--	0.95	8.12	0.56	4.31	(*93*)
P61	88.4	2.38	-5.41	--	0.70	1.99	0.45	0.64	
P62	10.5	1.80	-5.26	--	0.86	2.79	0.62	1.48	(*96*)
P63	72.1	1.81	-5.30	--	0.87	7.48	0.31	2.51	

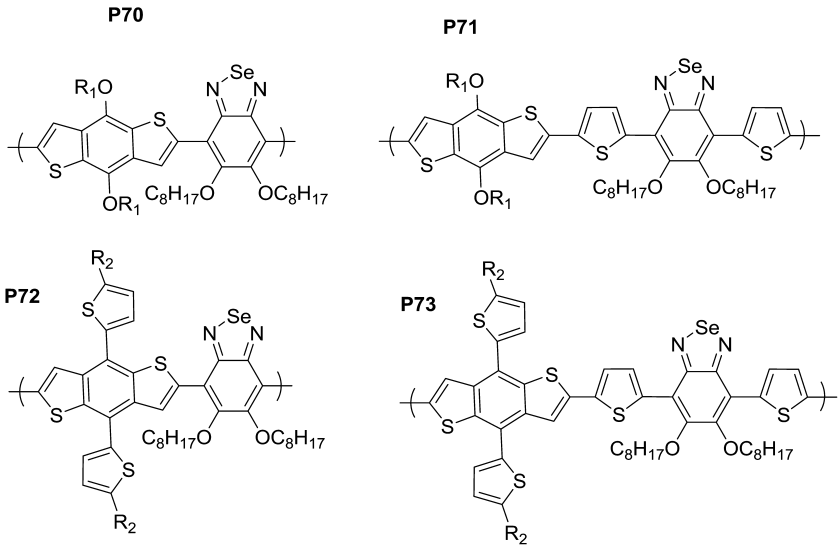

Figure 15. Structures of P70-P73.

The electronegative character of chosen heteroatoms for donor or acceptor monomers plays a vital role towards the energy profile of the polymer as a whole. More electronegative species help to deepen the HOMO energy level, and increasing the V_{OC} as a result. Changing a bridging atom, for example, from carbon, to silicon, to germanium improved the overall power conversion efficiencies. The selected linkage positions of the monomer units are just as important as heteroatom selection. This can affect polymer chain stacking ability and intramolecular charge transfer capabilities. Continuing from these design considerations, incorporation of conjugated side chains can help to enhance the optical properties of final copolymers.

The Use of Conjugated Side Chains

Conjugated side chains serve several benefits towards enhanced absorption of the solar photon flux. The energy levels and charge transporting properties of the polymer are maintained despite the choice of side chain (*9*). Additionally, the synthetic ease of manipulating the side chain makes it a very feasible and facile means of expanding light absorption.

Work done by the Huang group evaluated the impact of dodecyloxy, dodecylthiophene, and dodecylphenyl substitutions on anthracene's 9 and 10 positions in a benzothiadiazole copolymer (**P64-P69**, Figure 15) (*97*). They found that copolymers employing the conjugated side groups had an increased

In Polymer Composites for Energy Harvesting, Conversion, and Storage; Li, L., et al.;
ACS Symposium Series; American Chemical Society: Washington, DC, 2014.

bathochromic shift and broader absorptions with the thienyl analogues (**P66** and **P69**) demonstrating the best absorption properties and deeper HOMO levels. The best performing polymer with an octylhtiophene substitution (**P69**) had the best PCE of the polymer series at 4.34%. More OPV details can be found in Table 6.

Likewise, Hwang varied the types of alkyl chains attached to 2,1,3-benzoselenadiazoles both with and without thiophenes positioned in the side chain and also with and without thiophene spacers as seen in Figure 16 (**P70-P73**) (*98*). Polymers with the conjugated side chains were much more crystalline than those without, which was indicative of the enhanced intermolecular π-π stacking observable by X-Ray diffraction studies. The increased hole mobility contributed to higher PCEs, with the highest performing polymer analogue lacking the thiophene spacers. The thiophene spacers successfully reduced steric interactions between side chains, and subsequently resulted in a smaller bandgap, but the deeper HOMO level of **P72** led to higher V_{OC} values and thus a higher PCE of 3.57% compared to 3.18% Table 6).

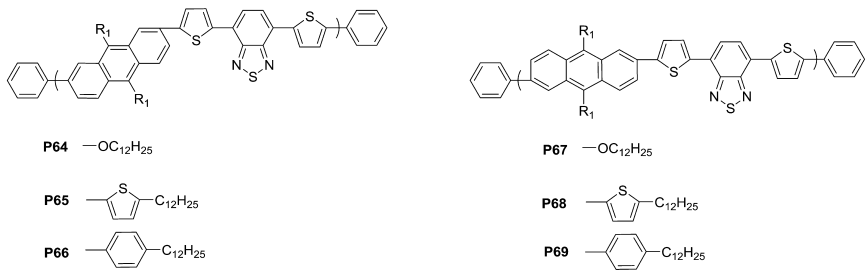

Figure 16. Structures of P64-P69.

Zhu et al. synthesized a ternary donor-acceptor-donor comprised of thiophene, BDT, and DPP units with DPP side chain units (as seen in Figure 17) based on the above rationale (**P74a**) (*99*). The absorption properties of the polymer as compared to binary copolymers lacking conjugated side chains demonstrated significantly broadened absorption properties with an "ideal" bandgap of 1.53 eV and several maxima. The π-π* transition of the polymer backbone was observed at 417 nm, while intracharge transport between the BDT and DThDPP units occurred at 602 nm as well as between BDT and the two DThDPP units at 723 nm. Additionally, this polymer demonstrated ambipolar properties, and was capable of conducting both holes at 1.45 x 10^{-4} cm^2/V s and electrons at 2.63 x 10^{-4} cm^2/V s. The polymer had a PCE of 4.36%, even with a relatively low molecular weight. As seen in Table 6, after slightly altering the structure of the polymer backbone, but maintaining use of the DPP pendant moiety, the group increased the molecular weight substantially to 1.34 x10^4 g/mol,

In Polymer Composites for Energy Harvesting, Conversion, and Storage; Li, L., et al.;
ACS Symposium Series; American Chemical Society: Washington, DC, 2014.

slightly increased the V_{OC} and FF to yield a slightly increased PCE of 4.36% (*99*). The group later published work on the same polymer, but end-capped with thiophene units (**P74b**). This led to a slightly higher V_{OC}, and despite the larger band gap of 1.73 eV, the PCE improved to 4.89% (granted, this increase could have been attributed to the use of $PC_{71}BM$ rather than the $PC_{61}BM$ used with their previous work) (*100*).

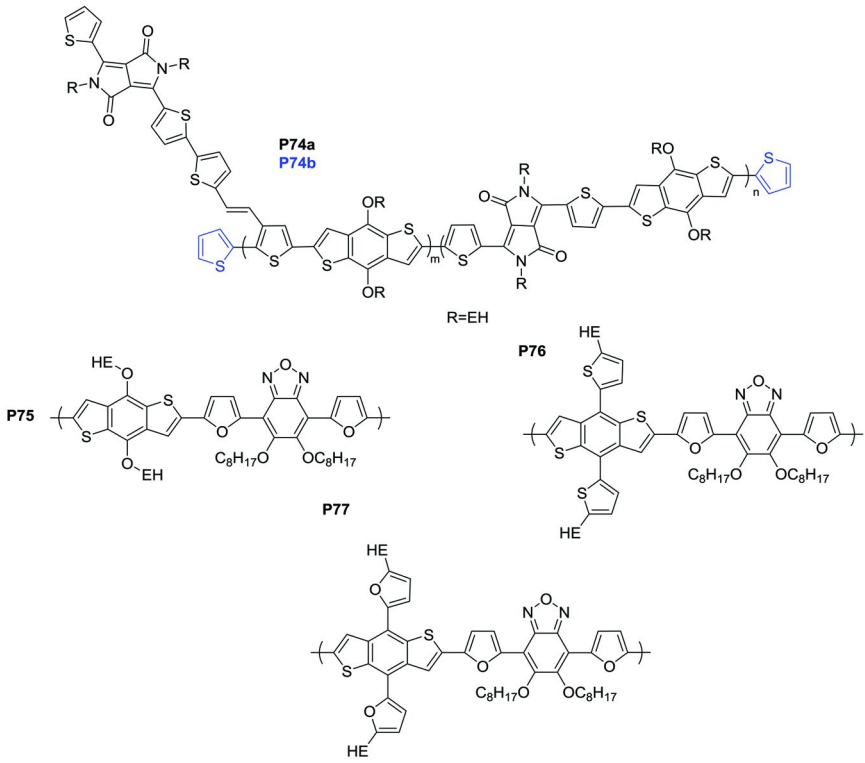

Figure 17. Polymer structures of P74a-P77.

A fairly recent study done by Ge et al. investigated the effects of employing furan versus thiophene conjugated moieties into the side chains of benzodithiophene monomers (**P75-P77**, Figure 17) (*101*). The monomers were copolymerized with benzooxidazole In general, the side chains contributed to a narrowing of the bandgap and an increase of the PCE, with the furan moiety (**P77**) contributing to the highest average PCE of 6.5%, with the highest achieving device reaching 7.0%. The furan contributed towards an improved polymer solubility and a deeper HOMO energy level because of its increased electron donating character and an optimum overlap with the π orbitals.

In Polymer Composites for Energy Harvesting, Conversion, and Storage; Li, L., et al.;
ACS Symposium Series; American Chemical Society: Washington, DC, 2014.

Table 6. Polymer Properties and Device Performance for P64-P77

	M_n (kg/mol)	E_g (eV)	HOMO (eV)	μ (cm^2/V s)	V_{OC} (V)	J_{SC} (mA/cm^2)	FF	PCE (η)	Ref.
P64	15.3	2.13	-5.48	6.6×10^{-6}	0.84	5.69	0.47	2.26	(*97*)
P65	18.3	1.86	-5.65	2.8×10^{-5}	0.96	8.58	0.39	3.21	
P66	28.6	1.85	-5.70	1.9×10^{-5}	0.94	8.56	0.47	3.80	
P67	14.8	2.15	-5.49	1.5×10^{-6}	0.78	6.59	0.35	1.82	
P68	22.7	1.89	-5.52	1.0×10^{-4}	0.90	9.10	0.41	3.33	
P69	26.8	1.85	-5.59	5.3×10^{-5}	0.98	9.57	0.48	4.34	
P70	25	1.74	-5.27	7.5×10^{-6}	0.76	7.01	0.46	2.45	(*98*)
P71	20	1.69	-5.20	1.1×10^{-5}	0.70	9.37	0.48	3.13	
P72	10	1.68	-5.31	2.0×10^{-3}	0.77	11.03	0.42	3.57	
P73	11	1.67	-5.10	4.7×10^{-4}	0.67	10.23	0.46	3.18	
P74a	1.59	1.53	-5.31	--	0.78	10.47	0.53	4.36	(*99*)
P74b	13.4	1.73	-5.34	--	0.84	10.04	0.56	4.89	(*100*)
P75	36.1	1.85	-5.34	μ_h [a] 3.1×10^{-4} μ_e 3.4×10^{-4}	0.83	10.6	0.647	5.6	(*101*)
P76	29.3	1.81	-5.44	μ_h [b] 8.6×10^{-5} μ_e 3.2×10^{-4}	0.86	9.1	0.586	4.5(5.0)	
P77	38.4	1.77	-5.40	μ_h [b] 2.0×10^{-4} μ_e 3.7×10^{-4}	0.83	12.7	0.62	6.5(7.0)	

[a] Solvent treated with ethanol. [b] Solvent treated with methanol.

Table 7. Device Performance and Properties of Polymers P78-P80

	M_n (kg/mol)	E_g (eV)	HOMO (eV)	μ ($cm^2/V\ s$)	V_{OC} (V)	J_{SC} (mA/cm^2)	FF	PCE (η)	Ref.
P78	22.9	1.60	-4.90	4.7×10^{-4}	0.6	13.3	0.658	5.24	(*57*, *103*)
P79	13.6	2.02	-5.35	--	0.82	6.4	0.70	4.6	(*104*)
P80	97.5	1.6	-5.15	5.8×10^{-4}	0.74	14.5	0.69	7.40	(*108*)

Optimizing Monomer Sequence

While a vast majority of research has designed push-pull polymers to have an alternating structure, more research is exploring the possibility of various sequences posing as a greater potential for improving charge transfer capabilities. Work by the Hutchison group suggested the main misconception of push-pull polymer theory is that the HOMO of the copolymer is a direct result of the HOMO of the electron-rich component and the LUMO of the electron-withdrawing unit (*26*). This could only logically hold true if there were absolutely no interaction between the two units; yet in reality, the polymer electronic structure is a combination of the two. Hutchison created a library of potential high performing polymers (from a total 90,000 studied) using computational genetic algorithms to combine a variety of monomers. Rather than solely pursuing dimers (as has been primarily studied in the past), they went as far as running computational experiments for trimers, hexamers, and even octamers. Of the best hypothesized polymers, none of them bore alternating sequences. In fact, the ABAB sequence led to a decrease in the ionization potential and excitation energy. Of the dimer copolymers, the best performing ones had a high degree of delocalization and electronic coupling (rather than ideal orbital energies as has been the motivation behind much push-pull polymer design).

Follow-up work in collaboration with the Meyer group investigated synthetic work of several trimers, tetramers, pentamers, and hexamers using an unsubstituted phenylene vinylene and a dialkoxy-substututed phenylene vinylene as the two units (**M1** and **M2** respectively, as seen in Figure 18) (*102*). They found that oligomers starting and ending with **M1** units resulted in smaller optical band gaps, higher oxidation potentials and higher melting temperatures. Starting and ending an oligomer with **M2**, on the other hand resulted in higher molar extinction coefficients. In terms of sequence, traditional alternating polymers fell in the middle in regards to bandgap, oxidation, and reduction potentials, and spectral properties. Semi-blocky oligomers (AABB, for example) had a well separated energy absorption band, with weaker absorptions attributed to excitations between the small blocks.

There are a multitude of monomer design options, including the overall architecture of the molecules. In regards to the effects of chosen monomer heteroatoms, more electronegative atoms lead to deeper HOMO energy levels, and subsequently increaseed V_{OC} values. These heteroatoms also play a role on morphology. The C-X bond length has an impact on chain packing because of the distance between the fused ring system and the attached alkyl chain. Additional attached electron-withdrawing functional groups, such as –CN, can be added to affect the HOMO energy level as well. The linkage of monomers and solubilizing alkyl chains are just as critical. Certain linkages can better accommodate quinoid structures while the chosen positions of the alkyl chain can affect molecular weight and morphology. Use of conjugated side chains is one of the simplest synthetic methods towards broadening absorption without sacrificing desired HOMO or LUMO energy levels. Similar to the effects of electronegative heteroatoms in the main chain, adding them to side chains can assist with polymer self-assembly. Adding entire monomer species to the side

chain can also help to minimize the bandgap. Lastly, recent work has explored the effects of monomer sequencing. While AB alternating copolymers have widely been adopted, this is primarily due to the misconception that the HOMO energy levels of the copolymer are a direct result of the chosen monomer species. Final polymer characteristics, such as the bandgap and HOMO energy levels are heavily dictated by monomer sequence.

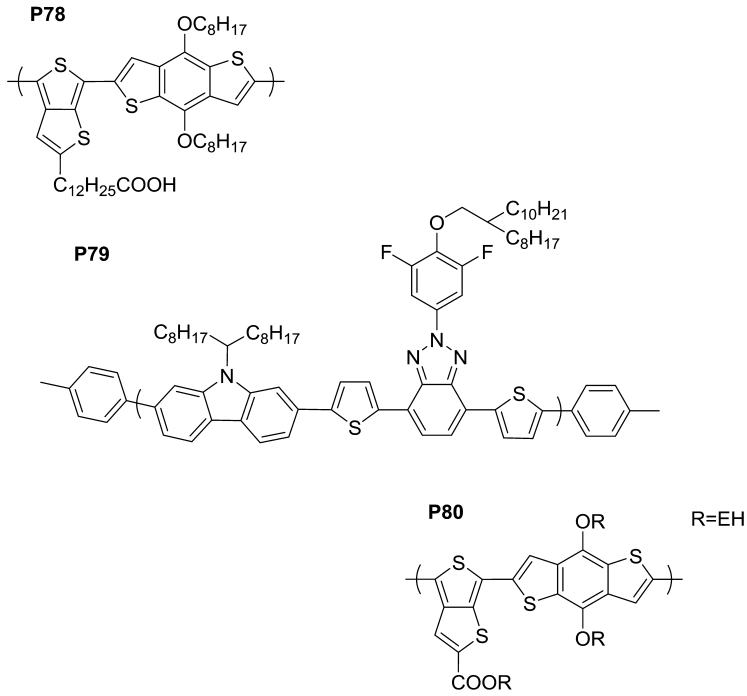

Figure 18. Structures of polymers P78-P80.

Towards Improving Morphology and Crystalline Structure

Chen et al. conducted an investigation of highly efficient ester-substituted thieno[3,4-*b*]thiophene copolymerized with a dialkoxyl benzodithiophene as seen in Figure 19 (**P78**), which achieved a maximum efficiency of 6.1% (Table 7) (*57*). Further studies to investigate the cause of this high efficiency led to a second study focusing primarily on the polymer's morphology (*103*). They discovered that the thienothiophene induces a rigid quinodal structure of the backbone while the benzodithiophene's fused tricyclic aromatic rings provide further rigid planarity that led to increased effective conjugation lengths and broader absorption properties (ε = 7.5 x 10^4 cm^{-1} at 690 nm). GISAXS and GIWAXS

In Polymer Composites for Energy Harvesting, Conversion, and Storage; Li, L., et al.;
ACS Symposium Series; American Chemical Society: Washington, DC, 2014.

experiments were used to determine that it was the parallel chain stacking relative to the substrate (27.3 Å stacking distance) that caused the superior charge transport properties as compared to P3HT:PCBM polymer systems, which organize perpendicularly. They also found that annealing was detrimental to the fibrous interpenetrating mix of the donor and acceptor phases formed in the neat film, and instead resulted in sub 100-200 nm phase-separated regions (5.24% PCE prior to annealing, and 1.92% post). This is contrary to the P3HT:PCBM blend, which has enhanced morphology and charge separation post-annealing. The larger domains formed in the polymer of study reduced the interfacial area between the two phases and reduced exciton formation (*103*).

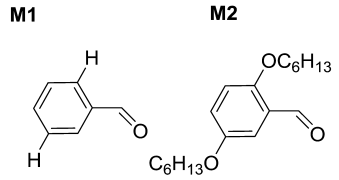

Figure 19. Monomers M1 and M2 utilized in sequence copolymers.

Work performed by Colsmann and coworkers focused on an alternating copolymer utilizing a carbazole donor and 2-phenyl-2H-benzotriazole acceptor (**P79**, Figure 19). They found that the use of DIO increased the PCE from 2.5% to 4.6% due to a substantial increase in FF and J_{SC} (*104*). The decrease in series resistance and increase in parallel resistance helped to improve the FF, and is indicative of a balanced electron and hole mobility (*105–107*) (see Table 7). The addition of DIO contributed to enhanced polymer aggregation that boosted absorption at 560 and 410 nm. X-ray scattering techniques determined that despite the amorphous morphology, the polymer still had face-on orientation relative to the substrate and ample π-π stacking that all contributed towards the improved OPV performance (*104*).

Yu and Li from the University of Chicago and Solarmer investigated the effects of fluorine on thieno[3,4-*b*]thiophene (**P80**, Figure 19) to deepen the HOMO energy level, and in turn improve the V_{OC}. Additional work utilized a branched side chain to improve solubility. The polymers organized itself into face-down conformation relative to the substrate. The highest achieved PCEs using DIO additive in chlorobenzene reached 7.40% with efficiencies of 6.22% without the additive, as seen in Table 7 (*108*).

Polymer morphology is a vital contributing factor towards an OPV device's success. The previous three examples have shown that perhaps a parallel chain stacking with respect to the substrate can better accommodate charge transfer vertically from the anode beneath to the hole transport layer and cathode above (in the case of traditional OPV architecture).

In Polymer Composites for Energy Harvesting, Conversion, and Storage; Li, L., et al.;
ACS Symposium Series; American Chemical Society: Washington, DC, 2014.

Conclusions

Organic photovoltaic PCEs have quickly advanced from a meager 1% efficiency in 1986, to over 10% today. These improvements are attributed to the multitude of device and polymer design techniques employed by researchers. This review provided a summary of the many synthetic modifications employed to tailor the final polymer properties, including methods to enhance quinoid stabilization, address polymer solubility through the choice of alkyl chains, improve polymer planarity through the use of conjugated spacers, and increase light absorption by taking advantage of side chains to introduce conjugated species. Big-picture design aspects such as overall monomer design and comonomer sequencing have also been discussed. While past research has been slightly conflicted towards the best methods of desigining these polymers, many researchers have started with electronic design to optimize the HOMO and LUMO energy levels. Most research attributes organic photovoltaics' shortcomings to the large optical bandgap, that limits the absorbed photon flux. Other studies have identified the issue to be with the HOMO energy level, as higher values (which would lead to a smaller bandgap), would be a detriment to the V_{OC}. Moreover, other studies have determined the that LUMO energy level has a larger influence over PCE values. While the motivation behind polymer design has varied, the many synthetic breakthroughs have all contributed towards the overall increase in organic semiconductor performance for OPVs.

Synthesis has now facilitated the use of polymers that can better stabilize quinoid structures. By fusing aromatic rings, double bonds can be forced between monomer units, allowing a method of circumventing the limitation of conjugation length that standard push-pull copolymers have. Research has determined that finding the ideal balance between aromatic and quinoid character can produce stable, high-performing polymers with very low bandgaps. While narrow bandgaps are ideal for optimum light absorption, various factors can inadvertently increase them, such as the selection and placement of alkyl chains. As discussed in the review, alkyl chains contribute not only towards solubility of the polymer, but affects the ability for polymer chain stacking and charge transfer capabilities. Regioregular placement of alkyl chains can minimize twisting of the polymer backbone, and researchers have explored the effects of alkoxy and siliyl alkyl groups as well. An alternative method of accommodating some of the lengthier and branched alkl chains has been to utilize spacers. While spacers initially started off as saturated units to occupy physical space between the monomers, conjugated, aromatic moieties such as alkenes, thiophenes, benzenes, and furans have been employed to not only prevent twisting from what would otherwise cause steric hindrances from neighboring alkyl chains, but contribute to the electronic properties of the polymer as well.

In all of the advances of monomer synthesis, molecular design to tailor final polymer properties has been the center of success towards improved PCE values. There has been a plethora of new molecules developed as electron-rich and electron-withdrawing units for push-pull copolymers. Selection of polymer backbone heteroatoms directly affect the polymer electronics, and thus its performance. It can also affect the ability for intramolecular charge transfer

and polymer chain stacking, such as with the deliberate selection of germanium bridged aromatic systems to better position alkyl chains further from the polymer main chain, thus increasing the available area for chain stacking. Likewise, placement of these monomers can directly affect charge transfer capabilities. Monomer linkage selection can drastically affect photovoltaic performance as does the chosen sequence. While a majority of researchers have employed the alternating donor-acceptor polymer architecture, new theoretical and preliminary experimental work is lending credibility towards the benefits of varying monomer sequence. This is based on the supposition that the monomers of choice do not directly coincide with the HOMO and LUMO energy levels of the copolymer, and that instead, this would be a result of no electronic interaction between the two units.

Lastly, monomer design can directly affect the final polymer morphology. Polymers with the some of the best charge transport properties have exhibited face-on orientation with respect to the OPV device substrate. While external methods have also been applied to improve polymer morphology, such as the addition of DIO to the solvent system to better improve the interfacial boundaries between the donor and acceptor phases.

The current trend of OPV polymer design has shifted ever-more towards computational predictions to combine a seemingly infinite number of combinations and calculate a number of figures of merit to screen for potential high-performing candidates. This has helped to identify ideal combinations, reveal structure-property relationships, and pinpoint the most significant properties that can improve or inhibit maximum PCEs. It is likely that experiemental work that stems from this field of research can lead to a competitive set of semiconducting polymers that can bring organic materials to the forefront of alternative energy applications.

References

1. Chiang, C. K.; Fincher, C. R.; Park, Y. W.; Heeger, A. J.; Shirakawa, H.; MacDiarmid, A. G.; Gau, S. C. *Phys. Rev. Lett.* **1977**, *39*, 1098–1101.
2. ElsenBaumer, R. L.; Jen, K. Y.; Oboodi, R. *Synth. Met.* **1986**, *15*, 169–174.
3. Ma, W.; Yang, C.; Gong, X.; Lee, K.; Heeger, a. J. *Adv. Funct. Mater.* **2005**, *15*, 1617–1622.
4. Li, G.; Shrotriya, V.; Huang, J.; Yao, Y.; Moriarty, T.; Emery, K.; Yang, Y. *Nat. Mater.* **2005**, *4*, 864–868.
5. Shaheen, S. E.; Brabec, C. J.; Sariciftci, N. S.; Padinger, F.; Fromherz, T.; Hummelen, J. C. *Appl. Phys. Lett.* **2001**, *78*, 841.
6. McCullough, R. D.; Williams, S. P.; Tristram-Nagle, S.; Jayaraman, M.; Ewbank, P. C.; Miller, L. *Synth. Met.* **1995**, *69*, 279–282.
7. Loewe, R. S.; Khersonsky, S. M.; McCullough, R. D. *Adv. Mater.* **1999**, *11*, 250–253.
8. Boudreault, P.-L. T.; Najari, A.; Leclerc, M. *Chem. Mater.* **2011**, *23*, 456–469.

9. Scharber, M. C.; Mühlbacher, D.; Koppe, M.; Denk, P.; Waldauf, C.; Heeger, a. J.; Brabec, C. J. *Adv. Mater.* **2006**, *18*, 789–794.
10. Deibel, C.; Dyakonov, V. *Reports Prog. Phys.* **2010**, *73*, 096401.
11. Henderson, S. *Phillips 66 Creates World-Record OPV Cell with 9.31% Efficiency*; http://www.solarnovus.com/phillips-66-creates-world-record-opv-cell-with-931-efficiency_N5571.html.
12. Deibel, C.; Dyakonov, V. *Rep. Prog. Phys.* **2010**, *73*, 096401.
13. Dimitrov, S. D.; Durrant, J. R. *Chem. Mater.* **2014**, *26*, 616–630.
14. Duan, C.; Huang, F.; Cao, Y. *J. Mater. Chem.* **2012**, *22*, 10416.
15. Takimiya, K.; Osaka, I.; Nakano, M. *Chem. Mater.* **2013**, *26*, 587–593.
16. Chochos, C. L.; Choulis, S. a. *Prog. Polym. Sci.* **2011**, *36*, 1326–1414.
17. Bian, L.; Zhu, E.; Tang, J.; Tang, W.; Zhang, F. *Prog. Polym. Sci.* **2012**, *37*, 1292–1331.
18. Mei, J.; Bao, Z. *Chem. Mater.* **2013**, *26*, 604–615.
19. Zhao, Z.; Zhang, F.; Zhang, X.; Yang, X.; Li, H.; Gao, X.; Di, C.; Zhu, D. *Macromolecules* **2013**, *46*, 7705–7714.
20. De Leeuw, D. M.; Simenon, M. M. J.; Brown, a. R.; Einerhand, R. E. F. *Synth. Met.* **1997**, *87*, 53–59.
21. Ajayaghosh, A. *Chem. Soc. Rev.* **2003**, *32*, 181.
22. Zhang, F.; Bijleveld, J.; Perzon, E.; Tvingstedt, K.; Barrau, S.; Inganäs, O.; Andersson, M. R. *J. Mater. Chem.* **2008**, *18*, 5468.
23. Zhou, H.; Yang, L.; Stoneking, S.; You, W. *ACS Appl. Mater. Interfaces* **2010**, *2*, 1377–83.
24. Havinga, E. E.; Hoeve, W. T.; Wynberg, H. *Synth. Met.* **1993**, *55-57*, 299–306.
25. Havinga, E. E.; Hoeve, W. T.; Wynberg, H. *Polym. Bull.* **1992**, *126*, 119–126.
26. O'Boyle, N. M.; Campbell, C. M.; Hutchison, G. R. *J. Phys. Chem. C* **2011**, *115*, 16200–16210.
27. Kanal, I. Y.; Owens, S. G.; Bechtel, J. S.; Hutchison, R. *J. Phys. Chem. Lett.* **2013**, *4*, 1613–1623.
28. Ikenoue, Y.; Wudl, F.; Heeger, a. J. *Synth. Met.* **1991**, *40*, 1–12.
29. Karikomi, M.; Kitamura, C.; Tanaka, S. *J. Am. Chem. Soc.* **1995**, *117*, 6791–6792.
30. Chen, W.; Jenekhe, S. A. *Macromol. Chem. Phys.* **1998**, *199*, 655–666.
31. Chen, W.-C.; Liu, C.-L.; Yen, C.-T.; Tsai, F.-C.; Tonzola, C. J.; Olson, N.; Jenekhe, S. a. *Macromolecules* **2004**, *37*, 5959–5964.
32. Chen, C.-H.; Hsieh, C.-H.; Dubosc, M.; Cheng, Y.-J.; Hsu, C.-S. *Macromolecules* **2010**, *43*, 697–708.
33. Umeyama, T.; Hirose, K.; Noda, K.; Matsushige, K.; Shishido, T.; Saarenpää, H.; Tkachenko, N. V.; Lemmetyinen, H.; Ono, N.; Imahori, H. *J. Phys. Chem. C* **2012**, *116*, 17414–17423.
34. Umeyama, T.; Hirose, K.; Noda, K.; Matsushige, K.; Shishido, T.; Hayashi, H.; Matano, Y.; Ono, N.; Imahori, H. *J. Phys. Chem. C* **2012**, *116*, 1256–1264.
35. Umeyama, T.; Watanabe, Y.; Oodoi, M.; Evgenia, D.; Shishido, T.; Imahori, H. *J. Mater. Chem.* **2012**, *22*, 24394.
36. Brédas, J. L. *J. Chem. Phys.* **1985**, *82*, 3808.

37. Bredas, J. L. *Synth. Met.* **1987**, *17*, 115–121.
38. Beŕube, N.; Gaudreau, J.; Côté, M. *Macromolecules* **2013**, *46*, 6873–6880.
39. Kim, J.-H.; Song, C. E.; Kim, H. U.; Kang, I.-N.; Shin, W. S.; Park, M.-J.; Hwang, D.-H. *J. Polym. Sci., Part A: Polym. Chem.* **2013**, *51*, 4136–4149.
40. Umeyama, T.; Hirose, K.; Noda, K.; Matsushige, K.; Shishido, T.; Saarenpää, H.; Tkachenko, N. V.; Lemmetyinen, H.; Ono, N.; Imahori, H. *J. Phys. Chem. C* **2012**, *116*, 17414–17423.
41. Afzali, A.; Dimitrakopoulos, C. D.; Breen, T. L. *J. Am. Chem. Soc.* **2002**, *124*, 8812–3.
42. Weidkamp, K. P.; Afzali, A.; Tromp, R. M.; Hamers, R. J. *J. Am. Chem. Soc.* **2004**, *126*, 12740–1.
43. Masumoto, A.; Yamashita, Y.; Go, S.; Kikuchi, T.; Yamada, H.; Okujima, T.; Ono, N.; Uno, H. *Jpn. J. Appl. Phys.* **2009**, *48*, 051505.
44. Hirao, A.; Akiyama, T.; Okujima, T.; Yamada, H.; Uno, H.; Sakai, Y.; Aramaki, S.; Ono, N. *Chem. Commun.* **2008**, 4714–6.
45. Matsuo, Y.; Sato, Y.; Niinomi, T.; Soga, I.; Tanaka, H.; Nakamura, E. *J. Am. Chem. Soc.* **2009**, *131*, 16048–50.
46. Ku, S.-Y.; Liman, C. D.; Cochran, J. E.; Toney, M. F.; Chabinyc, M. L.; Hawker, C. J. *Adv. Mater.* **2011**, *23*, 2289–93.
47. Cui, W.; Yuen, J.; Wudl, F. *Macromolecules* **2011**, *44*, 7869–7873.
48. Hong, W.; Guo, C.; Li, Y.; Zheng, Y.; Huang, C.; Lu, S.; Facchetti, A. *J. Mater. Chem.* **2012**, *22*, 22282–22289.
49. Yue, W.; Huang, X.; Yuan, J.; Ma, W.; Krebs, F. C.; Yu, D. *J. Mater. Chem. A* **2013**, *1*, 10116–10119.
50. Loewe, R. S.; Ewbank, P. C.; Liu, J.; Zhai, L.; McCullough, R. D. *Macromolecules* **2001**, *34*, 4324–4333.
51. McCullough, R.; Lowe, R. *J. Chem. Soc., Chem. Commun.* **1992**, 70–72.
52. Egbe, D. A. M.; Nguyen, L. H.; Hoppe, H.; Mühlbacher, D.; Sariciftci, N. S. *Macromol. Rapid Commun.* **2005**, *26*, 1389–1394.
53. Yue, W.; Zhao, Y.; Shao, S.; Tian, H.; Xie, Z.; Geng, Y.; Wang, F. *J. Mater. Chem.* **2009**, *19*, 2199–2206.
54. Li, Z.; Zhang, Y.; Tsang, S.-W.; Du, X.; Zhou, J.; Tao, Y.; Ding, J. *J. Phys. Chem. C* **2011**, *115*, 18002–18009.
55. Song, S.; Kim, T.; Bang, S. Y.; Heo, M.; Kim, J. Y.; Jin, Y.; Kim, I.; Suh, H. *Synth. Met.* **2013**, *177*, 65–71.
56. Havinga, E. E.; Meijer, E. W. *Mater. Sci. Eng.* **2001**, *32*, 1–40.
57. Liang, Y.; Feng, D.; Wu, Y.; Tsai, S.-T.; Li, G.; Ray, C.; Yu, L. *J. Am. Chem. Soc.* **2009**, *131*, 7792–9.
58. Wienk, M. M.; Turbiez, M.; Gilot, J.; Janssen, R. A. J. *Adv. Mater.* **2008**, *20*, 2556–2560.
59. George, Z.; Kroon, R.; Gehlhaar, R.; Gbabode, G.; Lundin, A.; Hellström, S.; Müller, C.; Geerts, Y.; Heremans, P.; Andersson, M. *Materials (Basel).* **2013**, *6*, 3022–3034.
60. Zade, S. S.; Zamoshchik, N.; Bendikov, M. *Chem.—Eur. J.* **2009**, *15*, 8613–8624.

61. Heeney, M.; Zhang, W.; Crouch, D. J.; Chabinyc, M. L.; Gordeyev, S.; Hamilton, R.; Higgins, S. J.; McCulloch, I.; Skabara, P. J.; Sparrowe, D.; Tierney, S. *Chem. Commun.* **2007**, 5061–3.
62. Chang, H.; Tsai, C.; Lai, Y.; Liang, W.; Hsu, S.; Hsu, C.; Cheng, Y. J. *Macromolecules* **2001**, *46*, 7715–7726.
63. Kim, J.-H.; Kim, H. U.; Lee, J.-K.; Park, M.-J.; Hyun, M. H.; Hwang, D.-H. *Synth. Met.* **2013**, *179*, 18–26.
64. Helgesen, M.; Krebs, F. C. *Macromolecules* **2010**, *43*, 1253–1260.
65. Miller, J. R.; Calcaterra, L. T.; Gloss, G. L. *J. Am. Chem. Soc.* **1984**, *106*, 3047–3049.
66. Wasielewski, M. R.; Niemczyk, M. P.; Svec, W. A.; Pewitt, E. B. *J. Am. Chem. Soc.* **1985**, *107*, 5562–5563.
67. McConnell, H. M. *J. Chem. Phys.* **1961**, *35*, 508–515.
68. Lu, K.; Fang, J.; Yan, H.; Zhu, X.; Yi, Y.; Wei, Z. *Org. Electron.* **2013**, *14*, 2652–2661.
69. Najari, A.; Beaupré, S.; Berrouard, P.; Zou, Y.; Pouliot, J.-R.; Lepage-Pérusse, C.; Leclerc, M. *Adv. Funct. Mater.* **2011**, *21*, 718–728.
70. Zhang, G.; Fu, Y.; Xie, Z.; Zhang, Q. *Polymer* **2011**, *52*, 415–421.
71. Mondal, R.; Ko, S.; Norton, J. E.; Miyaki, N.; Becerril, H. A.; Verploegen, E.; Toney, M. F.; Brédas, J.-L.; McGehee, M. D.; Bao, Z. *J. Mater. Chem.* **2009**, *19*, 7195–7197.
72. Huang, Y.; Guo, X.; Liu, F.; Huo, L.; Chen, Y.; Russell, T. P.; Han, C. C.; Li, Y.; Hou, J. *Adv. Mater.* **2012**, *24*, 3383–3389.
73. Sakthivel, P.; Song, H. S.; Chakravarthi, N.; Lee, J. W.; Gal, Y.-S.; Hwang, S.; Jin, S.-H. *Polymer* **2013**, *54*, 4883–4893.
74. Bronstein, H.; Chen, Z.; Ashraf, R. S.; Zhang, W.; Du, J.; Durrant, J. R.; Tuladhar, P. S.; Song, K.; Watkins, S. E.; Geerts, Y.; Wienk, M. M.; Janssen, R. A J.; Anthopoulos, T.; Sirringhaus, H.; Heeney, M.; McCulloch, I. *J. Am. Chem. Soc.* **2011**, *133*, 3272–3275.
75. Ding, P.; Chu, C.-C.; Liu, B.; Peng, B.; Zou, Y.; He, Y.; Zhou, K.; Hsu, C.-S. *Macromol. Chem. Phys.* **2010**, *211*, 2555–2561.
76. Wang, X.; Chen, S.; Sun, Y.; Zhang, M.; Li, Y.; Li, X.; Wang, H. *Polym. Chem.* **2011**, *2*, 2872–2877.
77. Wang, X.; Sun, Y.; Chen, S.; Guo, X.; Zhang, M.; Li, X.; Li, Y. *Macromolecules* **2012**, *45*, 1208–1216.
78. Cremer, J.; Ba, P.; Janssen, A. J. *Chem. Mater.* **2006**, *18*, 5832–5834.
79. Woody, K. B.; Henry, E. M.; Jagtap, S.; Collard, D. M. *Macromolecules* **2011**, *44*, 9118–9124.
80. Braunecker, W. A.; Owczarczyk, Z. R.; Garcia, A.; Kopidakis, N.; Larsen, R. E.; Hammond, S. R.; Ginley, D. S.; Olson, D. C. *Chem. Mater.* **2012**, *24*, 1346–1356.
81. Braunecker, W. A.; Oosterhout, S. D.; Owczarczyk, Z. R.; Larsen, R. E.; Larson, B. W.; Ginley, D. S.; Boltalina, O. V.; Strauss, S. H.; Kopidakis, N.; Olson, D. C. *Macromolecules* **2013**, *46*, 3367–3375.
82. Goldsmith, R. H.; Vura-weis, J.; Scott, A. M.; Borkar, S.; Sen, A.; Ratner, M. A.; Wasielewski, M. R.; Pennsyl, V. *J. Am. Chem. Soc.* **2008**, *130*, 7659–7669.

83. Hrobáriková, V.; Hrobárik, P.; Gajdos, P.; Fitilis, I.; Fakis, M.; Persephonis, P.; Zahradník, P. *J. Org. Chem.* **2010**, *75*, 3053–3068.
84. Li, Y.; Sonar, P.; Murphy, L.; Hong, W. *Energy Environ. Sci.* **2013**, *6*, 1684–1710.
85. Amb, C. M.; Chen, S.; Graham, K. R.; Subbiah, J.; Small, C. E.; So, F.; Reynolds, J. R. *J. Am. Chem. Soc.* **2011**, *133*, 10062–5.
86. Chu, T.; Lu, J.; Beaupr, S.; Zhang, Y.; Leclerc, M. *J. Am. Chem. Soc.* **2011**, *133*, 4250–4253.
87. Liu, B.; Chen, X.; He, Y.; Li, Y.; Xu, X.; Xiao, L.; Li, L.; Zou, Y. *J. Mater. Chem. A* **2013**, *1*, 570–577.
88. Seri, M.; Bolognesi, M.; Chen, Z.; Lu, S.; Koopman, W.; Facchetti, A.; Muccini, M. *Macromolecules* **2013**, *46*, 6419–6430.
89. Risko, C.; Kushto, G. P.; Kafafi, Z. H.; Kafati, Z. H.; Brédas, J. L. *J. Chem. Phys.* **2004**, *121*, 9031–9038.
90. Zhan, X.; Risko, C.; Amy, F.; Chan, C.; Zhao, W.; Barlow, S.; Kahn, A.; Bre, J.; Marder, S. R. *J. Am. Chem. Soc.* **2005**, *127*, 9021–9029.
91. Yamaguchi, S.; Tamao, K. *Bull. Chem. Soc. Jpn.* **1996**, *69*, 2327–2334.
92. Nielsen, C. B.; Ashraf, R. S.; Rossbauer, S.; Anthopoulos, T.; McCulloch, I. *Macromolecules* **2013**, *46*, 7727–7732.
93. Li, S.; He, Z.; Yu, J.; Chen, S.; Zhong, A.; Tang, R.; Wu, H.; Qin, J.; Li, Z. *J. Mater. Chem.* **2012**, *22*, 12523.
94. Li, Y.; Sonar, P.; Singh, S. P.; Soh, M. S.; van Meurs, M.; Tan, J. *J. Am. Chem. Soc.* **2011**, *133*, 2198–204.
95. Zhang, M.; Tsao, H. N.; Pisula, W.; Yang, C.; Mishra, A. K.; Müllen, K. *J. Am. Chem. Soc.* **2007**, *129*, 3472–3.
96. Li, Y.; Fu, Y.; Tong, H.; Xie, Z.; Wang, L. *J. Polym. Sci., Part A: Polym. Chem.* **2013**, *51*, 2910–2918.
97. Liu, C.; Cai, W.; Guan, X.; Duan, C.; Xue, Q.; Ying, L.; Huang, F.; Cao, Y. *Polym. Chem.* **2013**, *4*, 3949.
98. Shin, S. A.; Park, J. B.; Kim, J.-H.; Hwang, D.-H. *Synth. Met.* **2013**, *172*, 54–62.
99. Tan, H.; Yu, J.; Wang, Y.; Chen, J.; Tao, Q.; Liu, Y.; Huang, J.; Zhu, W. *Org. Electron.* **2013**, *14*, 1510–1515.
100. Tan, H.; Deng, X.; Yu, J.; Zhao, B.; Wang, Y.; Liu, Y.; Zhu, W.; Wu, H.; Cao, Y. *Macromolecules* **2013**, *46*, 113–118.
101. Wang, Y.; Liu, Y.; Chen, S.; Peng, R.; Ge, Z. *Chem. Mater.* **2013**, *25*, 3196–3204.
102. Norris, B. N.; Zhang, S.; Campbell, C. M.; Auletta, J. T.; Calvo-Marzal, P.; Hutchison, G. R.; Meyer, T. Y. *Macromolecules* **2013**, *46*, 1384–1392.
103. Guo, J.; Liang, Y.; Szarko, J.; Lee, B.; Son, H. J.; Son, H. J.; Rolczynski, B. S.; Yu, L.; Chen, L. X. *J. Phys. Chem. B* **2010**, *114*, 742–748.
104. Klein, M. F. G.; Pasker, F. M.; Kowarik, S.; Landerer, D.; Pfaff, M..; Isen, M.; Gerthsen, D.; Lemmer, U.; Höger, S.; Colsmann, A. *Macromolecules* **2013**, *46*, 3870–3878.
105. Ratcliff, E. L.; Meyer, J.; Steirer, K. X.; Armstrong, N. R.; Olson, D.; Kahn, A. *Org. Electron.* **2012**, *13*, 744–749.

106. Koster, L. J. a.; Mihailetchi, V. D.; Blom, P. W. M. *Appl. Phys. Lett.* **2006**, *88*, 093511.
107. Kröger, M.; Hamwi, S.; Meyer, J.; Riedl, T.; Kowalsky, W.; Kahn, a. *Appl. Phys. Lett.* **2009**, *95*, 123301.
108. Liang, Y.; Xu, Z.; Xia, J.; Tsai, S.-T.; Wu, Y.; Li, G.; Ray, C.; Yu, L. *Adv. Mater.* **2010**, *22*, E135–8.

Chapter 5

Thermal Stability and Ionic Conductivity of High-Temperature Proton Conducting Ionic Liquid−Polymer Composite Electrolyte Membranes for Fuel Cell Applications

Somisetti V. Sambasivarao*

Department of Chemical and Biological Engineering,
Colorado School of Mines,
Golden, Colorado 80401, U.S.A.
***E-mail: somissv@tigermail.auburn.edu.**

The current technology of polymer electrolyte membrane fuel cells (PEMFCs) is based on perfluorosulfonic acid (PFSA) polymer membranes operating at a typical temperature of 80°C. Important key issues and limitations of PFSA based PEMFCs include hydration levels, CO poisoning, and hydrogen. To overcome these limitations, high temperature polymer electrolyte membranes (PEMs) for operation above 120°C are under development. This review encompasses the high temperature PEMs operating above 100°C, focusing on ionic liquids (ILs), as well as the ionic conductivities (ICs) and thermal stabilities (TSs) of IL-polymer composite membranes. The best IL-polymer composite membranes with the maximum available ICs and high TSs are discussed. The effect of casting methods on the ICs and TSs of IL-polymer composite membranes is also presented. The IL-polymer composite membrane increases the ionic mobility of charge transport by creating an ordered network of ionic domains in the PEMs.

In Polymer Composites for Energy Harvesting, Conversion, and Storage; Li, L., et al.;
ACS Symposium Series; American Chemical Society: Washington, DC, 2014.

Introduction

Proton exchange membrane fuel cells (PEMFCs) are electrochemical devices with high power densities, low pollutant emissions, and advanced features (*1*, *2*). The PEMFCs technology that is currently available based on perfluorosulfonic acid (PFSA) polymer membranes as electrolytes. The PFSA membranes consist of carbon-fluorine backbone chains and perfluoro sulfonate side chain pendants (*3*). Some commercial PFSA membranes and their structures are given in Table 1.

Table 1. PFSA Membranes by Manufacturer. (Reproduced with permission from Reference (*3*). Copyright 2003 American Chemical Society.)

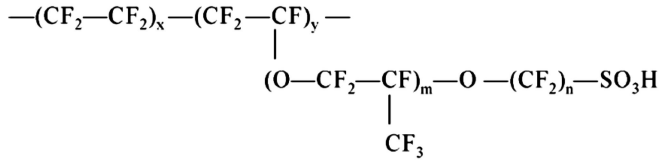

Structure parameter	Trade name and type	Equivalent weight	Thickness (μm)
	DuPont		
m = 1; x = 5 – 13.5 n = 2; y = 1	Nafion 120	1200	260
	Nafion 117	1100	175
	Nafion 115	1100	125
	Nafion 112	1100	80
	Asashi Glass		
m = 0, 1; n = 1 – 5	Flemion-T	1000	120
	Flemion-S	1000	80
	Flemion-R	1000	50
	Asashi Chemicals		
m = 0; n = 2 – 5 x = 1.5 – 14	Aciplex-S	1000 – 1200	25 – 100
	Dow Chemical		
m = 0; n = 2; x = 3.6 – 10	Dow	800	125

Fuel cells are one of the technologies actively supported by the U.S Department of Energy (DOE) to reduce the United States' dependence on foreign oil. PEMFCs directly utilize hydrogen gas as a fuel and have applications in vehicles and back-up power devices. The first practical fuel cell was invented

In Polymer Composites for Energy Harvesting, Conversion, and Storage; Li, L., et al.;
ACS Symposium Series; American Chemical Society: Washington, DC, 2014.

by W. T. Grubb, a scientist in the General Electric Company in 1955 who used an ion exchange resin membrane as the electrolyte (*4*, *5*). A typical PEMFC is shown in Figure 1 (*6*). The important characteristics (*7*) of polymer electrolyte membranes (PEMs) in PEMFCs are (1) PEMs should have a good electrolytic property (i.e. high ion mobility) (2) PEMs have negligible electrical conductivity (3) PEMs should be permeable to ions but allow only one type of charge (4) PEMs should be resistive to permeation of uncharged gases (5) PEMs should have a variable membrane area and thickness; and (6) PEMs should have good mechanical strength and durability over 10 years. A typical fuel cell consists of (1) a fuel electrode (anode) (2) an oxidant electrode (cathode) and (3) a proton exchange membrane.

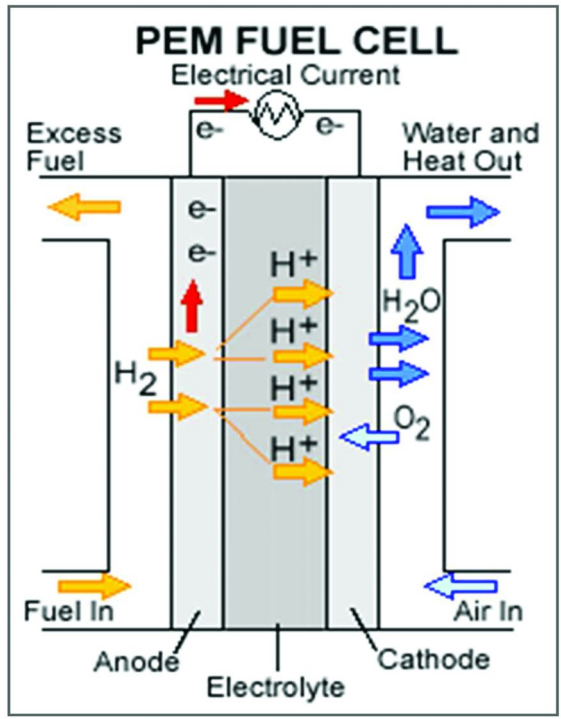

Figure 1. Schematic diagram of a simple PEM fuel cell. (Reproduced from Reference (6).)

In general, the humidified gases, hydrogen and oxygen, serve as fuel for the operation of PEMFCs. The two half electrochemical reactions that occur at both electrodes are as follows:

$$\text{Anode :} \quad H_2 \rightarrow 2H^+ + 2e^-$$

$$\text{Cathode :} \quad 1/2O_2 + 2H^+ + 2e^- \rightarrow H_2O$$

$$\text{Overall :} \quad H_2 + 1/2O_2 \rightarrow H_2O + \text{Electrical Energy} + \text{Heat Energy}$$

A number of excellent review articles with special importance to transport properties, structural properties, and applications of PFSA membranes are readily available in the literature (*1–3*, *8–11*). The purpose of this review is to summarize recent studies on the ionic conductivities and thermal stabilities of high temperature PEMs for practical applications of PEMFCs.

Need for High-Temperature Polymer Exchange Membranes (PEMs)

(1) PEMFCs require hydration for their operation at optimum temperatures. The presence of water makes the PEMFCs work at lower temperatures, typically at around 80°C (*1*, *3*). Low humidification hinders proton transport (*12*), while high humidification also has deleterious effects, namely condensing water and flooding the electrodes (*13*). Moreover, changes in the water content cause membrane swelling and shrinkage, which in turn leads to the deterioration of the membrane and its catalytic interface (*3*). (2) The CO poisoning effect is more pronounced at low operational temperatures (*14*). In order to minimize the CO effect, the PEMFCs operate at very high temperatures (*15*), and pure hydrogen is needed as a fuel to operate the PEMFCs (*3*). To fully achieve their benefits, as per DOE specifications, PEMFCs must be operated at temperatures of at least 120°C without humidification and at a proton conductivity of at least 0.1 S cm^{-1} (*2*, *16*, *17*).

Several methods are being employed to produce new PEMs with the goal of higher temperature and dry gas operation. The new methods can broadly be divided into two categories. The first one is to incorporate ionic liquids (ILs) into polymer membranes (*18*, *19*) and the second category is to incorporate inorganic proton conductors (*20*) and/or water retention systems (*21*) into the polymeric membrane. This review discusses the first category of IL-polymer composite membranes.

Ionic Liquid–Polymer Composite Membranes as High-Temperature PEMs

Ionic Liquids (ILs): ILs, often called room temperature ionic liquids (RTILs), contain anions and cations in a molten salt form with high thermal stability, and negligible vapor pressure. Unlike molecular solvents, RTILs don't possess volatility (*22*, *23*). ILs are excellent conductors as they are in ionic form. A simple list of IL forming ions from our previous work is presented in Figure 2. Based on the IL properties, ILs have numerous applications in electrochemistry

(*24*), separation science (*25*), catalysis (*26*), materials (*27*), and synthesis (*28*, *29*). The property of ionic conduction of ILs can greatly open the possibilities of using them as high temperature PEMs in the applications of PEMFCs (*30*, *31*).

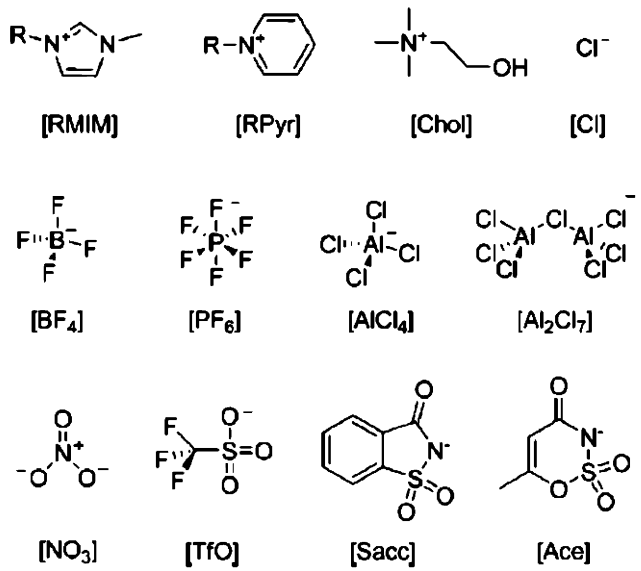

Figure 2. Ionic liquid-forming ions. R = methyl, ethyl, propyl, butyl, and hexyl. (Reproduced with permission from Reference (23). Copyright 2009 American Chemical Society.)

Ionic Liquid (IL)−Polymer Composite Membranes

Introducing ILs into PEMs makes them operate at higher temperatures without utilizing water for proton conduction. As there are no hydration levels in PEMs, there is no poisoning effect of water on electrodes and catalysts. ILs act as proton conductors in IL-composite polymer membranes. Overall these composite membranes works at temperatures above 100°C.

Padilha et al (*32*) studied the effect of two ILs (1-butyl 3-methyl imidazolium tetrafluoroborate [BMIM.BF_4] and 1-butyl 3-methyl imidazolium chloride [BMIM.Cl]) on Nafion, and reported the performance of PEMs with aqueous water IL mixture. They utilized aqueous solutions of ILs (aq. ILs) as proton conductors. The efficiency of PEMFCs can be enhanced by 61% if the ILs are used in the polymer membranes. Figure 3 shows the varied power densities with the concentration of ILs. The results indicate that the use of aqueous ILs increase current and power densities by at least 50 times over those of the PEMFCs with simple water. The power densities increase greatly, even at low concentrations of ILs. As aqueous ILs are weak electrolytes, the maximum power density is reached and then it gradually decreases with an increasing IL concentration.

In Polymer Composites for Energy Harvesting, Conversion, and Storage; Li, L., et al.;
ACS Symposium Series; American Chemical Society: Washington, DC, 2014.

These results suggest the use of aqueous IL solutions in PEMs which in turn is used in the PEMFCs for its enhanced performance. The authors inferred that this increase in PEMFC performance can facilitate the use of ILs as renewable energy materials (*32*).

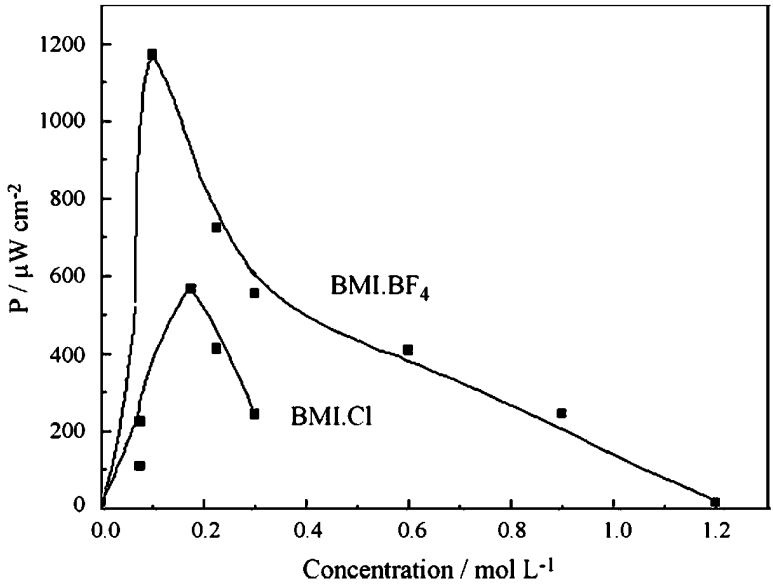

Figure 3. Effect of the concentration of BMIM.BF_4 (a) and BMIM.Cl (b) on the power density in a PEMFC at room temperature. (Reproduced with permission from Reference (32). Copyright 2010 Elsevier publications.)

Changing the ILs to 1-butyl 3-methyl imidazolium trifluoromethane sulfonate (BMIM.TfO) (*33*) causes the conductivities of the Nafion-IL composite membranes to exceed the 0.1 S cm^{-1} at 180°C. The composite membranes work in the temperature range of 100 to 200°C. High conductivities of the membranes are observed if these are subjected to heat treatments at elevated temperatures of 60 to 100°C. At higher temperatures, the ILs are absorbed deeply into the polymer membrane. However, if the polymer composites are cast at room temperature, their conductivities range from 6×10^{-5} S cm^{-1} at 23°C to 5.1×10^{-5} S cm^{-1} at 150°C. The low conductivity values are probably due to the formation of HBF_4 and triflate acid, and the IL component is not completely imbibed deeply into the membrane. The TGA scans for the composite IL membranes show that the decomposition of the IL doped membranes start at 350°C. The high temperature decomposition indicates that these membranes are suitable for higher operating temperature conditions in fuel cells, as there was no acid formation up to 200°C (*33*).

Li et al (*34*) studied anhydrous proton-conducting glass membranes doped with IL for intermediate-temperature fuel cells. The anhydrous membranes based on SiO_2 monoliths doped with varied loads of a protic ionic liquid

In Polymer Composites for Energy Harvesting, Conversion, and Storage; Li, L., et al.;
ACS Symposium Series; American Chemical Society: Washington, DC, 2014.

(diethylmethylammonium trifluoromethanesulfonate, [DEMA.TfO]) were studied. The ionic conductivities of glass membranes doped with DEMA.TfO are shown in Figure 4. The membranes with a lower content of DEMA.TfO have the conductivities in the order of 10^{-3} S cm^{-1} from 120°C to 220°C. These rates of conductivities are too low to be used as PEMs in fuel cells. The ionic conductivity is increased as the content of DEMA.TfO increases. The glass composites with DEAM.TfO greater than 70% show conductivity exceeding 10^{-2} S cm^{-1} and are capable of operating with anhydrous conditions in the working conditions of fuel cells. The hybrid glass composites with IL membranes also have excellent thermal stabilities. The samples of hybrid glass membranes are subjected to heating at 120°C for 180 h. The measured ionic conductivities are plotted against time. There is no decrease in conductivity numbers for the entire period as shown in Figure 5. There is no change in conductivity over a long period of heating times showing that the hybrid glass composite IL membranes have outstanding thermal stabilities. The addition of water in these glass membranes increases the conductivity of the membrane. The conductivity increases from 10^{-3} S cm^{-1} to 10^{-2} S cm^{-1} with relative humidity changing from 0 to 90% at 60°C. Phosphoric acid membranes undergo self-condensation at higher temperatures, which causes lower conductivity. So, the data in figures 4 and 5 clearly indicate that IL membranes are superior to phosphoric acid-based membranes to be used as PEMs in FCs. However, the glass hybrid membranes are brittle in nature. The authors (*34*) are currently working on improving the flexibility of the glass membranes.

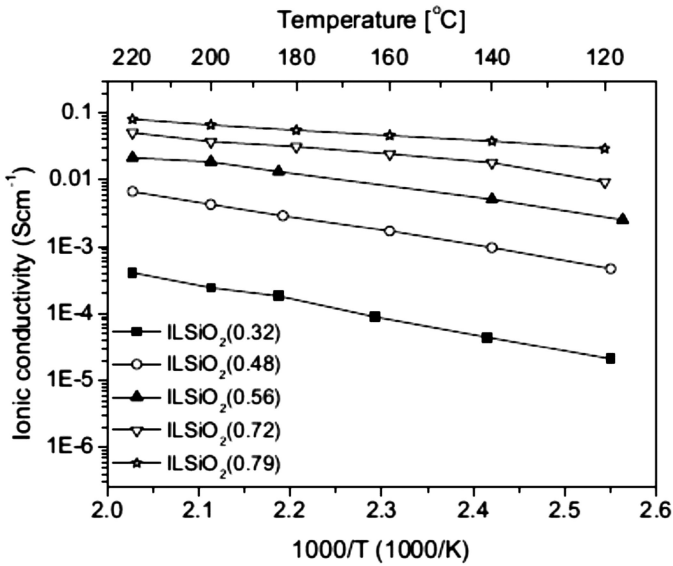

Figure 4. Anhydrous ionic conductivities of the [DEMA.TfO]/SiO_2 glass membrane as a function of temperature. (Reproduced with permission from Reference (34). Copyright 2012 Elsevier publications.)

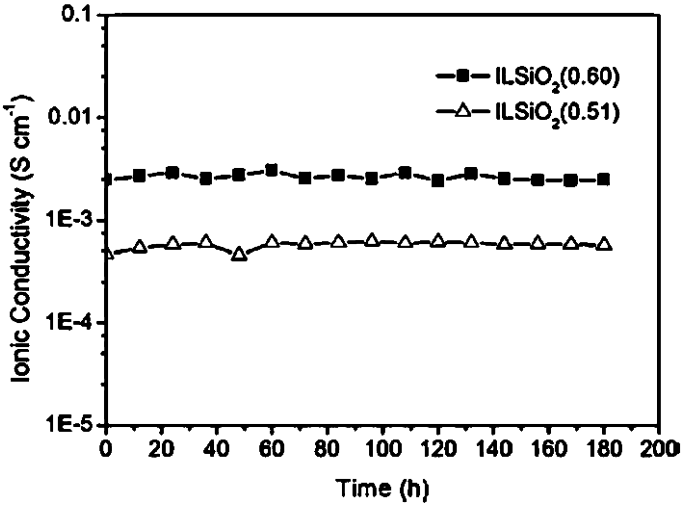

Figure 5. Ionic conductivities of the [DEMA.TfO]/SiO_2 glass membranes as a function of time. (Reproduced with permission from Reference (34). Copyright 2012 Elsevier publications.)

IL composites with copolymers can also be used as PEMs. In a study by Sekhon et al (*35*) on the development of IL composites with copolymers as non-humidified PEMs, a number of ILs based on 2,3-dimethyl-1-octylimidazolium cation ($DMOIM^+$) and various anions (BF_4^-, PF_6^-, $CF_3SO_3^-$, $N(CF_3SO_2)_2^-$ or TFSI, etc.) with different polymers (PAN, PMA, PEO, PMMA, PVdF, PVdF-HFP) were synthesized. Their preliminary results on tests of the PEM containing an IL (DMOIM.TFSI) in a real fuel cell with non-humid conditions show that the conductivity of the membrane with 2.74 S cm^{-1} at 130°C has good mechanical stability.

Kim et al. (*36*) has studied conductivity studies on poly(styrenesulphonate-*b*-methylbutylene) (S_nMB_m), a copolymer doped with two ILs from 25 to 165°C. Higher temperature increases the conductivity because of the higher mobility of charged transport. These membranes show good conductivity at higher temperatures indicating that the membranes have good thermal stability. Note that the amount of IL present in the membrane also influences the conductivity as 50wt% of MS IL have higher conductivity values. MS ILs have higher ionic conductivity values than the BF_4 ILs. The conductivity values for the composite copolymers are higher than those of pure styrine polymers. Nafion has intermediate conductivity between the coploymer-IL composite and styrene. Nafion has an intermediate ordering of nanodomains for charge transport, while the composite copolymer has highly ordered IL domains for the ion mobility. Figure 6 shows the conductivity for various composite polymers compared to that of Nafion and styrene polymers as PEMs in fuel cells.

In Polymer Composites for Energy Harvesting, Conversion, and Storage; Li, L., et al.;
ACS Symposium Series; American Chemical Society: Washington, DC, 2014.

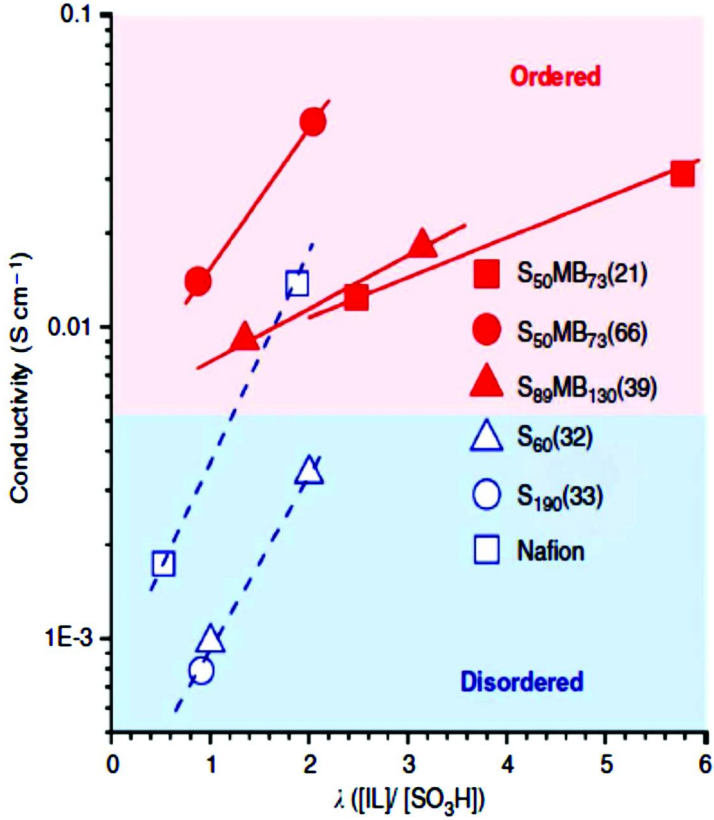

Figure 6. Enhanced proton transport with nanostructured S_nnMB_m/IL membranes. The in-plane conductivity of S_nMB_m/IL composite membranes and Nafion 117/IL as well as normal-to-plane conductivity of Sn/IL membranes as a function of the amount of absorbed IL per sulphonic acid group (λ) at 165 °C under anhydrous conditions. (Reproduced from Reference (36), Copyright 2010 Nature Publishing Group.)

Several studies are reviewed on polybenzimidazole (PBI) - phosphoric acid (H_3PO_4) composite membranes to be used as PEMs (*1*). One limitation in using these H_3PO_4 composite membranes is the leaching of H_3PO_4 when testing them as PEMs during long-term testing of fuel cells. Ye et al. (*37*) tested the applicability of ILs into the PBI-H_3PO_4 membranes. Novel membranes consisting of the 1-methyl-3-propyl-methylimidazolium dihydrogen phosphate ($PMIH_2PO_4$), anhydrous solvent H_3PO_4, and PBI were synthesized, investigating its stability and proton mobility. They were found to have good thermal and chemical stabilities; however, these membranes were not tested for their utility for a long-time operation in fuel cell conditions. The TGA scans for the H_3PO_4/PBI,

$PMIH_2PO_4$/PBI and H_3PO_4/ $PMIH_2PO_4$/PBI membranes with different component molar ratios are shown in Figure 7. All composite membranes are shown to have good thermal stability up to 200°C. As the thermal stability is around 200°C, these membranes can be operated at elevated temperatures.

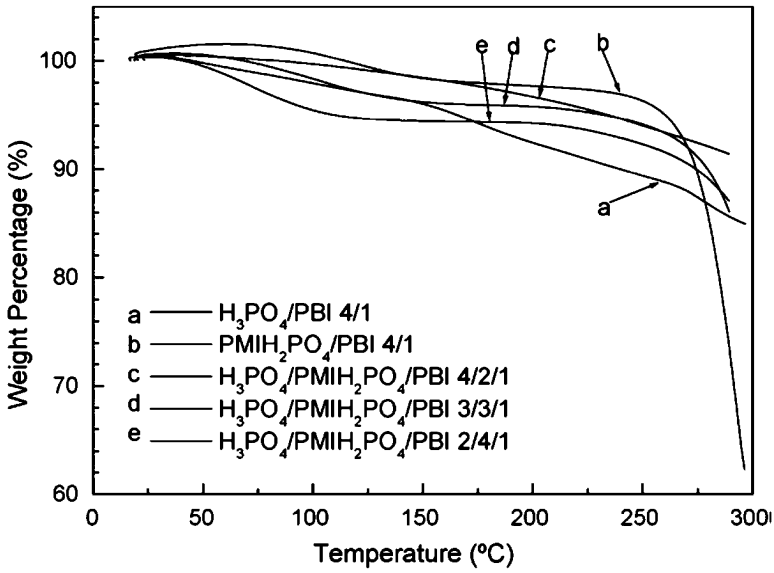

Figure 7. TGA of H_3PO_4/PBI, $PMIH_2PO_4$/PBI and H_3PO_4/ $PMIH_2PO_4$/PBI membranes. (Reproduced with permission from reference (37). Copyright 2008 Elsevier publications.)

Ionic conductivity plots of H_3PO_4/PBI, $PMIH_2PO_4$/PBI and H_3PO_4/ $PMIH_2PO_4$/PBI membranes under anhydrous condition are given in Figure 8. H_3PO_4/PBI and H_3PO_4/$PMIH_2PO_4$/PBI composite membranes have similar conductivity profiles. However, the conductivity profile for $PMIH_2PO_4$/PBI has weaker temperature dependence after 80°C. On incorporating ILs into the H_3PO_4/PBI complex, the conductivity significantly increases; a higher quantity of $PMIH_2PO_4$ in the complex yields a higher conductivity for the composite membrane. H_3PO_4/ $PMIH_2PO_4$/PBI composite membranes with 4/2/1, 3/3/1, and 2/4/1 molar ratios under completely non-aqueous conditions have conductivities of 0.84, 1.40 and 2.04 mScm−1 at 150°C, respectively.

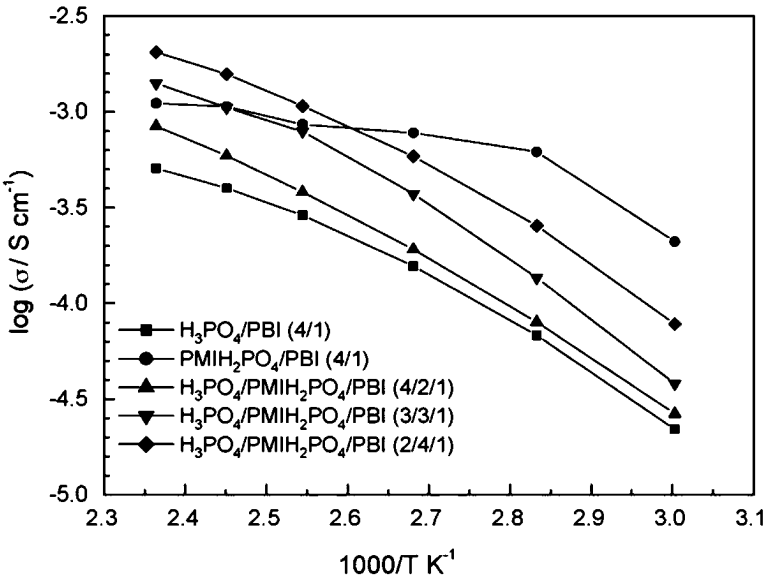

Figure 8. Temperature dependent ionic conductivity of H_3PO_4/PBI, $PMIH_2PO_4$/PBI and H_3PO_4/ $PMIH_2PO_4$/PBI membranes under anhydrous condition. (Reproduced with permission from Reference (37). Copyright 2008 Elsevier publications.)

Effect of Casting Methods on Ionic Liquid (IL)−Polymer Composite Membranes

There is significant effect of casting methods on the ICs and TSs of the IL-polymer composites. Park et al. (*38*) studied the annealing effect on the polymeric membrane prepared from Nafion with the ionic liquid, 1-ethyl-3-methylimidazolium tetrafluoroborate (EMIM.BF4). The composite membranes were investigated by using thermo-gravimetric analysis, ion conductivity, and small-angle X-ray scattering. The crystallinity of recast polymer composite membranes is increased from 12.8% for the non-annealed ones, to 14.7% for those annealed at 190°C. As the crystallinity increases, the ionic conductivity is also expected to increase in thermally activated polymer composites. The temperature effect on ionic conductivity of recast membranes is presented in Figure 9. It shows that the higher conductivity is observed for annealed composite membranes with $EMIM.BF_4$, but not for the non-annealed ones. The composite membranes are not thermally activated at low temperatures, but they are thermally activated at higher temperatures. Higher conductivity of the composite membranes is due to the formation of better ionic clusters for proton transport. Ionic cluster networks are formed with spherical ionic liquid clusters

In Polymer Composites for Energy Harvesting, Conversion, and Storage; Li, L., et al.;
ACS Symposium Series; American Chemical Society: Washington, DC, 2014.

and inter-connected ionic liquid domains. Annealing at 190°C significantly alters the composite membrane to render it more suitable for ionic conductivity. As the annealing temperature increases, the ionic conductivity also increases without altering the ion exchange capacity or water content.

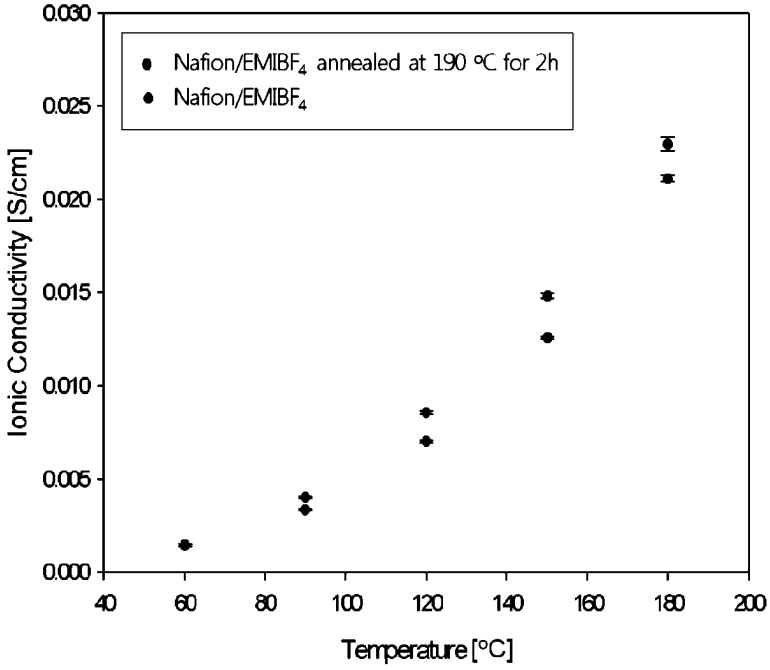

Figure 9. Variation of ionic conductivity (under anhydrous status) with temperature for the composite membranes containing EMIM.BF4 before and after annealing at 190°C for 2 h. (Reproduced with permission from Reference (38). Copyright 2011 Korean Electrochemical Society.)

The thermal stability of Nafion and its composite membranes containing EMIM.BF_4 was given in the thermo-gravimetric analysis of Figure 10. The TGA curves of Nafion and its composite membranes were distinguishable, and these were affected due to a decomposition of the side chain pendants (i.e. sulfonic acid groups) at ~300°C. The decomposition of polymer continues as the temperature increases, and a decomposition of the main chain starts at ~400°C. However, the composite membranes have better TGA curves and thermal stability after a temperature value of ~300°C at which decomposition of sulfonic acid groups take place. Since there is no change in the thermal stability observed for non-annealed TGA curves for Nafion and its composite IL membranes, the authors inferred that the better stability of the recast composite membranes, which were totally dried for TGA scans, was due to the effect of the ionic liquid contained in it.

In Polymer Composites for Energy Harvesting, Conversion, and Storage; Li, L., et al.;
ACS Symposium Series; American Chemical Society: Washington, DC, 2014.

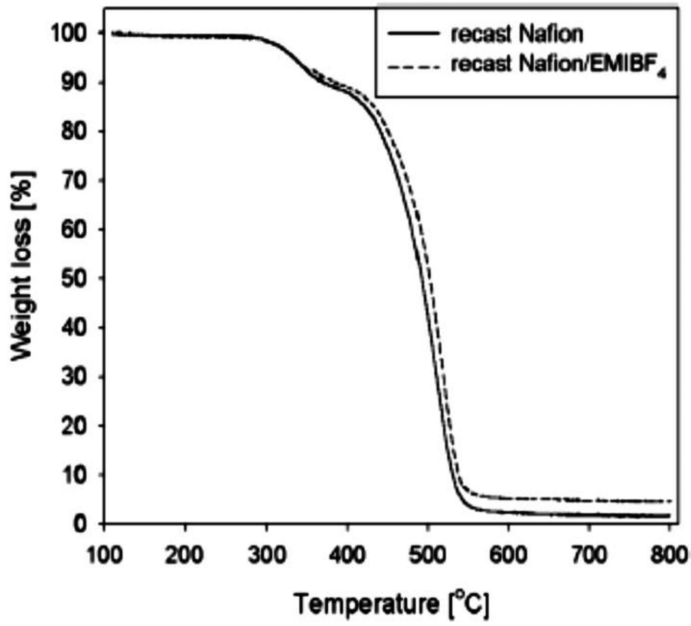

Figure 10. Thermo-gravimetric analysis curves of recast Nafion and composite membranes containing EMIM.BF4 under nitrogen atmosphere. (Reproduced with permission from Reference (38). Copyright 2011 Korean Electrochemical Society.)

Mechanisms of Proton Conduction in IL−Polymer Composite Membranes

It is important to note here that Nafion, and other PEMs do have only randomly organized hydrophilic domains. The conventional PEMs have low mobility of charged particles because domains of ion-conducting channels are discrete in nature and not-ordered. An ordered ionic domains are required to improve the transport properties of PEMFCs. This is possible only when the ILs be used in PEMs as composite membranes with the existing polymers like Nafion and sulphonated poly(aryl ether ketone) , or polymeric ionic liquids (*18*, *19*, *36*, *39*, *40*).

The proposed mechanism for proton conduction in the H_3PO_4/ $PMIH_2PO_4$/ PBI composite membranes from Reference (*37*) is presented in Figure 11. It is believed that the IL ($PMIH_2PO_4$) aid in proton transfer through the 3-dimensional hydrogen bonded network. IL acts as a plasticizer for PBI and facilitates the motion of PBI. The anion component of IL, $H_2PO_4^-$ a proton acceptor, functions as a proton exchange site, and undergoes structural reorganization while accepting H^+ from NH group of PBI and donating H^+ to H_3PO_4. $H_2PO_4^-$ acts as an anchor between H_3PO_4 and PBI. IL may also adjust the strength of the hydrogen bonding network optimized for proton transport. Overall the addition

In Polymer Composites for Energy Harvesting, Conversion, and Storage; Li, L., et al.;
ACS Symposium Series; American Chemical Society: Washington, DC, 2014.

of $PMIH_2PO_4$ to the H_3PO_4/PBI complex provides additional hydrogen bonds for faster proton transport to occur. As the quantity of IL is increasing in the H_3PO_4/$PMIH_2PO_4$/PBI composite membranes, the diffusion coefficient of proton is increasing. And the highest diffusion coefficient of proton 0.5×10^{-6} cm^2s^{-1} at 180°C is observed with the molar ratio of 2/4/1 in H_3PO_4/ $PMIH_2PO_4$/PBI.

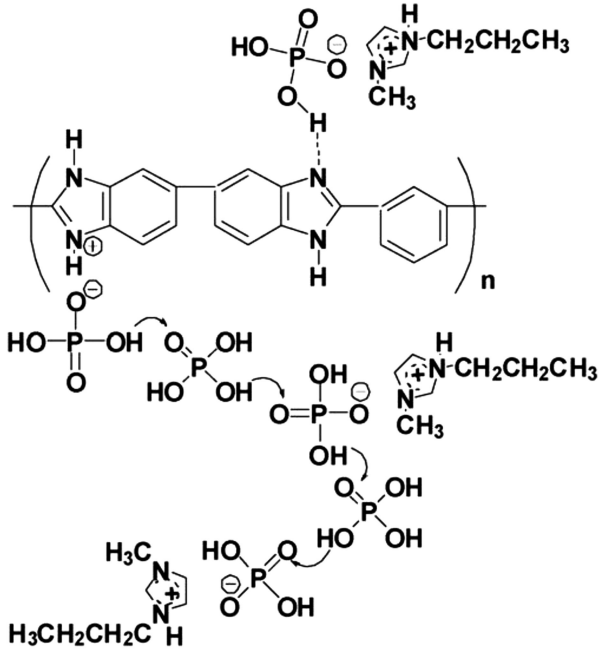

Figure 11. Scheme of the proton conduction mechanism in the H_3PO_4/$PMIH_2PO_4$/PBI membranes under anhydrous conditions. (Reproduced with permission from Reference (37). Copyright 2008 Elsevier publications.)

Conclusions

Important key issues regarding the working of PEMFCs, and limitations of PFSA based PEMFCs include hydration levels, CO poisoning, and hydrogen. To overcome these limitations, high temperature PEMs for operation above 120°C required and are currently under active development. This review gives an idea of the high temperature PEMs operating above 100°C, focusing on ILs, as well as the ionic conductivities (ICs) and thermal stabilities (TSs) of IL-polymer composite membranes. The best polymer-IL composite membranes with the maximum available ICs and high TSs are presented. The effect of casting methods on the ICs and TSs of the IL-polymer composites is also discussed. The conduction through the IL-polymer composite membranes is mainly occurred via a 3-dimensional network of hydrogen bonds. Overall the ILs-polymer composite membranes do provide an ordered ionic domain phase to improve the ionic transport.

In Polymer Composites for Energy Harvesting, Conversion, and Storage; Li, L., et al.;
ACS Symposium Series; American Chemical Society: Washington, DC, 2014.

Acknowledgments

S.V.S. greatly appreciated the reviewers and editors for their constructive criticisms and comments in bringing out this chapter.

References

1. Li, Q.; Jensena, J O.; Savinell, R. F.; Bjerruma, N. J. *Prog. Polym. Sci.* **2009**, *34*, 449–477.
2. Herring, A. H. *J. Macromol. Sci. Part C: Polym. Rev.* **2006**, *46*, 245–296.
3. Li, Q.; He, R.; Jensen, J. O.; Bjerrum, N. J. *Chem. Mater.* **2003**, *15*, 4896–4915.
4. Grubb, W. T. *J. Phys. Chem.* **1959**, *63* (1), 55–58.
5. Grubb, W. T.; Niedrach, L. W. *J. Electrochem. Soc.* **1960**, *107*, 131.
6. This image is a work of a United States Department of Energy (or predecessor organization) employee, taken or made as part of that person's official duties. As a work of the U.S. federal government, the image is in the public domain.
7. Page, K. A.; Rowe, B. W. In *Polymers for Energy Storage and Delivery: Polyelectrolytes for Batteries and Fuel Cells*; ACS Symposium Series 1096; American Chemical Society: Washington DC, 2012; pp 147−164.
8. Hickner, M. A.; Pivovar, B. S. *Fuel Cells.* **2005**, *5* (2), 213–229.
9. Rikukawa, M.; Sanui, K. *Prog. Polym. Sci.* **2000**, *25*, 1463–1502.
10. Smitha, B.; Sridhar, S.; Khan, A. A. *J. Membr. Sci.* **2005**, *259*, 10–26.
11. Kreuer, K-D.; Paddison, S. J.; Spohr, E.; Schuster, M. *Chem. Rev.* **2004**, *104*, 4637–4678.
12. Zawodzonski, T. A.; Neeman, M.; Sillerud, L. O.; Gottesfeld, S. *J. Phys. Chem.* **1991**, *95*, 6040.
13. Schuster, M. F. H.; Meyer, W. H. *Annu. Rev. Mater. Res.* **2003**, *33*, 233–261.
14. Oetjen, H.-F.; Schmidt, V. M.; Stimming, U.; Trila, F. *J. Electrochem. Soc.* **1996**, *143*, 3838.
15. Xiao, G.; Li, Q.; Hjuler, H. A.; Bjerrum, N. J. *J. Electrochem. Soc.* **1995**, *142*, 2890.
16. U.S. Department of Energy; *Hydrogen and Fuel Cells Program*; http://www.hydrogen.energy.gov/.
17. *Research and Development of Fuel Cells for Stationary and Transportation Applications*; http://web.mit.edu/mitei/docs/rfp-pdf/DE-FOA-0000360.pdf.
18. Nakamoto, H.; Watanabe, M. *Chem. Commun.* **2007**, *24*, 2539.
19. Mecerreyes, D. *Prog. Polym. Sci.* **2011**, *36*, 1629–1648.
20. Kreuer, K.-D. *Chem. Mater.* **1996**, *8*, 610–641.
21. Jalani, N. H.; Dunn, K.; Datta, R. *Electrochim. Acta* **2005**, *51*, 553–560.
22. Armand, M.; Endres, F.; MacFarlane, D. R.; Ohno, H.; Scrosati, B. *Nat. Mater.* **2009**, *8*, 621–629.
23. Sambasivarao, S. V.; Acevedo, O. *J. Chem. Theory Comput.* **2009**, *5*, 1038–1050.
24. MacFarlane, D. R.; Forsyth, M.; Howlett, P. C.; Pringle, J. M.; Sun, J.; Annat, G.; Neil, W.; Izgorodina, E. I. *Acc. Chem. Res.* **2007**, *40*, 1165–1173.
25. Han, X.; Armstrong, D. W. *Acc. Chem. Res.* **2007**, *40*, 1079–1086.

26. Van Rantwijk, F.; Sheldon, R. A. *Chem. Rev.* **2007**, *107*, 2757–2785.
27. Lodge, T. P. *Science.* **2008**, *321*, 50–51.
28. Zhang, Z. C. *Adv. Catal.* **2006**, *49*, 153–237.
29. Allen, C.; Sambasivarao, S. V.; Acevedo, O. *J. Am. Chem. Soc.* **2013**, *135* (3), 1065–1072.
30. Fuller, J.; Breda, A. C.; Carlin, R. T. *J. Electrochem. Soc.* **1997**, *144*, L67–L70.
31. Susan, M. A. B. H.; Kaneko, T.; Noda, A.; Watanabe, M. *J. Am. Chem. Soc.* **2005**, *127*, 4976–4983.
32. Padilha, J. C.; Basso, J.; Trindade, L. G.; Martini, E. M. A.; de Souza, M. O.; de Souza, R. F. *J. Power Sources* **2010**, *195*, 6483–6485.
33. Doyle, M.; Choi, S. K.; Proulx, G. *J. Electrochem. Soc.* **2000**, *147* (1), 34–37.
34. Li, H.; Jiang, F.; Di, Z.; Gu, J. *Electrochimica Acta* **2012**, *59*, 86–90.
35. Sekhon, S. S.; Krishnan, P.; Singh, B.; Yamada, K.; Kim, C. S. *Electrochimica Acta* **2006**, *52*, 1639–1644.
36. Kim, S. Y.; Kim, S.; Park, M. J. *Nat. Commun.* **2010**, *1*, 88.
37. Ye, H.; Huang, J.; Xu, J. J.; Kodiweera, N. K. A. C.; Jayakody, J. R. P.; Greenbaum, S. G. *J. Power Sources* **2008**, *178*, 651–660.
38. Park, J-S.; Shin, M-S.; Sekhon, S. S.; Choi, Y-W.; Yang, T-H. *J. Korean Electrochem. Soc.* **2011**, *14* (1), 9–15.
39. Rubatat, L.; Rollet, A. L.; Gebel, G.; Diat, O. *Macromolecules* **2002**, *35*, 4050–4055.
40. Chen, H.; Choi, J. H.; Cruz, D. S. l.; Winey, K. I.; Elabd, Y. A. *Macromolecules* **2009**, *42*, 4809–4816.

Chapter 6

Metal-Ligand Based Anion Exchange Membranes

M. S. Pawar,[1] Y. Zha,[1] M. L. Disabb-Miller,[2] Z. D. Johnson,[2] M. A. Hickner,[2] and G. N. Tew*,[2]

[1]Department of Polymer Science and Engineering, University of Massachusetts, Amherst, Massachusetts 01003, United States
[2]Department of Materials Science and Engineering, The Pennsylvania State University, University Park, Pennsylvania 16802, United States
***E-mail: tew@mail.pse.umass.edu.**

Metal-containing polymers made with a range of metals, ligands, counterions and with different morphologies have been previously studied for their magnetic, opto-electronic and thermochromic properties. Presently, we are exploring the potential of transition metal-terpyridine-based complexes as polyelectrolytes for fuel cell membranes. A water soluble Ruthenium (II) bisterpyridine complex was covalently connected to a norbornene monomer and copolymerized with dycyclopentadiene (DCPD) *via* ring-opening metathesis polymerization (ROMP) to prepare a crosslinked membrane. Unlike traditional organic cations, the metal center in this membrane has two associated counterions. This system was also studied for its conductivity and chemical, thermal and mechanical stability. The conductivity, thermal stability and mechanical properties exhibited by these membranes were comparable to the conventional organic cations. These membranes demonstrated good alkaline stability and methanol tolerance. This study suggests that metal-ligand-based anionic exchange membranes (MLAEMs) represent an entirely new class of materials.

In Polymer Composites for Energy Harvesting, Conversion, and Storage; Li, L., et al.; ACS Symposium Series; American Chemical Society: Washington, DC, 2014.

Background

Metallosupramolecular Polymers

Organic polymers are used in a wide variety of applications because of their simple processing and fabrication, outstanding mechanical properties and straightforward synthetic approaches, which make elaborate architectures like block, star and dendritic architectures possible (*1*). Progress of the characterization techniques along with the improvements in synthetic routes for inorganic analogues make integration of inorganic components into macromolecular frameworks increasingly possible. Inorganic-organic hybrid polymer architectures give rise to increased functionality, complex morphologies and novel materials with tailored properties. The development of metallosupramolecular polymers which employ metal ligand interactions has been important in this regard. Incorporation of metal centers into polymers allows for diverse and hitherto inaccessible optical, redox, magnetic, electro and thermochromic properties while using conventional methods of polymer processing (*2*). Unlike organic polymers, which only have covalent or static bonding between carbon and other atoms, the principal advantage of metal-ligand interactions is their flexible and directional bonding characteristics (*3*). This is due to the difference in the kinetic and thermodynamic stabilities of different metal-ligand interactions which gives rise to either static or dynamic interactions between the metal and the ligands. Thus, kinetically inert or labile complexes differing only in oxidation states can be formed and reversible switching between these two states is possible (*4*). In addition, the complexes' properties can be tuned by appropriate selection of the metal ion, the ligands, and the corresponding counterion.

The metal ion can be chosen from the first row, transition, or lanthanide metals and with a multitude of ligands available for chelation, the opportunities for the design of metal-ligand complexes with tailored properties are endless. The variation in the size of the metal ion produces different responses to stimuli like pH and temperature. The ligands determine the strength and therefore the reversibility of interactions. The counterion affects the interaction of the complex with the surrounding molecules thus determining the solubility (*5*). In contrast to carbon, which has a maximum coordination number of four and is thus limited to either square planar or tetrahedral geometries, the array of co-ordination numbers and consequently the plethora of geometries available in the case of metallopolymers produce a cornucopia of properties (*1*). This can lead to a variety of novel structural, conformational and morphological features, which are difficult to attain in conventional purely organic polymers.

2,2′:6′,2″-terpyridine and other functionalized terpyridines have been ubiquitously used as ligands for metal complexation in many metallopolymers due to their strong binding to transition metal ions, reversibility on response to stimuli, and beneficial bonding geometries. This makes them interesting ligands for the fabrication of functional materials (*3*, *6*). The metals in the polymers can be positioned in the main chain or the side chain giving polymers with different architectures like linear, dendritic, heteroarmed etc. Metallosupramolecular

In Polymer Composites for Energy Harvesting, Conversion, and Storage; Li, L., et al.;
ACS Symposium Series; American Chemical Society: Washington, DC, 2014.

polymers generally contain terpyridines as chain extenders by having polymers end-functionalized with terpyridine in the main chain. Additionally, diblock and triblock copolymers with novel star and heteroarm architectures can be made by using functionalized terpyridine as radical initiators for living and controlled polymerizations (*7*, *8*). Dendrimers with metal complexes in the core, on the surface, and throughout the structure have also been researched extensively for catalytic and biomedical applications (*9–11*). The metals can also be incorporated in the side chain of the polymer by use of terpyridine-functionalized monomers containing a polymerizable functional group. Previous systems developed using this method lacked controlled molecular weight distributions and architectures (*12*). A lot of research has been done since then (*13–15*) to obtain precise functional control using different polymerization techniques.

Our lab has synthesized methylmethacrylate-based random copolymers and amine functionalized metal complexes with terpyridine units incorporated into the side chain for obtaining structures with tunable properties (*16*, *17*, *41*). We also reported block copolymers made with living controlled radical polymerization routes like ATRP, RAFT, NMP as well as with indirect post-polymerization strategies using activated esters. These strategies overcame the difficulties encountered in traditional synthesis and characterization (*18*). These techniques produced controlled molecular weights and molecular weight distributions. Also, for the first time, the metal ligand complexes were localized to only one block of the polymer. In another first, terpyridine functionalized poly(methylmethacrylate)-based copolymers were complexed with different lanthanide ions to create lanthanide alloys with reversible thermochromism for potential use as sensors (*19*). These polymeric complexes were also used to synthesize a soluble and processable true white light emitting system and access a range of colors by simple variation of metal-ligand ratios (*20*). Most recently, we reported unique cyclic metallosupramolecular brushes and cyclic polymer-transition metal gels with characteristic reversibility under certain stimuli (*21*). All this work emphasized the advantages of metallosupramolecular chemistry to provide a robust platform for the design of functional materials by controlled synthesis techniques. This has opened up exciting new avenues for using metallosupramolecular polyelectrolytes as membranes for fuel cells (*22*).

Anion Exchange Membranes

Anion exchange membranes (AEMs) have become indispensable in a variety of practical applications like the desalination and deionization of water, electro dialysis, etc (*23*). They help overcome the drawbacks of liquid electrolyte fuel cells such as carbon dioxide intolerance, electrolyte degradation and electrode weeping by virtue of their anchored cationic moieties (*24*). In contrast to proton exchange membranes (PEMs), the AEMs can function efficiently with oxygenated hydrocarbon fuels due to the facile electrokinetics at both the electrodes. The non-noble metal catalyst stability at high pH also eliminates the need to use noble metal catalysts at high loadings. In addition to cost reduction, high power output and energy density are accomplished as a result of the reduced mixed potential and mass transport losses due to direction of the flow of hydroxide ions. Unlike

PEMs, the flow of hydroxide ions opposes the direction of the flow of water, which reduces the mixed potential engendered by fuel crossover and the severe flooding of the cathode due to electroosmosis of water (*24*).

A majority of the AEMs reported in the literature possess monovalent benzyl trimethyl ammonium functional groups incorporated into the polymers such as quaternized poly(ether-imide) (*25*), poly(arylene ether sulfone) (*26*), poly(phenylene oxide) (*27*), radiation induced grafted polymers (*28*) and crosslinked cyclic olefin networks (*29*). Their degradation poses a significant problem to the mechanical and chemical stability of the membranes at high alkalinity, particularly at operating temperatures of 80 °C (*30*, *31*).

Attempts to overcome this hurdle, along with obtaining higher conductivity, have led to several different approaches. Block copolymers have been synthesized to induce microphase separation, which leads to the formation of continuous ionic channels in one phase and a hydrophobic second phase that improves the mechanical stability of the membranes (*32*). Recently, Coates *et. al.* (*29*) reported a tetra-ammonium functionalized crosslinked membrane that facilitated continuous ionic domains and high ionic content without the undesirable effect of excessive swelling. This helped maintain a high concentration of ions in the membrane while bolstering its mechanical stability. Efforts have also been directed to incorporate alternative cationic groups like guanidinium (*33*), sulphonium (*34*), pyridinium (*35*), phosphonium (*36*), and imidazolium (*37*) into the membranes. These membranes have exhibited better hydroxide ion conductivity owing to their high basicity and greater water affinity along with enhanced thermal and chemical stability. The primary limitation of these membranes, however, is that they all consist of monovalent organic cation centers which can only associate with one ion per group. The intrinsic ability of multivalent charged metal cations to associate with multiple anionic groups can potentially increase the ion exchange capacity of the membrane leading to increase in its ionic conductivity.

Bis(terpyridine) Ru(II) complexes are thermal and pH stable (*38*). The redox potentials of these complexes are well outside the limit of redox potentials of fuel cell (*39*). Therefore, the chance of them being degraded by the redox processes occurring within the cell is very rare. These complexes have a divalent charged metal ion center with two counter ions associated with it. Additionally, with Cl^- as a counterion, instead of the hydrophobic counterions like PF_6^- and BF_4^- (*40*), the complex becomes soluble in water. This facilitates the requisite ion exchange to bicarbonate and hydroxide ions to prepare the respective ion conducting AEMs. The augmented water solubility imparts hydrophilic character to the membrane, which contributes to the high ionic conductivity of the AEM. Crosslinking preserves the mechanical integrity of the membrane while mitigating the effect of the swelling due to the high water uptake (*29*).

In this chapter, hydrophilic, crosslinked AEMs containing a bis(terpyridine) Ru (II) complex and a hydrophobic crosslinker with different compositions are described. The membranes were made using ring-opening metathesis polymerization (ROMP) and characterized in an attempt to meet the requirements of a good AEM such as high conductivity, good chemical and thermal stability and low fuel crossover.

In Polymer Composites for Energy Harvesting, Conversion, and Storage; Li, L., et al.;
ACS Symposium Series; American Chemical Society: Washington, DC, 2014.

Experimental

Materials and Instrumentation

All materials were used without further purification unless otherwise specified. Lithium aluminum hydride was purchased from Acros Organics. Dimethyl sulfoxide (DMSO), 2,2′:6′,2″-terpyridine, 4′-chloro-2,2′:6′,2″-terpyridine, Ruthenium chloride hydrate ($RuCl3 \cdot 3H_2O$), and *N*-ethylmorpholine were purchased from Alfa Aesar. Tetrahydrofuran (THF), chloroform, dichloromethane (DCM), acetone, methanol, anhydrous diethyl ether, ethyl acetate, anhydrous sodium sulfate (Na_2SO_4), hydrochloric acid (HCl), potassium hydroxide (KOH), sodium hydroxide (NaOH), and sodium bicarbonate ($NaHCO_3$) were purchased from Fisher Scientific. THF and DCM were distilled over Na^0/benzophenone and CaH_2 prior to use, respectively. The *exo*-5-norbornene-2-carboxylic acid and Grubbs' 2nd generation catalyst (G2) were purchased from Sigma-Aldrich. Dicyclopentadiene (DCPD) was purchased from Acros Organics and was run through a short alumina column prior to use. Deuterated methanol, DMSO and chloroform for NMR spectroscopy were purchased from Cambridge Isotope Laboratories, Inc.

The Bruker DPX-300 MHz spectrometer was used to record the ^1H and ^{13}C NMR spectra. All chemical shifts were expressed in δ (ppm) and referenced to residual solvent protons as the internal standard. The abbreviations for splitting patterns are the following: s, singlet; br s, broad singlet; d, doublet; dd, doublet of doublets; t, triplet; q, quartet; m, multiplet. The ultraviolet-visible (UV-Vis) spectra were recorded using a PerkinElmer Lambda 25 UV/Vis Spectrometer, calibrated with spectroscopic grade acetonitrile.

Synthesis of *exo*-5-Norbornene-2-methanol (2)

Compound **2** (Figure 1) was prepared by dissolving Compound **1** (2.76 g, 20.0 mmol) into 70mL THF in a round bottom flask having an outlet needle connected to an oil bubbler. 12.5 mL of lithium aluminum hydride was then added to it dropwise under ice cold conditions after which the reaction mixture was allowed to warm to room temperature and stir overnight. Excess Lithium aluminum hydride was removed by reacting it with 150 mL of 1M hydrochloric acid, which was added dropwise under ice cold conditions. The solvent was removed under reduced pressure and the product was subsequently extracted in chloroform. The chloroform layer was then dried over Na_2SO_4 and removed by rotary evaporation to obtain a clear liquid product. Yield: 2.03 g (16.3 mmol, 82%). ^1H NMR ($CDCl_3$): δ 6.09 (m, 2H), 3.70 (q, 1H), 3.55 (q, 1H), 2.82 (s, 1H), 2.75 (s, 1H), 1.61 (m, 1H), 1.42 (s, 1H), 1.36-1.21 (m, 3H), 1.10 (m, 1H). ^{13}C NMR ($CDCl_3$): δ 136.81, 136.46, 67.54, 44.96, 43.24, 41.86, 41.51, 29.51. EI-MS (m/z): $[M]^+$ calculated for $C_8H_{12}O$, 124.2; found, 124.1.

In Polymer Composites for Energy Harvesting, Conversion, and Storage; Li, L., et al.;
ACS Symposium Series; American Chemical Society: Washington, DC, 2014.

Synthesis of the Terpyridine-Functionalized Monomer (3)

In a round bottom flask, compound **2** (1.85 g, 14.94 mmol) was dissolved in a suspension of KOH in 20 mL DMSO at 80 °C. In another flask, 4′-chloro-2,2′:6′,2″-terpyridine (2.00 g, 7.47 mmol) was dissolved in 20 mL DMSO by preheating the solution to 80 °C and the two solutions were then added together and continued to stir for 48 hours. The color of the mixture turned brownish red immediately on mixing and continued to darken further for the duration of the reaction. The reaction mixture was cooled to room temperature and then poured in ice cold water. The resultant precipitated white solid was filtered and washed with water. Recrystallization from methanol gave pure product. Yield: 1.68 g (4.73 mmol, 63%). ^{1}H NMR ($CDCl_3$): δ 8.69 (m, 2H), 8.62 (m, 2H), 8.02 (s, 2H), 7.85 (m, 2H), 7.33 (m, 2H), 6.14 (m, 2H), 4.29 (q, 1H), 4.12 (t, 1H), 2.90 (s, 2H), 1.96 (m, 1H), 1.40-1.28 (m, 4H). ^{13}C NMR ($CDCl_3$): δ 167.34, 157.05, 156.18, 149.04, 136.92, 136.84, 136.44, 123.83, 121.38, 107.40, 72.40, 45.14, 43.75, 41.68, 38.47, 29.59. FAB-MS (m/z): $[M + H]^+$ calculated for $C_{23}H_{21}ON_3$, 356.4; found, 356.3. UV/Vis (Acetonitrile): λ_{max} = 277, 240 nm.

Synthesis of Mono-terpyridine Ru(III) Complex Functionalized Monomer (4)

Compound **4** was prepared by refluxing a solution of Compound **3** (1.07g, 3.00 mmol) in 200 mL methanol, after which an equimolar quantity of $RuCl_3$. $3H_2O$ was added to it. Overnight refluxing of the solution was carried out and the resultant mixture cooled to -20 °C. The mixture was then filtered, washed with ice cold water and diethyl ether and the resulting brown precipitate collected, yielding 1.60g of product. ^{1}H NMR (DMSO-d_6): δ 6.23 (s, 2H), 3.88 (br, 2H), 3.24 (s, 1H), 2.92 (s, 1H), 1.62-1.46 (m, 5H), 0.41 (s, 2H). ^{13}C NMR (DMSO-d_6): δ 137.11, 136.44, 134.00, 45.48, 42.92, 41.22, 28.24. FAB-MS (m/z): $[M + H]^+$ calculated for $C_{23}H_{21}ON_3RuCl_3$, 563.9; found, 564.3. UV/Vis (Acetonitrile): λ_{max} = 394, 276 nm.

Synthesis of the Bis(terpyridine)Ru(II) Complex-Functionalized Monomer (5)

A solution of compound **4** (0.84 g, 1.5 mmol) and an equivalent amount of 2,2′:6′,2″-terpyridine (0.35 g, 1.5 mmol) was dissolved in 100 mL methanol and refluxed for half an hour after which an excess of *N*-ethylmorpholine (1 mL, 7.95 mmol) was added to it. The solution changed color from orange to red after this addition and was refluxed overnight. The solvent was then removed under reduced pressure and the solid partitioned between 100 mL of chloroform and water. The aqueous layer was removed by rotary evaporation after washing it three (3*50mL) consecutive times with chloroform. The resultant product was dried and obtained as a red powder with a yield of 1.30 g. ^{1}H NMR (Methanol-d_4): δ 8.96 (d, 2H),

8.74 (m, 4H), 8.65, (s, 2H), 8.45 (t, 1H), 8.02-7.94 (m, 4H), 7.56 (m, 2H), 7.41, (m, 2H), 7.32-7.21 (m, 4H), 6.25 (m, 2H), 4.70 (q, 1H), 4.55 (t, 1H), 4.04 (br, 2H), 3.81 (br, 2H), 3.48 (br, 2H), 3.24 (q, 2H), 3.12 (br, 2H), 3.08 (s, 1H), 3.00 (s, 1H), 2.15 (m, 1H), 1.65-1.49 (m, 4H), 1.38 (t, 3H). ^{13}C NMR (Methanol-d_4): δ 168.39, 159.91, 159.88, 157.45, 157.43, 153.55, 153.29, 139.45, 139.34, 138.45, 137.44, 136.81, 129.06, 128.98, 126.07, 125.81, 125.09, 112.56, 75.83, 65.25, 53.73, 52.74, 46.19, 45.24, 43.17, 40.03, 30.71, 9.42. FAB-MS (m/z): [M - *N*-ethylmorpholinium chloride - Cl]$^+$ calculated for $C_{44}H_{46}O_2N_7RuCl_3$, 725.2; found, 724.9. UV/Vis (Acetonitrile): λ_{max} = 482, 307, 269.

Synthesis of Bisterpyridine Ruthenium(II) Complex-Based Anion Exchange Membranes

Following is the procedure for the synthesis of a representative AEM:

Compound **5** and DCPD were dissolved in a chloroform/MeOH co-solvent mixture in a vial. In another vial, the G2 catalyst was dissolved in chloroform. The catalyst was subsequently added into the first vial and the mixture was stirred thoroughly for about one minute. It was then transferred onto a flat, smooth aluminum pan preheated to 40 °C (diameter ~ 4 cm, depth ~ 1 cm). The pan was covered with a glass disk with greater diameter than the pan itself to control the rate of evaporation. For complete evaporation, the glass disk was removed after an hour and the pan was then heated to around 70 °C for another hour. After cooling, the membrane was removed from the pan, immersed consecutively in 100%, 70 vol %, and 30 vol % aqueous MeOH solutions for 6 hours each before finally transferring into deionized, degassed water. It was soaked in DI water for a period of atleast 24 hours with consecutive washing every three hours to ensure complete removal of the byproduct *N*-ethylmorpholinium chloride. Table 1 shows the different ratios of monomer to crosslinker and the amount of catalyst used to obtain membranes with the desired IECs.

Table 1. Quantities of Monomer, Crosslinker, and Catalyst Used in the Membranes of Different Composition

*Ratio **5**:DCPD*	*IEC*	*Monomer **5** (mmol)*	*Monomer **5** (gms)*	*DCPD (mmol)*	*DCPD (gms)*	*G2[a] (mmol)*	*G2[a] (gms)*
1:10	1.0	0.053	0.048	0.53	0.070	0.0011	0.0009
1:5	1.4	0.076	0.069	0.38	0.05	0.0015	0.0013
1:2	2.0	0.112	0.102	0.224	0.030	0.0022	0.0019

[a] Amount of G2 catalyst calculated on the basis of structures of the monomers.

Synthesis of AEMs in Bicarbonate Form by Ion Exchange

The AEMs in the chloride form were ion exchanged to the bicarbonate form by soaking them overnight in a 1 M Sodium bicarbonate solution and subsequently washed with DI water for three hours each, three consecutive times to remove any excess ions.

Measurement of AEM Ionic Conductivity

AC impedance spectroscopy with a Solartron SI 1260A Impedance/Gain-Phase Analyzer (Oak Ridge,TN) was performed on the samples for ionic conductivity measurements. Two-point in-plane geometry at frequencies ranging from 1MHz to 100 Hz with a 10 mV AC excitation was used to measure the impedance of free standing membranes. The humidity was varied from 22% to 95% while the oven temperature was held constant at 30 °C. An Espec SH-241 (Osaka, Japan) humidity chamber was used to control humidity and a digitally controlled water bath (VWR International LLC, Radnor, PA) was used to control temperature during conductivity measurements. The impedance data is modeled on an ideal resistor or parallel capacitor-resistor circuit and the resistance of the membrane was calculated from the intersection of the impedance plot with the real axis.

Ionic conductivity (σ) was calculated by the following formula:

$$\sigma = \frac{l}{RA}$$

where R is the resistance of the membrane, l = length between electrodes and A is the cross sectional area of the membrane available for ionic current.

To measure the bicarbonate conductivity, AEMs in chloride form were ion exchanged by immersing in sodium bicarbonate solution overnight and rinsed thoroughly to remove excess ions. For hydroxide conductivity measurements, the membranes were immersed in 1M NaOH solution for one hour followed by extensive washing with degassed 18.5 MΩ water for removal of excess ions. The conductivity measurements were then done by placing the membranes in conductivity cells that were immersed in degassed water blanketed with flowing argon. The conductivity was measured with the blanketed argon flow for three hours after which the flow was stopped and the membranes exposed to atmospheric CO_2 for the rest of the duration of the conductivity measurement.

Measurement of AEM Alkaline Stability

Monomer **5** was dissolved in 1M NaOH or 10M KOH aqueous solution and heated to 80 °C over time. An AEM in the bicarbonate form with IEC = 1.4 was also soaked in 10M KOH or 1M NaOH aqueous solution for 48 hours and the UV-Vis spectra of both the monomer and the membrane was recorded at different times.

In Polymer Composites for Energy Harvesting, Conversion, and Storage; Li, L., et al.;
ACS Symposium Series; American Chemical Society: Washington, DC, 2014.

Measurement of AEM Water Uptake

For measuring water uptake as a function of relative humidity, the membranes were weighed on a Mettler-Toledo AB304-S/FACT (Columbus, Ohio) scale at different relative humidities ranging from 22% to 95% at 30 °C. The Espec SH-241 (Osaka, Japan) humidity chamber was used to control the humidity and temperature. The liquid water uptake measurements were done by taking a fully swollen membrane out of water, blotting out the excess surface water and weighing them immediately. Accurate sample mass was obtained by soaking the samples in water for 5-10 minutes for complete rehydration and the measurement was repeated 3-5 times. The membranes were then heated overnight at 50 °C in vacuum to dry them out completely and weighed again. The water uptake was calculated using the following formula:

$$\text{Water uptake} = \frac{m_{dry} - m_{wet}}{m_{dry}}$$

m_{dry} is the weight of the dry membrane and m_{wet} is the weight of the wet membrane.

The water uptake of the membranes in the chloride forms for the IEC = 1.0, 1.4, 2.0 was 368, 78, 28 wt% respectively. The water uptake of these membranes in the bicarbonate forms was 410, 102, 27 wt% respectively.

Measurement of AEM Dimensional Swelling

Three samples with specific dimensions (0.6cm*0.6cm*100μm) were cut from an AEM in bicarbonate form when fully swollen in water. The samples were introduced in different concentrations (2M, 6M, 10M) of methanol solutions preheated to 80 °C and their length, breadth and height measured immediately after heating them for two hours in these solutions. These three samples from each AEM were used to calculate the average dimensional swelling ratios.

Measurement of Membrane Mechanical Properties

Dynamic mechanical analysis (TA instruments DMA Q800) was used to characterize the AEMs in the bicarbonate form at room temperature. For complete hydration, the membranes were immersed in water for at least 24 hours and then tested immediately after being removed from the water. The tensile test was done at a preload force of 0.01 N, soak time of 5 min and a force ramp rate of 1N/min.

Results and Discussion

Synthesis

As shown in Figure 1, three straightforward and high yielding steps were used for making the monomer **5**. The product was easily purified from organic impurities by precipitation due to the presence of chloride counterions as opposed to the previously used non-coordinating counterions (*13*, *38*, *41*). The hydrophobic

In Polymer Composites for Energy Harvesting, Conversion, and Storage; Li, L., et al.;
ACS Symposium Series; American Chemical Society: Washington, DC, 2014.

counterions make the complex water insoluble and can decrease the water uptake of the membrane. The presence of the hydrophilic chloride counterion makes the complex water soluble and the membrane hydrophilic. The ion exchange capacity and therefore the conductivity of the membranes is directly proportional to the water uptake and hydrophilicity. The *N*-ethyl morpholinium chloride byproduct formed was also soluble in water and hence the separation of the byproduct was difficult. It was, however, achieved easily by washing it from the crosslinked membranes later. The main advantage of using this synthesis technique was that there was no need for the post-functionalization of the polymer to incorporate cationic groups, a general method employed for many AEMs (*42*, *43*), as the monomer already has the cationic metal centre present in it.

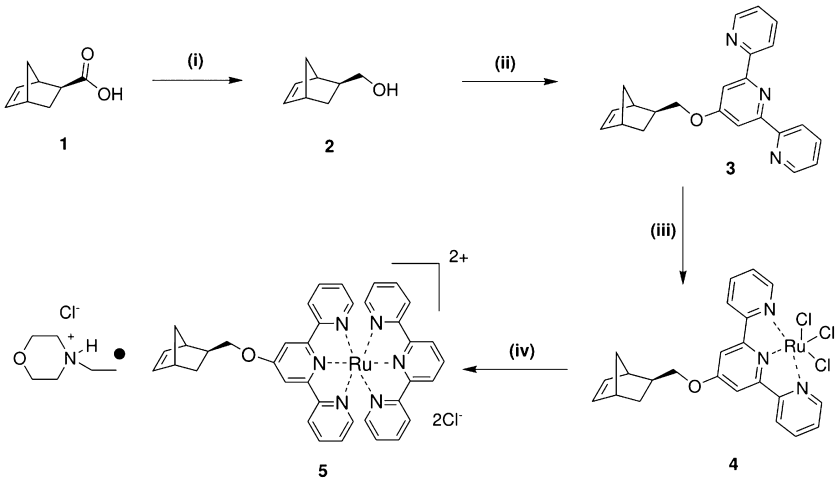

(i) Lithium aluminum hydride, THF, RT, overnight; (ii) 4'-chloro-2,2':6',2"-terpyridine, KOH, DMSO, 80°C, 48 hrs; (iii)$RuCl_3.3H_2O$, MeOH, reflux, 24h; (iv) 2,2':6',2"-terpyridine, N-ethylmorpholine, MeOH, reflux, 24h.

Figure 1. Synthesis of water-soluble Ruthenium (II) bis(terpyridine) based monomer ***5*** *with chloride counterions. (i) Lithium aluminum hydride, THF, RT, overnight; (ii) 4'-chloro-2,2':6',2"-terpyridine, KOH, DMSO, 80 °C, 48 hrs; (iii)* $RuCl_3.3H_2O$*, MeOH, reflux, 24h; (iv) 2,2':6',2"-terpyridine, N-ethylmorpholine, MeOH, reflux, 24h.*

ROMP was used for crosslinking the membranes using Grubb's second generation catalyst as it is fast and functional group tolerant. Since the technique is not air/moisture sensitive, the membrane casting process is greatly simplified by not having to maintain air or moisture free conditions for solvent casting. Figure 2 shows the membrane casting and crosslinking process for the synthesis of a crosslinked AEM. The membrane was cast by dissolving the monomer **5** and DCPD in a vial containing a mixture of chloroform/methanol. In another vial, the G2 catalyst was dissolved in chloroform, then added to the first vial and mixed

In Polymer Composites for Energy Harvesting, Conversion, and Storage; Li, L., et al.;
ACS Symposium Series; American Chemical Society: Washington, DC, 2014.

thoroughly for 1 minute before transferring it to a smooth aluminum pan. The pan was preheated to 40 °C and crosslinking continued until all the solvent evaporated to give a thin, translucent membrane. The byproduct *N*-ethylmorpholinium chloride was then removed from the membranes by soaking them in water and continuous rinsing every three hours for over two days. The disappearance of the C-O-C ring stretching vibration band at 1110 cm^{-1} confirmed the removal of the byproduct from the membrane by IR Spectroscopic analysis.

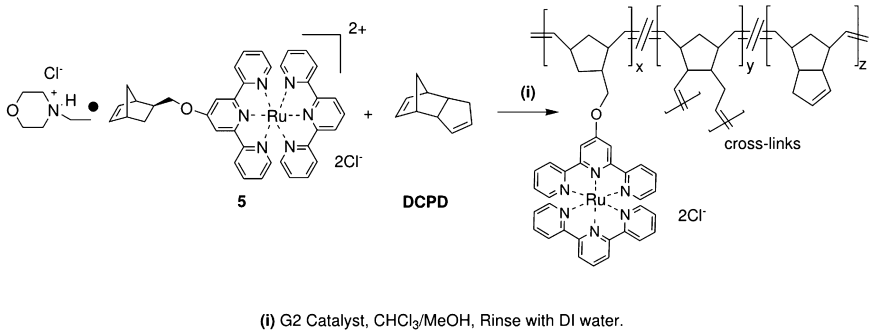

Figure 2. Synthesis of a representative AEM in chloride form. (i) G2 Catalyst, $CHCl_3$/MeOH, Rinse with DI water.

The membranes were made with different compositions with the aim of comparing their properties at different theoretical ion exchange capacities (IECs). The ion exchange capacity of the membrane is defined as the number of moles of ion exchangeable groups (n_{OH^-}) per unit dry mass of the polymer (m_{dry}). It is calculated by the following equation:

$$\text{Theoretical IEC} = \frac{n_{OH^-}}{m_{dry}}$$

Membranes about 105 ± 3 μm were prepared and characterized in their as prepared chloride, hydroxide as well as bicarbonate form.

Alkaline Stability

At cell operating temperatures of 80 °C, the alkaline stability of the complex and the membranes assumes special significance. Degradation of the quaternary ammonium complexes is known to occur in such conditions (*28*). UV-Visible spectroscopy was used to characterize the alkaline stability of the complex as it was a fast and easy way to monitor the stability of a solution by observing its spectrum over time. The complex was heated to 80°C in 1 M NaOH solution and the two ligand centered absorption peaks and the metal ligand charge transfer peak (~480 nm), characteristic to the ruthenium complex, were monitored over time.

In Polymer Composites for Energy Harvesting, Conversion, and Storage; Li, L., et al.;
ACS Symposium Series; American Chemical Society: Washington, DC, 2014.

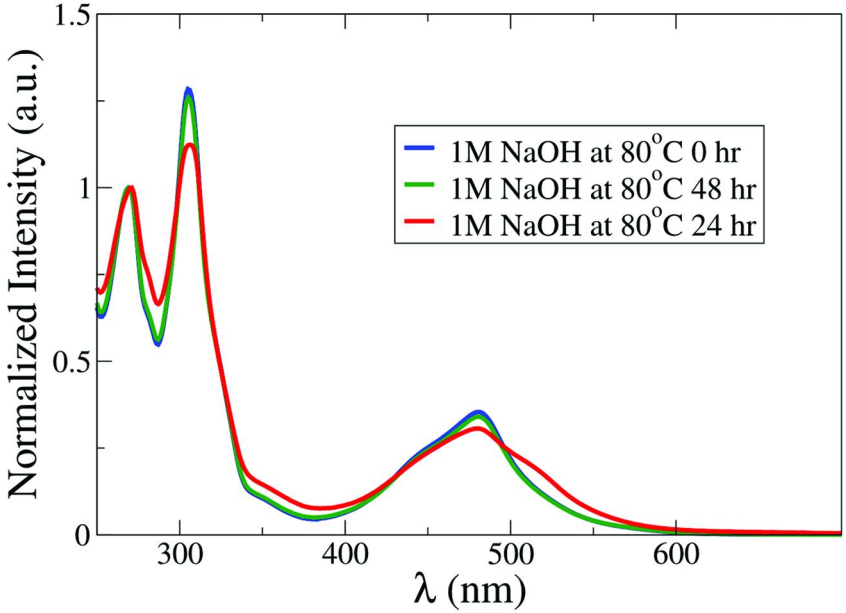

*Figure 3. UV-Vis spectra of monomer **5** in 1M NaOH aqueous solution over 48 hours at 80 °C. Intensity was normalized using the ligand-centered absorption peak at 270 nm.*

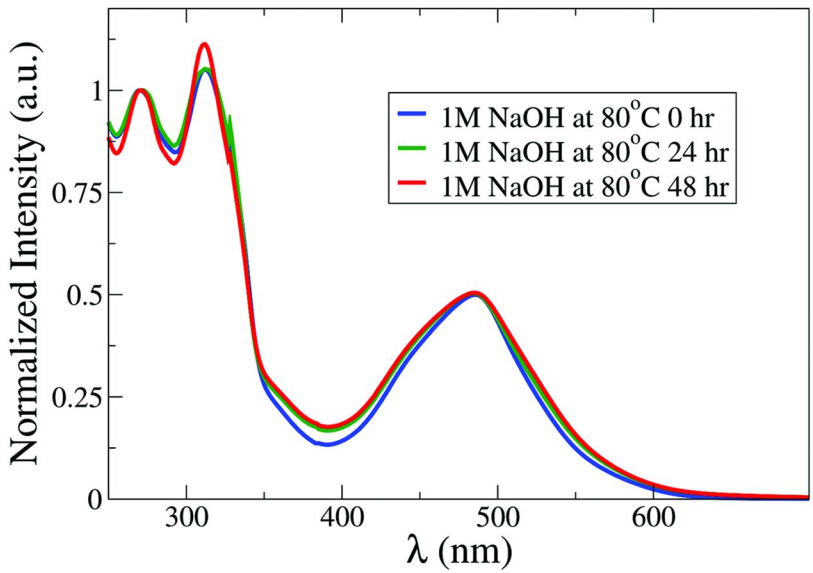

Figure 4. UV-Vis spectra of the AEM in bicarbonate form with IEC = 1.4 immersed in 1 M NaOH aqueous solution over 48 hours at 80 °C. Intensity was normalized using the ligand-centered absorption peak at 270 nm.

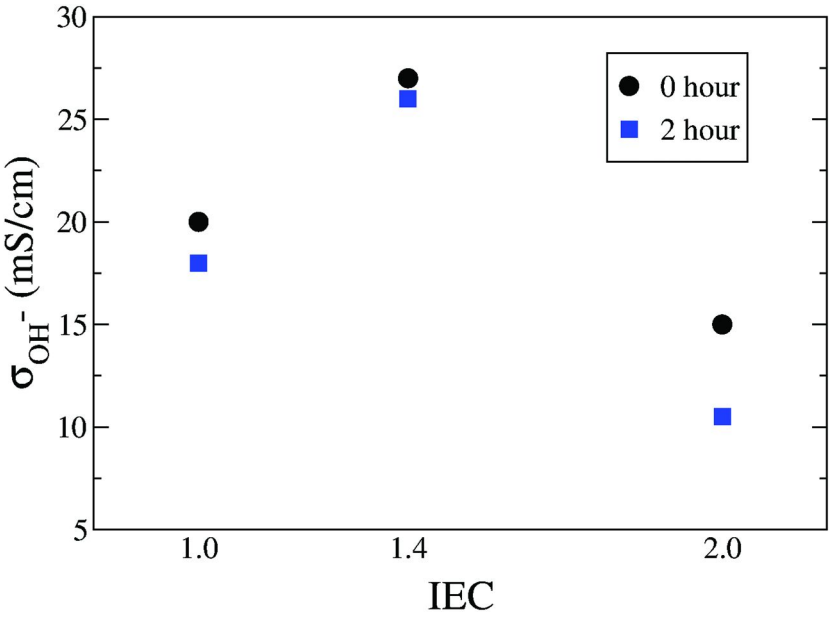

Figure 5. Variation of hyrdroxide conductivities of the samples when exposed to 1M KOH for 2 hours. Samples were exposed to liquid water and conductivities measured at 30 °C.

As shown in Figure 3, the spectrum did not undergo any major changes upon heating at 80 °C for upto 48 hours. The crosslinked membranes were also characterized by UV-Vis spectroscopy by converting them in bicarbonate form and heating them in 1M NaOH solution at 80 °C with the spectra taken over a period of 48 hours (Figure 4). The membranes were found to be stable with very little changes to the spectra over time. Figure 5 shows that the membranes also did not exhibit any considerable decline in their hydroxide conductivity when exposed to 1M KOH alkaline solutions for 2 hours.

In order to complement the chemical, mechanical, and thermal stability of the membranes, the issue of bicarbonate formation when the membranes are exposed to air or when the fuel is impure also needs to be addressed for good conductivity. The OH^- ions are rapidly converted to carbonate or bicarbonate ions on reaction with CO_2 in the fuel or atmosphere. This can lead to a reduced pH level in the cathode and alter the kinetics of oxygen reduction reaction or increase the cell resistance (*44*). Hickner and colleagues (*42*) have shown that there is a loss in the conductivity of the AEMs with exposure to air because of the conversion of the membranes to their bicarbonate form. This might be due to the inherent lower mobility of the HCO_3^- ions in solution. The hydroxide conductivities thus need

to be measured in an inert atmosphere to limit the formation of bicarbonate ions, which can lead to underestimation of the conductivities. Figure 6 shows the decline in conductivity of the membranes as an effect of the conversion to bicarbonate form from the hydroxide form. The conductivity declines sharply in the first two hours after exposure but upon complete conversion remains fairly constant. They also have similar conductivities to their corresponding membranes that have been ion exchanged to their bicarbonate form prior to testing. The effect of the bicarbonate conversion needs to be investigated in depth for the overall stability, power density and the performance of the fuel cell. For minimal CO_2 exposure from the atmosphere, the hydroxide conductivity measurements in this study were carried out under an active argon blanket. All the conductivity measurements on the membranes have been done on their bicarbonate forms.

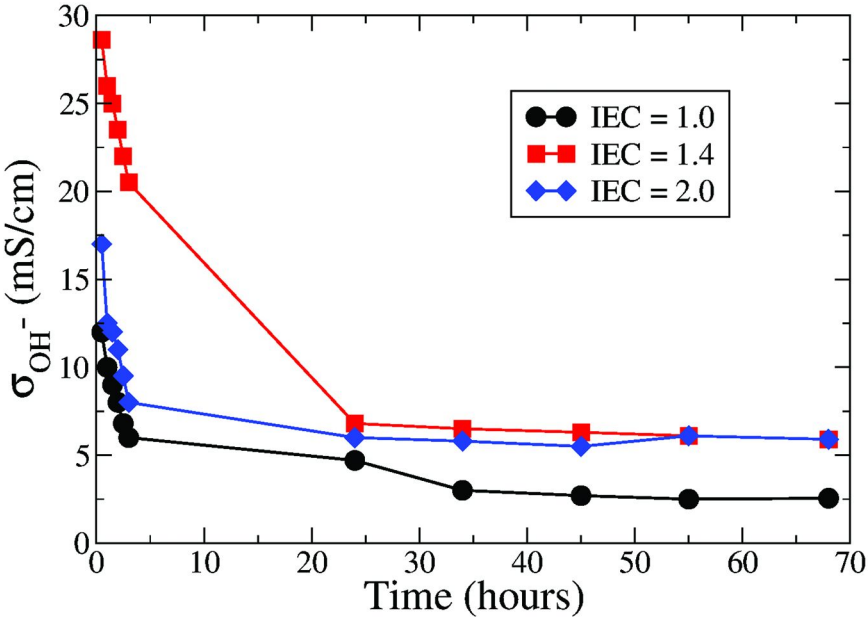

Figure 6. Decline in conductivity of the AEMs in hydroxide form when exposed to atmosphere over time. Samples were exposed to liquid water and conductivities measured at 30 °C.

The conductivity variation with repect to the relative humidity for a representative membrane with IEC = 2.0 is shown in Figure 7. As with the membranes reported in literature, the conductivities increased with the relative humidity (*45*).

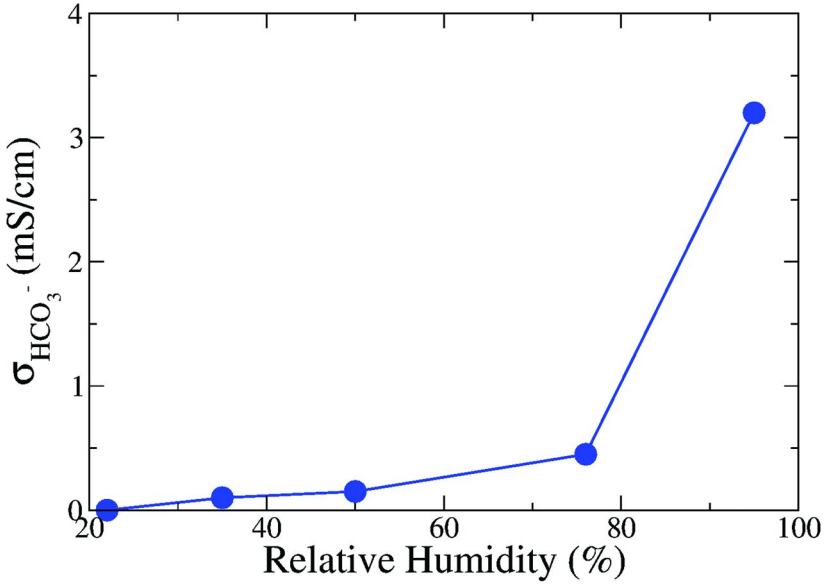

Figure 7. Dependence of the conductivity of an AEM with IEC = 1.8 on relative humidity at 30 °C.

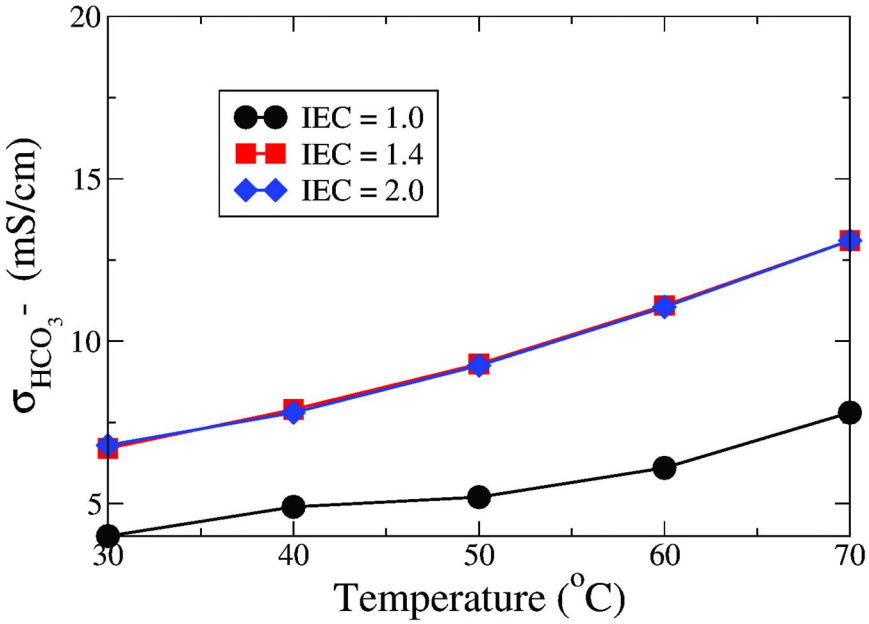

Figure 8. Dependence of conductivity on temperature for the AEMs in bicarbonate form. Samples were exposed to liquid water and conductivities measured at 30 °C.

With full hydration, all of the membranes showed linear increase in conductivity with an increase in temperature (*29*). As seen in Figure 8, the conductivities of the membranes with IEC = 1.4 and 2.0 are greater over the same range of temperatures than the ones with IEC= 1.0. This can be because the amount of hydrophobic crosslinker DCPD in the membranes with IEC = 1.0 is greater and consequently the water uptake is lower than the membranes with the other two compositions. The membranes with IEC = 1.4 and 2.0 show a bicarbonate conductivity of 9.8mS/cm at 50 °C. In comparison, AAEMs by Varcoe and Slade and Coates *et. al.* had bicarbonate conductivities of 22 mS/cm at 50°C (*29*, *46*). Thus, the AEMs reported here have comparable conductivities (10.1-25.7 mS/cm) (*42*) to the membranes based on other organic cations reported in literature.

The hydroxide to bicarbonate conductivity ratio of the membranes should be 4.4 based on dilute solution ion mobilites (*47*). The values were observed as expected for the membrane with IEC = 1.4 and were lower for the membrane with IEC = 1.0 presumably due to the lower water uptake and hence lesser ion mobility. The membrane with IEC = 2.0 showed lower conductivity ratios possibly because of the decrease in the ion concentration due to high water uptake thus, reducing the density of charge carriers (Figure 9). This showed that membranes should be prepared with optimum IECs based on their water uptake in order to obtain better ion concentrations and higher conductivities.

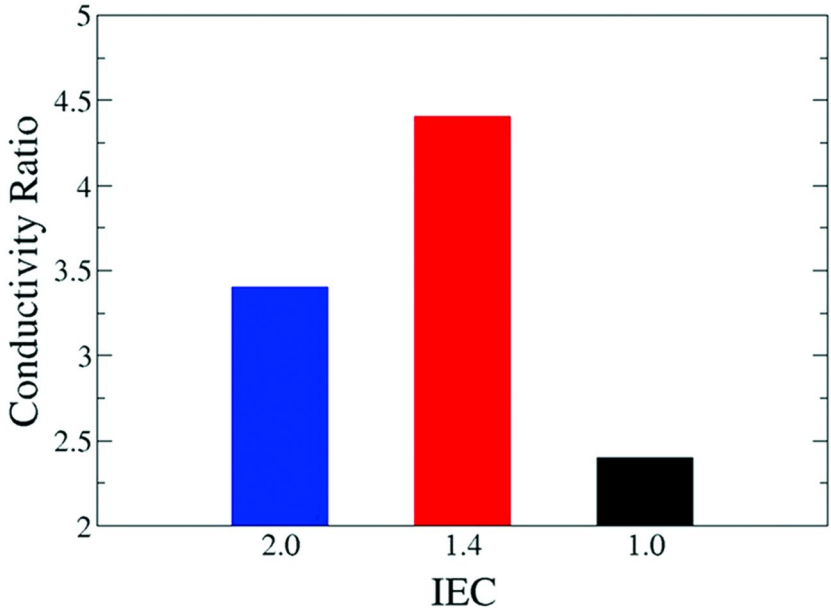

Figure 9. Conductivity ratios of hydroxide to bicarbinate for the three AEMs. Samples were exposed to liquid water and conductivities measured at 30 °C.

In Polymer Composites for Energy Harvesting, Conversion, and Storage; Li, L., et al.;
ACS Symposium Series; American Chemical Society: Washington, DC, 2014.

Mechanical Properties

Membranes need to be tough to survive the processing required to incorporate them into the membrane electrode assembly of cells as well as to withstand the operating conditions within the fuel cell. Water uptake and the consequent swelling of membranes can induce stresses on the membranes that it needs to withstand. Hence, the mechanical stability of the membranes, was studied by DMA. Table 2 lists the mechanical properties of the membranes with respect to the amount of crosslinker. As expected, the mechanical properties improved with increased amounts of crosslinker because of the increased crosslinking density and mechanical properties decreased with the amount of water uptake. The membranes showed comparable mechanical properties to the membranes reported by Coates *et. al.* crosslinked by ROMP, with a tensile stress at break ranging from 0.6-27 MPa and tensile strain at break varying from 53-87% (*29*, *48*). These mechanical properties indicated that these membranes could be used in fuel cells with satisfactory performance (*49*).

Table 2. Variation of Anion Exchange Membrane Properties with Varying Ratios of DCPD

	Composition		
Ratio of **5** : DCPD	1:2	1:5	1:10
Theoretical IEC (mequiv/g)	2.0	1.4	1.0
liquid water uptake (wt %)	432	126	30
$\sigma_{30\ °C}$ (mS/cm)[a]	19.6	28.6	14.1
Tensile stress at break (MPa)[b]	0.6±0.1	6.2±0.4	27.0±0.5
% Tensile strain at break[b]	53±2	80±11	87±16

[a] Hydroxide conductivity at 30 °C. [b] Mechanical measurements by Dynamic Mechanical Analysis.

Methanol Crossover

Employing liquid fuels like ethanol can make fuel cells much greener as the fuel can be produced from renewable sources like biomass. Hence, replacing hydrogen-based fuel cells with direct methanol and other liquid supplied fuels is gaining interest because of the high volumetric energy density and conversion efficiencies of the liquid fuels (*50*). Converting the existing petroleum distribution networks to liquid fuels also eliminates the need to generate new hydrogen distribution infrastructures, thus making the fuel cells more economical (*28*) The problem of fuel crossover is not as severe in AEM DMFCs as compared to PEMs, but an optimal concentration of methanol needs to be maintained in the anode as very low concentrations can increase mass transport losses (*34*).

In Polymer Composites for Energy Harvesting, Conversion, and Storage; Li, L., et al.;
ACS Symposium Series; American Chemical Society: Washington, DC, 2014.

Additionally, the greater the concentration of the fuel, the greater is the energy efficiency achieved by the fuel cells. With this in mind, we decided to test the membranes for dimensional stability at different concentrations of methanol. As shown in Figure 10, the membranes showed no significant changes in volume with respect to the volume when fully swollen in water in 2M and 6M aqueous methanol solutions. Very little differential swelling was seen for membranes with IEC = 1.4 and IEC = 1.0 in 10M aqueous methanol solutions making them good potential candidates in DMFCs.

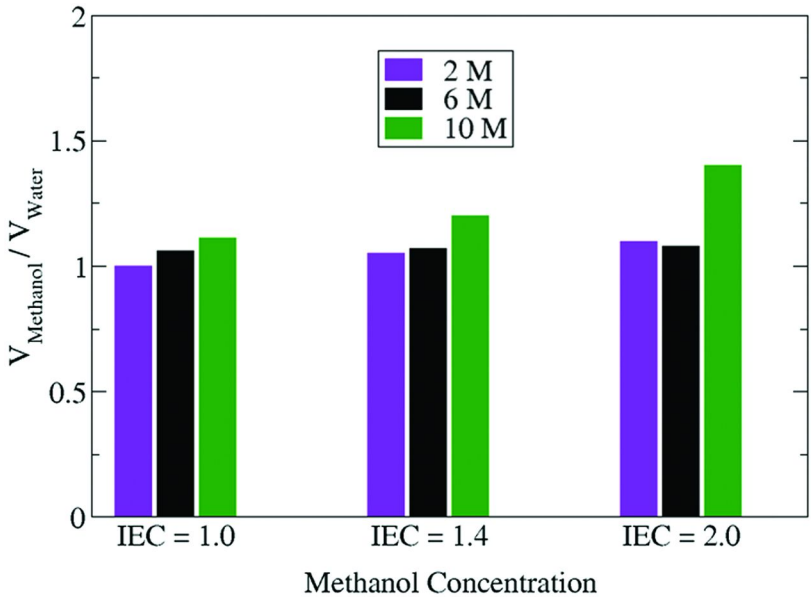

Figure 10. Dimensional Swelling of the AEMs in their bicarbonate form immersed in aqueous methanol solutions of different concentrations for 2 hours at 80°C. $V_{methanol}$ is the volume of membrane in methanol and V_{water} is the volume in water.

Conclusions

Polymers with metal-ligand groups represent a growing class of materials that can be used in a variety of functional devices and applications by virtue of their unique and hitherto unseen properties. Terpyridine ligands and their various metal complexes have extensively been incorporated into different controlled polymeric architectures. In this work, a water soluble Ruthenium(II) bisterpyridine complex-functionalized norbornene monomer was synthesized with a Cl^- counterion. This was subsequently crosslinked with a hydrophobhic co-monomer using ROMP to make novel multivalent fuel cell membranes. These membranes exhibited better thermal and alkaline stability and comparable conductivities and mechanical properties to membranes based on conventional

In Polymer Composites for Energy Harvesting, Conversion, and Storage; Li, L., et al.;
ACS Symposium Series; American Chemical Society: Washington, DC, 2014.

organic cations. The effect of atmospheric CO_2 on the membrane performance and functioning has also been studied. Additionally, this system is a potential candidate for DMFCs due to its high methanol tolerance. Further investigations are underway to replace the metal cation center with alternatives. This will help provide a better understanding of these polyelectrolyte systems and their mechanism of action. This will also be used to tune ion exchange capacity and consequently the conductivity of the membranes. These alternatives can help in improving the membrane stability while making these promising materials more cost effective. In addition, tuning the morphologies of these membranes by different synthetic routes will also be examined for the overall improvement in performance. These materials, by virtue of their functionality, have the potential to be used in a variety of other applications.

References

1. Manners, I. *Synthetic Metal-Containing Polymers*; Wiley-VCH Weinheim: Cambridge, 2004; pp 16−18.
2. Balzani, V.; Juris, A.; Venturi, M.; Campagna, S.; Serroni, S. *Chem. Rev. (Washington, DC, U.S.)* **1996**, *96*, 759–833.
3. Schubert, U. S.; Andres, P. R. *Adv. Mater. (Weinheim, Ger.)* **2004**, *16*, 1043–1068.
4. Manners, I.; Schubert, U. S.; Whittell, G. R.; Hager, M. D. *Nat. Mater.* **2011**, *10*, 176–188.
5. Harris, E. K. Ph.D. Thesis, University of Basel, Basel, Germany, 2010.
6. Lehn, J. M. *Supramolecular Chemistry, Concepts and Perspectives*; VCH-Weinheim: Germany, 1995.
7. Fraser, C. L.; Johnson, R. M. *Macromolecules* **2004**, *37*, 2718–2727.
8. Fraser, C. L.; Smith, A. P. *Macromolecules* **2003**, *36*, 2654–2660.
9. Govender, P.; Therrien, B.; Smith, G. S. *Eur. J. Inorg. Chem.* **2012**, *2012*, 2853–2862.
10. Newkome, G. R.; He, E. *J. Mater. Sci.* **1997**, *7*, 1237–1244.
11. Schubert, U. S.; Eschbaumer, C. *Angew. Chem., Int. Ed.* **2002**, *41*, 2893–2926.
12. Potts, K. T.; Usifer, D. A. *Macromolecules* **1988**, *21*, 1985–1991.
13. Gohy, J. F.; Lohmeijer, B. G. G.; Varshney, S. K.; Schubert, U. S. *Macromolecules* **2002**, *35*, 7427–7435.
14. Lamba, J. J. S.; Fraser, C. L. *J. Am. Chem. Soc.* **1997**, *119*, 1801–1802.
15. Sleiman, H. F.; Chen, B.; Metera, K. *Macromolecules* **2005**, *38*, 1080–1090.
16. Tew, G. N.; Aamer, K. A.; Shunmugam, R. *Polymer* **2005**, *46*, 8440–8447.
17. Tew, G. N.; Kalzia, K. J. *Macromolecules* **2002**, *35*, 6090–6093.
18. Tew, G. N.; Shunmugam, R. *J. Polym. Sci., Part A: Polym. Chem.* **2005**, *43*, 5831–5843.
19. Tew, G. N.; Shunmugam, R. *J. Am. Chem. Soc.* **2005**, *127*, 13567–13572.
20. Tew, G. N.; Shunmugam, R. *Polym. Adv. Technol.* **2007**, *18*, 940–945.
21. Zhang, K.; Zha, Y.; Peng, B.; Chen, Y.; Tew, G. N. *J. Am. Chem. Soc.* **2013**, *135*, 15994–15997.

22. Zha, Y.; Disabb-Miller, M. L.; Johnson, Z. D.; Hickner, M. A.; Tew, G. N. *J. Am. Chem. Soc.* **2012**, *134*, 4493–4496.
23. Tongwen, X. *J. Membr. Sci.* **2005**, *263*, 1–29.
24. Varcoe, J. R.; Slade, R. C. T. *Fuel Cells* **2005**, *5*, 213–229.
25. Wang, G.; Weng, Y.; Chu, D.; Xie, D.; Chen, R. *J. Membr. Sci.* **2009**, *326*, 4–8.
26. Zhou, J.; Unlu, M.; Vega, J. A.; Kohl, P. A. *J. Power Sources* **2009**, *190*, 285–292.
27. Tongwen, X.; Weihua, Y. *J. Membr. Sci.* **2001**, *190*, 159–166.
28. Varcoe, J. R.; Slade, R. C. T.; Lam How Yee, E. *Chem. Commun. (Cambridge, U.K.)* **2006**, 1428–1429.
29. Coates, G. W.; Robertson, N. J.; Kostalik, H. A.; Clark, T. M.; Mutolo, P. F.; Abruña, H. D. *J. Am. Chem. Soc.* **2010**, *132*, 3400–3404.
30. Zagorodni, A. A.; Kotova, D. L.; Selemenev, V. F. *React. Funct. Polym.* **2002**, *53*, 157–171.
31. Neagu, V.; Bunia, I.; Plesca, I. *Polym. Degrad. Stab.* **2000**, *70*, 463–468.
32. Hwang, G-J.; Ohya, H. *J. Membr. Sci.* **1998**, *149*, 163–169.
33. Wang, J. H.; Li, S. H.; Zhang, S. B. *Macromolecules* **2010**, *43*, 3890–3896.
34. Zhang, B.; Gu, S.; Wang, J.; Liu, Y.; Herring, A. M.; Yan, Y. *R. Soc. Chem. Adv.* **2012**, *2*, 12683–12685.
35. Bauer, B.; Strathmann, H.; Effenberger, F. *Desalination* **1990**, *79*, 125–44.
36. Noonan, K. J. T.; Hugar, K. M.; Kostalik, H. A.; Lobkovsky, E. B.; Abruna, H. D.; Coates, G. W. *J. Am. Chem. Soc.* **2012**, *134*, 18161–18164.
37. Qiu, B.; Lin, B.; Qiu, L.; Yan, F. *J. Mater. Chem.* **2012**, *22*, 1040–1045.
38. Tew, G. N.; Aamer, K. A.; De Jeu, W. H. *Macromolecules* **2008**, *41*, 2022–2029.
39. Collin, J. P.; Guillerez, S.; Sauvage, J. P.; Barigelletti, F.; DeCola, L.; Flamigni, L.; Balzani, V. *Inorg. Chem.* **1991**, *30*, 4230–4238.
40. Schubert, U.; Hofmeier, H.; Newkome, G. R. *Modern Terpyridine Chemistry*; Wiley-VCH: Weinheim: Germany, 2006.
41. Tew, G. N.; Aamer, K. A. *Macromolecules* **2007**, *40*, 2737–2744.
42. Hickner, M. A.; Yan, J. *Macromolecules* **2010**, *43*, 2349–2356.
43. Valade, D.; Boschet, F.; Améduri, B. *J. Polym. Sci., Part A: Polym. Chem.* **2010**, *48*, 5801–5811.
44. Yanagi, H.; Fukuta, K. *ECS Trans.* **2008**, *16*, 257–262.
45. Xu, K.; Oh, H.; Hickner, M. A.; Wang, Q. *Macromolecules* **2011**, *44*, 4605–4609.
46. Varcoe, J. R.; Slade, R. C. T.; Yee, E. L. H.; Poynton, S. D.; Driscoll, D. J.; Apperley, D. C. *Chem. Mater.* **2007**, *19*, 2686–2693.
47. Dean, J. A. *Lange's Handbook of Chemistry*, 15th ed.; McGraw-Hill: New York, 1999.
48. Coates, G. W.; Clark, T. M.; Robertson, N. J.; Kostalik, H. A.; Mutolo, P. F.; Abruña, H. D. *J. Am. Chem. Soc.* **2009**, *131*, 12888–12889.
49. Wang, J. H.; Zhao, Z.; Gong, F. X.; Li, S. H.; Zhang, S. B. *Macromolecules* **2009**, *42*, 8711–8717.
50. Zhao, T. S.; Li, Y. S.; Shen, S. Y. *Front. Energy Power Eng. China* **2010**, *4*, 443–458.

Chapter 7

Polymeric Nanocomposites of Te and Bi_2Te_3 Nanowires in PEDOT:PSS: Synthesis and Electrical Transport Studies

Kim Anderson and Greg Szulczewski*

Department of Chemistry, The University of Alabama, 250 Hackberry Lane, Tuscaloosa, Alabama 35487
***E-mail: gjs@ua.edu.**

Thin films containing Te and Bi_2Te_3 nanowires in the polymer PEDOT:PSS were made by drop casting and characterized by scanning electron microscopy, Raman spectroscopy and x-ray photoelectron spectroscopy. Scanning electron microscopy images revealed that the morphology and aspect ratio of the Te nanowires depends on the ratio of PEDOT to PSS used in the synthesis. Electrical conductivity measurements on the Te thin films were measured from 77-300 K and the results were fit to the variable-range hopping model. The results suggest that the improved conductivity of the Te nanocomposites can largely be explained by conducting PEDOT:PSS segments between the Te nanowires. Adding dimethyl sulfoxide increases the electrical conductivity of the composites, but to a much more significant effect in the case of Bi_2Te_3 films. Overall the results underscore the importance of nanoscale connections on the electrical conduction pathways in these polymeric thin films.

Keywords: Te; Bi_2Te_3; PEDOT:PSS; nanowires; electrical conductivity

In Polymer Composites for Energy Harvesting, Conversion, and Storage; Li, L., et al.;
ACS Symposium Series; American Chemical Society: Washington, DC, 2014.

Introduction

There has been a growing interest in the development of polymeric-based thermoelectric materials due to the intrinsic low thermal conductivity of polymers and the ability to process soft-matter by low-temperature, solution-based techniques (*1–9*). The unitless figure of merit, ZT, sets one criteria to measure the effectiveness of a thermoelectric material. The figure of merit is defined as

$$ZT = (\sigma S^2 / \kappa) T \quad (1)$$

where σ is the electrical conductivity in S/m, S is the Seebeck coefficient in V/K, and κ is the thermal conductivity in W m^{-1} K^{-1}, and T is the average temperature between the hot and cold side of a device in K. From equation (1) it is clear that in order to increase the figure of merit, σ and S must be large and κ must be small. These properties are not independent of another and make it challenging to design an efficient thermoelectric material (*10*). In general, insulators are poor conductors of heat and charge, while metals are good conductors of heat and charge. Some bulk inorganic semiconductors, like Te and Bi_2Te_3, have good electrical conductivity, low thermal conductivity, and a high Seebeck coefficient. In fact Bi_2Te_3 and its alloys have been the most widely studied thermoelectric materials over the past half-century (*11*). However, due to the low efficiency of converting heat into electrical power the number of practical applications has been limited, which requires ZT to be greater than one.

Electrically conducting polymers are unique materials because they tend to have a low thermal conductivity due to structural disorder. Although some polymers can have a large electrical conductivity they tend to have low Seebeck coefficients (*12*). On the other hand, composites of electrically conducting polymers and inorganic nanostructures (*13*), carbon nanotubes (*14–18*), and semiconducting nanowires (*19–26*) have shown significant promise as new classes of thermoelectric materials because the physical properties can be modulated by tuning the composition. Recently, the commercially available, water soluble, highly conducting PEDOT:PSS polymer has found much success as the matrix for this new class of thermoelectric materials.

As an introduction, we will briefly highlight some of the results that are most relevant to our studies. In 2010 Kim *et al*. reported thermoelectric properties from a composite derived from carbon nanotubes and PEDOT:PSS that showed a ZT value of about 0.02 at room temperature (*18*). The work highlighted the critical role of stabilizers to control the morphology of the carbon nanotubes and polymer. Later in 2010, Zhang *et al*. formed a composite between PEDOT:PSS and ball-milled Bi_2Te_3 powders (*26*). Several important findings emerged from this work. First, the authors were unable to prepare films by drop casting a mixture of the two components. However they found that drop casting a layer of PEDOT:PSS onto a layer of Bi_2Te_3 particles enabled them to measure the electrical conductivity and Seebeck coefficient of the composite film. Second, they found that the sign of the Seebeck coefficient was determined by the Bi_2Te_3 component. Specifically,

In Polymer Composites for Energy Harvesting, Conversion, and Storage; Li, L., et al.;
ACS Symposium Series; American Chemical Society: Washington, DC, 2014.

when n-type and p-type Bi_2Te_3 was used the sign of the Seebeck coefficient was negative and positive, respectively. Finally, they reported that rinsing the Bi_2Te_3 particles with dilute HCl was critical to achieve high power factors. Zhang *et al*. concluded there was a high contact resistance between the Bi_2Te_3 particles and PEDOT:PSS layer. See *et al*. published a novel strategy to make a composite thermoelectric by synthesizing Te nanorods directly in PEDOT:PSS (*25*). One of the main advantages of this approach is that smooth films could be prepared by drop casting. The resultant films exhibited a room temperature ZT value of about 0.1.

In this chapter, we report the synthesis of Te nanowires in PEDOT:PSS and the charge transport mechanism in thin films by measuring the electrical conductivity as a function of temperature. In addition, we made composites films of water-soluble Bi_2Te_3 nanowires in PEDOT:PSS. The effect of DMSO as secondary dopant to improve the electrical conductivity of the films was also examined.

Experimental

Materials

All chemicals were purchased from commercial sources. Bismuth chloride (Strem, 99.99%), bismuth nitrate pentahydrate (Acros, 98%), sodium tellurite (Alfa Aesar, 99.5%), telluric acid (Alfa Aesar, 99%), L-ascorbic acid (Fisher, 99.9%), hydrazine monohydrate (Alfa Aesar, 99%), thioglycolic acid (Sigma Aldrich, 99%), Orgacon ICP 1050 PEDOT:PSS (Sigma Aldrich, ~1% by weight polymer in water), Clevious P VP AI 4083 PEDOT:PSS (Heraues, ~1% by weight polymer in water), polyvinylpyrrolidone (Sigma Aldrich, average molecular weight 55,000 g/mol).

Methods

Tellurium nanowires were synthesized following the method similar to the one reported by See *et al*. (*25*) In a 100 mL round bottom flask 1 gram of ascorbic acid was added to 40 mL of ~18 MΩ-cm water and stirred until completely dissolved. Next, 1 mL of filtered (though a 0.5 micron membrane syringe) PEDOT:PSS, either Orgacon ICP 1050 or Clevious P VP AI 4083, was added to the stirred solution. Next, 70 milligrams of $Te(OH)_6$ was added and the temperature was increased to ~90 °C with continuous stirring for 12-18 hours. The reaction products were purified by two centrifugation cycles (30 minutes at 9000 rpm). The recovered solids were re-suspended in 1-2 mL of deionized water. Attempts to synthesize Bi_2Te_3 nanowires in PEDOT:PSS followed the same procedure described above, except 0.2 mmol of either bismuth chloride (0.0625

g) or bismuth nitrate pentahydrate (0.0970g) was added to the reaction mixture. We also adopted the synthesis reported by Purkayastha *et al*. to synthesize thioglycolic-capped Bi_2Te_3 nanowires (*27*). In a typical synthesis, 0.162 mmol (37.0 mg) of $Te(OH)_6$ was dissolved in 2 mL of 18 MΩ-cm water. In a separate beaker, 0.107 mmol (33.5 mg) of bismuth chloride was dissolved in 0.4 mL nitric acid and diluted with 1.5 mL 18 MΩ water. To the bismuth chloride solution, 1.08 mmol (75 µL) thioglycolic acid was added and the solution turned from colorless to yellow. The solutions were then transferred to a three-neck round-bottom flask containing 70 mL of 18 MΩ-cm water pre-heated to 80°C. After two minutes, 3 mL of hydrazine monohydrate was added. The solution turned black upon the addition of the hydrazine monohydrate and then refluxed at ~ 90°C for ~6 hours while stirring. After cooling to room temperature, the solution was filtered and the black precipitate was dried at ~ 70 °C.

Thin films of the nanowire/PEDOT:PSS nanocomposites were made on 1 x 1 cm pieces of a Si(100) wafer bearing a 600 nm oxide layer or 1 x 1 cm SiO_2(110) single crystal (MTI Inc.) The substrates were cleaned by sonication in acetone and isopropanol for 30 minutes then dried with a stream of nitrogen gas. Finally the substrates were placed in an UV/ozone cleaner for 10 minutes. Thin films were made by drop casting the dispersions onto the clean substrates at room temperature followed by heating on a hot plate to ~90 °C for about 30 minutes. The samples were allowed cool back to room temperature and immediately measured by a two-point method using Indium contacts. Current versus voltage curves were measured with a Keithley 2400 source meter. All curves were ohmic and the measured sheet resistance was converted to conductivity after the film thickness was measured by profilometry. Raman spectra were taken with 633 nm excitation using a Jobin-Yvon micro–Raman spectrometer in a back-scattering geometry. X-ray photoelectron spectra were measured with a Kratos Axis 165 using a monochromatic Al source (1486.6 eV). The pass energy of the hemispherical analyzer was set to 160 eV for the survey scan and 80 eV for high-resolution scans. Scanning electron microscopy images were recorded with a JEOL model 7000 operating at 20 keV. Atomic composition was determined from x-ray analysis using a JOEL 8600 microprobe equipped with a wavelength-dispersive detector.

Results and Discussion

Figure 1 and Figure 2a show SEM images of Te nanowires synthesized by reduction of $Te(OH)_6$ in Orgacon and Clevious PEDOT:PSS, respectively. The presence of the polymer was verified by XPS shown in Figure 2b. The O(1s), C(1s) and S(2s) peaks are observed near 520 eV, 285 eV, and 230 eV, respectively. The main Te peaks are observed near 573 eV, 170 eV, 110 eV, and 41 eV for the 3d, 4s, 4p, and 4d orbitals, respectively. The Te nanorods synthesized in Orgacon are approximately 920 nm long and 50 nm wide, in contrast, they are only about 430 nm long and 40 nm wide when synthesize in Clevious. The reason for the

different length Te nanorods is not completely understood, but is most likely due to the different size of PEDOT:PSS colloidal particles. The Orgacon has a PEDOT:PSS weight ratio of 1:1.6 while the ratio is 1:6 in the Clevious product. Dilute solutions of PEDOT:PSS particles have been measured by dynamic light scattering and small-angle x-ray scattering to determine the average radius of gyration and contour length, respectively (*28–33*). There are two important results from these studies. First, the average PEDOT:PSS particle size decreases with increasing solution temperature. Specifically, Friedel *et al*. observed that average colloidal particle diameter in the Clevious PEDOT:PSS formulation decreases from ~90 nm to ~40 nm when the temperature is increased from 20°C to 90°C (*30*). Second, the average particle size is smaller for the more conducting grades of PEDOT:PSS. We suspect the larger PEDOT:PSS particles inhibit the diffusion of Te atoms formed during the chemical reduction and therefore produce shorter Te nanorods.

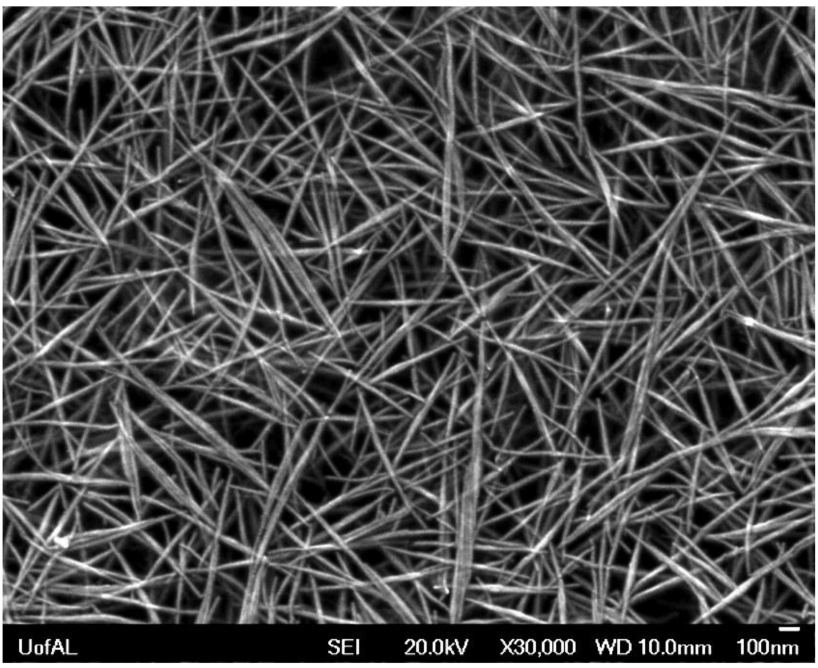

Figure 1. Scanning electron microscopy image of Te nanowires synthesized in Orgacon ICP 1050 PEDOT:PSS.

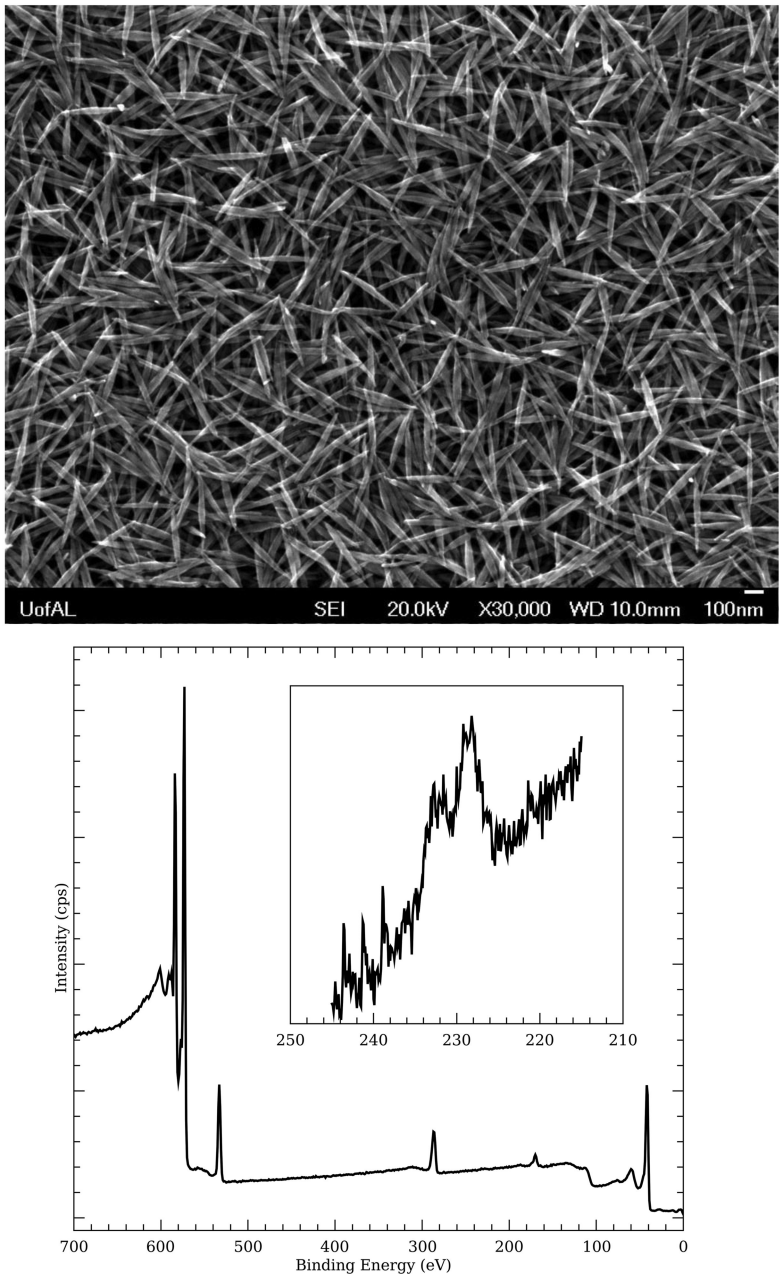

Figure 2. (Top) Scanning electron microscopy image of Te nanowires synthesized in Clevious P VP AI 4083 PEDOT:PSS. (Bottom) XPS survey scan with S(2s) region expanded as an inset. The low binding energy peak is due to PEDOT, while the high binding energy peak is due to PSS.

In Polymer Composites for Energy Harvesting, Conversion, and Storage; Li, L., et al.;
ACS Symposium Series; American Chemical Society: Washington, DC, 2014.

The important role of the polymer can be seen in another experiment. When polyvinylpyrolidone was used in place of PEDOT:PSS (while keeping the same total concentration of polymer ~1 mg/mL) in the synthesis, a very different Te morphology was observed. Figure 3 shows an SEM image of the Te nanowires formed from the reduction of telluric acid with ascorbic acid in the presence of polyvinylpyrolidone. Tri-tipped, spine-like nanowiskers are observed. A similar morphology was reported of Mayers and Xia (*34*). They found that the reduction of telluric acid by hydrazine in ethylene glycol formed very distinct wiskers (i.e., spines, filaments, and needles) depending on the reaction temperature. However, they only observed the tri-tipped Te nanowiskers above 182°C. Our results are consistent with the temperature required to grow spine-like whiskers from the vapor-growth of tellurium, which has been assigned to an axial dislocation mechanism (*35*, *36*). The origin of this difference is not clearly understood, but certainly the polymer serves as a templating agent and further studies are needed to elucidate the precise details of the growth mechanism. Nonetheless, our general observations are consistent with the many reports in the literature that demonstrate the tendency of Te to grow one-dimensional nanostructures from chemical reduction reactions (*37–44*).

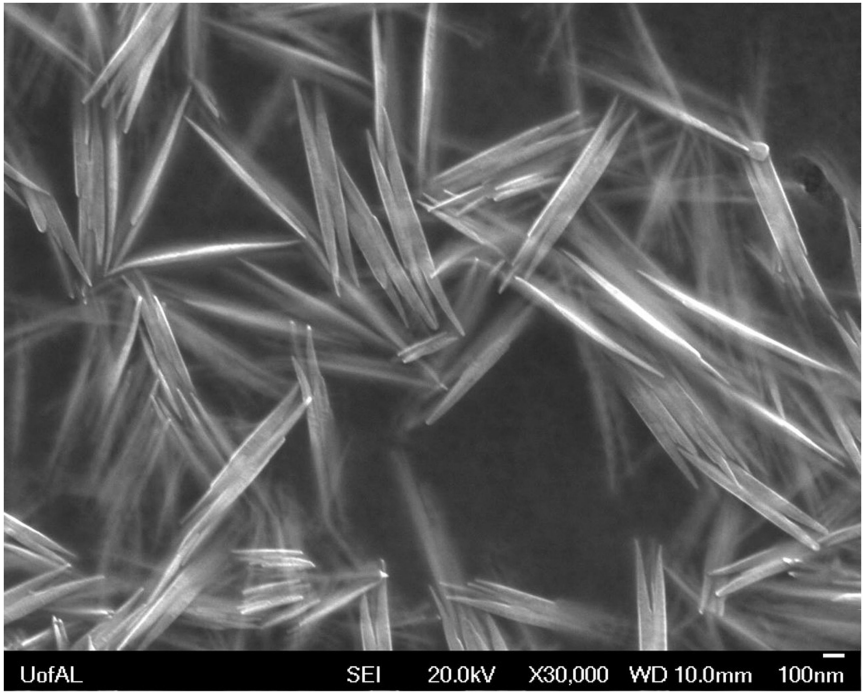

Figure 3. Scanning electron microscopy image of Te nanowires synthesized in polyvinylpyrrolidone.

Figures 4 and 5 show SEM of images of nanowires produced when $BiCl_3$ and $Bi(NO_3)_3$ were added to the reaction, respectively. Based on previous reports we assign the segments to Bi_2Te_3 (*45–49*). Microprobe x-ray analysis indicates the presence of Bi, but Raman spectroscopy (see below) suggests the main phase is Te. When $BiCl_3$ was used in the synthesis the nanorods are approximately 840 nm long and 50 nm wide with about 5 Bi_2Te_3 segments per nanorod. The average Te/Bi atomic ratio for this sample was 4.76, much greater than the expected Te/Bi = 1.5 for pure Bi_2Te_3. In contrast, when $Bi(NO_3)_3$ was added to the synthesis the Te nanorods are approximately 600 nm long and 50 nm wide with about 8 Bi_2Te_3 segments per nanorods. The average Te/Bi atomic ratio for this sample was 2.43. Why do more of these segments grow on the Te template when using $Bi(NO_3)_3$? We suspect the different nanowire length and Bi_2Te_3 density is due to partial hydrolysis of $BiCl_3$, which produces BiOCl and lowers the concentration of free Bi^{3+} ions. Although it is difficult to completely understand the reaction mechanism we suspect that the higher concentration of free Bi^{3+} ions leads to the higher density of Bi_2Te_3 segments grown on the Te nanowire template. The growth of Bi_2Te_3 onto Te is likely due to the close lattice match. The c-axis and a-axis for bulk Te is 5.94 Å and 4.40 Å, respectively, while the c-axis and a-axis for bulk Bi_2Te_3 is 30.46 Å (about 5 times the c-axis of pure Te) and 4.39 Å, respectively.

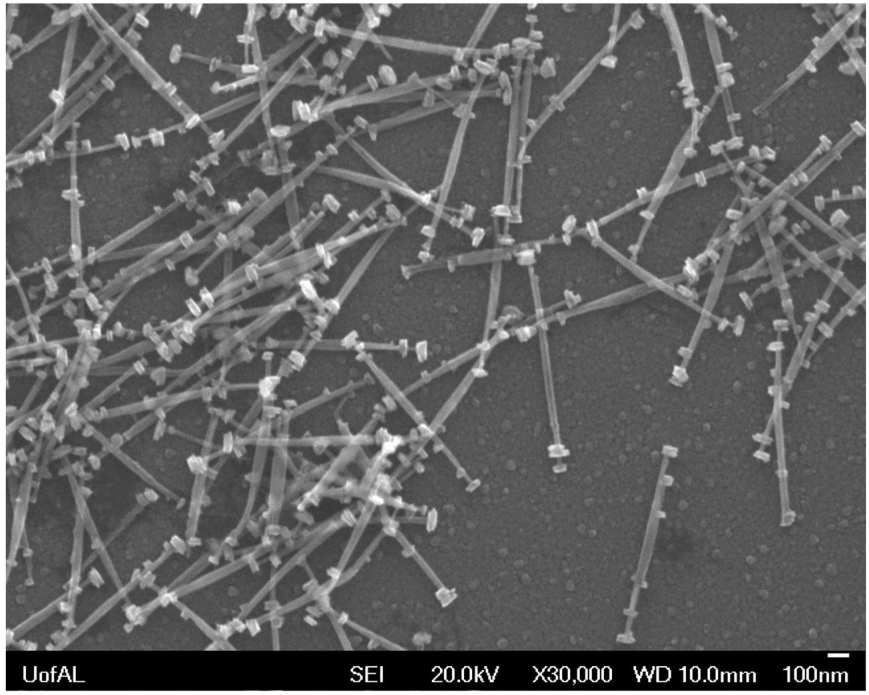

Figure 4. Scanning electron microscopy image of Te nanowires after using $BiCl_3$ in the synthesis.

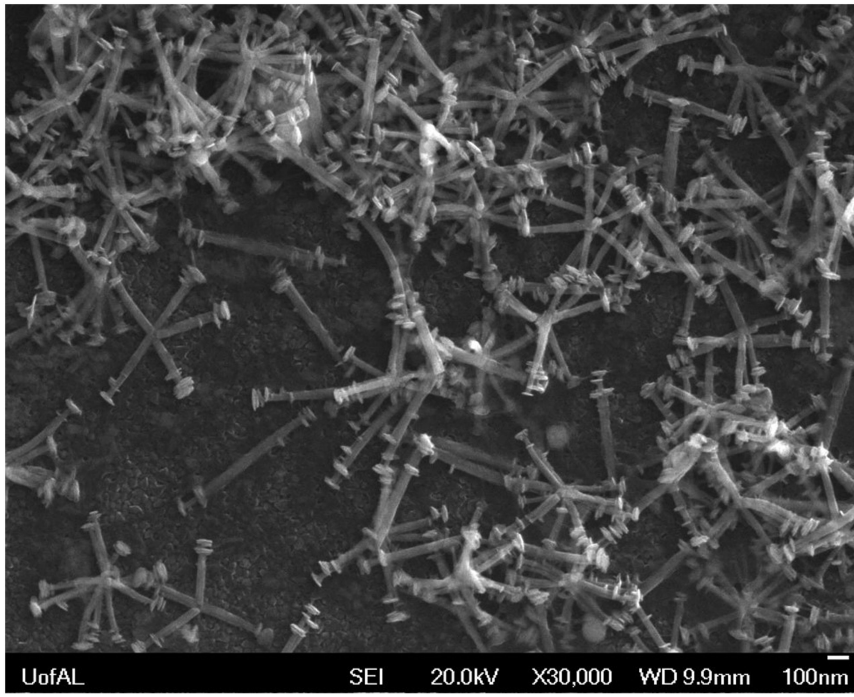

Figure 5. Scanning electron microscopy image of Te nanowires after using $Bi(NO_3)_3$ in the synthesis.

Figure 6 shows the low-frequency Raman spectra of films containing the Bi_2Te_3 segments on the Te nanowires. The spectrum has two main peaks at 120 cm^{-1} and 140 cm^{-1} that can be assigned to Te phonon modes (*37*). The peaks are very narrow and suggest the Te nanowires are highly crystalline. In fact, the spectra are very similar to a published report on bulk single crystals (*50*). The absence of any signal from the Bi_2Te is attributed to the small volume fraction of the segments on the Te nanowires. Since these synthetic conditions were unable to grow Bi_2Te_3 nanorods directly in the PEDOT:PSS solution, we used a method reported in the literature (*27*). Figure 7 shows the SEM image of thioglycolic acid-capped Bi_2Te_3 nanowires. The nanorods are approximately 400 nm long and 40 nm wide. The thioglycolic acid ligand affords water solubility to the nanorods and allows them to be dispersed into PEDOT:PSS. Figure 8 shows an x-ray photoelectron survey spectrum for the synthesized thiogylcolic acid capped-Bi_2Te_3 nanowires. The main Te photoelectrons at 583 eV and 573 eV can be assigned to the spin-orbit splitting of the Te 3d orbitals, while peak near 42 eV can be assigned to the Te 4d orbital. The main photoelectron peaks for Bi occur at 464, 440, 162, 157, 27 and 24 eV and correspond to the $4d_{3/2}$, $4d_{5/2}$, $4f_{7/2}$, $4f_{5/2}$, $5d_{3/2}$ and $5d_{5/2}$ levels, respectively. These values are in good agreement with the literature (*51*). The peaks near 532, 285, and 162 eV correspond to the O(1s),

In Polymer Composites for Energy Harvesting, Conversion, and Storage; Li, L., et al.;
ACS Symposium Series; American Chemical Society: Washington, DC, 2014.

C(1s) and S(2p) levels from the thioglycolic acid ligands on the nanowire surface. In addition to sulfur on the surface, energy dispersive x-ray analysis reveals the nanowires are sulfur-doped, which is consistent with the original report (*27*).

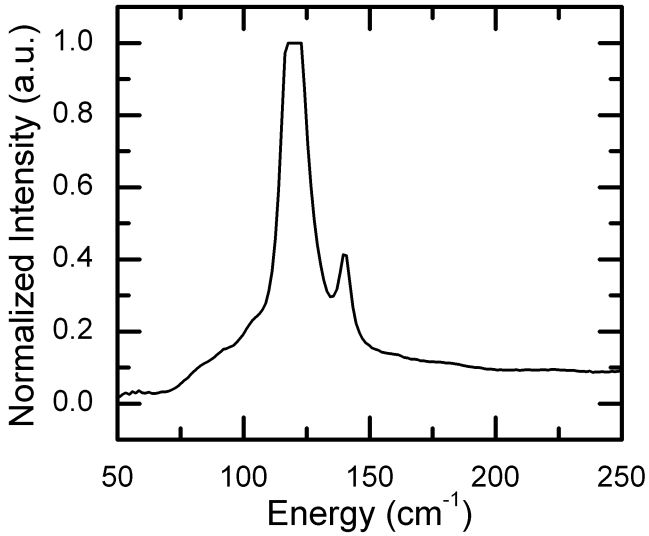

Figure 6. Raman spectrum of nanowires shown in Figure 4.

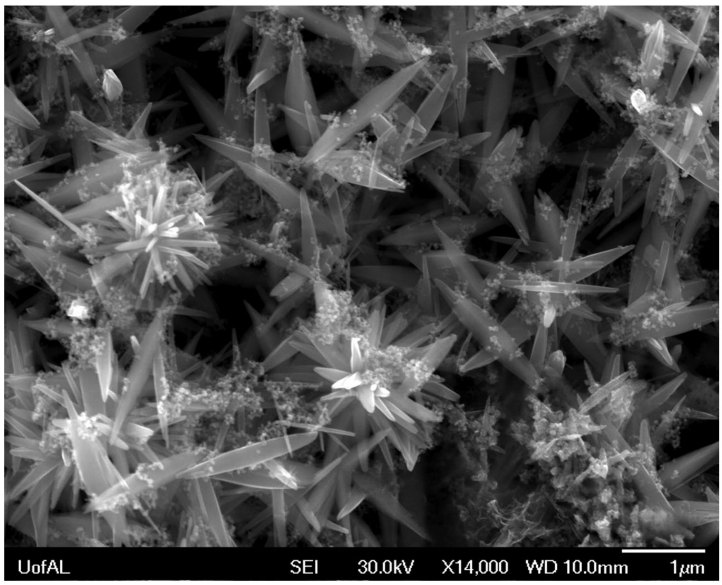

Figure 7. Scanning electron microscopy image of thiolglycolic acid-capped Bi_2Te_3 nanowires.

In Polymer Composites for Energy Harvesting, Conversion, and Storage; Li, L., et al.;
ACS Symposium Series; American Chemical Society: Washington, DC, 2014.

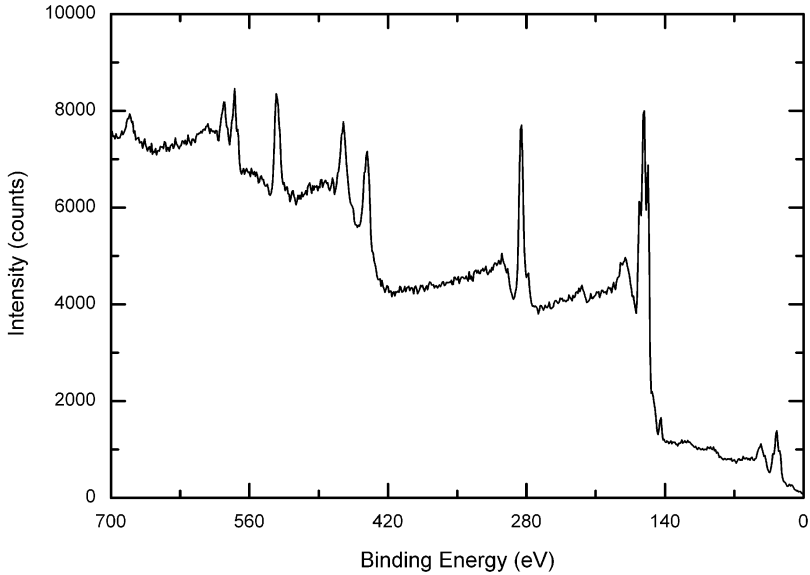

Figure 8. X-ray photoelectron spectra of thiolglycolic acid-capped Bi_2Te_3 nanowires.

The electrical transport in PEDOT:PSS films has been widely studied due to its important role in organic light emitting diodes and organic photovoltaic device fabrication (*52*). Many authors have used Mott's variable-range hopping model to interpret temperature-dependent conductivity, σ(T), measurements of PEDOT:PSS thin films. The generic form of Mott's equation is expressed below

$$\sigma(T) = \sigma_0 \, exp\left[-\left(\frac{T_0}{T}\right)^{\alpha}\right] \qquad \text{Eq. (2)}$$

where T_o is a measure of the effective energy barrier for hopping of the carriers between localized states and $\alpha = 1/(1+D)$ where D is the dimensionality of the hopping process (*53*). There are many reports of the temperature-dependent conductivity of PEDOT:PSS films (*54–62*). Although most authors report one-dimensional variable range hopping, there are several possible explanations for the different α values in PEDOT:PSS films. First, the conductivity of PEDOT:PSS in known to be very anisotropic. For example, Nardes *et al*. showed that in P VP AI 4083 PEDOT:PSS films, the lateral and vertical transport followed three-dimensional and one-dimensional variable-range hopping, respectively (*63*). Second, the transport also depends on the film thickness. In this regard some groups have made films by spin coating and others by drop casting. Typically the former method produces films less than 100 nm in thickness, while the latter produces films greater than 1 μm in thickness. Third, the drying temperature, time, and environment (e.g., ambient, vacuum, or dry-box) can vary substantially between labs. Finally, it is possible to achieve satisfactory "looking" fits on a ln(σ) versus T^{α} plot, but one needs to carefully examine the correlation coefficients to statistically determine the "best" linear fit (*63*).

In Polymer Composites for Energy Harvesting, Conversion, and Storage; Li, L., et al.;
ACS Symposium Series; American Chemical Society: Washington, DC, 2014.

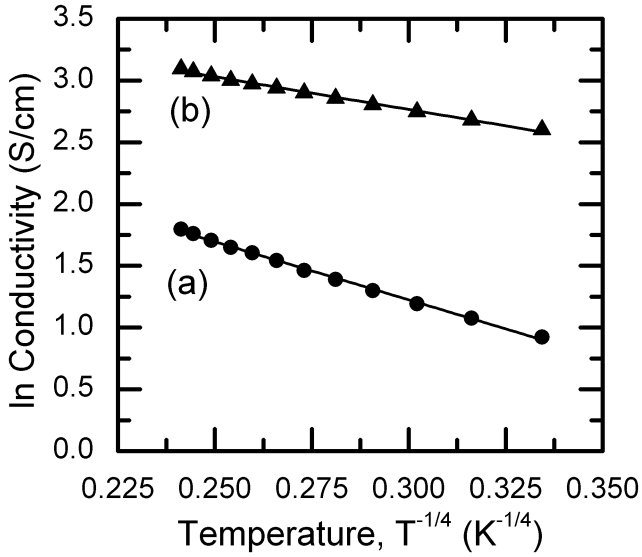

Figure 9. Temperature-dependent conductivity of (a) Te/PEDOT:PSS film and (b) Te/PEDOT:PSS film with 4% DMSO.

Figure 9 shows the temperature-dependent electrical conductivity of Te/PEDOT:PSS and Te/PEDOT:PSS with 4% DMSO films plotted on a logarithmic scale versus $T^{-0.25}$, which is consistent with three-dimension variable–range hopping. We made films with 1, 2, 4 and 8% by weight DMSO and found that the conductivity did not increase beyond 4%. In order to make a comparison to the other films, we used the 4% DMSO in all the doping studies. For all the Te films we studied, the highest correlation coefficients ($R > 0.995$) were found for three-dimension variable range hopping. Using the numerical values from the slope of the linear regression we calculated the T_o parameter, which is a measure of the effective energy barrier for hopping of the carriers between localized states. In Motts model, T_o is inversely proportional to the density of states at the Fermi energy and an effective localization length (*53*). As a result, a decreased value of T_o can be attributed to either an increase in density of states at the Fermi energy and/or a longer effective localization length. In addition, the PEDOT:PSS ratio has a significant impact on the electrical conductivity. For example, Stöker *et al*. reported that the electrical conductivity decreases from ~ 2 S/cm to ~ 10^{-3} S/cm when the PEDOT:PSS changed from 1:1 to 1:7 (*64*). By using impedance and Seebeck measurements Stöker *et al*. were able to show that the charge carrier density is independent of PSS content. This result suggests the mobility is improved by reducing the hopping distance between the PEDOT centers. Similarly, we expect the hopping of carriers between Te nanowires limits the conductivity of the films because the room-temperature conductivity drops from 6 S/cm to 0.1 S/cm when the PEDOT:PSS is changed

from Orgacon to Clevious. The films made of Clevious were still found to obey the three-dimension variable-range hopping and the T_o value was 2.7 x 10^6 K, remarkably close to the value determined by Nardes *et al*. for pure Clevious P VP AI 4083 films (3.2 x 10^6 K) (*63*).

Table 1 summarizes the room-temperature electrical conductivity values of various nanowires in the different polymers. There are clear differences between the films with and without DMSO. In the cast of the pure Te nanowires, the composite synthesized from the Orgacon PEDOT:PSS has the highest conductivity. In contrast, the composite synthesized in a non-conducting polymer (i.e., polyvinylpryrolidone) has the lowest conductivity. In the case of the segmented Te nanowires, the composites have intermediate values of conductivity (~1 S/cm). For the TGA-capped Bi_2Te_3 nanorods, the electrical conductivity does not vary significantly as the weight percent is increased from 25% to 75%, but increases considerably upon addition of the 4% DMSO. SEM images (not shown) of the Bi_2Te_3 nanowires in the PEDOT:PSS indicate an inhomogeneous distribution in the dried films. As a result, conduction is dominated by the PEDOT:PSS, which is consistent with other reports in the literature (*61*, *62*, *65*, *66*).

Table 1. Summary of Room Temperature Conductivity Values for Te Nanowires and Thioglycolic Acid-Capped Bi_2Te_3 Nanowires in PEDOT:PSS

Film	*σ (S/cm) at 300 K no DMSO*	*σ (S/cm) at 300 K 4% DMSO*
Te in Orgacon	6	22
Te in Clevious	0.1	4
Te in polyvinyl pyrolidone	$< 10^{-6}$	n/a
Te/Bi_2Te_3 from $Bi(NO_3)_3$ in Orgacon	1	n/a
Te/Bi_2Te_3 from $BiCl_3$ in Orgacon	0.6	n/a
25 wt% TGA-Bi_2Te_3 in Orgacon	2	244
50 wt% TGA-Bi_2Te_3 in Orgacon	1	106
75 wt% TGA-Bi_2Te_3 in Orgacon	1	17

n/a = not measured.

In Polymer Composites for Energy Harvesting, Conversion, and Storage; Li, L., et al.;
ACS Symposium Series; American Chemical Society: Washington, DC, 2014.

Conclusions

In summary, five main conclusions can be drawn from this work.

1. The ratio of PEDOT:PSS controls the aspect ratio of Te grown by chemical reduction of Telluric acid. Te nanorods with an aspect ratio of ~19:1 are formed when the PEDOT to PSS ratio is 1:1.6. In contrast, Te nanorods with an aspect ratio of ~11:1 are formed when the PEDOT to PSS ratio is 1:6.
2. Using temperature-dependent electrical conductivity measurements we conclude that charge transport in Te/PEDOT:PSS films can be adequately described by Motts three-dimensional variable-range hopping model between 77 and 300 K.
3. Attempts to synthesize Bi_2Te_3 nanowires by reduction of telluric acid in the presence of $BiCl_3$ or $Bi(NO_3)_3$ were unsuccessful. The synthesis presumably yields Bi_2Te_3 segments along Te nanorods.
4. Bi_2Te_3 nanowires capped with thioglycolic acid were dispersed into PEDOT:PSS and thin films were made by drop casting. The resulting films are rough due to micro-phase separation of the nanorods from the polymer.
5. The addition of 4% DMSO as a secondary dopant to Te/PEDOT:PSS films modestly increased the room temperature conductivity. In contrast, the addition of 4% DMSO to the Bi_2Te_3/PEDOT:PSS films increased the room temperature conductivity in proportion to the amount of polymer added, which supports the conclusion that the transport is largely dominated by the polymer.

Acknowledgments

The authors thank the College of Arts and Sciences at the University of Alabama for funding this work and Ali Yousuf and David Wallace for help with the synthesis. We also thank Ed Ellingsworth for measuring the Raman and XPS spectra and Rob Holler for the microprobe analysis.

References

1. Kim, G. H.; Shao, L.; Zhang, K.; Pipe, K. P. *Nat. Mater.* **2013**, *12*, 719–723.
2. He, M.; Qiu, F.; Lin, Z. *Energy Environ. Sci.* **2013**, *6*, 1352–1361.
3. Park, T.; Park, C.; Kim, B.; Shin, H.; Kim, E. *Energy Environ. Sci.* **2013**, *6*, 788–792.
4. Yue, R.; Xu, J. *Synth. Met.* **2012**, *162*, 912–917.
5. Poehler, T. O.; Katz, H. E. *Energy Environ. Sci.* **2012**, *5*, 8110–8115.
6. Dubey, N.; LeClerc, M. *J. Polym. Sci., Part B: Polym. Phys.* **2011**, *49*, 467–475.
7. Bubnova, O.; Crispin, X. *Energy Environ. Sci.* **2012**, *5*, 9345–9362.
8. Budnova, O.; Khan, Z. U.; Malti, A.; Braun, S.; Fahlman, M.; Berggren, M.; Crispin, X. *Nat. Mater.* **2011**, *10*, 429–433.

9. Xuan, Y.; Liu, X.; Desbief, S.; Leclere, P.; Fahlman, M.; Lazzaroni, R.; Berggren, M.; Cornil, J.; Emin, D.; Crispin, X. *Phys. Rev. B* **2010**, *82*, 115454.
10. Synder, G. J.; Toberer, E. S. *Nat. Mater.* **2008**, *7*, 105–114.
11. Heremans, J. P.; Dresselhaus, M. S.; Bell, L. E.; Morelli, D. T. *Nat. Nanotechnol.* **2013**, *8*, 471–473.
12. Mateeva, N.; Niculescu, H.; Schlenoff, J.; Testardi, L. R. *J. Appl. Phys.* **1998**, *83*, 3111–3117.
13. Du, J. Y.; Shen, S. Z.; Cai, K.; Casey, P. S. *Prog. Polym. Sci.* **2011**, *37*, 820–841.
14. Moriarty, G. P.; De, S.; King, P. J.; Kham, U.; Via, M.; King, J. A.; Coleman, J. N.; Grunlan, J. C. *J. Polym. Sci., Part B: Polym. Phys.* **2013**, *51*, 119–123.
15. Hewitt, C. A.; Kaiser, A. B.; Roth, S.; Crpas, M.; Czerw, R.; Carroll, D. L. *Nano Lett.* **2012**, *12*, 1307–1310.
16. Meng, C.; Liu, C.; Fan, S. *Adv. Mater.* **2010**, *22*, 535–539.
17. Yao, Q.; Chen, L.; Zhang, W.; Liufu, S.; Chen, X. *ACS Nano* **2010**, *4*, 2445–2451.
18. Kim, D.; Kim, Y.; Choi, K.; Grunlan, J. C.; Yu, C. *ACS Nano* **2010**, *4*, 513–523.
19. Song, H.; Liu, C.; Zhu, H.; Kong, F.; Lu, B.; Xu, J.; Wang, J.; Zhoa, F. *J. Electron. Mater.* **2013**, *42*, 1268–1274.
20. Yee, S. K.; Coates, N. E.; Majumdar, A.; Urban, J. J.; Segalman, R. A. *Phys. Chem. Chem. Phys.* **2013**, *15*, 4024–4032.
21. Coates, N. E.; Yee, S. Y.; McColloch, B.; See, K. C.; Majumdar, A.; Segalman, R. A.; Urban, J. J. *Adv. Mater.* **2013**, *25*, 1629–1633.
22. He, M.; Ge, J.; Feng, X.; Wang, X.; Lu, H.; Yang, Y.; Qiu, F. *Energy Environ. Sci.* **2012**, *5*, 8351–8358.
23. Wang, Y. Y.; Cai, K. F.; Yao, Z. *J. Nanopart. Res.* **2012**, *14*, 848.
24. Wang, Y.; Cai, K.; Yao, X. *ACS Appl. Mater. Interfaces* **2011**, *3*, 1163–1166.
25. See, K. C.; Freser, J. P.; Chen, C. E.; Majumdar, A.; Urban, J. J.; Segalman, R. A. *Nano Lett.* **2010**, *10*, 4664–4667.
26. Zhang, B.; Sun, J.; Katz, H. E.; Fang, F.; Oplia, R. L. *ACS Appl. Mater. Interfaces* **2010**, *11*, 3170–3178.
27. Purkayastha, A.; Lupo, F.; Kim, S.; Borca-Tasciuc, T.; Ramanath, G. *Adv. Mater.* **2006**, *18*, 496–500.
28. Bagchi, D.; Menon, R. *Chem. Phys. Lett.* **2006**, *425*, 114–117.
29. Choudhury, P. K.; Bagchi, D.; Suchand Sangeeth, C. S.; Memon, R. *J. Mater. Chem.* **2011**, *21*, 1607–1614.
30. Friedel, B.; Brenner, T. J. K.; McNeil, C. R.; Steiner, U. *Org. Electron.* **2011**, *12*, 1736–1745.
31. Yan, H.; Arima, S.; Mori, Y.; Kagata, T.; Sato, H.; Okuzaki, H. *Thin Solid Films* **2009**, *517*, 3299–3303.
32. Friedel, B; Keivanidis, P. E.; Brenner, T. J. K.; Abrusci, A.; McNeil, C. R.; Friend, R. H.; Greeham, N. C. *Macromolecules* **2009**, *42*, 6741–6747.
33. Knappe, P.; Bienert, R.; Weidner, S.; Thunemann, A. F. *Polymer* **2010**, *51*, 1723–1727.

34. Mayers, B; Xia, Y. *J. Mater. Chem.* **2002**, *12*, 1875–1881.
35. Furuta, N.; Itinose, H.; Maruyama, N.; Ohasi, Y. *Jpn. J. Appl. Phys.* **1972**, *11*, 1113–1118.
36. Furuta, N.; Ohasi, Y.; Itinose, H.; Igarashi, Y. *Jpn. J. Appl. Phys.* **1975**, *14*, 929–934.
37. Liu, J.-W.; Chen, F.; Zhang, M.; Qi, H.; Zhang, C.-L.; Yu, S.-H. *Langmuir* **2010**, *26*, 11372–11377.
38. Vinoid, T. P.; Yang, M.; Kim, J.; Kotov, N. A. *Langmuir* **2009**, *25*, 13545–13550.
39. Sreeprasad, T. S.; Samal, A. K.; Pradeep, T. *Chem. Mater.* **2009**, *21*, 4527–4550.
40. Lin, Z.-H.; Yang, Z.; Chang, H.-T. *Cryst. Growth Des.* **2008**, *8*, 351–357.
41. Qian, H.-S.; Yu, S.-H.; Gong, J.-Y.; Luo, L.-B.; Fei, L.-F. *Langmuir* **2006**, *22*, 3830–3835.
42. Xi, G.; Liu, Y.; Wang, X.; Liu, X.; Peng, Y.; Qian, Y. *Cryst. Growth Des.* **2006**, *6*, 2567–2570.
43. Zhu, Y.-J.; Wang, W.-W.; Qi, R.-J.; Hu, X.-L. *Angew. Chem., Int. Ed.* **2004**, *43*, 1410–1414.
44. Tang, Z.; Wang, Y.; Sun, K.; Kotov, N. A. *Adv. Mater.* **2005**, *17*, 358–363.
45. Cheng, L.; Chen, Z.-G.; Yang, L.; Han, G.; Zu, H.-Y.; Synder, G. J.; Lu, G.-Q.; Zou, J. *J. Phys. Chem. C* **2013**, *117*, 12458–12464.
46. Fang, H.; Feng, T.; Yang, H.; Ruan, X.; Wu, Y. *Nano Lett.* **2013**, *13*, 2058–2063.
47. Zhang, G.; Fang, H.; Yang, H.; Jauregui, L. A.; Chen, Y. P.; Wu, Y. *Nano Lett.* **2012**, *12*, 3627–3633.
48. Wang, W.; Goebl, J.; He, L.; Aloni, S.; Hu, Y.; Zhen, L.; Yin, Y. *J. Am. Chem. Soc.* **2010**, *132*, 17316–17324.
49. Lu, W.; Ding, Y.; Chen, Y.; Wang, Z. L.; Fang, J. *J. Am. Chem. Soc.* **2005**, *127*, 10112–10116.
50. Pines, A. S.; Dresselhaus, G. *Phys. Rev. B* **1971**, *4*, 356.
51. Mehta, R. J.; Zhang, Y.; Karthik, C.; Singh, B.; Siegel, R. W.; Borca-Tasciuc, T.; Ramanath, G. *Nat. Mater.* **2012**, *11*, 233–240.
52. Kirchmeyer, S.; Reuter, K. *J. Mater. Chem.* **2005**, *15*, 2077–2088.
53. Mott, N.; Davis, E. A. *Electronic Processes in Non-Crystalline Materials*; Clardeon: Oxford, 1979.
54. Luo, J.; Billep, D.; Waechtler, T.; Otto, T.; Toader, M.; Gordan, O.; Sheremet, E.; Martin, J.; Hietschold, M.; Zhan, D. R. T.; Gessner, T. *J. Mater. Chem. A* **2013**, *1*, 7576–7583.
55. Wei, Q.; Mukaida, M.; Naitoh, Y.; Ishida, T. *Adv. Mater.* **2013**, *25*, 2831–2836.
56. Gasiorowski, J.; Menon, R.; Hingerl, K.; Dachev, M.; Sariciftic, N. S. *Thin Solid Films* **2013**, *536*, 211–215.
57. Kim, N.; Lee, B. H.; Choi, D.; Kim, G.; Kim, H.; Kim, J.-R.; Lee, J.; Kahng, Y. H.; Lee, K. *Phys. Rev. Lett.* **2012**, *109*, 106405.
58. Takano, T.; Masunaga, H.; Fujiwara, A.; Okuzaki, H.; Sasaki, T. *Macromolecules* **2012**, *45*, 3859–3865.
59. Xia, Y.; Ouyang, J. *ACS Appl. Mater. Interfaces* **2012**, *4*, 4131–4140.

60. Xia, Y.; Ouyang, J. *ACS Appl. Mater. Interfaces* **2010**, *2*, 474–485.
61. Ouyang, J.; Xu, Q.; Chu, C.-W.; Yang, Y.; Li, G.; Shinar, J. *Polymer* **2004**, *45*, 8443–8450.
62. Kim, J. Y.; Jung, J. H.; Lee, D. E.; Joo, J. *Synth. Met.* **2002**, *126*, 311–316.
63. Nardes, A. M.; Kemerink, M.; Janssen, R. A. J. *Phys. Rev. B* **2007**, *76*, 085208.
64. Stöcker, T; Köhler, A.; Moos, R. *J. Polym. Sci., Part B: Polym. Phys.* **2012**, *50*, 976–983.
65. Crispin, X; Marciniak, S; Osikowicz, W.; Zotti, G.; Denier Van Der Gon, A. W.; Louwet, F.; Fahlman, M.; Groenendaal, L.; De Schryver, F.; Salaneck, W. R. *J. Polym. Sci., Part B: Polym. Phys.* **2003**, *41*, 2561–2583.
66. Jönsson, S. K. M.; Salaneck, W. R.; Fahlman, M. *J. Electron Spectrosc. Relat. Phenom.* **2004**, *137-140*, 805–809.

Chapter 8

Polymer−Ceramic Nanocomposite Dielectrics for Advanced Energy Storage

Sasidhar Siddabattuni[1,2] and Thomas P. Schuman[*,2]

[1]Department of Chemistry, Sri Sathya Sai Institute of Higher Learning, Vidyagiri, Prashanthi Nilayam, Andhra Pradesh 515134, India
[2]Chemistry Department, Missouri University of Science and Technology, 400 W. 11th Street, Rolla, Missouri 65409, U.S.A.
[*]E-mail: tschuman@mst.edu.

Inclusions of nanosized ceramic particles in a polymer matrix influence the dielectric properties of their composite more when compared to conventional microcomposites through a greater interfacial contact area between the filler particles and the polymer per volume. This review summarizes the research of and potential for polymer−ceramic nanocomposite use as electrostatic energy storage materials. A particular focus is made on the role of the interfacial region, properties and characterizations, and the significance of controlling the nanofiller surface for improving the energy storage capacity by nanocomposite dielectric capacitor films. Various types of surface modifications and methodologies that have been applied to ceramic nanofillers in an effort to control dielectric properties of the polymer nanocomposites are reviewed. Special mention is made of new structure-property-relationships at the interface through altering the chemical and electronic nature of the particle-polymer interface. Recent research results suggest that ligands, as a function of their electron density influence at the filler surface, reduce filler surface conductivity to maximize the dielectric energy storage density while reducing dielectric losses. The article concludes by briefly revisiting theoretical models of the filler-polymer interface structure property as an influence on properties of polymer−ceramic nanocomposite dielectrics.

In Polymer Composites for Energy Harvesting, Conversion, and Storage; Li, L., et al.;
ACS Symposium Series; American Chemical Society: Washington, DC, 2014.

Introduction

Various mobile electronic devices, stationary power systems, hybrid electric vehicles and pulse power applications require electrical energy storage devices. In particular, due to the growing requirements for compact, low-cost electronics and electrical power systems, there is a growing need for capacitors that can accumulate a large amount of energy and deliver it nearly instantaneously, which is generally difficult to achieve with other energy storage technologies like batteries or ultracapacitors. "Pulse power," as ability to store and deliver nearly instantaneously a large amount of power, is needed for a variety of military and commercial applications. Over time, these applications demand ever higher energy and power densities, more power stored per less volume, as well as higher charge-discharge current capabilities (*1*, *2*).

Future pulsed-power and power electronic capacitors suggest dielectric material goals with ultimate energy storage densities of >30J/cm^3, operating voltages of >10kV, and millisecond-microsecond charge/discharge times with reliable operation near the dielectric breakdown limit. Importantly, at 2 and 0.2 J/cm^3, respectively, the operating characteristics of current-generation pulsed power and power electronic capacitors utilizing either ceramic or polymer based dielectric materials remain significantly short of these goals. A nearly order-of-magnitude improvement in energy density will require the development of dramatically different materials behavior that substantially increase intrinsic dielectric energy densities while reliably operating as close as possible to the dielectric breakdown limit (*3*).

In general, the energy density (U) of a dielectric material can be derived from Equation 1, where E is applied electric field and D is electric displacement. Dielectric materials store electrical energy as work in

$$U = \int EdD \tag{1}$$

the form of charge separation when the electron distributions around constituent atoms or molecules are polarized by an external electric field (*2*, *4*). The energy stored in a capacitor is equal to the work done, W, in charging the capacitor that can be released when a load is connected, as expressed in Equation 2, where C is the capacitance and V is the voltage applied. The maximum energy stored, W_{max}, is a function of the maximum voltage that can be applied without a catastrophic arc discharge through the dielectric material of the capacitor, called dielectric breakdown voltage (where $V=V_b$), and capacitance (Equation 3) (*5*).

$$W = \frac{1}{2}CV^2 \tag{2}$$

$$W_{\max} = \frac{1}{2}CV_b^{\,2} \tag{3}$$

In Polymer Composites for Energy Harvesting, Conversion, and Storage; Li, L., et al.;
ACS Symposium Series; American Chemical Society: Washington, DC, 2014.

For a simple linear response of electrical displacement as a function of applied voltage by the dielectric material, the maximum energy density (U_{max}) is defined by Equation 4, where ε_r is the relative dielectric permittivity, E_b is the dielectric breakdown strength (DBS, in volts per thickness), ε_o is the permittivity of free space (8.8542×10^{-12} F/m), *A* is the electrode contact area of the dielectric, and *t* is the electrode separation thickness. In general, the DBS of a dielectric material decreases with increases in specimen thickness, operating temperature, frequency, and/or humidity (*3–5*).

$$U_{\max} = \frac{W_{\max}}{volume} = \frac{\frac{1}{2}CV_b^2}{A\times t} = \frac{1}{2}\frac{\varepsilon_0\varepsilon_r(A/t)V_b^2}{A\times t} = \frac{1}{2}\varepsilon_0\varepsilon_r\left(\frac{V_b}{t}\right)^2 = \frac{1}{2}\varepsilon_0\varepsilon_r(E_b)^2 \qquad (4)$$

The permittivity or dielectric constant of a dielectric material can be expressed as shown in Equation 5 where ε' and ε'' are the real and imaginary parts, respectively, of the complex permittivity, ε^*, and $j=\sqrt{-1}$ The real part of the permittivity, i.e., the permittivity or dielectric constant, indicates the ability of the material to store energy from applied electric field. Mechanisms to store electrical energy are enhanced through polarization and relaxation of the dielectric as space charge motion, dipole orientation, ionic motion, and electron motion. The permittivity of a dielectric material is a constant in D.C. fields when there is not significant dielectric saturation and decreases with increasing D.C. fields upon dielectric saturation.

Under A.C. fields, permittivity of a dielectric material can strongly depend on the frequency of the applied field with respect to the material's ability to respond to applied field by polarization and relaxation mechanisms. The imaginary component of the permittivity is called dielectric loss that is a result of a non-elastic polarization or relaxation per material structure and frequency dependence of its polarization mechanisms. For an energy storage device, dielectric loss should be as low as possible (*2*, *5*).

$$\varepsilon^* = \varepsilon' - j\varepsilon'' = \varepsilon_0\varepsilon_r - j\varepsilon'' \qquad (5)$$

This article takes special interest in the imaginary permittivity since, while ideally zero, it is often a material limiting factor for a successful device. The ratio of imaginary part to the real part of the permittivity is defined as a dissipation factor, DF, also known as a loss tangent as it is proportional to dielectric loss as shown in Equation 6. In general, dielectric loss results from the sum of space charge distortion, dipolar, interfacial-ionic motion, and conduction losses.

Distortional losses are related to electronic and ionic polarization mechanisms. The interfacial loss originates from an excessively polarized interface induced by, e.g., fillers in the composites and specifically the movement of ions or rotation of the atoms, molecules, or particulates in an alternating field. Conduction loss is attributed to D.C. resistive conductivity of the material, representing a current density as a flow of charge per area through the dielectric material. In general, dielectric loss increases with increase in temperature,

In Polymer Composites for Energy Harvesting, Conversion, and Storage; Li, L., et al.;
ACS Symposium Series; American Chemical Society: Washington, DC, 2014.

humidity, voltage and frequency of the applied voltage (*5*). Importantly, loss performs work on the material as a dissipative relaxation in the form of heat energy through viscous or ion motion ($\mu \cdot d$) or resistive flow ($I^2 \cdot R \cdot t$).

$$\text{Dissipation factor (DF)} = \tan\delta = \frac{\varepsilon''}{\varepsilon'} \quad (6)$$

As presented in Equation 4, the maximum energy density that can be stored in a linear capacitor is proportional to the permittivity of the dielectric material and to the square of the breakdown strength of the dielectric material. Improvements in permittivity, dielectric film thickness, and breakdown strength are thus sought to increase energy storage density of dielectric capacitors. A low dielectric loss is preferred both to reduce dissipated energy and thermal sensitivity. Generally, a dissipation factor under 0.001 (0.1%) is considered to be quite low, smaller being better, and 5% (0.05) or larger is considered high but acceptable loss values are application dependent.

Polymer−Ceramic Nanocomposites (PCNs)

Inorganic ceramic materials can have very large permittivities but are limited by relatively small breakdown strengths, poor processability, and mechanical properties due to high sintering temperature, volumetric shrinkage during sintering, dislocations, and residual porosity. On the other hand, organic based polymers typically have higher breakdown strengths, viscoelastic mechanical properties and excellent processability but suffer smaller permittivity. Miniaturization and the current need for high-power density, high voltage capacitors and power-storage devices have stimulated a new field of research interest in PCNs.

By incorporating high permittivity inorganic nanoparticles into a polymer matrix with low dielectric loss and high breakdown strength, one may be able to develop new composite materials that have improved dielectric properties, dielectric strength, permittivity and dielectric losses, and retain unique attributes of polymers (*4*, *6–8*). While the conventional microcomposites can alter certain desired properties of the composite materials, e.g., mechanical and thermal properties, it often comes with the compromise of other properties being negatively affected in, e.g., their electrical properties. Interestingly, the newly emerging PCNs may provide significant film thickness, polycrystalline loss, field concentration, conductivity and breakdown resistance improvements as combined electrical, thermal and mechanical properties of great benefit to the capacitor industry (*9*, *10*).

In designing the PCNs, a compromise of DBS against dielectric permittivity ultimately results, e.g., when improving permittivity through raised filler content that approaches a percolation threshold, to increase the energy storage density with the added challenge of maintaining low dielectric loss. Consequently, much research is dedicated to improvement of polymer nanocomposite materials through a better understanding of the physical phenomena governing composite dielectric permittivity as a function of filler concentration and its influences on breakdown

field strength. As both of these issues involve the polymer-filler interface, a better understanding of the chemistry and structure at the filler-polymer interface is a priority (*2*).

Role of Polymer−Ceramic Interface

The transition from microparticles to nanoparticles yields dramatic changes in physical properties. Nanoscale materials have larger surface areas for a given volume. Since many important chemical and physical interactions are governed by surfaces and surface properties through chemical activity, a nanostructured material can have substantially different properties than a larger-dimensional material of the same composition (*11*). Thus, the most distinctive feature of polymer nanocomposites in comparison with conventional microcomposites is the participation of large interfacial surface area between the nanoparticles and the polymer matrix.

The smaller the radius r of the embedded nanoparticles, the larger the surface area to volume ratio by a factor $-(3/r^2)$, which leads to larger interfacial regions (*12*, *13*). For filler nanoparticles at modest loadings, the surface area and surface tension/energy associated with the interfaces becomes dominant in nanocomposites compared to microcomposites (see references to Lewis model, below). The properties of interfacial areas, often referred to as having finite thickness as an interfacial volume or phase, may differ substantially from either the base polymer matrix or the nanoparticle material (*14*, *15*).

PCNs have exhibited enhanced electrical breakdown strength and voltage endurance compared to their unfilled or micrometer sized particle filled counterparts (*14*, *15*). Improvement in the dielectric properties of PCNs compared to pure polymer matrix could be due to several factors such as change in polymer morphology at the interface and local charge distributions because of nanoparticle surface; change in density and the energy depth of electron 'trap' sites due to change in local structure at the interface, which affect charge mobility and electron site state stability; increase in probability for scattering mechanisms, and so forth. Thus, there may be potential to fabricate improved dielectric materials by manipulating the interface between filler and matrix without loss of the dielectric characteristics of the bulk material (*16*), except characteristics strictly related to particle size (*12*). Theoretical arguments have been made suggesting that large, inclusion-matrix interfacial areas should potentially afford greater polarization levels, dielectric response, and breakdown strength (*3*, *17–19*) though currently the polarizations at interfacial areas can account for a majority of dielectric loss. Thus, electrical control of the interface is said to play a major role in the property enhancement of PCNs leading to enhanced energy storage capacity.

The interfacial region can act as dielectric and store energy unto itself in a nanocomposite dielectric, which is a summation of stored energy in each constituent phase and the interfacial volume between these two phases.

$$U = f_1 U_{e1} + f_2 U_{e2} + f_{12} U_{e12} \quad (7)$$

In Polymer Composites for Energy Harvesting, Conversion, and Storage; Li, L., et al.;
ACS Symposium Series; American Chemical Society: Washington, DC, 2014.

where f_1 , f_2 , f_{12} , are volume fractions of 1st phase, 2nd phase, and interfacial phase, respectively, and U_{e1}, U_{e2}, and U_{e12} are energy density in 1st phase, 2nd phase and interfacial phase, respectively. The potential for large amounts of energy storage within the interfacial volume of the PCNs demands a clear understanding of interfacial effects related to polymer-filler interaction, and its modification, to improve nanocomposite properties.

Control of the Polymer−Particle Interface

As the properties of PCNs are influenced by the interfacial region, design and control of the interface becomes very important. Failure to control the interfacial energy can simply result in agglomeration of nanoparticles in polymer matrix leading to undesirable film quality, through phase separation and inhomogeneity (*20*, *21*). Hydrophilic nanoparticles in a hydrophobic polymer matrix provide the surface energy driving force toward minimization of interfacial contact area and system cumulative surface energy, resulting in aggregation and poor interfacial contact and adhesion. For example, agglomeration of ceramic filler particles gives rise to paths for electron conduction of high dielectric loss as well as undesirable porosity, which results in dielectric failures at much lower field strengths (*4*).

Thus, providing for proper dispersion of nanoparticles in polymer plays an important aspect in PCN synthesis and design. A means to reduce interfacial tension, equalizing the surface energies of the filler and polymer at their point of contact and stabilization of the dispersion to prevent agglomeration after the dispersion has been produced, are critical to these. Without proper dispersion and distribution of filler particles in polymer, the high surface area of nano-sized particles is compromised and the aggregates act as failure nucleation site defects rather than as more uniform, better dispersed field loads over more uniform permittivity distribution and across durable interfacial regions that were promised through design of an interface and use of nanoparticles (*22*).

Numerous methodologies have been utilized to synthesize PCNs of excellent dispersion, toward creation of strong interfacial regions. Dispersion of nanoparticles in polymer matrix can be obtained by, e.g., direct, high shear mixing; in-situ polymerization in the presence of nanoparticles; in-situ precipitation of nanoparticles within the polymer matrix; or by an ex-situ method, where the particles are surface modified and the surface modified preformed nanoparticles are incorporated into the polymer matrix (*23*, *24*).

Inter-nanoparticle interactions, through strong polar-polar interaction and differential surface energies compared to the polymer matrix, are so strong that the shear force provided by conventional direct high shear mixing facilities often fails to break apart nanoparticle agglomerates in either polymer melt or solution, though prewetted particles have been observed to be more readily dispersed (*24*). For example, $BaTiO_3$, SiO_2 and Al_2O_3 particles are often found agglomerated in polymer matrices. Though a high energy sonication process has been found to be an effective method to improve the particle dispersion, the energy of high frequency, high energy sonication is still insufficient to disperse finer nanoparticles (*23*, *24*).

In Polymer Composites for Energy Harvesting, Conversion, and Storage; Li, L., et al.;
ACS Symposium Series; American Chemical Society: Washington, DC, 2014.

An in-situ polymerization method provides a means to disperse the nanofillers in the monomer or monomer solution by following standard polymerization of the resulting mixture (*23*). A few examples are nano SiO_2/Nylon 6 (*25*), TiO_2/poly(methyl methacrylate) (PMMA) (*26*), or calcium carbonate ($CaCO_3$)/PMMA (*27*). One advantage of the in situ polymerization method is the potential to graft polymer directly onto the particle surface, yielding well-dispersed PCNs. Appropriate dispersion of the nanofiller in the monomer is a key result of this method, which may require modification of the nanoparticle surface with suitable initiator or coupling agents functional group and proper control of the processing conditions.

Another method for producing nanoparticle-filled polymer dispersions is an in-situ nanoparticle processing or formation. By mixing ceramic metal oxide precursor with a polymer, followed by a sol-gel reaction, well dispersed ceramic-polymer nanocomposites can be prepared. The in situ precipitation method also provides tremendous opportunity to tune the structure and interface of PCNs (*28*).

An alternate approach for improved dispersion is to utilize preformed, commercially available nanoparticles but lower the surface energy of the particles to be similar to that of the polymer by surface modification with coupling agent. Organic surface modified (shell), inorganic (core) nanofillers are then blended in a polymer matrix through high shear, in a solution or melt process, to form the PCN. In general, surface modification of inorganic fillers means introduction of organic and/or inorganic coatings onto the fillers, which utilize physical and chemical bonding interactions between the fillers and the modifiers (*23*). Surface modification of nanoparticles can be obtained by using suitable surfactants that yield weak adsorptive interfaces, e.g., titanates or surfactants/dispersants, or stronger covalent interfacial bonding to the surface of metal oxide nanoparticles, e.g., using phosphates, phosphonates, or silanes as coupling agents or dispersants which have the capability to yield stable organic to oxide interface complexation (*29*, *30*).

Effect of Interface Manipulation on Dielectric Properties of PCNs

Examples of the interfacial manipulation of various ceramic nanoparticles using above mentioned methods, and their resulting influence on dielectric properties of the resulting PCNs in different polymer matrices, is discussed below.

In Situ Methods

Guo et al. effectively prepared dispersed isotactic polypropylene grafted $BaTiO_3$, TiO_2 and ZrO_2 composites via an in situ metallocene catalyzed polymerization technique (*3*, *31*). The composites exhibited very low leakage current densities, dielectric permittivity as high as 6.1, and dielectric breakdown resistance as high as ~ 600 MV/m for 13.6 vol.-% $BaTiO_3$/PP composites. Breakdown resistance results of the composites indicated that inclusion of the

In Polymer Composites for Energy Harvesting, Conversion, and Storage; Li, L., et al.;
ACS Symposium Series; American Chemical Society: Washington, DC, 2014.

metal oxide nanoparticles can significantly enhance the dielectric breakdown resistance. Energy densities of the resulting PCNs were estimated to be as high as 9.4 J/cm^3.

As a part of the in situ polymerization process, nanoparticles were coated with methylaluminoxane (MAO) co-catalyst. As a result of MAO treatment, the nanoparticles have deposited on their surface a thin layer of Al_2O_3 (ε_r~10) created by ambient exposure of the MAO coated nanoparticles, as shown in Figure 1. An Al_2O_3 layer at the interface was anticipated to benefit both breakdown stability and permittivity enhancement through creation of a gradient permittivity decrease and reduced field contrast between the high ε_r nanoparticles and the lower ε_r polymer, to reduce localized field concentration. It was speculated that, in these well-dispersed 0-3 composites, interfaces between the ceramic nanoparticle and polymer phases would create effective electron scatters and transport centers, thus reducing the breakdown probability. Moreover, well-dispersed ceramic nanoparticles should prevent degradation tree growth and thus increase the long term breakdown strength.

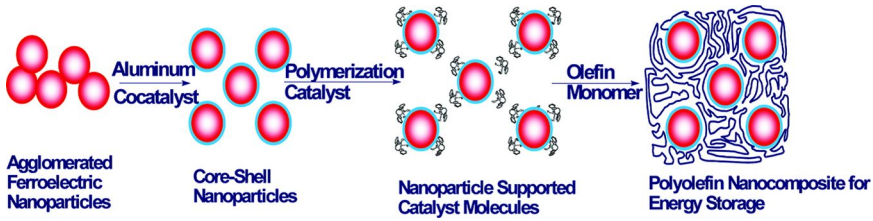

Figure 1. Synthesis of polypropylene-metal oxide nanocomposites. Reproduced with permission from reference (3). Copyright 2010 American Chemical Society.

Similar to Guo et al., Fredin et al. also reported the effective method for synthesizing highly dispersed composites of isotactic polypropylene grafted onto $BaTiO_3$, ZrO_2, MgO, $SrTiO_3$, and $Ba_{0.5}Sr_{0.5}TiO_3$ nanofillers via in situ metallocene catalyzed polymerization technique employing MAO co-catalyst for the polymerization reaction that generates Al_2O_3 layer at the interface. A variable Al_2O_3 layer thickness was achieved via a layer-by-layer MAO coating process (*32*).

The dielectric properties of the PCNs were reported to be remarkably insensitive to the particle identity but increasing the Al_2O_3 thickness at the nanoparticle/polymer interface significantly reduced the high field loss at applied voltages close to breakdown resistance. Such PCNs exhibited higher permittivity and breakdown fields, relatively less dielectric losses, and thus greater energy storage density than the isotactic polypropylene polymer matrix.

Importantly, dielectric loss of the composites was reported to be largely proportional to the internal, i.e., interfacial, surface area between filler and polymer within the sample. Increasing the internal nanoparticle surface area

In Polymer Composites for Energy Harvesting, Conversion, and Storage; Li, L., et al.;
ACS Symposium Series; American Chemical Society: Washington, DC, 2014.

increased the dielectric loss approximately linearly. Proper adjustment of the materials parameters yielded recoverable energy storage capacity as high as 2.05 J/cm^3 for 6.6 vol.-% loaded MgO/PP nanocomposite, and total energy storage capacity as high as 15.6 J/cm^3 for 7.5 vol.-% loaded ZrO_2/PP nanocomposite at voltages close to breakdown.

Homogeneous $Ba_{0.7}Sr_{0.3}TiO_3$ (BST)/polyimide nanocomposites were prepared by Beier et al. via an in situ polymerization, whereby extremely small (sub-10nm) BST nanocrystals were blended with the monomers (1,3-bis (4-aminophenoxy)benzene and pyromellitic dianhydride) prior to spin-casting and thermal imidization (*33*). At a 10 vol.-% BST particle loading, PCNs with 24% increase in breakdown resistance, about 50% reduction in the dielectric loss (tan $\delta > 0.04$; 4%) and maximum calculated energy storage density more than twice (~ 107% increase) that of pure polymer were reported. Hysteresis losses for the ferroelectric filler composite were not reported. Enhanced interfacial interactions that mitigate space-charge buildup at the interface, suppressed interfacial polarization, and/or scattering effects were thought to be the reason behind the improved dielectric properties. The dielectric loss indicates there are still polar losses associated with the filler interface; however, the polyimide based PCNs exhibited excellent dielectric and thermal stability compared to poly(vinylidene difluoride) (PVDF) based $BaTiO_3$ PCNs.

Well-dispersed, calcium copper titanate (CCTO)/polyimide nanocomposites with high dielectric permittivity were prepared via in situ polymerization by Yang et al (*34*). The composites exhibited remarkably enhanced dielectric permittivity of ~171, which is about 50 times higher than pure polyimide, but a large tan δ of ~0.45 at 100 Hz was observed at a critical nano-CCTO concentration of 16 vol.-%. The relatively low concentration of nanofiller retained the flexibility of polymer.

Although the resulting tan δ value was somewhat higher than that of polyimide/CCTO microcomposites (tan δ~0.2) (*35*), it was less than that of the analogous but ferroelectric PVDF/nano-CCTO polymer matrix composites (tan δ~48) (*36*) at 100Hz and room temperature. It was suggested that a high dielectric permittivity originated from large internal interfacial area and remarkable Maxwell-Wagner-Sillars effect at percolation in which nomadic charge carriers were blocked at internal CCTO-polyimide interfaces. Facile processability, flexibility, and excellent dielectric behavior make polyimide/CCTO PCNs as potential candidates for practical application in high charge storage capacitors and other electronic devices but limited in, e.g., pulse power type applications due to ferroelectric hysteresis and/or dissipation factor losses.

Xie et al. prepared the $BaTiO_3$/poly (methyl methacrylate) (PMMA) nanocomposites via in situ atom transfer radical polymerization (ATRP) (*37*). It was observed that the PCNs prepared via an ATRP method exhibited excellent quality of polymer-particle dispersion, lower dielectric losses, and higher thermal conductivity compared to the PCNs prepared through traditional solution blending methodology. Cooling becomes an important technical challenge in the modern microelectronics devices and high power equipment where ferroelectric, high dielectric constant nanoparticles are used (*38*). Therefore, low dielectric loss and high thermal conductivity are highly desirable for high permittivity polymer nanocomposites.

In Polymer Composites for Energy Harvesting, Conversion, and Storage; Li, L., et al.;
ACS Symposium Series; American Chemical Society: Washington, DC, 2014.

Recent advances reveal that coating of filler particles with an insulation layer assist in reduction of dielectric loss (*39*). Moreover, thermal conductivity of nanocomposite is also affected by the interface structure as interfacial thermal resistance. Strong adhesion between nanoparticles and polymer matrix will improve transfer of thermal vibrations and enhance the thermal conductivity of polymer nanocomposites (*40*). Lower dielectric loss and improved conductivity of the $BaTiO_3$/PMMA nanocomposites prepared via in situ ATRP polymerization were attributed to strong interfacial bonding between $BaTiO_3$ and PMMA polymer.

Polizos et al. prepared PCNs composed of in situ synthesized TiO_2 nanoparticles (≤ 5nm particle diameter) in an epoxy matrix (at 2.5 wt.-% ~ 0.76 vol.-%) (*41*). Nanoparticles were uniformly dispersed in epoxy polymer compared to the quality of ex situ nanoparticles dispersion in epoxy. Significant reduction in the dielectric loss and a 20% increase in the dielectric breakdown strength were observed compared to pristine polymer. Improvement in the dielectric properties of the in situ synthesized TiO_2 nanocomposites in epoxy polymer was attributed to a restriction in the mobility of the polymer chains due to stronger polymer-particle interface.

Tuncer et al. have reported the dielectric properties of in situ synthesized nanoparticulate TiO_2 in polyvinyl alcohol (PVA) polymer for cryogenic capacitor applications (*42*). The dielectric breakdown strength of the PCNs between 10 and 30 wt.-% (~3.3 to 11.7 vol.-%) TiO_2, measured under liquid nitrogen, showed significant increase in the dielectric strengths compared to unfilled PVA.

Ex Situ Methods

Tang et al. reported a novel approach to prepare high energy density nanocomposite capacitors with fast discharge speed (*43*). The PCNs were prepared with a high aspect ratio $Ba_{0.2}Sr_{0.8}TiO_3$ nanowires in PVDF melt that were quenched in ice water to achieve the highest breakdown strengths and energy storage properties. The melt quenching process was employed to modify the crystallization of the PVDF in the nanocomposites. Based on the FTIR spectra, Tang explained that the quenched PVDF is primarily of γ phase (840, 812, 775 cm^{-1}) while the unquenched or annealed PVDF is dominated by the β phase (see Figure 2). The γ-PVDF has reduced ferroelectric loss. As expected (and desirable), the quenched PVDF films gave higher dielectric strengths (~536.1 MV/m) compared to β phase PVDF films (~443.8 MV/m). To increase compatibility between the filler and matrix, the $Ba_{0.2}Sr_{0.8}TiO_3$ nanowires were treated with ethylenediamine since amines are well-known to provide strong interaction with PVDF. Dispersion and charge uniformity at the ceramic/polymer interface were improved.

The maximum energy storage density of the resulting PCNs, calculated from D-E loop measurement, was reported to be ~14.8 J/cm^3 at a dielectric breakdown resistance field (~450 MV/m field) and at a 7.5 vol.-% particle concentration. The nanocomposites also exhibited relatively low hysteresis and capable of sub-microsecond discharge. The improved energy storage efficiency was attributed to a combination of non-ferroelectric structure (pyroelectric

In Polymer Composites for Energy Harvesting, Conversion, and Storage; Li, L., et al.;
ACS Symposium Series; American Chemical Society: Washington, DC, 2014.

phase) of the BST, the quenching process to obtain a γ-PVDF phase, a stronger polymer-particle interface, and homogenous dispersion due to surface functionalized BST. The discharge speed of the nanocomposites was reported to be only 2.3 μs across a 20 kΩ resistor, which was faster than commercial biaxially oriented polypropylene (2.8 μs) at the same RC time constant.

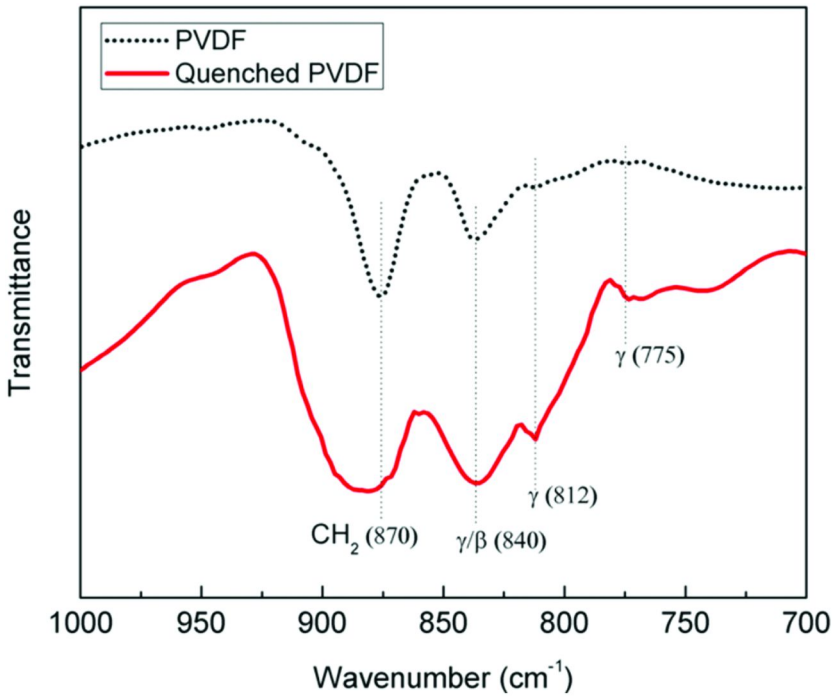

Figure 2. FTIR spectra of PVDF, before and after quenching process. Reproduced with permission from reference (43). Copyright 2013 American Chemical Society.

Utilizing the quenching process and/or surface functionalization using coupling agents, Tang et al. also reported other PCN systems (*44*, *45*) with enhanced dielectric properties and fast discharge speeds. Energy storage densities as high as 12.4 J/cm^3 were obtained for 7.5 vol.-% silane (3-aminopropyltriethoxysilane) functionalized TiO_2 nanowires in PVDF composite (*44*). In comparison, 10.4 J/cm$_3$ energy storage density was obtained for a 17.5 vol.-% surface functionalized $BaTiO_3$ nanowires in poly(vinylidene fluoride-trifluoroethylene-chlorofluoroethylene) (P(VDF-TrFE-CFE)) matrix composite (*45*).

In Polymer Composites for Energy Harvesting, Conversion, and Storage; Li, L., et al.;
ACS Symposium Series; American Chemical Society: Washington, DC, 2014.

In order to control the interfacial interactions and to obtain homogeneously dispersed PCNs, Kim et al. modified the surface of $BaTiO_3$ nanoparticles with pentafluorobenzyl phosphonic acid (PFBPA) or polyoxyethylene oxide organophosphonate coupling agents (*20*, *46*). Surface functionalization decreased the degree of particle aggregation when dispersed in poly(vinylidenefluoride-co-hexafluoropropylene) or polycarbonate as matrices, respectively. They reported increased dielectric constant, dielectric breakdown strength, and lower dielectric loss of the nanocomposites compared to untreated nanocomposites. Particle concentrations up to 50 vol.-% of the surface functionalized particle in-polymer were achieved in the nanocomposites that gave maximum estimated extractable energy density of about 7-8 J/cm^3.

Li et al. has shown excellent progress in the surface functionalization of TiO_2 for incorporation into ferroelectric copoly (vinylidene fluoride-trifluoroethylene-chlorotrifluoroethylene) (P(VDF-TrFE-CTFE)) (*47*). Rod-shaped TiO_2 nanoparticles were hydrogen peroxide treated that activated the surface of the nanoparticles for subsequent coating with Ba-OH surface groups through a simple reflux reaction of the TiO_2 with a CO_2-free barium hydroxide solution. TiO_2/P(VDF-TrFE-CTFE) nanocomposites made with these particles exhibited a much-improved energy density compared with the neat polymer. For 10 vol.-% modified-TiO_2, the energy density was reported to be ~6.9 J/cm^3 at 200 MV/m, which represents a ~45 % increase relative to the neat polymer matrix of energy density of ~4.7 J/cm^3 at the same field. Dielectric loss tangents showed little variation as a function of the TiO_2 concentration, indicating that the surface-modified nanoparticles were well-dispersed and homogenous in the polymer matrix and consequently, the dielectric loss mainly originates from the polymer matrix but was not significantly decreased upon the addition of particles.

Li et al. reported preparation of a different ferroelectric copolymer, P(VDF-CTFE), with telechelic phosphonic acid groups as shown in Scheme 1. Reactive phosphonate terminal groups of the polymer were subsequently utilized for direct coupling with ZrO_2 fillers to yield covalent-bonded PCNs (*48*). It was demonstrated that covalent assembly of the telechelic polymer matrix and ceramic filler not only led to highly dispersed nanofillers without additional surface modification but also provided composite stability and offered enhanced interfacial interactions for greater polarization response under the applied fields. Interestingly, the PCNs exhibited remarkable dielectric breakdown resistance and greatly improved energy densities compared to the matrix. The reported energy density was ~11.2 J/cm^3 for 9.1 wt.-% ZrO_2 in P(VDF-CTFE) at 270 MV/m, which corresponded to a ~60% increase in comparison to the polymer matrix. Improvements in energy storage capability of the nanocomposites has been rationalized on the changes of polymer microstructure and arise of the electric displacement induced by uniformly dispersed nanofillers.

Siddabattuni et al. modified the surface of $BaTiO_3$ nanoparticles (~35 nm diameter) utilizing a bi-functional organophosphate coupling agent, 2-aminoethyl dihydrogen phosphate for dispersion and covalent reactivity within the epoxy polymer matrix (Figure 3) (*6*). It was reported that the phosphate group of the coupling agent bonds mixed bi- and tri-dentate with the surface of oxide nanofillers. The ligand both aid in dispersion and provide a free amino group

of the reagent that reacts with the epoxy polymer to produce a covalent bond interface between the particle surface and the polymer matrix. Hydrogen peroxide pretreatment was utilized before surface modification to greatly improve the reactivity of $BaTiO_3$ toward the phosphate ligand compared to untreated particles. Interfacially covalent bonded $BaTiO_3$/epoxy PCNs reduced MW relaxation loss (tan δ, @10^{-2} Hz), raised the matrix glass transition temperature, and enhanced the dielectric breakdown resistance compared to unmodified particle dispersions or dispersions of particles produced with a physisorbed surfactant. At a 5 vol.-% concentration of surface modified $BaTiO_3$ inclusions in epoxy yielded calculated energy storage densities about 175% higher compared to the pure epoxy for a 70 μm thick dielectric film, whereas composite films of 30 μm achieved calculated energy densities of 4.6 J/cm^3.

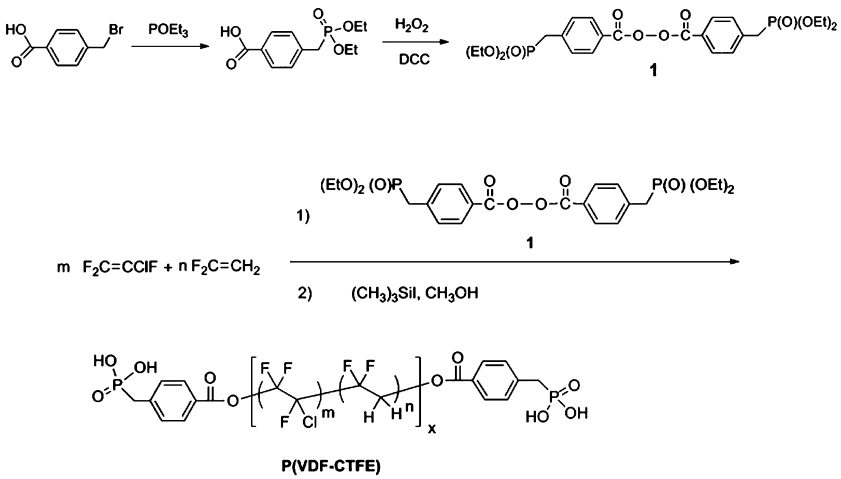

Scheme 1. Synthesis of phosphonic acid terminated P(VDF-CTFE) using functional benzoyl peroxide initiator (1). Reproduced with permission from reference (48). Copyright 2010 American Chemical Society. (Note: $POEt_3$ - triethyl phosphite; DCC – dicyclohexylcarbodiimide.)

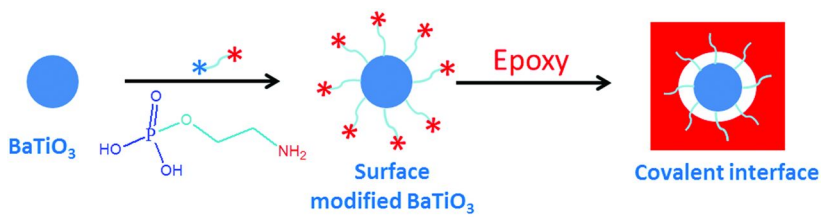

Figure 3. Synthesis of covalent bonded $BaTiO_3$/epoxy nanocomposite.

In Polymer Composites for Energy Harvesting, Conversion, and Storage; Li, L., et al.;
ACS Symposium Series; American Chemical Society: Washington, DC, 2014.

Use of polymeric surface modifying agents like polydopamine and poly(vinyl pyrrolidone) have been also reported in the literature, which have enhanced the quality of dispersion between ferroelectric ceramic nanoparticles and ferroelectric polymers (*49*, *50*). Improvement in the dielectric properties of the resulting PCNs were reported to be due to a stronger interface between polymer and particle.

Structure-Property-Relationship at the Interface of PCNs

The choice of functional groups on the particle surface can affect the interfacial structure between particles and polymer in PCNs and hence their dielectric properties and most work has studied the dispersion of particles. However, little experimental work has examined through structure-property methods how the electrical nature of a polymer−particle interface perturbs electrical properties toward a more optimized dielectric composite design. For example, Roy et al. modified the surface of silica nanoparticles with three different silane coupling agents, triethoxyvinylsilane (TES), n-(2-aminoethyl) 3-aminopropyltrimethoxysilane (AEAPS), and hexamethyldisilazane (HMDS) (*51*).

AEAPS and HMDS are both polar molecules that create an incompatible interface with the host polymer, XLPE. TES is non-polar and provides an opportunity for covalent bonding (and thus a strong interface) within an addition polymerizing polymer matrix. There were incremental improvements in dielectric breakdown resistance for the AEAPS and HMDS modified nanosilica composites and TES nanosilica filled composites exhibited a still higher breakdown strength. Voltage endurance test results exhibited a similar trend.

An incremental improvement in endurance times for the surface modified nanosilica composites was reported. The proposed mechanism leading to the differences in breakdown strength, due to surface treatment of the nanofillers, was either due to the defect reduction via chemical linkage between particle and polymer or, due to the introduction of deep trap sites in the polymer, due to the surface modifier groups. However, actual influence of the surface groups on materials properties that enabled higher breakdown strength was not determined.

Siddabattuni et al. have investigated how the structure of the interfacial layer between filler and polymer influences dielectric properties of the composite (*6*, *16*, *29*). A series of self-assembled monolayer structures, from electron rich to electron poor organophosphate coupling groups, were applied to titania and barium titanate nanoparticles and then applied the surface modified particles within dielectric composites of epoxy polymer. In this way, the role of chemical and electronic nature of polymer-particle interface on the dielectric properties of the filler, and subsequent effect on the nanocomposites, was investigated.

The dielectric property characterization data indicated significant reductions in leakage current, and dielectric loss, and improvement in dielectric breakdown strength resulted when electropositive, i.e., electron deficient, ligand groups were located on the particle surface. Increasingly electronegative, i.e., electron-donating, organophosphate ligand groups on the particle surface resulted in larger D.C. leakage current, tan δ loss, and reduced breakdown strengths.

In Polymer Composites for Energy Harvesting, Conversion, and Storage; Li, L., et al.;
ACS Symposium Series; American Chemical Society: Washington, DC, 2014.

Permittivity was not significantly affected but was a function of the volume concentration of the high permittivity filler except at low (~10^{-2} Hz) frequency where Maxwell Wagner relaxation raised imaginary and complex permittivity.

A list of organophosphate coupling agent structures used in these studies is shown in Figure 4. Electrostatic potential maps of the organophosphate surface modifier series (Figure 5) show strong electron withdrawing group controls the extent to which the aromatic ring is electropositive, i.e., electron withdrawn, nature of the ligand within the series.

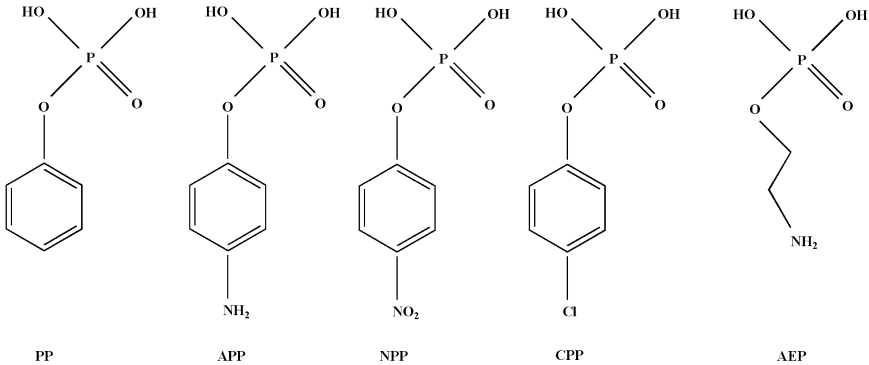

Figure 4. Molecular structures of organophosphate ligands: phenyl phosphate (PP) ; aminophenyl phosphate (APP); nitrophenyl phosphate (NPP); chlorophenyl phosphate (CPP); and aminoethyl phosphate (AEP). Reproduced with permission from reference (16). Copyright 2013 American Chemical Society.

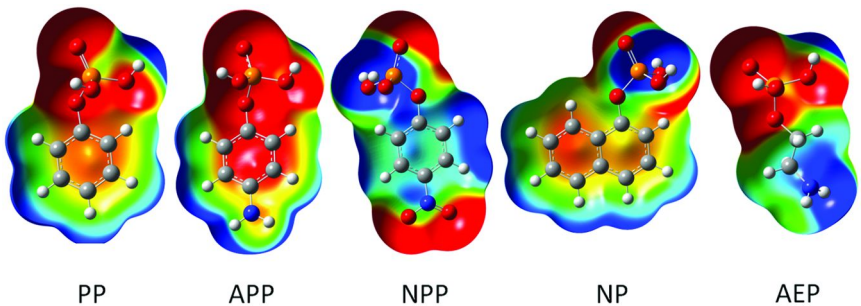

Figure 5. Electrostatic potential maps of surface modifiers obtained from DFT modeling. Red color indicates negative charge, whereas blue color indicates positive charge. Reproduced with permission from reference (16). Copyright 2013 American Chemical Society.

A Hammett linear free energy relationship (Equation 8), where *m* is a proportionality (slope) constant, σ is the Hammett coefficient substituent property variable, and *k* is a reaction rate in comparison with the reaction rate of a control, unmodified molecule (k_o), has historically been used to describe and rationalize the chemical structural differences of substituted phenyl groups toward chemical reactivity of aromatic organic compounds. Substituent functional groups that can be attached to aromatic benzene ring via para, meta, or ortho positions influence the free energy of ionization through polarization (σ_l), resonance (σ_r), or combination of polarization and resonance (σ_p, for para substituents) stabilization of the benzene ring charge states. Charge state stability, as influenced by the different electronic effects of resonance and/or polarity, gives rise to differences in reaction rates (*k*) (*52*).

$$m\sigma = \log\left(\frac{k}{k_o}\right) \tag{8}$$

Siddabattuni et al. have suggested that ligand charge stabilization properties as described by a Hammett relationship might be analogous to an ability for electron conduction, ion absorption, or surface state trap depth of the dielectric particle under the influence of electric field (*16*). A correlation of surface functional group Hammett coefficients to Weibull DBS (E_o), or leakage current ($i_{l\sigma}$) of nanocomposites plotted as either log (E/E_o) or log ($i_{l\sigma}/i_{lo}$), respectively, versus Hammett constants, σ, found a direct correlation to the influence of ligand polarity..

Linear correlations were not observed with either the para substituent Hammett coefficient, as a combined polarity and resonance effect, or a resonance effect contribution to dielectric properties of the composite. Hence, greater electropositive polarity at the particle surface was observed to correlate to minimized composite leakage current and maximized DBS. Based on the interfacial structure property relationship, Siddabattuni et al. reported maximum energy density of ~8 $J \cdot cm^{-3}$ for TiO_2-epoxy nanocomposites and ~9.5 $J \cdot cm^{-3}$ for $BaTiO_3$-epoxy nanocomposites at 30 vol.-% particle concentration.

Though more research is required to explain the exact reasons for the improved dielectric properties of PCNs based on interfacial-structure-property relationship, it is clear that the role of interface in PCNs is beyond the scope of simply an improved dispersion requirement. Impedance spectroscopy of the surface modified particles showed that the ligands alter the surface conductivity (resistance) of the particle surfaces (*16*, *53*). The bare particles appear, during impedance analysis, quite metallic in nature (see Figure 6). The real impedance of the particles was increased and the imaginary impedance decreased as a function of the electron deficiency per indicated by Hammett correlation plots and appears to not be simply a barrier mechanism. Hammett correlation was suggested as a tool for the design of new interfaces for enhanced dielectric properties of the PCNs.

In Polymer Composites for Energy Harvesting, Conversion, and Storage; Li, L., et al.;
ACS Symposium Series; American Chemical Society: Washington, DC, 2014.

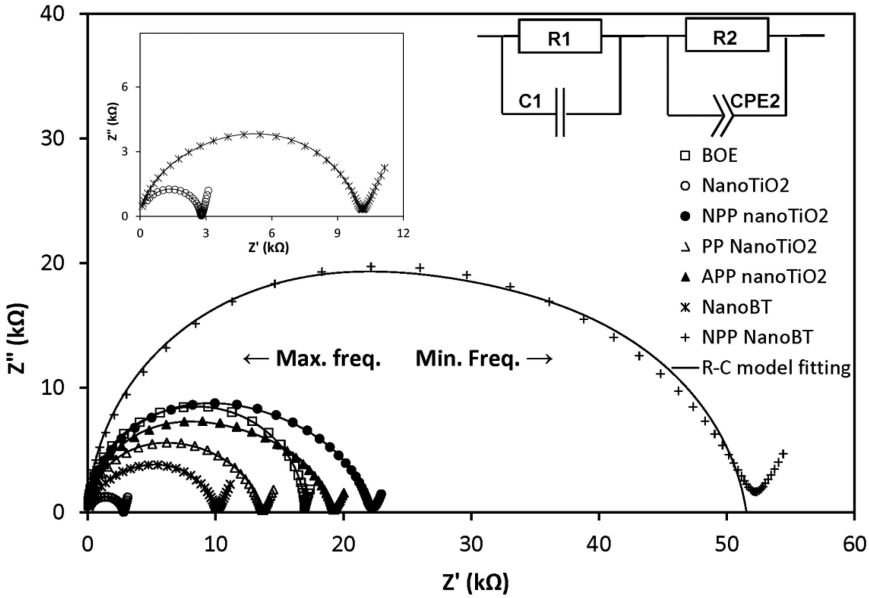

Figure 6. Nyquist plots are shown for impedance spectra of 20 vol.-% TiO_2 and BT based powders' slurries in a butoxyethanol suspension fluid showing control of surface conductivity for SAM modified powder varies as a function of the SAM structure. Inset are the bare nanoparticle dispersion slurry impedance spectra and an equivalent circuit model used to extract solvent and particle resistance. R1 and R2 are solvent and particle resistance values, respectively, C1 and CPE2 are solvent capacitance and constant phase element of the particles, respectively. R-C model fit shows the equivalent circuit behavior. Reproduced with permission from reference (16). Copyright 2013 American Chemical Society.

Models To Depict the Effect of Interface

The creation of an interfacial region between the polymer and filler has a direct impact on the dielectric properties of PCNs. Several models have been proposed to understand the complicated nature of interfaces and to interpret the property changes due to the addition of nanofillers in polymers. Some important models are summarized below.

Lewis Model

The Lewis model is based on the idea that the material property does not change abruptly but gradually over the course of several nanometers at the interface, over a finite thickness of an interfacial layer between polymer and filler that becomes behavior dominating for particles of sufficiently small radius and high volume concentration in the composite. Each atom or molecule in this

interfacial region will interact with its surroundings via short- and long-range forces. On a broad scale, these forces can be short range repulsive forces or electrostatic forces, including multiple ion and dipole interactions that can be attractive as well as repulsive (*12*, *54*).

Lewis utilized the concept of electrical double layer in surface chemistry to explain this interfacial region. As shown in Figure 7, the particles become charged due to equalization of Fermi level and/or chemical potential, which can cause spontaneous processes like ionization of surface groups or adsorption of ions from the matrix polymer. Responding to the charges on particle surface, polymer in the vicinity of particles will form a charge distribution (double) layer.

Two mechanisms are involved. One is an induced polarization of polymer molecules through electronic, ionic or dipolar polarization. The other mechanism is associated with a diffuse space charge double layer formation given the occurrence of charge injection in the system. The increment of nanoparticle loading in a dielectric composite will eventually lead to an overlap of the diffuse double layers, forming a conducting path through the overlapped layers and can readily form a dielectric breakdown (treeing) event. While bulk charge accumulation is reduced due to this internal conductivity, leakage currents, entirely through double layers of the nanocomposite, is increased (*54*, *55*).

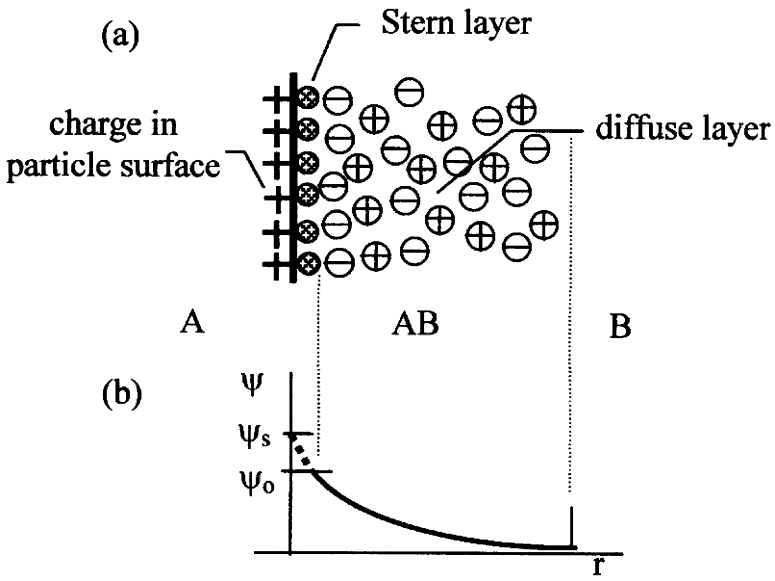

Figure 7. a) The diffuse electrical double layer produced by a charged particle A in a matrix B containing mobile ions. b) The resulting electrical potential distribution ψ(r). Reproduced with permission from reference (54). Copyright 2004 IEEE.

The dielectric should present few defects, providing resistance to tunneling across interfaces. Low dielectric contrast, good interfacial contact and bond strength between matrix and filler (as linked to dispersion quality), and low free ionic impurity are essential to minimizing electrical conductivity but can be in conflict with a goal of increasing permittivity. Defects can also result due to interfacial structures changed under influence of applied field. Surface modification is a means to control the defect structure at the particle surface both to enable dispersion, interfacial strength, and reduce free ion content.

To explain the behavior of nanocomposite polymers under electrical stress, Lewis proposed a simple model by considering the specific conditions for a titanium dioxide / polyethylene composite. In the model, it was shown how the combination of particle and polymer interface entities can act as distributed electron-hole recombination centers. According to this model, each recombination center terminates the passage of an electron between the electrodes and therefore space charge was reduced (*56*).

Multicore Model

A model analogous to Lewis' but of a multi-core structure was proposed by Tanaka (*57*) to explain the effect of interfaces electrically and chemically in the composites with chemical interaction between filler particles and polymer matrix at various distances from the particle surface. Tanaka described the interactions of a spherical inorganic particle with the surrounding medium via three layers, as shown in Figure 8, with a decreasing amount of coupling to the particle. For a particle diameter between 20 and 50 nm and inter-particle distance between 40 and 100nm, the combined thickness of the layers was assumed between 10 and 30 nm.

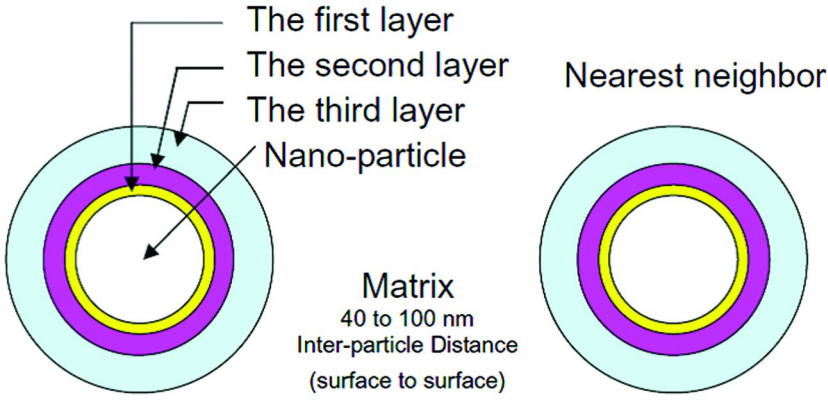

Figure 8. Multicore model for nanoparticle-polymer composites. Reproduced with permission from reference (57). Copyright 2005 IEEE.

The first layer was called a 'bonded' layer in which the particles are bonded with polymers through coupling agents. The bonded layer is merely present when there is chemical interaction between the surface of particles and polymer molecular chains. The second layer is called a 'bound' layer and comprises polymer chains strongly interacted with the bonded layer and the surface of particles. Polymer chains loosely coupled with the second layer form the third layer called a 'loose' layer, which can also feel the influence of inner layers. The thickness of each layer depends on the strength of the polymer-nanofiller interaction.

Given the presence of interfacial layers, polymer behavior will be altered dramatically at the interface. Polymer molecules residing at the interfacial zone tend to exhibit different chain conformation and chain mobility from those in the matrix, crystallinity, and charge distribution. Many reports have suggested altering of physical and electrical properties of polymer nanocomposites, such as free volume (*18*), glass transition temperature (*6*, *29*), and the internal field and space charge distribution (*58*).

Tsagaropoulos' Model

Tsagaropoulos also supported the perception of layers formed between nanoparticles and polymer, introducing a model which demonstrates the morphology of the polymer chains in layers (*55*, *59*). The model is based on the EHM (of Eisenberg, Hird and Moore) ionomer model for the morphology of random ionomers taking into account the formation of a tightly bound layer and a loosely bound layer of restricted mobility. According to Tsagaropoulos' model, the layer at a distance of 1 to 20 Å from the nanoparticle surface is generally thought to be a tightly bound layer. The polymer is physically if not chemically adsorbed and its chain dynamics are greatly slowed as a consequence. Chain dynamics as influenced by filler surfaces can be assessed by nuclear magnetic resonance (*60*) and thermal (*61*) measurements. At larger distances of about 25 to 90 Å from the nanoparticle surface, the polymer is believed to be less tightly bound, possessing intermediate dynamics, and is considered loosely bound. A third layer is also assumed, unrestricted bulk polymer (*62*).

According to this model, the loosely bound polymer exhibits its own glass transition, whereas the tightly bound does not participate in the glass transition event. Experiments on a variety of polymer/silica nanocomposites have shown that they exhibit two glass transitions, the usual bulk glass transition of the polymer and the glass transition of loosely or tightly bound polymer (*61*). According to the EHM model, the restricted mobility regions can have their own glass transition temperature. At low nanofiller concentrations, the inter-particle distances are large and the mobility of the polymer next to the tightly bound layers is unaffected. As a consequence, these regions cannot form a second glass transition, although the temperature of the first glass transition may be decreased. With increasing particle concentration, the inter-particle separation distance decreases, where the loosely bound layers augment. When the loosely bound layers overlap at a critical inter-particle separation distance (d_{cr}), the loosely bonded layers can exhibit their own glass transition temperature. Increasing the

nanoparticle concentration further, the polymer regions with reduced mobility gradually decrease in lieu of immobilized ones. Thus, the loosely bound layers are converted into tightly bound layers, leading to a distinct second T_g. The schematic model of the morphological transformations in particle filled polymers is shown in Figure 9. Tsagaropoulos' model validity is illustrated by the fact that it has been applicable to explain various experimental results (*55*, *59*).

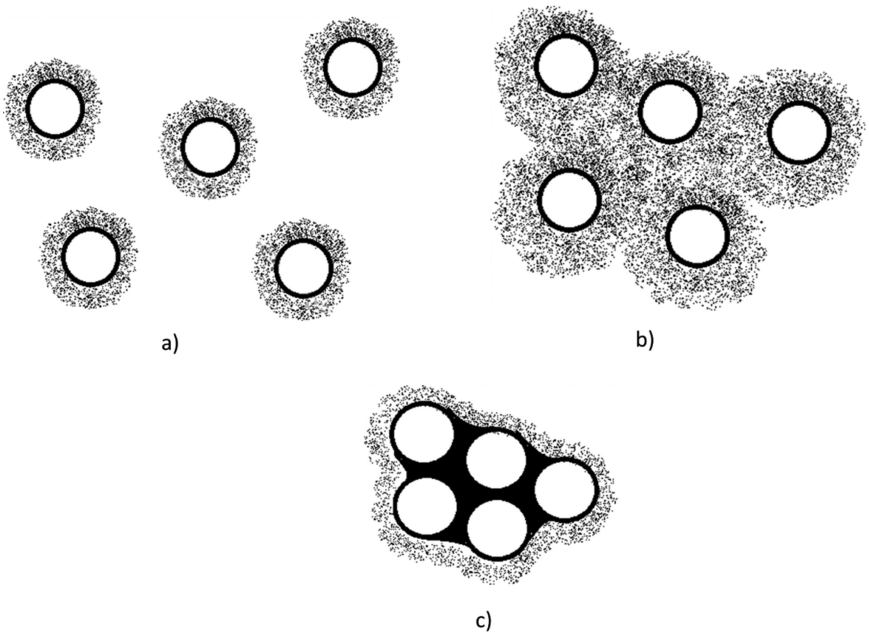

Figure 9. Model of the morphological transformations in filled polymers with varying inter-particle distances, d. a) at $d > d_{cr}$; b) at $d \sim d_{cr}$; c) at $d < d_{cr}$. Reproduced with permission from reference (58). Copyright 1995 IEEE.

Interphase Volume Model

Raetzke published the interphase volume model to correlate the interfacial region –which she termed as 'interphase'- with some improved macroscopic parameters such as the resistance to electrical treeing, partial discharge and high voltage arcing (*63*). Volume fraction of interphase in polymer due to the addition of nanofillers can be estimated from this model. In the model, the nanoparticle diameter (spherical), the mass densities of the matrix material and filler material, and the interphase thickness are needed as input parameters.

The model assumes that the spherical nanoparticles are uniformly dispersed in the matrix polymer. The model shows how the volume fraction of the interphase is bound to a maximum, depending on particle size and filler volume fraction. With the interphase volume model, a maximum interphase volume can be formed at lower filler concentrations. Raetzke concluded that different matrix polymers

have a different chemical character and particle interactions strongly depend on this. Therefore, the results can be compared only within the same matrix polymer. Although the model describes quite well the often found saturation effect in nanocomposites, an increase of the filler loading above 10 wt.-% does not have an advantageous effect on macroscopic parameters. Further explanation of the nature of the interphase is missing from the model description.

Polymer Chain Alignment Model

More recently, Andritsch has proposed the polymer chain alignment model (*64*), which assumes that the surface functionalized nanoparticles can lead to an alignment of polymer chains at the interface as shown in Figure 10. This chain alignment in combination with the filler material leads to a restructuring of the host polymer at the interface. The physical properties of this aligned and restructured polymer network at the interface are different from those of the bulk polymer and the particle.

Hence, it can be envisaged that the nanoparticles act as crosslinking centers, locally aligning the polymer but also reducing chain mobility at the polymer-particle interface. The latter may explain how nanoparticles can in fact reduce the permittivity of a composite. According to this model, particles without surface modification have weaker interaction with the host polymer due to the absence of an aligned and restructured network around it (*65*).

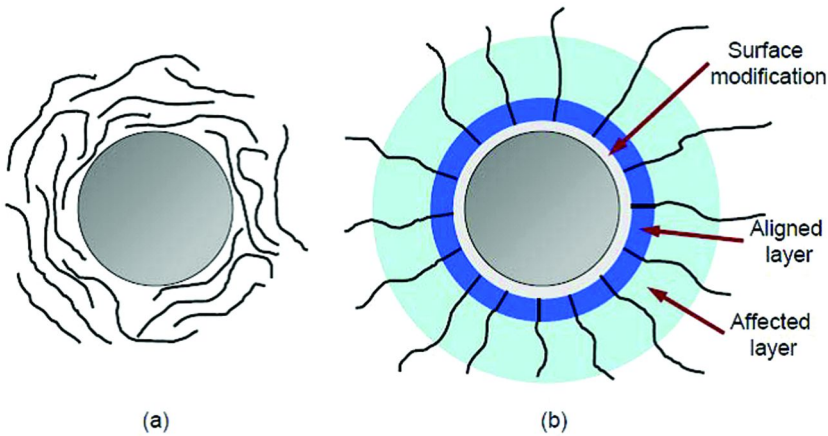

Figure 10. Nanoparticle in polymer matrix without (a) and with (b) surface modification. Reproduced with permission from reference (61). Copyright 2011 American Chemical Society.

A point of departure for this model from others is the way in which local morphology of the nanocomposites is changed in the vicinity of the nanoparticles. This morphology is assumed to be strongly affected by surface functionalization of the nanoparticles. The extent of structural changes of the interface, i.e., how

In Polymer Composites for Energy Harvesting, Conversion, and Storage; Li, L., et al.;
ACS Symposium Series; American Chemical Society: Washington, DC, 2014.

fast the transition from particle surface to unmodified polymer occurs, depends on particle shape, size, surface properties, and surface modification. A restructuring of the aligned layer is linked to an increasingly rigid polymer structure at the interface that in turn improves the dielectric properties of the PCNs (*64*, *65*).

The chain alignment model is based on experiments with epoxy resin filled with nanoparticles that have been modified with silane coupling agent, however, the model is not limited to epoxy resin. Also the model assumes the material properties of PCNs strongly depend on processes prior to and during polymerization so long as the interfacial structures are affected by the process. Any combination of a polymer host material and particles with compatibilizing surface treatment is expected to behave in a similar fashion, where ability to affect interfacial structure will affect dielectric properties (*66*).

Summary

Recent developments in the area of surface functionalization of nanofiller particles provide for enhanced dielectric properties of polymer−ceramic nanocomposites. Research results suggest that the role of interface is not only for attaining/improved quality of dispersion between polymer and nanofiller but a manipulation of the dielectric properties of the composites based on structures, chemical and electrical, of the interface. While particle surface conductivity can lead to increased permittivity, it does so at the expense of increased dielectric loss and higher probability for dielectric breakdown events at lower, rather than higher, voltages. Covalent interfaces or other surface modifications of the filler particles have moved forward interfacial control to help solve interfacial conductivity of filler particles. Even then, the electronic structure and properties of the filler surface, in addition to providing for good matrix interaction, dispersion and potential as a barrier resistance, must be considered for optimal effect.

By proper control of the interface, a more positive effect of inclusion of high permittivity nanoparticles in a dielectric composite might be brought into full advantage, leading to enhanced electrostatic energy storage properties. While the mechanism of interfacial influence on dielectric properties improvement of the composites has been proposed through several models, no one clear picture has emerged as a solution. The control and design of polymer-filler interfaces, while improved, remain incomplete and interface control remains a future need for advancing polymer−ceramic composite, energy storage dielectric capacitors.

Acknowledgments

The authors acknowledge support for preparation of this article through a grant from the U. S. Office of Naval Research, award No. N00014-11-1-0494.

References

1. Chu, B.; Zhou, X.; Ren, K.; Neese, B.; Lin, M.; Wang, Q.; Bauer, F.; Zhang, Q. M. *Science* **2006**, *313*, 334–336.
2. Barber, P.; Balasubramanian, S.; Anguchamy, Y.; Gong, S.; Wibowo, A.; Gao, H.-S.; Ploehn, H. J.; Loye, H.-C. Z. *Materials* **2009**, *2*, 1697–1733.
3. Guo, N.; DiBenedetto, S. A.; Tewari, P.; Lanagan, M. T.; Ratner, M. A.; Marks, T. J. *Chem. Mater.* **2010**, *22*, 1567–1578.
4. Wang, Q.; Zhu, L. *J. Polym. Sci. Part B: Polym. Phys.* **2011**, *49*, 1421–1429.
5. Siddabattuni, S. V. Ph.D. thesis, Missouri University of Science and Technology, Rolla, Missouri (MO), 2011.
6. Siddabattuni, S.; Schuman, T. P.; Dogan, F. *Mater. Sci. Eng. B* **2011**, *176*, 1422–1429.
7. Nayak, S.; Rahaman, M.; Pandey, A. K.; Setua, D. K.; Chaki, T. K.; Khastgir, D. *J. Appl. Polym. Sci.* **2013**, *127*, 784–796.
8. Tang, H.; Ma, Z.; Zhong, J.; Yang, J.; Zhao, R.; Liu, X. *Colloids Surf., A* **2011**, *384*, 311–317.
9. Lau, K. Y.; Piah, M. A. M. *Malaysian Polym. J.* **2011**, *6*, 58–69.
10. Cao, Y.; Irwin, P. C.; Younsi, K. *IEEE Trans. Dielectr. Electr. Insul.* **2004**, *11*, 797–807.
11. Hussain, F.; Hojjati, M.; Okamoto, M.; Gorga, R. E. *J. Compos. Mater.* **2006**, *40*, 1511–1575.
12. Lewis, T. J. *J Phys. D: Appl. Phys.* **2005**, *38*, 202–212.
13. Nelson, J. K.; Hu, Y. *J Physics D: Appl. Phys.* **2005**, *38*, 213–222.
14. Roy, M.; Nelson, J. K.; MacCrone, R. K.; Schadler, L. S.; Reed, C. W.; Keefe, R.; Zenger, W. *IEEE Trans. Dielectr. Electr. Insul.* **2005**, *12*, 629–643.
15. Smith, R. C.; Liang, C.; Landry, M.; Nelson, J. K.; Schadler, L. S. *IEEE Trans. Dielectr. Electr. Insul.* **2008**, *15*, 187–196.
16. Siddabattuni, S.; Schuman, T. P.; Dogan, F. *ACS Appl. Mater. Interfaces* **2013**, *5*, 1917–1927.
17. Saha, S. K. *Phys. Rev. B* **2004**, *69*, 125416/1–4.
18. Nelson, J. K.; Utracki, L. A.; MacCrone, R. K.; Reed, C. W. *IEEE Conf. Electr. Insul. Dielectr. Phenom.* **2004**, 314–317.
19. Li, J. *Phys. Rev. Lett.* **2003**, *90*, 217601/1–4.
20. Kim, P.; Jones, S. C.; Hotchkiss, P. J.; Haddock, J. N.; Kippenlen, B.; Marder, S. R.; Perry, J. W. *Adv. Mater.* **2007**, *19*, 1001–1005.
21. Gilbert, L. J.; Schuman, T. P.; Dogan, F. In *Advances in Electronic and Electrochemical Ceramics*; Dogan, F., Kumta, P., Ed.; John Wiley & Sons, Inc.: Hoboken, NJ, 2005; Vol. 179, 17−26.
22. Schadler, L. S. In *Nanocomposite Science and Technology*; Ajayan, P. M., Schadler, L. S., Brawn, P. V., Eds.; Wiley-VCH: Weinheim, Germany, 2003; Chapter 2, 77−153.
23. Rong, M. Z.; Zhang, M. Q.; Ruan, W. H. *Mater. Sci. Technol.* **2006**, *22*, 787–796.
24. Tan, D.; Cao, Y.; Tuncer, E.; Irwin, P. *Mater. Sci. Appl.* **2013**, *4*, 6–15.
25. Yang, F.; Ou, Y.; Lu, Z. *J. Appl. Polym. Sci.* **1998**, *69*, 355–361.

26. Zhang, Y.; Zhou, G. E.; Zhang, Y. H.; Li, L.; Yao, L. Z.; Mo, C. M. *Mater. Res. Bull.* **1999**, *34*, 701–709.
27. Avella, M.; Errico, M. E.; Martuscelli, E. *Nano Lett.* **2001**, *1*, 213–217.
28. Wang, S.; Wang, M.; Lei, Y.; Zhang, L. *J. Mater. Sci. Lett.* **1999**, *18*, 2009–2012.
29. Schuman, T. P.; Siddabattuni, S.; Cox, O.; Dogan, F. *Compos. Interfaces* **2010**, *17*, 719–731.
30. Choi, S.-H.; Kim, I.-D.; Hong, J.-M.; Park, K.-H.; Oh, S.-G. *Mater. Lett.* **2007**, *61*, 2478–2481.
31. Guo, N.; DiBenedetto, S. A.; Kwon, D.-K.; Wang, L.; Russell, M. T.; Lanagan, M. T.; Facchetti, A.; Marks, T. J. *J. Am. Chem. Soc.* **2007**, *129*, 766–767.
32. Fredin, L. A.; Li, Z.; Ratner, M. A.; Lanagan, M. T.; Marks, T. J. *Adv. Mater.* **2012**, *24*, 5946–5953.
33. Beier, C. W.; Sanders, J. M.; Brutchey, R. L. *J. Phys. Chem. C* **2013**, *117*, 6958–6965.
34. Yang, Y.; Zhu, B.-P.; Lu, Z.-H.; Wang, Z.-Y.; Fei, C.-L.; Yin, D.; Xiong, R.; Shi, J.; Chi, Q.-G.; Lei, Q.-Q. *Appl. Phys. Lett.* **2013**, *102*, 042904/1–5.
35. Dang, Z. M.; Zhou, T.; Yao, S. H.; Yuan, J. K.; Zha, J. W.; Song, H. T.; Li, J. Y.; Chen, Q.; Yang, W. T.; Bai *J. Adv. Mater.* **2009**, *21*, 2077–2082.
36. Yang, W. H.; Yu, S. H.; Sun, R.; Du, R. X. *Acta. Mater.* **2011**, *59*, 5593–5602.
37. Xie, L.; Huang, Y.; Lie, F.; Huang, X.; Jiang, P. *11th Proc. IEEE Int. Conf. Solid Dielectr.*; June 30– July 4, 2013, Bologna, Italy.
38. Huang, X. Y.; Jiang, P. K.; Xie, L. Y. *Appl. Phys. Lett.* **2009**, *45*, 242901/1–3.
39. Kobayashi, Y.; Kurosawa, A.; Nagao, D.; Konno, M. *Polym. Eng. Sci.* **2009**, *49*, 1069–1075.
40. Yu, J. H.; Huang, X. Y.; Wang, L. C.; Peng, P.; Wu, C.; Wu, X. F.; Jiang, P. K. *Polym. Chem.* **2011**, *2*, 1380–1388.
41. Polizos, G.; Tuncer, E.; Sauers, I.; More, K. L. *Appl. Phys. Lett.* **2010**, *96*, 152903/1–3.
42. Tuncer, E.; Sauers, I.; James, D. R.; Ellis, A. R.; Paranthaman, M. P.; Goyal, A.; More, K. L. *Nanotechnology* **2007**, *18*, 325704/1–5.
43. Tang, H.; Sodano, H. A. *Nano Lett.* **2013**, *13*, 1373–1379.
44. Tang, H.; Sodano, H. A. *Appl. Phys. Lett.* **2013**, *102*, 063901/1–4.
45. Tang, H.; Lin, Y.; Sodano, H. A. *Adv. Energy Mat.* **2013**, *3*, 451–456.
46. Kim, P.; Doss, N. M.; Tillotson, J. P.; Hotchkiss, P. J.; Pan, M.-J.; Marder, S. R.; Li, J.; Calame, J. P.; Perry, J. W. *ACS Nano* **2009**, *3*, 2581–2592.
47. Li, J.; Seok, S. I.; Chu, B.; Dogan, F.; Zhang, Q.; Wang, Q. *Adv. Mater.* **2009**, *21*, 217–221.
48. Li, J.; Khanchaitit, P.; Han, K.; Wang, Q. *Chem. Mater.* **2010**, *22*, 5350–5357.
49. Song, Y.; Shen, Y.; Liu, H.; Lin, Y.; Li, M.; Nan, C.-W. *J. Mater. Chem.* **2012**, *22*, 16491–16498.
50. Yu, K.; Niu, Y.; Zhou, Y.; Bai, Y.; Wang, H. *J. Am. Ceram. Soc.* **2013**, *96*, 2519–2524.
51. Roy, M.; Nelson, J. K.; MacCrone, R. K.; Schadler, L. S. *J. Mater. Sci.* **2007**, *42*, 3789–3799.

52. Carey, F. A.; Sundberg, R. J. *Advanced Organic Chemistry – Part A*, 5th ed.; Springer: New York, 2007; Chapter 3, 253−388.
53. Siddabattuni, S.; Petrovsky, V.; Schuman, T. P.; Dogan, F. *J. Am. Ceram. Soc.* **2013**, *96*, 1490–1496.
54. Lewis, T. J. *IEEE Trans. Dielectr. Electr. Insul.* **2004**, *11*, 739–753.
55. Pitsa, D.; Danikas, M. G. *Nano* **2011**, *6*, 497–508.
56. Lewis, T. J. *Proc. IEEE Int. Conf. Solid Dielectr.* **2007**, 11–14.
57. Tanaka, T.; Kozako, M.; Fuse, N.; Ohki, Y. *IEEE Trans. Dielectr. Electr. Insul.* **2005**, *12*, 669–681.
58. Ma, D. L.; Siegel, R. W.; Hong, J. I.; Schadler, L. S.; Martensson, E.; Onneby, C. *J. Mater. Res.* **2004**, *19*, 857–863.
59. Tsagaropoulos, G.; Eisenberg, A. *Macromolecules* **1995**, *28*, 6067–6077.
60. Blum, F. D. *Colloids Surf.* **1990**, *45*, 361–376.
61. Blum, F. D.; Young, E. N.; Smith, G.; Sitton, O. C. *Langmuir* **2006**, *22*, 4741–4744.
62. Danikas, M. G. *J. Electr. Eng.* **2010**, *61*, 241–246.
63. Raetzke, S.; Kindersberger, J. *IEEE Trans. Dielectr. Electr. Insul.* **2010**, *17*, 607–614.
64. Andritsch, T.; Kochetov, R.; Morshuis, P. H. F.; Smit, J. J. *Proc. IEEE Conf. Electr. Insul. Dielectr. Phenom.* **2011**, 624–627.
65. Kochetov, R.; Andritsch, T.; Morshius, P. H. F.; Smit, J. J. *IEEE Trans. Dielectr. Electr. Insul.* **2012**, *19*, 107–117.
66. Andritsch, T. Ph.D. Thesis, Delft University of Technology, Delft, Netherlands, 2010.

Chapter 9

Carbon Nanotube-Based Polymer Composite Thermoelectric Generators

Corey A. Hewitt and David L. Carroll*

**Center for Nanotechnology and Molecular Materials,
Wake Forest University, Winston Salem, NC 27105, United States
*E-mail: carroldl@wfu.edu.**

Carbon nanotube-based polymer composites possess several properties that make them ideal for use in low powered waste heat recovery applications not suitable to nonorganic crystalline materials even though their thermoelectric performance is lower, such as their light weight and flexible physical structure. Additionally, the favorable thermoelectric properties of the carbon nanotubes with moderate Seebeck coefficients and potentially large electrical conductivities result in modest power factors, while the low thermal conductivity of the polymer host aids in maintaining a temperature gradient across the composite. In order to effectively utilize a thermoelectric material in a practical application, they must be combined in a thin film device structure consisting of alternating p-type and n-type elements that are connected electrically in series and thermally in parallel. The device performance is then dictated by the intrinsic thermoelectric properties of the individual layers in the device. Ultimately, the total power output is limited by several extrinsic properties of the specific application.

Introduction to Thermoelectrics

Materials that are capable of the solid-state conversion between thermal energy and electrical energy are known as thermoelectrics (*1*). When a thermoelectric material is exposed to a temperature gradient, free charge carriers within the material are thermally driven from the hot end to the cold end, resulting in a potential difference. In the simplest sense, thermoelectric materials

In Polymer Composites for Energy Harvesting, Conversion, and Storage; Li, L., et al.;
ACS Symposium Series; American Chemical Society: Washington, DC, 2014.

are quantified by their Seebeck coefficient (α) given by the ratio between the voltage generated (V_{TE}) and the temperature difference (ΔT) across the material (*2*). Currently, thermoelectrics are only used in small scale applications and as a supplement to more efficient forms of generating electrical power (*3*). This restriction on applications is due to a limiting factor on the theoretical maximum Carnot efficiency of thermoelectrics for high powered applications that reduces the efficiency to well below that of currently used mechanical heat engines (*4*). The Carnot efficiency will only be achieved if the limiting factor, known as the (dimensionless) figure of merit, reaches an infinite value. In reality, of course, this is unobtainable; even so, the past fifty years of thermoelectric development have only resulted in figure of merit values not much greater than unity (*1*, *5*). A figure of merit of around 15-20 would be required to match the present performance efficiency of currently used high power heat engines (*4*). Fortunately, the efficiency drop off as the power level decreases for mechanical heat engines is much more rapid than that of thermoelectrics. This leads to a crossover in efficiencies below about 10 W. Additionally, thermoelectrics are a renewable source that functions to convert available waste heat into electrical power. It is the efficiency cross over and waste heat recovery that drives the development of thermoelectrics for use in low power applications.

Thermoelectric power (TEP) can be explained qualitatively by first considering a material at thermal equilibrium with a uniform charge distribution. As one end is heated creating a temperature difference between the ends, "hot" charge carriers from the heated end become more energized and begin to diffuse to the opposite end of the material. If the material is electrically isolated, the charge carriers will build at the cold end resulting in a potential difference. This potential difference, in turn, creates an electric field which forces the "cold" charge carriers back to the hot end. At equilibrium, the "hot" and "cold" currents become equal and opposite resulting in a maximum potential difference for the given ΔT, hence the Seebeck coefficient (*2*).

A more formal interpretation of the Seebeck coefficient can be described using the energy band structure for a n-doped thermoelectric material exposed to a temperature gradient, as shown in Figure 1. It should be pointed out that the use of band structure is typically reserved for steady state systems, however, it can safely be assumed that over short distances the system is close to steady state so the band structure provides a satisfactory explanation. Since the position of the Fermi energy E_F is inversely related to temperature for a n-doped material, E_F shifts up as T decreases effectively bending the valence band E_{VB}, conduction band E_{CB}, and donor level E_d energies downward at the cold side. This energy band bending, combined with the wider soft zone around EF for the Fermi-Dirac energy distribution $f(E,T)$ at the hot end leads to a nonuniform concentration of charge carriers. Although carriers are forced (F_T) to the cold side to reestablish uniform carrier concentration, the temperature gradient is a constant so equilibrium cannot be reached. The transfer of charge to the cold side does not occur indefinitely, however, since the buildup of charge on the cold side generates an internal electric field with an opposing force (F_E). Once F_T and F_E are equal in magnitude and opposite in direction, the system reaches equilibrium on a macroscopic scale and V_{TE} reaches its maximum value. This is the scenario illustrated in Figure 1.

In Polymer Composites for Energy Harvesting, Conversion, and Storage; Li, L., et al.;
ACS Symposium Series; American Chemical Society: Washington, DC, 2014.

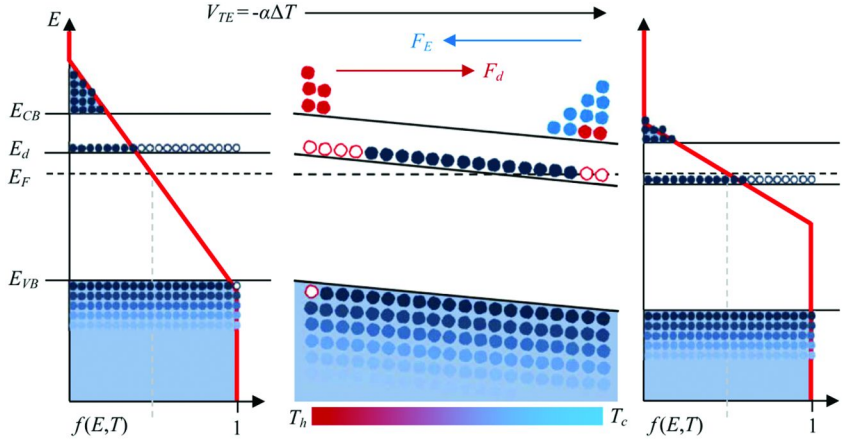

Figure 1. Simplified band structure and energy distributions for a n-type thermoelectric material exposed to a temperature gradient before equilibrium is reached. Band bending has been exaggerated for illustration only.

The end goal is to utilize thermoelectric materials by creating a useable potential via TEP; therefore, some method of determining the effectiveness of a material is needed. This is done quantitatively through a parameter known as the dimensionless figure of merit (*6*), given by

$$ZT = \frac{\alpha^2 \sigma}{\kappa} T \qquad (1)$$

where σ, κ, and T are the electrical conductivity, thermal conductivity, and absolute temperature, respectively. This quantity appears as a material property factor limiting the maximum obtainable Carnot efficiency derived by considering the heat flow through a thermoelectric element (*6*).

This result arrived at theoretically can also be justified qualitatively. Since α is directly proportional to V_{TE}, it is reasonable that ZT increase with increasing α since a higher V_{TE} is desirable. Electrical conductivity is a measure of how well charge carriers move through the material; therefore, ZT should also be directly proportional to σ to minimize the internal resistance of the material. Finally, since ΔT must be maintained to create V_{TE}, it is favorable to have a low thermal conductivity, so ZT is inversely proportional to κ. For materials with low thermal conductivities that are intended for use where moderate waste heat is available, it is typical for only the power factor ($PF = \alpha^2\sigma$, numerator of Z) to be reported since it directly relates to the thermoelectric power output potential of the material.

Increasing ZT or PF is the ultimate goal for any fundamental research and development of new or existing thermoelectric materials. From the relationship for ZT in Equation 1, it is clear in which direction improvements in α, σ, and κ must be in an attempt to meet the idealized "phonon glass- electron crystal" (PGEC) structure in which κ is reduced by inhibiting phonon propagation as in a glass and σ is maximized as it is in crystals. This task is greatly complicated, however by

In Polymer Composites for Energy Harvesting, Conversion, and Storage; Li, L., et al.;
ACS Symposium Series; American Chemical Society: Washington, DC, 2014.

the interrelationships between these three quantities. This situation is most clearly illustrated for metallic or degenerate semiconductors with parabolic bands in the energy independent scattering approximation where an expression for the Seebeck coefficient can be derived from the standard Mott formulation and is given by

$$\alpha = \frac{8\pi^2 k_B^2 m^*}{3eh^2} T\left(\frac{\pi}{3n}\right)^{2/3} \quad (2)$$

where m^* and n are the effective mass and concentration of the charge carriers, respectively, and h is Planck's constant (*7*). Hence, an inverse relationship between α and σ arises since $\sigma = ne\mu_c$, where μ_c is the charge carrier mobility.

Further complicating the ability to increase ZT is the relationship between σ and the carrier contribution to the thermal conductivity κ_c through the Wiedmann-Franz law given by $\kappa_c = L\sigma T$, where L is the Lorenz factor. Thereofore, it is clear that a compromise must be met between the three thermoelectric parameters in order to maximize ZT. Evidently, this occurs when n is between 10^{19} and 10^{20} cm^{-3} which lies in the region for highly doped semiconductors (*7*).

The efficiency for a thermoelectric material is scaled by a factor containing ZT where the maximum Carnot efficiency is obtained as $ZT \rightarrow \infty$. Practically, very large ZT values are not necessary since a $ZT \approx 20$ would make thermoelectrics competitive with currently used high power mechanical heat engines (*3*, *4*). Unfortunately, even reaching a $ZT \approx 20$ is quite ambitious since bismuth telluride ($ZT \approx 1$) remains the most practical material since its discovery about fifty years ago (*8*, *9*). Only modest improvements in ZT have been made since, peaking around 10-15 years ago with reported values of up to 2.5 after the prediction by M. S. Dresselhaus that quantum confinement of in-plane carrier transport through the use of quantum wells and superlattices could result in an increased ZT (*10–13*).

Current research focuses on complex materials such as nanostructured bulk alloys (*14–16*), skutterudites (*17–19*), and clathrates (*20–22*), however, confirmed ZT values of 3 have yet to be realized. Reaching a $ZT \approx 3$ is significant because it is at this efficiency for which it is predicted that thermoelectric materials will become more efficient and commercially practical than current mechanical heat engines for low power applications (*23*). This prediction considers the fact that the efficiency of a mechanical heat engine decreases more rapidly than that of a thermoelectric material as the power level drops. Below a power level of about 10 W, the efficiency of mechanical heat engines becomes less than that of a thermoelectric material with a $ZT = 3$.

In order to utilize thermoelectric materials in low powered applications, materials which are capable of harvesting waste heat in dynamic applications is a necessity. Although bismuth telluride is a well performing thermoelectric material, it is impractical in many applications due to its weight, rigidity, and fragility. Alternatively, investigation of the thermoelectric properties of carbon nanotubes (CNTs) and CNT-based thin film polymer composites have shown initial promise for the incorporation of these materials into dynamic applications. Although this topic is fairly new and interesting in its own right, the potential practical benefits from using CNT-based composites as small scale thermoelectric power generators is what drives the investigation. Current CNT/polymer

In Polymer Composites for Energy Harvesting, Conversion, and Storage; Li, L., et al.;
ACS Symposium Series; American Chemical Society: Washington, DC, 2014.

composites have a reported *ZT* of 0.02 to 0.05, but due to their heterogeneous structure, have the potential to be increased by fine tuning α, σ, and κ (*24*). Improvements in *ZT* can also arise from the enhancement of these properties for CNTs in general as well.

Introduction to Carbon Nanotubes

Since the first published report of "helical microtubules of graphitic carbon" credited to S. Iijima in 1991 (*25*), CNTs have been championed as being one of the most promising new materials with an array of potential applications (*26*, *27*). This enthusiasm stems from CNT's favorable electronic properties which allow for near ballistic transport in structurally pure CNTs (*28–31*), and mechanical properties that result in tensile strengths greater than that of iron (*32–34*).

The backbone of carbon nanotubes is their two dimensional crystalline structure called graphene. Essentially, graphene is a 2D single layer hexagonal lattice of carbon atoms strongly σ bonded in plane to their three nearest neighbors through sp^2 hybridization, shown in Figure 2. The carbon-carbon distance denoted a_C is 1.421 Å. Graphene layers can also form weak π bonds in the third dimension through the p orbitals in graphene resulting in graphite. The crystalline structure of graphite is an ABAB planar stacking arrangement with four C atoms per unit cell (*35*).

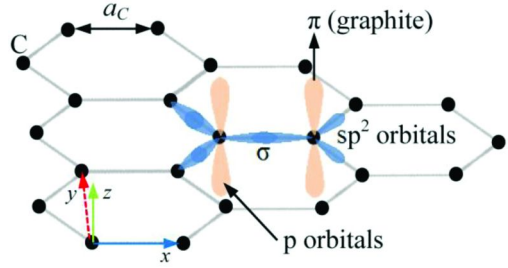

Figure 2. Graphene comprised of sp^2 bound carbon atoms in a 2D hexagonal lattice. C atoms are σ bonded through sp^2 orbitals, while graphene interlayer π bonds through p orbitals are formed in graphite.

A single walled carbon nanotube (SWNT) is formed by rolling a finite layer of graphene whereby the carbon atoms form a cylindrical hexagonal lattice. The necessity that the lattice must be continuous around the nanotube circumference allows for only a discrete array of possible nanotubes defined by their chiral vector. The chiral vector **C**, which points radially around the axis of the nanotube between identical C atoms in the lattice, determines the helicity of the nanotube and is given by

$$\mathbf{C} = n\mathbf{a_1} + m\mathbf{a_2} \quad (3)$$

where n and m are integer numbers of the graphene unit vectors $\mathbf{a_1}$ and $\mathbf{a_2}$, respectively. Figure 3 illustrates the possible chiral vectors up to $n = m = 6$ where

In Polymer Composites for Energy Harvesting, Conversion, and Storage; Li, L., et al.;
ACS Symposium Series; American Chemical Society: Washington, DC, 2014.

$m \leq n$, and tubes where $n,m \leq 2$ are experimentally unstable or unphysical (*36*). This figure also provides the bandgap energies (E_g) for each chirality, highlighting the fact that carbon nanotubes can range from metallic like to semiconducting like conductivities despite graphene being a zero bandgap semiconductor. This range in conduction types for SWNTs is due to the necessity that the carbon lattice must be circumferentially continuous which leads to only certain allowable one dimensional discretized k vectors within the continuous two dimensional Brillouin zone of graphene. If the discretized k vectors include the Dirac points (zero points within the graphene Fermi surface) then the SWNT is metallic, otherwise it is semiconducting.

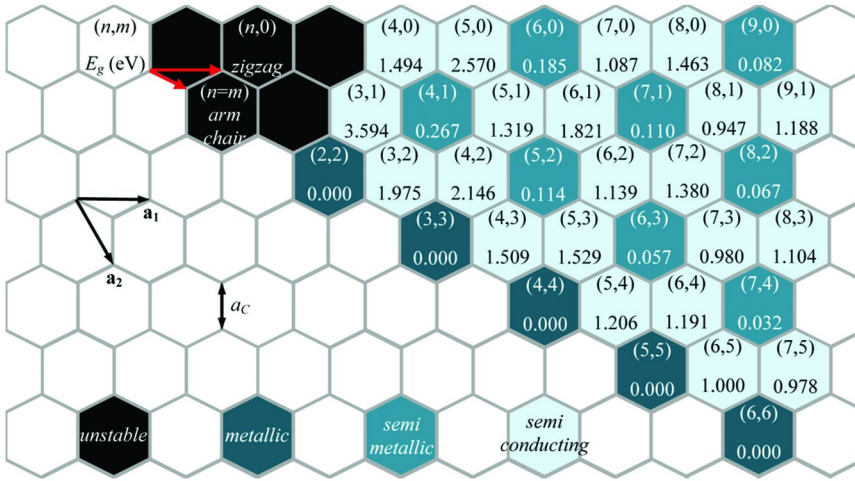

Figure 3. Graphene lattice illustrating the chiral vector defined by the integer number (n,m) of unit vectors $\mathbf{a_1}$ *and* $\mathbf{a_2}$ *that comprise it. Bandgap energies are also shown indicating that CNTs can range from metallic like to semiconducting like conduction.*

Carbon Nanotube Conductivity

As mentioned previously, CNTs can have conductivities ranging from metallic to semiconducting depending on their chirality. For metallic *armchair* SWNTs where $n = m$, it is theoretically possible to have ballistic axial electron transport, however, experimentally this condition has not been realized for length scales over 140 nm due to disorder and defects along the tube wall (*31*, *37*, *38*). The conduction along the length of a single pure SWNT is important, yet the lack of suitable individual CNT dimensions, purity, and manipulation techniques have so far hindered wide scale use in small scale applications. Therefore, buckypapers, which are mats composed of a disordered network of individual CNTs as in Figure 4, are significant because of their processability and ability to be scaled up indefinitely, provided there are enough CNTs.

In Polymer Composites for Energy Harvesting, Conversion, and Storage; Li, L., et al.;
ACS Symposium Series; American Chemical Society: Washington, DC, 2014.

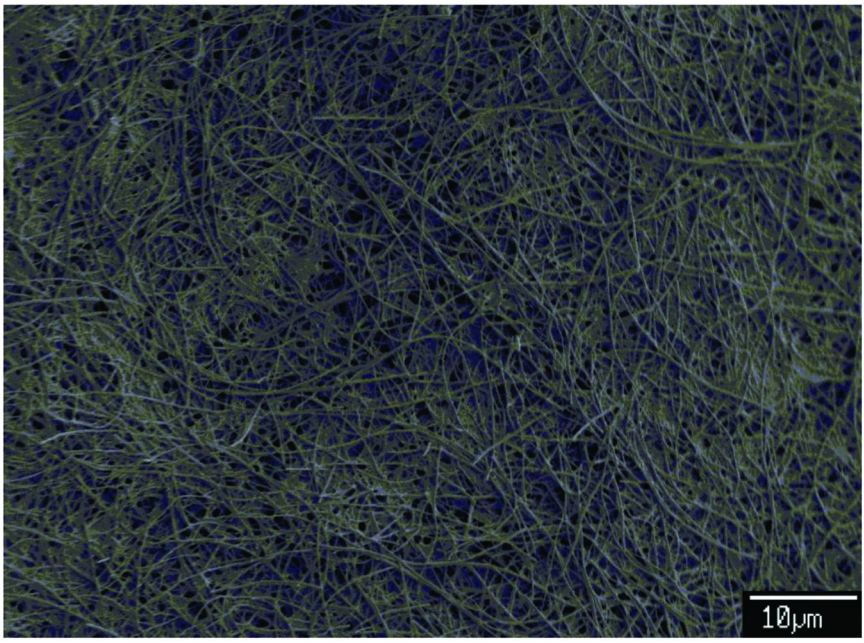

Figure 4. Scanning electron micrograph of a buckypaper consisting of CNTs with an average diameter of 25 nm.

One potential disadvantage of buckypapers, however, is the introduction of tube-tube contacts which ultimately dominates and reduces the total conductivity of the buckypaper (*29*). Consequently, charge carriers are forced to transfer through the tube-tube barriers by one of two processes. For high conductivity buckypapers, conduction is through a process known as thermal fluctuation assisted tunneling whereby highly conducting regions (nanotubes) are separated by small barrier regions (tube-tube junctions). In addition to tunneling through the barrier regions, activated conduction occurs due to thermal fluctuations. At absolute zero activated conduction ceases, however, tunneling is still possible which results in a characteristic nonzero conductivity at 0 K (*39*, *40*). The thermal fluctuation assisted tunneling model is given by

$$\sigma(T) = \sigma_0 \exp\left(\frac{-T_1}{T_S + T}\right) \tag{4}$$

where σ_0 is a constant, T_1 is a constant related to the energy barrier for hopping from tube to tube, and T_S is the thermally activated conduction temperature known as the Sheng parameter (*40*).

For lower conductivity samples, the barrier width become too large for tunneling, therefore, conduction occurs through a process known as variable range hopping where carriers hop between localized states within the band gap of

the material. Since this conduction type is strictly driven by thermal energy, the conductivity goes to zero at 0 K (*29*, *41*, *42*). The variable range hopping model is given by

$$\sigma(T) = \sigma_0 \exp\left[-\left(\frac{T_1}{T}\right)^{1/\,1+d}\right] \tag{5}$$

where T_1 is the energy barrier constant, σ_0 is a constant, and d describes the density of packed tubes and inter-junction contacts (*42*, *43*). A dimension $d = 2$ represents a low space-filling percolation of current through the CNT/polymer matrix (*43*).

Practically, the smallest component of a buckypaper is a nanotube rope or bundle, which is a group of axially aligned nanotubes that are bound together by weak Van Der Walls forces between the p orbitals of the outer wall (*29*, *44*). Room temperature electrical conductivities for ropes are on the order of 10^6 Sm^{-1}, in a region classified as "glassy metals" below that of highly conducting crystalline materials like copper (10^8 Sm^{-1}), and above that of short range order materials like polyaniline and other conducting polymers (10^5 Sm^{-1}) (*38*, *45–48*). Much work has been done in an attempt to increase the conductivity of CNT buckypapers through chemical modification of the CNTs (*49–53*), and physical manipulation of the CNT network (*50*, *54–60*), however, 10^6 Sm^{-1} remains the benchmark electrical conductivity.

For thermoelectric applications, the use of buckypapers does have an advantage. The potential for ballistic conduction in individual CNTs means that thermal conductivity will be high as well, with theoretical calculations on the order of 10^3 $Wm^{-1}K^{-1}$ (*61*), compared to 10^2 $Wm^{-1}K^{-1}$ for copper. Based on the definition of ZT in Equation 1 a high κ is unfavorable; therefore, buckypapers allow for a method to reduce the thermal conductivity of the total CNT network through reductions in the phonon contribution to the total κ by introducing barriers at the tube-tube junctions. Reductions in κ to values on the order of 10-100 $Wm^{-1}K^{-1}$ for CNT buckypapers have been reported (*62–64*). This is a promising approach, however, it must be met with caution since any attempt to reduce κ through the electronic contribution with lead to a direct reduction in σ as well.

Carbon Nanotube Thermoelectric Power

The final thermoelectric parameter affecting the figure of merit is the Seebeck coefficient α, also referred to as the TEP. Due to the wide range of chiralities and variations in conduction from metallic to semiconducting, individual CNTs exhibit a range of Seebeck coefficients since it is dependent on the charge carrier concentration, among other factors. Although there are reports on the TEP of individual CNTs (*44*, *65–68*), due to the intended application of thermoelectrics as power generating materials, the thermoelectric power output of individual CNTs would be incredibly small (on the order of 10^{-15} W). Additionally, the TEP of CNTs when incorporated into buckypapers is not as drastically affected as it is for κ and σ. This is because the TEP depends on the thermally weighted contributions to the

In Polymer Composites for Energy Harvesting, Conversion, and Storage; Li, L., et al.;
ACS Symposium Series; American Chemical Society: Washington, DC, 2014.

total α from the CNTs and tube-tube junctions. Since the component of ΔT across the junctions is much smaller than that of the CNTs, the total TEP of a buckypaper is on the order of that for individual CNTs (*29*, *46*).

Initial reports on the thermoelectric properties of SWNTs quickly elucidated that the TEP of CNTs is rather unique. Values for the room temperature TEP proved to be much larger than that expected and compared to values for graphitic carbon which has values of about -4 μVK^{-1} due to its near equal concentration of both holes and electrons resulting in metallic like TEP (*69*, *70*). P. C. Eklund *et al*. demonstrated that the TEP of SWNTs can be varied from 10 to 60 μVK^{-1} by varying the growth catalyst resulting in different transition metal impurities (*71*). They speculated that the range in TEP values observed to that point were due to interactions between the spin of the CNT conduction electrons and the magnetic moment of the transition metal impurities, otherwise known as the Kondo effect (*71*, *72*).

Of additional perplexity is the positive sign of the TEP for CNTs. Several reports by K. Bradley *et al*. indicated that the intrinsic TEP of CNTs was actually negative and large, but is almost always measured as positive due to oxygen impurities formed during synthesis since each oxygen atom accepts approximately 0.1 electron from the CNT (*73*, *74*). They deduced this result after heating the CNTs in vacuum and then exposing them to various pure gases in the chamber. Under vacuum and atmospheric pressure for inert gases, the TEP was about -50 μVK^{-1}, but transitioned back to +60 μVK^{-1} when oxygen was reintroduced. Subsequent independent reports have confirmed this result (*41*, *67*, *75*). Further, the oxygen impurity doping has been shown to be a CNT surface doping effect, where the TEP of CNTs can transition from positive to negative values as the CNT diameter is increased. This is attributed to the fact that the total oxygen to carbon ratio decreases as diameter increases, effectively reducing the overall positive doping by oxygen (*76*, *77*).

Many further reports on the thermoelectric power of CNTs have resulted in a range of magnitudes similar to that reported by P. C. Eklund indicating that the TEP of CNT buckypapers is highly sensitive to the CNT synthesis conditions and resulting chirality, defects, dopants, and impurities (*29*, *56*, *65*, *75*, *78–83*). Since it is necessary to have materials exhibiting both p-type and n-type behavior for use in thermoelectric generators (details given below), the effects of doping are of particular interest because they can be used to obtain air stable n-type CNTs. Nitrogen is a known n-type substitution dopant that results in room temperature values around -12 μVK^{-1} and metallic diffusion temperature dependent TEP (*78*). The polymer polyethylenimine (PEI) is also an effective n-type dopant by adsorbing onto the walls of the nanotubes and donating the lone pair electrons from the amine group within its repeating unit (*84*). Seebeck coefficients for saturation PEI doped CNTs are as large as -40 μVK^{-1} with power factors in the range of 10 $\mu Wm^{-1}K^{-2}$ (*51*, *85*, *86*). Additionally, a recent study by Y. Nonoguchi *et al.* introduced and compared an array of possible n-type dopants for CNTs (*87*). Among the dopants studied, triphenylphosphine resulted in the highest negative TEP of -72 μVK^{-1} with a power factor of 26 $\mu Wm^{-1}K^{-2}$. This dopant, and other phosphine derivatives, proves to be effective due to electron donor doping by the phosphor (*88*).

In Polymer Composites for Energy Harvesting, Conversion, and Storage; Li, L., et al.;
ACS Symposium Series; American Chemical Society: Washington, DC, 2014.

Further investigation into the TEP of CNTs has resulted in a range in temperature dependent behavior as well. For buckypapers consisting of metallic like CNTs with small TEP magnitudes, the temperature dependent behavior follows closely to that expected for linear metallic like diffusion thermopower (*71*). As the range in chiralities within the buckypaper broadens to include semiconducting CNTs and the TEP magnitudes increase, however, the temperature dependent behavior becomes nonlinear, typically characterized by nearly linear diffusion thermopower like behavior at low temperatures, and a continually decreasing $d\alpha/dT$ at higher temperatures (*56*, *70*, *71*, *78*, *79*, *89*). This behavior has been attributed to the heterogeneous nature of the buckypaper which contains a range of CNT types. Therefore, the net TEP will be dependent upon contributions from the magnitude and temperature dependent behavior of each type of CNT present. This physical description is quantitatively represented with a heterogeneous model consisting of a linear metallic term plus a $T^{1/2}$ semiconducting term that is exponentially weighted which represents the freezing out of the semiconducting contribution at low T (*42*, *90*, *91*). The resulting heterogeneous model is given by

$$\alpha(T) = bT + cT^{1/2} \exp\left[-\left(\frac{T_1}{T}\right)^{1/1+d}\right] \tag{6}$$

where b and c are constants governing the metallic and semiconducting contributions, respectively, T_1 is an energy barrier constant, and d is the dimensionality of the conducting material. At absolute zero both contributions go to zero resulting in a net zero thermoelectric power as expected, while the decrease in slope of α versus T at higher temperatures is a result of the thermally activated semiconductor contribution to the total TEP.

CNT-Based Composites

Since the thermoelectric properties of CNTs are intrinsic, they remain true when they are incorporated into a polymer composite as well. The purpose of synthesizing CNT-based composites is to take advantage of these favorable properties of CNTs as well as those of the polymer as they relate to thermoelectrics. Of course, the resulting thermoelectric properties of the composite will be a compromise between the properties of the individual components, but the overall effect is to either increase the net ZT, or improve the physical structure of the material for a specific application.

In regards to the thermoelectric properties of CNT-based composites, polymers have the most direct effect on the conductivities. Nonconducting polymers typically have low thermal conductivities as well due to their amorphous structure consisting of randomly oriented and electrically insulating molecular chains, resulting in both low phonon and electron contributions to thermal conductivity. When CNTs are incorporated into a polymer composite, it introduces polymer into the tube-tube junctions which acts as a phonon scattering

In Polymer Composites for Energy Harvesting, Conversion, and Storage; Li, L., et al.;
ACS Symposium Series; American Chemical Society: Washington, DC, 2014.

point while still allowing the electronic charge carriers to hop across the barrier, decreasing the thermal conductivity and slightly decoupling the relationship between σ and κ_c. Clearly, σ will decrease as well due to the hopping potential required for carriers to travel from tube to tube, however, the overall effect on *ZT* will be positive. Since the dependence between the two conductivities does not always occur collinearly, there is typically a specific CNT loading that exhibits the optimum thermoelectric performance (*92*, *93*).

The thermal and electrical conductivities of CNT-based composites have been investigated quite continuously over the last decade. Results focusing on CNT loadings in the composites clearly exhibit the expected behavior in that the resulting composite conductivities are weighted averages of the individual component conductivities. Since the CNTs form a conducting matrix through the composite consisting of a low conductivity polymer, as the CNT loading increases so too does the total composite electrical and thermal conductivities (*54*, *94–98*). Thermal conductivities are reduced semilinearly from 10-100 $Wm^{-1}K^{-1}$ for buckypapers to nearly 10^{-1} $Wm^{-1}K^{-1}$ for low CNT loadings (*62*, *64*, *92*). Electrical conductivities range from 10^4-10^5 Sm^{-1} for pure buckypapers, and decrease slowly until the CNT loading reaches about 50 wt%, at which point the conductivity rapidly goes to zero as the CNT loading decreases below the percolation threshold of about 5 wt% (*99*, *100*). The normalized temperature dependent electrical conductivity has also been shown to be governed by the same mechanisms as that for the buckypapers (either variable range hopping or fluctuation assisted tunneling), depending on the CNT loading (*43*, *99*, *101*). Essentially, as the CNT concentration decreases, the temperature dependent conductivity of the composite transitions from a high conductivity composite governed by fluctuation assisted tunneling to a low conductivity composite governed by variable range hopping. This transition region occurs within the range of CNT loadings (10-20%) for which the extrapolated absolute zero conductivity changes from nonzero to zero (*39*, *99*, *100*).

The investigation of the TEP of CNT-based composites has also begun within the last decade, though not nearly as extensively as the conductivities. Reports have mainly focused on varying the CNT and polymer types, and composite component ratios (*24*, *86*, *92*, *93*, *102–105*). As mentioned previously, a number of polymers such as PEI readily dope CNTs and drastically affect their TEP, while other nondoping polymers such as PVDF do not alter the TEP (*87*, *100*). The most notable findings are that for doping polymers the TEP depends only on the CNT to dopant polymer ratio (*85*, *87*), and for nondoping polymers the TEP is only weakly dependent on the CNT loading (*93*). This is for the same reason described earlier for why the tube-tube junctions do not significantly alter the TEP of CNT buckypapers compared to individual CNTs. The thermally weighted contribution to the total TEP of the polymer filled tube-tube junctions is small compared to that of the individual CNTs. The thermoelectric temperature dependent behavior of CNT composites is also unaffected by polymer type or the CNT concentration, where CNT composites ranging from 5 wt% CNTs to pure buckypapers exhibit identical behavior described by the heterogeneous model introduced above (*99*, *100*, *106*). These results indicate that *ZT* and the power factor are unaffected by the incorporation of CNTs into a nondoping polymer matrix; therefore, the net

In Polymer Composites for Energy Harvesting, Conversion, and Storage; Li, L., et al.;
ACS Symposium Series; American Chemical Society: Washington, DC, 2014.

effect on *ZT* is only dependent on the ratio between the electrical and thermal conductivities. Conversely, the power factor will always decrease with decreasing CNT concentration since the electrical conductivity decreases as well.

Physically, carbon nanotube-based polymer composites are more durable than pure buckypapers, since the molecular chains of the polymer become entangled around and between the carbon nanotubes. From a processing standpoint, composite preparation is relatively simple and inexpensive compared to current high *ZT* materials. Additionally, the thin film flexible physical structure of CNT-based composites allows for them to be considered in applications not suitable for rigid semi-crystalline high performance materials. Overall, these benefits must be met with compromise over the reduction in electrical conductivity, however, they result in a material that is more suitable to dynamic applications where other types of thermoelectric materials would not be applicable whatsoever, such as low powered personal and wearable electronics.

Thermoelectric Generators

Once the thermoelectric properties of a material are known and it has been determined that its performance is suitable, it is common for the material to be combined into a multiple thermoelectric element device as shown in Figure 5. This device structure requires the combination of alternating p-type and n-type bulk thermoelectric materials that are connected electrically in series through metallic interconnects and thermally in parallel between ceramic substrates (*7*, *107*). Heat is then absorbed through one substrate and expelled through the opposite substrate creating a temperature difference across the device, and generating a net thermoelectric voltage given by

$$V_{TE} = N(\alpha_p - \alpha_n)\Delta T \tag{7}$$

where α_p and α_n are the p-type and n-type material Seebeck coefficients, respectively, and N is the number of p-type/n-type pairs (called a thermocouple, TC) (*106*). This expression for V_{TE} illustrates the effectiveness of combining multiple alternating elements, rather than having a single bulk material (with Seebeck coefficient α) as shown in Figure 5 which would generate a $V_{TE} = \alpha\Delta T$.

Despite the ability to increase V_{TE} for a given ΔT by increasing N, the total peak thermoelectric power output P_{TE} will not change. This is because the power output is also dependent on the internal resistance of the device, so for different devices with constant ΔT and varying N but equal total thermoelectric material volume, the increase in V_{TE} is exactly canceled by the increase in the total internal device resistance (*108*). This relationship is exemplified by the simplified expression for the peak P_{TE} given by

$$P_{TE} = \frac{V_{TE}^2 tw\sigma_{av}}{4L} \tag{8}$$

where σ_{av} is the average electrical conductivity of the device, and the factor of 4 comes from the necessary condition to achieve peak power output in which the load resistance is equal to the internal resistance of the device (*106*, *108*). Of

course, for practical applications it is typically the load resistance which is fixed, therefore this demonstrates why it is often necessary to combine the thermoelectric elements in this device structure in order to maximize P_{TE}.

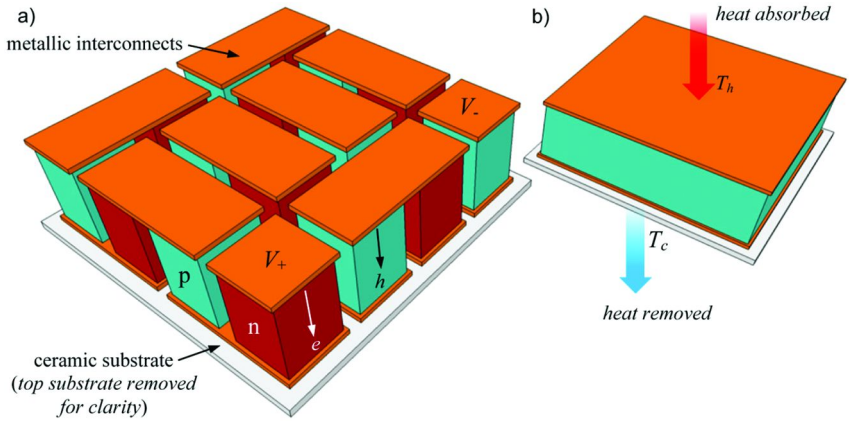

Figure 5. a) Thermoelectric device composed of alternating bulk p-type and n-type materials connected electrically in series and thermally in parallel. When heat flows through the device creating a temperature difference $T_h - T_c$ a thermoelectric voltage V_{TE} is generated across the terminal metal interconnects. b) Device structure composed of a single p- or n-type material used to illustrate the thermoelectric power output.

Each thermocouple subunit comprising the complete multiple element device is very similar in structure to a p/n diode, except for one key difference. For a p/n diode, the p-type and n-type materials are in direct contact resulting in a depletion zone and large localized internal field centered around the interface. For the thermocouple subunit, however, the p-type and n-type materials are separated by a metallic interconnect which results in Schottky or Ohmic contacts at the metal/thermoelectric interface. Additionally, when subject to a temperature gradient that further bends the bands of the thermoelectric material by increasing the carrier concentration on the hot side, current is allowed to flow through the device. The typical band structure for a p-type/n-type thermocouple exposed to a ΔT is shown in Figure 6 in the same state as that described in Figure 1.

For the thin film CNT-based polymer composite thermoelectric materials, however, the physical device architecture shown in Figure 5 is not appropriate since the temperature gradient runs parallel to the surface of the thin films. Therefore, the novel device architecture shown in Figure 7 was introduced for thin film thermoelectrics that utilizes the same bulk thermoelectric device operating principle in which the thermoelectric elements are connected electrically in series and thermally in parallel (*106*). Alternating p-type and n-type CNT

In Polymer Composites for Energy Harvesting, Conversion, and Storage; Li, L., et al.;
ACS Symposium Series; American Chemical Society: Washington, DC, 2014.

composite layers are separated by staggered polymer insulating layers (such as pure polyvinylidene fluoride, PVDF) that prevent conduction between successive thermoelectric layers except at the interconnects. Since this device structure operationally functions the same as the bulk thermoelectric device structure, the V_{TE} and P_{TE} can be determined from Equations 7 and 8, respectively, with the same load resistance matching condition for peak P_{TE} output.

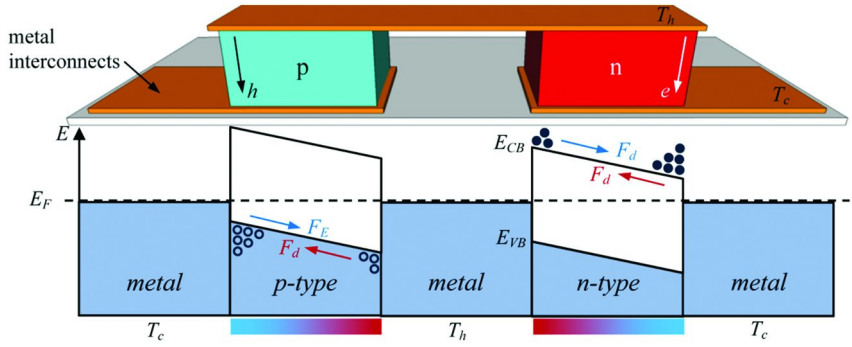

Figure 6. Simplified band structure for a single p-type/n-type thermocouple with metal interconnects between thermoelectric elements.

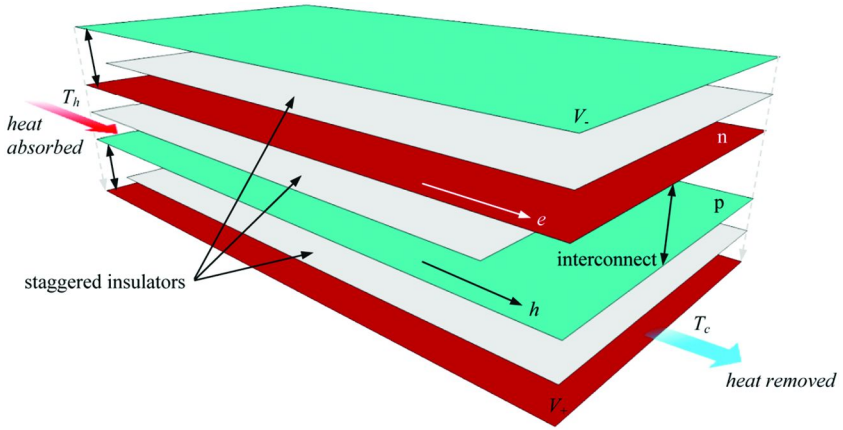

Figure 7. Thermoelectric device composed of alternating p-type and n-type thin film thermoelectric layers, where staggered insulator layers are used to block conduction between alternating p-type and n-type thermoelectric layers except in the interconnect regions.

In Polymer Composites for Energy Harvesting, Conversion, and Storage; Li, L., et al.;
ACS Symposium Series; American Chemical Society: Washington, DC, 2014.

Performance and Application

Since the thermoelectric properties of a given CNT-based polymer composite are intrinsic, the maximum thermoelectric power output ultimately depends on the specific application parameters. There are a number of extrinsic properties that affect V_{TE} and P_{TE} including the temperature gradient (ΔT), the absolute temperature (T), the dimensions of the composite device (L, w, t), and the load resistance connected in series with the device (R_l). These parameters are illustrated in the simple P_{TE} test circuit shown in Figure 8. The temperature effects influence the thermoelectric power output through the voltage generated by the material since this voltage is linearly proportional to the temperature gradient via the Seebeck coefficient, which is also temperature dependent. Since the Seebeck coefficient is intrinsic to the material, however, the dimensions of the film or the load resistance do not affect the thermoelectric voltage.

Alternatively, the dimensions and R_l do affect the thermoelectric power output through the current generated within the circuit. As expected for a thin film material, the internal resistance is directly proportional to the length, and indirectly proportional to the width and thickness of the film, while the maximum power output occurs when the load resistance matches the internal resistance of the film. These effects combine in general to determine the total thermoelectric power output given by

$$P_{TE}(T,\Delta T,R_l,D)=\left(\frac{\alpha(T)\Delta T}{R_l+L/wt\sigma(T)}\right)^2 R_l \tag{9}$$

where $\alpha(T)$ and $\sigma(T)$ are the temperature dependent Seebeck coefficient and electrical conductivity, respectively (*108*).

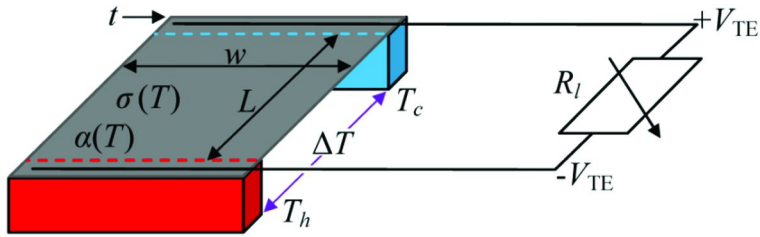

Figure 8. Extrinsic parameters that affect the power output of a CNT-based polymer composite thermoelectric generator. Reproduced with permission from Ref. (108), 2012, Elsevier.

Power output from the multilayered thin film device architecture introduced above was first demonstrated using 20 wt% CNT/PVDF composites for the thermoelectric material, where the p-type layers utilized as-synthesized CNTs and the n-type layers utilized nitrogen doped CNTs (*106*). The resulting average

In Polymer Composites for Energy Harvesting, Conversion, and Storage; Li, L., et al.;
ACS Symposium Series; American Chemical Society: Washington, DC, 2014.

room temperature power factor (*PF*) of this device was 0.5 μWm^{-1}K^{-2}. The power factor is important because it is directly related to the potential device power output (P_D) through P_{TE} (Equation 8 for the load resistance matching condition), and is given by

$$P_D = \frac{t_i w_i \Delta T^2}{4L_t} PF \tag{10}$$

where t_i and w_i are the thickness and width of an individual conducting layer, respectively, and L_t is the total conduction path length through the multilayered device. Further studies have produced multielement CNT-based composite thermoelectric devices consisting of PEI doped CNTs with power factors around 9 μWm^{-1}K^{-2} (*85*, *103*, *109*), polyaniline coated CNTs ($PF \approx 1.3$ μWm^{-1}K^{-2}) (*110*), printable CNT-polystyrene elements ($PF \approx 0.15$ μWm^{-1}K^{-2}) (*111*), and triphenylphosphine doped CNTs ($PF \approx 27$ μWm^{-1}K^{-2}) (*87*).

These power factors can be used to calculate the potential power output using Equation 10 for specific temperature gradients and device dimensions. Practically, for a device used in ambient conditions, the maximum safe ΔT is about 50 K to avoid reaching the melting point of the base polymer and compromising the device structure. In regards to the dimensions, the device can theoretically be scaled to any size. Several proposed applications include wearable fabrics that collect waste body heat, sleeves for cooling lines in industrial applications, wraps around engine exhaust pipes, and large surface area sheets to collect heat from locations such as attics and walls. Considering the power factors for the highest performing triphenylphosphine doped CNT-based polymer devices, estimated power outputs include 0.08 W from a full body suit at a ΔT of 5 K, and 45 W from a large sheet covering a typical roof of surface area 150 m^2 and a ΔT of 15 K. Ultimately, for a device exposed to a safe ΔT of 50 K with the associated necessary L_t, the maximum power density is about 1 W/m^2.

Conclusion

The thermoelectric properties of carbon nanotubes have been investigated quite extensively since their discovery, while those of CNT-based composites have grown in interest over the last decade. Regardless of this growing knowledge base, however, practical use of CNTs as energy harvesting thermoelectric materials in low powered applications has not yet been realized for several reasons. Aside from the financial restriction causing the cost of CNTs to remain high due to the lack of commercially viable applications (*112*), the thermoelectric performance of CNTs has remained relatively low with no clear direction for systematic improvements due to the sometimes unexpected and unfavorable relationship observed between the thermoelectric parameters of semiconducting materials. Fortunately, this trend may begin to be overturned with the recent work of J. Sun *et al*. in which they demonstrate that the electrical conductivity and Seebeck coefficient may simultaneously be increased in a small regime by intentionally introducing ground state hole carriers (through doping) at an orbital energy below that of the hole energy for the major component (*113*). Additionally,

In Polymer Composites for Energy Harvesting, Conversion, and Storage; Li, L., et al.;
ACS Symposium Series; American Chemical Society: Washington, DC, 2014.

the incorporation of CNTs into a polymer composite matrix may have the ability to slightly decouple the relationship between σ and α as exemplified in preliminary studies mentioned above (*87*, *100*).

Precise control and understanding of the specific variables that affect the thermoelectric parameters would allow for the fine tuning of these intrinsic properties in order to maximize *ZT* and finally realize real world applications. Nevertheless, due to their relatively low obtainable power factors, the scalability, flexibility, and relative ease of fabrication will be the keys to utilizing CNT composites in real world applications not suited to more fragile crystalline materials like bismuth telluride with high power factors. Additionally, the intended applications are those in which heat is otherwise being lost to the environment, so any amount that can be captured would be beneficial, particularly in systems which include a battery for storing scavenged energy. With available technologies such as these CNT-based polymer composite thermoelectric generators, we can begin to rethink the way we harvest and use energy with a tangible goal of future sustainability.

References

1. Vineis, C. J.; Shakouri, A.; Majumdar, A.; Kanatzidis, M. G. *Adv. Mater.* **2010**, *22* (36), 3970–3980.
2. Egli, P. H., *Thermoelectricity*; John Whiley & Sons: New York, 1960.
3. Vining, C. B. *Nat. Mater.* **2008**, *7*, 765–766.
4. Vining, C. B. *Nat. Mater.* **2009**, *8*, 83–85.
5. Dresselhaus, M. S.; Chen, G.; Tang, M. Y.; Yang, R.; Lee, H.; Wang, D.; Ren, Z.; Fleurial, J.-P.; Gogna, P. *Adv. Mater.* **2007**, *19*, 1043–1053.
6. Goldsmid, H. J. *Thermoelectric Refrigeration*; Plenum Press: New York, 1964.
7. Snyder, G. J.; Toberer, E. S. *Nat. Mater.* **2008**, *7*, 106–114.
8. Das, V. D.; Soundararajan, N. *Phys. Rev. B* **1988**, *37* (9), 4552–4559.
9. Goldsmid, H. J. *Proc. Phys. Soc. London, Sect.B* **1956**, *69*, 203–209.
10. Hicks, L. D.; Dresselhaus, M. S. *Phys. Rev. B* **1993**, *47* (19), 12727–12731.
11. Venkatasubramanian, R.; Siivola, E.; Colpitts, T.; O'Quinn, B. *Nature* **2001**, *413*, 597.
12. Harman, T. C.; Taylor, P. J.; Walsh, M. P.; LaForge, B. E. *Science* **2002**, *297*, 2229–2232.
13. Harman, T. C.; Spears, D. L.; Manfra, M. J. *J. Electron. Mater.* **1996**, *25*, 1121–1127.
14. Poudel, B.; Hao, Q.; Ma, Y.; Lan, Y.; Minnich, A.; Yu, B.; Yan, X.; Wang, D.; Muto, A.; Vashaee, D.; Chen, X.; Liu, J.; Dresselhaus, M. S.; Chen, G.; Ren, Z. *Science* **2008**, *320*, 634–638.
15. Joshi, G.; Lee, H.; Lan, Y.; Wang, X.; Zhu, G.; Wang, D.; Gould, R. W.; Cuff, D. C.; Tang, M. Y.; Dresselhaus, M. S.; Chen, G.; Ren, Z. *Nano Lett.* **2008**, *8* (12), 4670–4674.

16. Wang, X. W.; Lee, H.; Lan, Y. C.; Zhu, G. H.; Joshi, G.; Wang, D. Z.; Yang, J.; Muto, A. J.; Tang, M. Y.; Klatsky, J.; Song, S.; Dresselhaus, M. S.; Chen, G.; Ren, Z. F. *Appl. Phys. Lett.* **2008**, *93*, 193121.
17. Koza, M. M.; Johnson, M. R.; Viennois, R.; Mutka, H.; Girard, L.; Ravot, D. *Nat. Mater.* **2008**, *7*, 805–810.
18. Nolas, G.; Morelli, D.; Tritt, T. *Annu. Rev. Mater. Sci.* **1999**, *29*, 89–116.
19. Park, K. H.; Kim, I. H.; Choi, S. M.; Seo, W. S.; Cheong, D. I.; Kang, H. *J. Electron. Mater.* **2013**, *42*, 1377–1381.
20. Christensen, M.; Abrahamsen, A. B.; Christensen, N. B.; Juranyi, F.; Andersen, N. H.; Lefmann, K.; Andreasson, J.; Bahl, C. R. H.; Iversen, B. B. *Nat. Mater.* **2008**, *7*, 811–815.
21. Karttunen, A.; Faessler, T. *ChemPhysChem* **2013**, *14*, 1807–1817.
22. Koga, K.; Suzuki, K.; Fukamoto, M.; Anno, H.; Tanaka, T.; Yamamoto, S. *J. Electron. Mater.* **2009**, *38*, 1427–1432.
23. Tritt, T.; Boettner, H.; Chen, L. *MRS Bull.* **2008**, *33*, 366–368.
24. Kim, D.; Kim, Y.; Choi, K.; Grunlan, J. C.; Yu, C. *ACS Nano* **2009**, *4* (1), 513–523.
25. Iijima, S. *Nature* **1991**, *354*, 56–58.
26. Esumi, K.; Ishigami, M.; Nakajima, A.; Sawada, K.; Honda, H. *Carbon* **1995**, *34*, 279–281.
27. Desposito, J. *Electron. Design* **1998**, *46*, 30–31.
28. Kwon, Y.-K.; Tománek, D. *Phys. Rev. B* **1998**, *58*, R16.
29. Kaiser, A. B.; Park, Y. W.; Kim, G. T.; Choi, E. S.; Düsberg, G.; Roth, S. *Synth. Met.* **1999**, *103*, 2547–2550.
30. Zhang, Z.; Lieber, C. M. *Appl. Phys. Lett.* **1993**, *62*, 2792–2794.
31. White, C. T.; Todorov, T. N. *Nature* **1998**, *393*, 240–242.
32. Ruoff, R. S.; Lorents, D. C. *Carbon* **1995**, *33*, 925–930.
33. Iijima, S.; Brabec, C.; Maiti, A.; Bernholc, J. *J. Chem. Phys.* **1996**, *104*, 2089–2092.
34. Treacy, M. M. J.; Ebbesen, T. W.; Gibson, J. M. *Nature* **1996**, *381*, 678–680.
35. Dresselhaus, M. S.; Dresselhaus, G.; Eklund, P. C. *Science of Fullerines and Carbon Nanotubes*; Academic Press Inc.: San Diego, 1996.
36. Zhao, X.; Liu, Y.; Inoue, S.; Suzuki, T.; Jones, R. O.; Ando, Y. *Phys. Rev. Lett.* **2004**, *92*, 125502.
37. Tans, S.; Devoret, M.; Dai, J.; Thess, A.; Smalley, R. E.; Geerligs, L.; Dekker, C. *Nature* **1997**, 474–477.
38. Kaiser, A. B. *Rep. Prog. Phys.* **2001**, *64*, 1–49.
39. Kaiser, A. B.; Skákalová, V. *Chem. Soc. Rev.* **2011**, *40*, 3786–3801.
40. Sheng, P. *Phys. Rev. B* **1980**, *21* (6), 2180–2195.
41. Morgan, C.; Alemipour, Z.; Baxendale, M. *Phys. Status Solidi A* **2008**, *205* (6), 1394–1398.
42. Kaiser, A. B.; Düsberg, G.; Roth, S. *Phys. Rev. B* **1998**, *57* (3), 1418–1421.
43. Carroll, D. L.; Czerw, R.; Webster, S. *Synth. Met.* **2005**, 155, 694–697.
44. Skákalová, V.; Kaiser, A. B.; Woo, Y.-S.; Roth, S. *Phys. Rev. B* **2006**, *74*, 085403.
45. Kaiser, A. B. *Synth. Met.* **1991**, *45*, 183–196.
46. Kaiser, A. B. *Adv. Mater.* **2001**, *13*, 927–941.

47. Kaiser, A. B.; Subramaniama, C. K.; Gilberda, P. W.; Wessling, B. *Synth. Met.* **1995**, *69*, 197–200.
48. Subramaniam, C. K.; Kaiser, A. B.; Gilberd, P. W.; Liu, C.-J.; Wessling, B. *Solid State Commun.* **1996**, *97* (3), 235–238.
49. Skákalová, V.; Kaiser, A. B.; Dettlaff-Weglikowska, U.; Hrnčariková, K.; Roth, S. *J. Phys. Chem. B* **2005**, *109*, 7174–7181.
50. Ryu, Y.; Yin, L.; Yu, C. *J. Mater. Chem.* **2012**, *22*, 6959.
51. Ryu, Y.; FreemanYu, D., C. *Carbon* **2011**, *49*, 4745–4751.
52. Lee, R. S.; Kim, H. J.; Fischer, J. E.; Thess, A.; Smalley, R. E. *Nature* **1997**, *388*, 255–257.
53. Sumanasekera, G. U.; Adu, C. K. W.; Fang, S.; Eklund, P. C. *Phys. Lett.* **2000**, *85* (5), 1096–1099.
54. Shina, M. K.; Kima, Y. J.; Kima, S. I.; Kimb, S.-K.; Haiwon, Leeb; Spinks, G. M.; Kima, S. J. *Sens. Actuators B* **2008**, *134*, 122–126.
55. Hecht, D.; Hu, L.; Grüner, G. *Appl. Phys. Lett.* **2006**, *89*, 133112.
56. Baxendale, M.; Lim, K. G.; Amaratunga, G. L. *Phys. Rev. B* **2000**, *61* (19), 12705–12708.
57. Hone, J.; Llaguno, M. C.; Nemes, N. M.; Johnson, A. T.; Fischer, J. E.; Walters, D. A.; Casavant, M. J.; Schmidt, J.; Smalley, R. E. *Appl. Phys. Lett.* **2000**, *77* (5), 666–668.
58. Li, Q.; Li, Y.; Zhang, X.; Chikkannanavar, S. B.; Zhao, Y.; Dangelewicz, A. M.; Zheng, L.; Doorn, S. K.; Jia, Q.; Peterson, D. E.; Arendt, P. N.; Zhu, Y. *Adv. Mater.* **2007**, *19*, 3358–3363.
59. Peng, H.; Sun, X. *Chem. Phys. Lett.* **2009**, *471*, 103–105.
60. Postma, H. W. C.; Jonge, M. d.; Yao, Z.; Dekker, C. *Phys. Rev. B* **2000**, *62* (16), 653–656.
61. Che, J.; Çağın, T.; III, W. A. G. *Nanotechnology* **2000**, *11*, 65–69.
62. Gonnet, P.; Liang, Z.; Choi, E. S.; Kadambala, R. S.; Zhang, C.; Brooks, J. S.; Wang, B.; Kramer, L. *Curr. Appl. Phys.* **2006**, *6*, 119–122.
63. Hone, J.; Whitney, M.; Piskoti, C.; Zettl, A. *Phys. Rev. B* **1999**, *59* (4), 2514–2516.
64. Itkis, M. E.; Borondics, F.; Yu, A.; Haddon, R. C. *Nano Lett.* **2007**, *7* (4), 900–904.
65. Small, J. P.; Perez, K. M.; Kim, P. *Phys. Rev. Lett.* **2003**, *91*, 256801.
66. Small, J. P.; Shi, L.; Kim, P. *Solid State Commun.s* **2003**, *127*, 181–186.
67. Kang, D.; Park, N.; Ko, J.-h.; Bae, E.; Park, W. *Nanotechnology* **2005**, *16*, 1048–1052.
68. Yu, C.; Shi, L.; Yao, Z.; Li, D.; Majumdar, A. *Nano Lett.* **2005**, *5* (9), 1842–1846.
69. Tian, M.; Chen, L.; Li, F.; Wang, R.; Mao, Z.; Zhang, Y. *J. Appl. Phys.* **1997**, *82* (6), 3164–3166.
70. Hone, J.; Ellwood, I.; Muno, M.; Mizel, A.; Cohen, M. L.; Zettl, A.; Rinzler, A. G.; Smalley, R. E. *Phys. Rev. Lett.* **1998**, *80* (5), 1042–1045.
71. Grigorian, L.; Sumanasekera, G. U.; Loper, A. L.; Fang, S. L.; Allen, J. L.; Eklund, P. C. *Phys. Rev. B* **1999**, *60* (16), 309–311.
72. Mahan, G. D. *Thermoelectricity in Metals and Alloys*; Taylor & Francis: London, 1997.

73. Bradley, K.; Jhi, S.-H.; Collins, P. G.; Hone, J.; Cohen, M. L.; Louie, S. G.; Zettl, A. *Phys. Rev. Lett.* **2000**, *85* (20), 4361–4354.
74. Collins, P. G.; Bradley, K.; Ishigami, M.; Zettl, A. *Science* **2000**, *287*, 1801–1804.
75. Romero, H. E.; Sumanasekera, G. U.; Mahan, G. D.; Eklund, P. C. *Phys. Rev. B* **2002**, *65*, 205410.
76. Hewitt, C. A.; Craps, M.; Czerw, R.; Carroll, D. L. *Synth. Met.* **2013**, *184*, 68–72.
77. Hewitt, C. A.; Kaiser, A. B.; Craps, M.; Czerw, R.; Carroll, D. L. *J. Appl. Phys.* **2013**, *114*, 083701.
78. Choi, Y.-M.; Lee, D.-S.; Czerw, R.; Chiu, P.-W.; Grobert, N.; Terrones, M.; Reyes-Reyes, M.; Terrones, H.; Charlier, J.-C.; Ajayan, P. M.; Roth, S.; Carroll, D. L.; Park, Y.-W. *Nano Lett.* **2003**, *3* (6), 839–842.
79. Vavro, J.; Llaguno, M. C.; Fischer, J. E.; Ramesh, S.; Saini, R. K. *Phys. Rev. Lett.* **2003**, *90* (6), 87–93.
80. Kong, W. J.; Lu, L.; Zhu, H. W.; Wei, B. Q.; Wu, D. H. *J. Phys.: Condens. Matter* **2005**, *17*, 1923–1928.
81. Meng, J. F.; Shekar, N. V. C.; Badding, J. V. *Mater. Lett.* **2005**, *59*, 3973–3975.
82. Mirza, S. M.; Grebel, H. *Appl. Phys. Lett.* **2008**, *92*, 203116.
83. Yu, C.; Ryu, Y.; Yin, L.; Yang, H. *ACS Nano* **2011**, *5* (2), 1297–1303.
84. Shim, M.; Javey, A.; Kam, N. W. S.; Dai, H. *J. Am. Chem. Soc.* **2001**, *123*, 11512–11513.
85. Hewitt, C. A.; Montgomery, D. S.; Barbalace, R. L.; Carlson, R. D.; Carroll, D. L. *J. Appl. Phys.* **2014** accepted for publication.
86. Freeman, D. D.; Choi, K.; Yu, C. *PLoS One* **2012**, *7*, e47822.
87. Nonoguchi, Y.; Ohashi, K.; Kanazawa, R.; Ashiba, K.; Hata, K.; Nakagawa, T.; Adachi, C.; Tanase, T.; Kawai, T. *Sci. Rep.* **2013**, *3*, 3344.
88. Campos-Delgado, J.; Maciel, I. O.; Cullen, D. A.; Smith, D. J.; Jorio, A.; Pimenta, M. A.; Terrones, H.; Terrones, M. *ACS Nano* **2010**, *4*, 1696–1702.
89. Kunadian, I.; Andrews, R.; Mengüç, M. P.; Qian, D. *Carbon* **2009**, *47*, 589–601.
90. Kaiser, A. B. *Phys. Rev. B* **1989**, *40* (5), 2806–2813.
91. McIntosh, G. C.; Kaiser, A. B. *Curr. Appl. Phy.* **2001**, *1*, 145–148.
92. Yu, C.; Choi, K.; Yin, L.; Grunlan, J. C. *ACS Nano* **2011**, *5* (10), 7885–7892.
93. Yu, C.; Kim, Y. S.; Kim, D.; Grunlan, J. C. *Nano Lett.* **2008**, *8* (12), 4428–4432.
94. Sundaray, B.; Subramanian, V.; Natarajan, T. S.; Krishnamurthy, K. *Appl. Phys. Lett.* **2006**, *88*, 143114.
95. Xu, Y.; Ray, G.; Abdel-Magid, B. *Composites, Part A* **2006**, *37*, 114–121.
96. Du, J.-H.; Bai, J.; Cheng, H.-M. *eXPRESS Polym. Lett.* **2007**, *1* (5), 253–273.
97. Haggenmueller, R.; Guthy, C.; Lukes, J. R.; Fischer, J. E.; Winey, K. I. *Macromolecules* **2007**, *40*, 2417–2421.
98. Muñoz, E.; Suh, D.-S.; Collins, S.; Selvidge, M.; Dalton, A. B.; Kim, B. G.; Razal, J. M.; Ussery, G.; Rinzler, A. G.; Martinez, M. T.; Baughman, R. H. *Adv. Mater.* **2005**, *17* (8), 1064–1067.

99. Hewitt, C. A.; Kaiser, A. B.; Roth, S.; Craps, M.; Czerw, R.; Carroll, D. L. *Appl. Phys. Lett.* **2011**, *98*, 183110.
100. Hewitt, C. A.; Carroll, D. L. *J. Nano Energy Power Res.* **2014** accepted for publication.
101. Kymakis, E.; Amaratunga, G. A. *J. Appl. Phys.* **2006**, *99*, 084302.
102. Zhan, G. D.; Kuntz, J. D.; Mukherjee, A. K.; Zhu, P. X.; Koumoto, K. *Scr. Mater.* **2006**, *54*, 77–82.
103. Yu, C.; Murali, A.; Choi, K.; Ryu, Y. *Energy Environ. Sci.* **2012**, *5*, 9481.
104. Wang, L.; Jia, X.; Wang, D.; Zhu, G.; Li, J. *Synth. Met.* **2013**, *181*, 79–85.
105. Piao, M.; Na, J.; Choi, J.; Kim, J.; Kennedy, G. P.; Kim, G.; Roth, S.; Dettlaff-Weglikowska, U. *Carbon* **2013**, *62*, 430–437.
106. Hewitt, C. A.; Kaiser, A. B.; Roth, S.; Craps, M.; Czerw, R.; Carroll, D. L. *Nano Lett.* **2012**, *12*, 1307–1310.
107. Snyder, G. J. *Interface* **2008**, 54–56.
108. Hewitt, C. A.; Carroll, D. L. *Synth. Met.* **2012**, *162*, 2379–2382.
109. Kim, S. L.; Choi, K.; Tazebay, A.; Yu, C. *ACS Nano* **2014**, *8*, 2377–2386.
110. Yan, H.; Kou, K. *J. Mater. Sci.* **2014**, *49*, 1222–1228.
111. Suemori, K.; Hoshino, S.; Kamata, T. *Appl. Phys. Lett.* **2013**, *103*, 153902.
112. Endo, M.; Kim, Y. A.; Muramatsu, H.; Yanagisawa, T.; Hayashi, T.; Dresselhaus, M. S. *New Diamond Front. Carbon Technol.* **2004**, *14*, 1–10.
113. Sun, J.; Yeh, M.-L.; Jung, B. J.; Zhang, B.; Feser, J.; Majumdar, A.; Katz, H. E. *Macromolecules* **2010**, *43*, 2897–2903.

Subject Index

In Polymer Composites for Energy Harvesting, Conversion, and Storage; Li, L., et al.; ACS Symposium Series; American Chemical Society: Washington, DC, 2014.

E

M

In Polymer Composites for Energy Harvesting, Conversion, and Storage; Li, L., et al.; ACS Symposium Series; American Chemical Society: Washington, DC, 2014.

O

P

S

In Polymer Composites for Energy Harvesting, Conversion, and Storage; Li, L., et al.;
ACS Symposium Series; American Chemical Society: Washington, DC, 2014.

T

V

In Polymer Composites for Energy Harvesting, Conversion, and Storage; Li, L., et al.;
ACS Symposium Series; American Chemical Society: Washington, DC, 2014.